UNIVERSITY OF CALIFORNIA
RIVERSIDE

The Dual Role of Neural-Immune Signaling in the Brain: Constitutive and Post-Traumatic Toll-Like Receptor 4 Regulation of Hippocampal Dentate Network Excitability and Memory Function

A Dissertation submitted in partial satisfaction
of the requirements for the degree of

Doctor of Philosophy

in

Neuroscience

by

Susan Thy Nguyen

March 2024

Dissertation Committee:
Dr. Vijayalakshmi Santhakumar, Chairperson
Dr. Todd Fiacco
Dr. Meera Nair

The Dissertation of Susan Thy Nguyen is approved:

_____

_____

_____

Committee Chairperson

University of California, Riverside

ACKNOWLEDGEMENTS

Chapters One and Two and the Appendices are reprints of previously published papers which I co-authored throughout my PhD. As such, I would like to thank all the corresponding authors whose collaborations helped guide my project and provided me with invaluable experience both in writing and experimentation. I would also like to thank the UCR Graduate Division, the American Epilepsy Society, and National Institutes for Health for the financial support I received that allowed me to pursue my research.

Thank you to my very first PI, Dr. Aldrin Gomes at UC Davis, who helped foster my love for science and encouraged and supported my efforts to pursue graduate school throughout the years. To my guidance committee members, Dr. Todd Fiacco and Dr. Meera Nair, whose support helped shape my project. To all my professors, lab mates, and colleagues at UC Riverside that I have had the pleasure to work with, who have provided me with guidance and support both professionally and personally. To all the new friends I made in Riverside and all my lifelong friendships for joining me in all the random adventures and for all the emotional support during some of life's most challenging moments. Thank you to my family, and especially my parents, for their love and for keeping me grounded and supporting my efforts despite being hours from home.

Lastly, I would like to thank my mentor and advisor, Dr. Viji Santhakumar, for all the scientific guidance, discussions, and countless edits that helped develop my skills as a researcher. Everything that I have accomplished in these years would not have been possible without your support. Thank you.

In loving memory of my father, Hoang Minh Nguyen.

ABSTRACT OF THE DISSERTATION

The Dual Role of Neural-Immune Signaling in the Brain:
Constitutive and Post-Traumatic Toll-Like Receptor 4 Regulation of Hippocampal Dentate Network Excitability and Memory Function

by

Susan Thy Nguyen

Doctor of Philosophy, Graduate Program in Neuroscience
University of California, Riverside, March 2024
Dr. Vijayalakshmi Santhakumar, Chairperson

Neuroimmune signals within the brain have a dual role in modulating neurophysiology both at baseline and in response to injury and infection. The primary focus of existing literature is on how inflammatory cascades affect network excitability following injury or in disease states. In these studies, we focus on the innate immune receptor, Toll-Like Receptor 4 (TLR4), and identify its novel neurophysiological roles in regulating hippocampal dentate excitatory and inhibitory networks under basal conditions and after fluid percussion injury (FPI) which impact working memory and behavior. Using CLI-095, a specific TLR4 antagonist, and a combination of local field potential recordings in the presence of glial metabolic inhibitors and whole cell voltage clamp recordings, we demonstrate a constitutive role of TLR4 in the uninjured dentate gyrus. This basal TLR4 signaling is absent in the presence of glial metabolic inhibitors and selectively modulates granule cell GABAergic inhibitory currents. In uninjured mice, blocking TLR4 decreased input driven evoked inhibitory post synaptic currents (eIPSCs) and impaired both working

memory function in a Morris Water Maze task and spatial pattern separation in a Novel Object Location Task. In contrast, glial signaling is not required for TLR4 modulation of dentate excitability after brain injury. Specifically, neuronal expression of TLR4 enhances excitatory calcium permeable AMPA currents and reduces inhibitory GABA currents one week after brain injury. FPI resulted in early hilar somatostatin (SST) neuron loss, decreased eIPSC amplitude, and impaired working memory and spatial pattern separation at one week. Consistent with our finding that TLR4 is expressed on SST, but not parvalbumin interneurons, cell-type specific deletion of TLR4 in SST neurons identified that TLR4 expression in SST neurons as crucial for the injury-induced decrease in dentate eIPSC and behavioral deficits. These results indicate a differential role for cell-type specific TLR4 signaling in modulating of synaptic currents in granule cells from control and FPI mice. These studies demonstrate a novel role of TLR4 in modulating inhibitory synapses at baseline as well as after injury and provides promising therapeutic potential whereby acute targeting of TLR4 signaling after brain injury may limit post-injury increases in dentate excitability by augmenting synaptic inhibition.

Table of Contents

List of Figures

Introduction

Chapter 1

Chapter 2

Chapter 3

Appendix B

INTRODUCTION

Immunology and neuroscience have traditionally been studied as separate systems, with communication between the two initially thought to be mediated solely through circulating immune signals via the vascular system (Dantzer, 2018). Decades of research in the field of neuroimmunology have propelled the understanding that innate immune cells within the brain also produce the same cytokines locally as in the periphery (Dantzer, 2018). As our knowledge of neuroimmune signaling evolved, initial studies targeted the immune response in relation to disease and injury and demonstrated that neuroinflammation can contribute to acute and long-term changes within neuronal networks (Vezzani et al., 2011). Focus on immune receptors, ligands, and released cytokine signals, also revealed that these neuroimmune mediators are not only involved in an inflammatory response but are also constitutively expressed in low levels within in the brain and play a fundamental role in synaptic physiology and plasticity (Beattie et al., 2002; Pribiag & Stellwagen, 2014; Stellwagen & Malenka, 2006). As such, these innate immune receptors and their signaling molecules can affect both basal functions of neuronal networks, mediating developmental and homeostatic regulation of cellular and neuronal processes, and responses to neurological insult by initiating and mediating an inflammatory response.

Traumatic brain injury (TBI) is a bump, blow, or jolt to the head that results in disruption of normal function in the brain. TBI results in initial mechanical damage to cells within the brain, as well as a secondary injury through inflammatory responses that can lead to edema, hyperexcitability, and further cell death (Bramlett & Dietrich, 2007). TBI sequelae include

increased inflammatory response, involving activation of microglia, recruitment of macrophages, and the release of inflammatory mediators (Amor & Woodroofe, 2014). Mild to moderate fluid percussion injury (FPI) leads to acute cell death and results in an increase in the innate immune receptor Toll-like receptor 4 (TLR4) expression in the hippocampal dentate gyrus, which is correlated with increased seizure susceptibility and severity (Li et al., 2015). Initial studies blocking TLR4 signaling using specific pharmacological antagonists show that suppressing this signaling pathway early after injury may result in improved neurological and behavioral outcomes, however the same treatment in uninjured control animals led to opposing effects and poorer outcomes (Korgaonkar, Li, et al., 2020; Li et al., 2015). These contrasting effects may be explained by the dual role of inflammatory signaling molecules in mediating an immune response after cellular damage and their role in synaptic physiology at baseline. As such, elucidating any underlying differences between TLR4 regulation of neuronal activity in the injured and uninjured brain is crucial for therapeutic targeting.

Toll-Like Receptors

Toll-like receptors (TLRs) are an innate pattern recognition receptor involved in recognizing and mediating an immune response due to injury or infection. Mammalian TLRs were first identified based on their similarity to the *Drosophila Toll* that is involved in mediating immune responses in the fly. A mutation in a TLR gene was initially studied to investigate development of dorsal-ventral patterning in the fly, but it was found that a mutation in this gene also resulted in increased prevalence of fungal infections (Lemaitre

et al., 1996), leading to the discovery that TLR genes were involved in innate immunity. Since this initial discovery, a total of 13 TLRs have been identified in mice, with ten homologs found in humans.

TLRs are receptors that are expressed on immune cells such as macrophages and dendritic cells in the periphery, as well as in microglia, astrocytes, and neurons in the brain (Kleen & Holmes, 2010). As part of the innate immune system, TLRs participate in the first line of defense for protection against pathogens and cellular injuries. TLRs bind to pathogen associated molecular patterns (PAMPs), signals with highly conserved motifs expressed by various classes of micro-organisms, as well as danger-associated molecular patterns (DAMPs), endogenous ligands that are typically released during cellular injury (Matzinger, 2002). TLR1, TLR2, TLR4, TLR5, and TLR6 are expressed on extracellular membranes, whereas TLR3, TLR7, TLR8, and TLR9 are expressed in intracellular endosomes (Trotta et al., 2014).

Each TLR is activated by specific PAMPs and DAMPs, with some overlap in ligand specificity. Binding of TLRs with its specific ligand results in the recruitment of one of two different pathways within the cell, a MyD88-dependent pathway and a MyD88-independent pathway, named for the involvement of myeloid differentiation primary response gene 88. There are slight variations in the signaling pathways in some TLRs, however generally, most TLRs recruit a MyD88-dependent pathway, whereas TLR3 recruits a MyD88-independent pathway. TLR4 is unique in that it results in the recruitment of both a MyD88-dependent pathway and a MyD88-independent pathway (Akira & Takeda, 2004) (**Figure I.1)**.

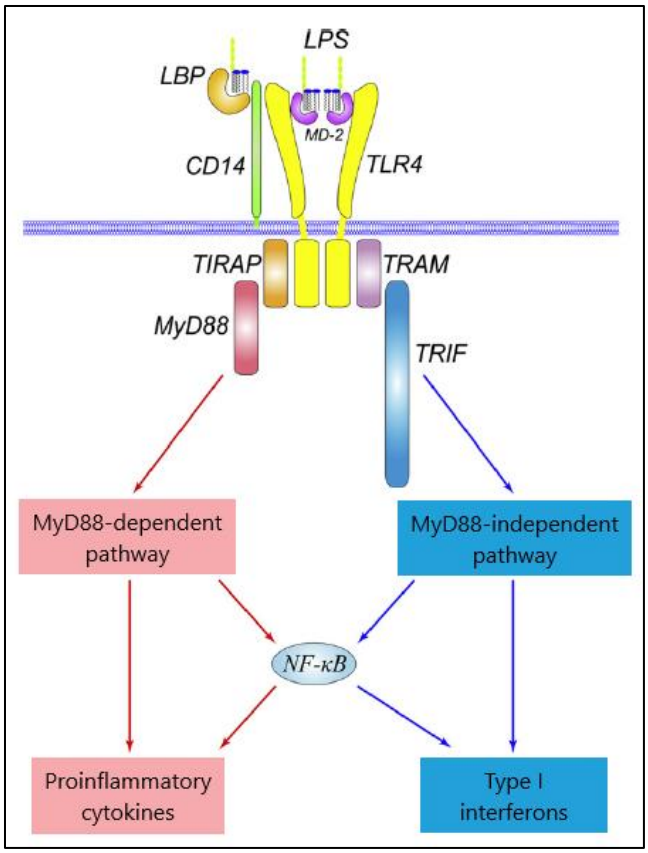

Figure I.1: Simplified overview of LPS/TLR4 signaling pathway. TLR4 signaling can be MyD88-dependent and MyD88-independent, leading to the production of proinflammatory cytokines and Type I interferons. ***Adapted from Lu et al. (2008).***

Lipopolysaccharide (LPS) is a common activator for TLR4 on monocytes and macrophages. This process requires LPS to bind to an LPS binding protein (LBP), forming a complex that associates with a protein called cluster of differentiation 14 (CD14) located on the membrane, and recruiting an extracellular myeloid differentiation factor 2 protein (MD2). In the TLR4 MyD88-dependent pathway, MyD88 recruits interleukin-1 (IL-1) receptor associated kinases (IRAKs) and tumor necrosis factor (TNF) receptor-associated factors (TRAF6) that result in activation of transforming growth factor-b-activated kinase

1 (TAK1). This, in turn, activates mitogen-activated protein kinases (MAPK) and IKK, which leads to the induction of the transcription factor nuclear factor-kappaB (NF-κB), while MAPK kinases lead to the activation of other transcription factors such as AP1. Together with NF-κB, these transcription factors lead to the production of proinflammatory cytokines including interleukin 12 (IL-12), TNFα, and IL-1β (Akira & Takeda, 2004, 2004; Lu et al., 2008).

The MyD88-independent pathway involves the recruitment of adaptor proteins TIR-domain-containing adaptor protein inducing interferon-B (TRIF) and TRIF-related Adaptor Molecule (TRAM). This TRIF-TRAM interaction results in the activation of the transcription factor Interferon Regulatory Factor-3 (IRF3) through TRAF3. This signaling pathway ultimately leads to the production of type 1 interferons(Lu et al., 2008; Takeda & Akira, 2004, 2004).

TLR4 ligands also include some viral proteins, polysaccharide, and endogenous proteins including high-mobility group box 1, or HMGB1. HMGB1 similarly interacts with TLR4 and MD2, requiring the coreceptor CD14 to initiate the signaling pathway. TLR4 signaling is required for HMGB1 mediated TNFα release, as it is not increased in TLR4 or CD14 knockout models. HMGB1 also leads to the release of MCP-1, IP-10, and MIP1α and has been shown to activate the TLR4 NF-κB pathway in epilepsy models (Maroso et al., 2010; Shi et al., 2019).

Cytokines produced through this pathway act as signals that trigger several inflammatory processes including changes in vascular permeability or activation of lymphocytes. However, under basal conditions in the naïve brain and during development, cytokines

such as TNFα have been shown to impact neurophysiology and synaptic plasticity (Beattie et al., 2002; Pribiag & Stellwagen, 2014; Stellwagen & Malenka, 2006).

Hippocampal Circuitry and Inhibition in the Dentate

The hippocampus is one of the most well studied areas of the brain due to its well-defined laminar structure and important role in learning and memory, as first discovered in the landmark case study of the patient known as H.M (Eichenbaum, 2013). The hippocampus has also been of interest in epilepsy research, having the lowest seizure threshold of any comparable brain region. The structure and networks within the hippocampus predispose its susceptibility to seizure activity.

Generally, the hippocampus forms the "trisynaptic circuit," consisting of three major synaptic areas from projection neurons. Neurons from the entorhinal cortex (EC) project to cells in the dentate gyrus (DG), which then project to the hippocampal area Cornu Ammonis 3 (CA3), and onward to pyramidal cells in the CA1 region. More specifically, afferent inputs into the hippocampus arise from layer II of the entorhinal cortex and project through the subiculum onto dentate granule cells via perforant path fibers. These perforant path (PP) fibers terminate onto the dendrites of granule cells within the outer and middle molecular layers, depending on where they originate. PP fibers that originate from the medial EC terminate onto dendrites in the middle molecular layer, whereas PP fibers originating from the lateral EC terminate onto dendrites in the outer molecular layer. A subset of layer II EC afferents also project directly to CA3, and neurons from layer III of the EC project to CA1 (**Figure I.2a**) and the subiculum. Dentate granule cells then project their axons, known as mossy fibers (MF) onto the proximal dendrites of CA3 pyramidal

cells. Dentate GCs and their MF projections also synapse onto cells within the hilus. These cells include excitatory mossy cells (MCs) as well as several different types of inhibitory interneurons. CA3 pyramidal cells project their axons, Schaffer collaterals, onto the dendrites of CA1 pyramidal cells. The pyramidal cells in CA1 then project back to both the subiculum and deeper layers of the entorhinal cortex. As such, information entering the EC from other cortical areas can project through the entire hippocampal circuit and return to where it originated. This circuit, and any underlying transformation of signaling across this circuit, is believed to be critical for the encoding of information for long-term memory, novelty, and pattern separation (Yassa & Stark, 2011). However, this reentering loop is also proposed to underlie the suscepticility of the circuit for recurrent seizure activity.

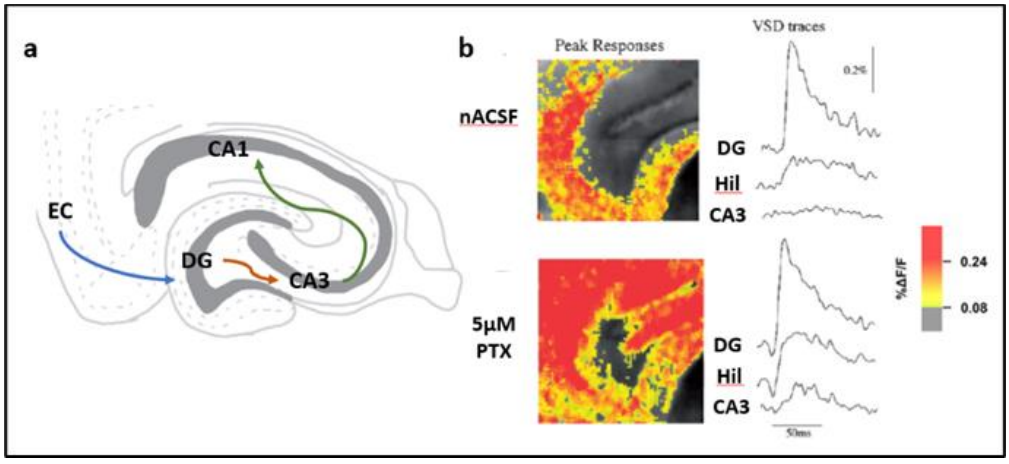

Figure I.2: **a)** Simplified schematic of hippocampal "trisynaptic circuit" showing perforant path fibers (blue) from the entorhinal cortex to the dentate gyrus, the mossy fibers (orange) from the dentate to CA3, and Schaffer collaterals (green) from CA3 to CA2. **b)** Voltage-sensitive calcium images (left) and %ΔF/F (right). Under normal conditions, input from the PP is filtered by the dentate (top) however with 5µM picrotoxin (bottom), the dentate is unable to filter EC input, leading to increased activity in the hilus and CA3. ***From Coulter DA and Carlson GC (2007).***

The dentate region of the hippocampus is of particular interest in the formation of memory as well as for its susceptibility to hyperexcitability and epileptogenesis. The DG is considered the "functional gate" of the hippocampus, whereby initial input from the EC is filtered and sparsed or separated out as it passes through the DG and sent onwards towards CA3. Calcium imaging studies of the hippocampal circuit demonstrate that though high levels of activity in the EC, which project towards the DG, while the dentate granule cells (GCs) exhibit relatively low levels activity with sparse firing) (Piatti et al., 2013). Additionally, voltage-sensitive dye imaging studies found that stimulation of the PP afferents showed high levels of activity in the molecular layer of the dentate that failed to traverse through the granule cell layer (GCL) to the hilus and CA3(Coulter & Carlson, 2007). In the presence of a low dose of the $GABA_A$ receptor antagonist, picrotoxin, PP stimulation results in high throughput of activity to the DG, hilus, and CA3 regions, indicating that this sparse firing is mediated by GABAergic signaling within the dentate (Coulter & Carlson, 2007) (**Figure I.2b**).

The diverse population and number of inhibitory interneurons within the DG are crucial in maintaining the blanket of inhibition necessary for sparse firing of dentate GCs. Initial morphological studies have identified at least 21 different interneuron types in the hilus (Houser, 2007). These interneurons can be recruited directly through EC inputs to provide feedforward inhibition onto GCs or through GC or MC synapses providing feedback inhibition back onto GCs.

Interneuron types can be classified by their location and terminal fields as well as their neurochemical identity (**Figure I.3**). Because of their complexities, typically a

combination of both classification levels are used to identify more specific subtypes of interneurons and their projections (Houser, 2007). All interneurons within the DG use GABA as their primary neurotransmitter, and thus can be identified using GAD65 and GAD67 staining.

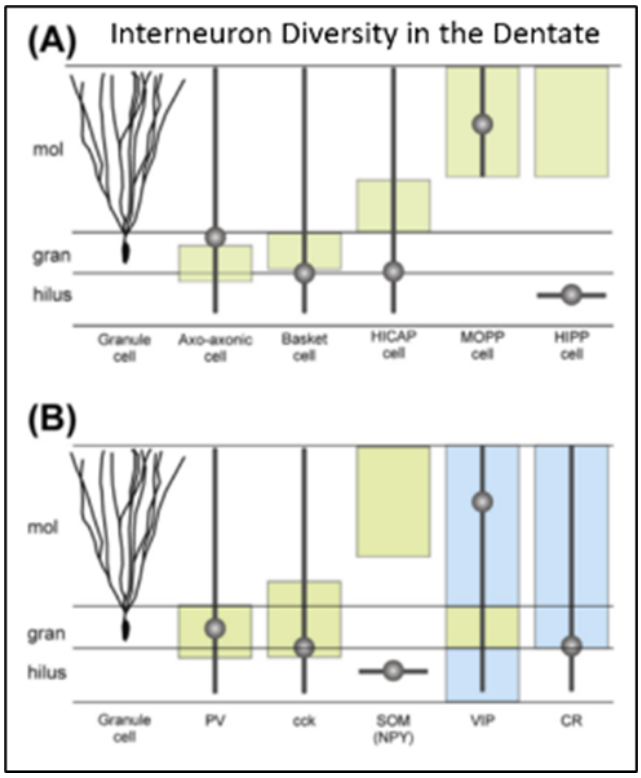

Figure I.3: Diversity of interneuron subtypes within the dentate gyrus. Interneurons within the dentate can be classified by the location of their cell bodies and terminal projections (top) or by their neurochemical identity (bottom). The dentate gyrus has numerous different types of interneurons that all use GABA as their primary neurotransmitter, providing powerful inhibition onto granule cells at various locations. ***Image from Cappaert et al. in The Rat Nervous System, 4th Ed.***

Although there are neurochemically diverse interneurons, including those expressing parvalbumin (PV), cholecystokinin (CCK), somatostatin (SST), calretinin, and

neuropeptide Y (NPY) in the DG, this project will focus on PV and SST expressing interneurons.

Parvalbumin is a calcium-binding protein that is expressed in interneuron subtypes characterized by fast and sustained firing, the basket cells and axo-axonic cells. PV basket cells typically project perisomatically, or around the cell body of neurons, and are mostly fast-spiking interneurons. PV interneurons receive excitatory inputs from mossy fibers of GCs as well as direct afferent input from the EC, providing strong feedback and feed-forward inhibition onto GCs. Basket cells are the most prominent subtype of PV interneurons in the DG. Their cell bodies are typically located at the border of the granule cell layer (GCL) and hilus, though some can be found within the GCL. Basket cell projections form a plexus that surround and synapse onto GC bodies. Basket cells have a wide distribution and can synapse with as many as 10,000 GCs.

Axoaxonic cells are a second class of PV interneurons whose cell bodies are located at the outer border of the granule cell layer as well as inside the inner molecular layer and the hilus. Their axons form an extensive branch and provide a series of *en passant* synapses along the axon initial segment (AIS) of GCs. Along with basket cells, these PV-expressing interneurons can exert powerful inhibition to GC outputs due to their perisomatic and AIS projections.

Somatostatin is a neuropeptide that is expressed in a subpopulation of dentate hilar interneurons. SST interneurons are the most abundant type of interneuron found in the DG. Many SST interneurons are considered HIPP (Hilar-Perforant Path) cells, as their cell bodies are located in the hilus and their axons project through the GCL to terminate onto

distal dendrites of GCs located in the outer molecular layer, where PP fibers from lateral EC terminate (**Figure I.3**). MFs from granule cells synapse heavily onto SST interneurons in the hilus, and these interneurons are in an ideal position to modulate PP inputs in response to GC activity. SST interneurons are sensitive to excitotoxicity, making them especially vulnerable to damage in epilepsy and traumatic brain injury (Frankowski et al., 2019; Lowenstein et al., 1992; Toth et al., 1997). Studies have also shown that SST neuron integrity within the dentate gyrus is critical for pattern separation performance in mice (Morales et al., 2020).

Pattern Separation

Pattern separation is the ability to discriminate between similar experiences and is vital for episodic memory (Yassa & Stark, 2011). Recording and imaging data across the hippocampus have demonstrated that the dentate gyrus serves a functional role in pattern separation (Leutgeb et al., 2007). Lesion studies were the first to demonstrate that the DG is required for spatial pattern separation in rats. In one study, Hunsaker et al. (2008) used a novel object location task in which animals were initially (training phase) placed in an experimental field with two objects located 60cm apart. Later in a testing phase, animals were placed back into the same environment, however the objects were shifted and placed 40cm apart. DG-lesioned animals spent less time exploring the objects, indicating that they were unable to recognize the novel locations of the shifted objects, or unable to discriminate the difference between the training and test phases of the experiment

(Hunsaker et al., 2008) (**Figure I.4a**). Kahn et al (2019) also demonstrated that increasing or decreasing dentate granule cell activity, using excitatory and inhibitory chemogenetic DREADDs (designer receptors exclusively activated by designer drugs), can impact performance on spatial object location, indicating that the precise tuning of granule cell activity is critical for pattern separation performance (Kahn et al., 2019) (**Figure I.4b**). Furthermore, in a study using optogenetic halorhodopsin to suppress SST neurons specifically in the dentate, Morales et al (2020) demonstrated that dentate SST cells regulate pattern separation behavior by modulating GC activity (Morales et al., 2020).

Electrophysiological recordings and fMRI data indicate that pattern separation in the DG is largely dependent on the degree of input similarity (Leutgeb et al., 2007). When the inputs are more similar, or that there are fewer differences between input signals, the DG produces a more robust difference in outputs. These studies looked at visual or spatial input similarities and their respective activity levels within the dentate circuit, however a recent study by Madar et al. (2019) demonstrated this ability within dentate granule cells. The authors used hippocampal slice recordings in mice and provided artificial input spiketrains with known levels of similarity, generated by varying the spike timing, to the perforant path and recorded the output spiketrain from GCs. In their study, they found that GC outputs firing were more dissimilar than the input spiketrains, indicating that single dentate granule cells within the circuit perform temporal pattern separation of spiketrain inputs from the perforant path (Madar et al., 2019a, 2019b).

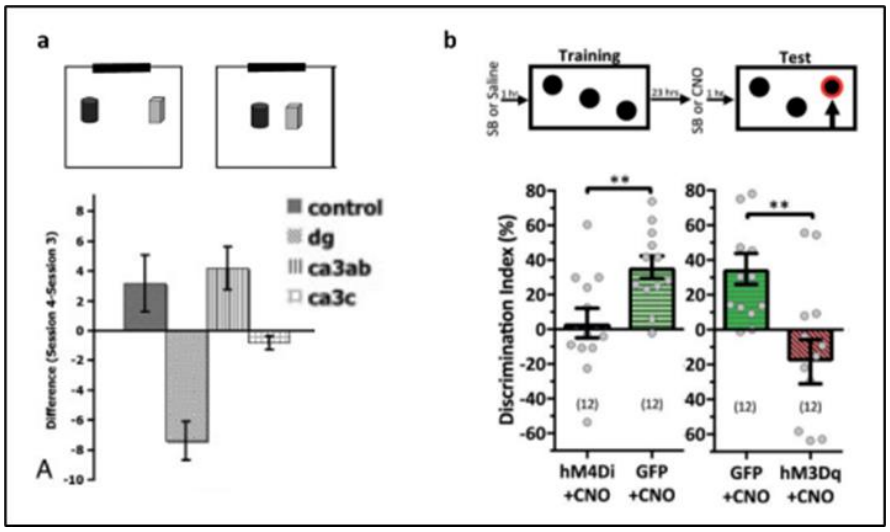

Figure I.4: Pattern separation performance is dependent on DG activity a) Object location task paradigm (top), shows that lesions in the dentate gyrus lead to impairments in performance compared to control and lesions in other hippocampal areas. ***adapted from Huntsaker et al (2008)***. b) Similar object location task paradigm, demonstrating effect of activating and inhibiting the DG using chemogenetic DREDDs on pattern separation performance. ***adapted from Kahn et al (2019)***

Several studies have proposed that the robust inhibition of the dentate is critical for pattern separation (Braganza et al., 2020; Cayco-Gajic & Silver, 2019). Studies demonstrate that the feedback inhibitory circuits within the dentate are crucial for pattern separation, and that the sparse firing resultant of this robust inhibitory network underlies GC ability to perform pattern separation (Senzai & Buzsáki, 2017). Lastly, though some studies have demonstrated that pattern separation is impaired in injury models (Ngwenya & Danzer, 2019), no studies to date have looked at correlation between cellular pattern separation and behavioral pattern separation and the effect of traumatic brain injury and role of immune receptors in these dynamics.

Innate Immune Signaling in Regulating Baseline Network Function

Recent studies have started to identify the importance of immune signaling molecules in neuronal development, synaptic plasticity, and function. In fact, several immune molecules have been found to be expressed in both neurons and immune cells and play a role in both the central nervous system and the immune system (Morimoto & Nakajima, 2019). Key inflammatory and anti-inflammatory cytokines including IL-1β, IL-6, TNFα, and TGF-β have been shown to be expressed in neurons, microglia, and astrocytes within the central nervous system and be involved in the regulation of cell proliferation, cell survival, as well as synapse development (Bauer et al., 2007; Knuesel et al., 2014). Although immune cells and signaling molecules have been demonstrated to be involved in the development and maintenance of synapses, their impact on neurophysiology has only recently been explored. Maintenance of neuronal activity is crucial for proper functioning of brain networks and any disruptions in baseline activity can adversely impact memory and behavior. As such, the cells and molecules involved in maintaining neural states are essential for normal functioning of the brain.

Recent studies have examined how immune signaling molecules and their receptors are directly involved in modulating neuronal activity. However, the vast majority of these studies focus on a disruption in network balance due to disease or injury (Vezzani et al., 2011; Villasana-Salazar & Vezzani, 2023). A few studies have shown, however, that cytokines such as TNFα and IL-17a, and IL-4 also have important roles in baseline neuromodulation (Yang et al., 2023). TNFα, of particular interest, is a cytokine produced downstream in the TLR4 pathway, and has been shown to regulate neuronal circuit

plasticity and homeostasis by modulating AMPA and GABA receptor trafficking at excitatory and inhibitory synapses, respectively (Pribiag & Stellwagen, 2013; Stellwagen et al., 2005; Stellwagen & Malenka, 2006) (**Figure I.5**). Recent studies have also shown that TLR4 plays a role in neurogenesis, cell proliferation, cell survival, and neurite development (Barak et al., 2014).

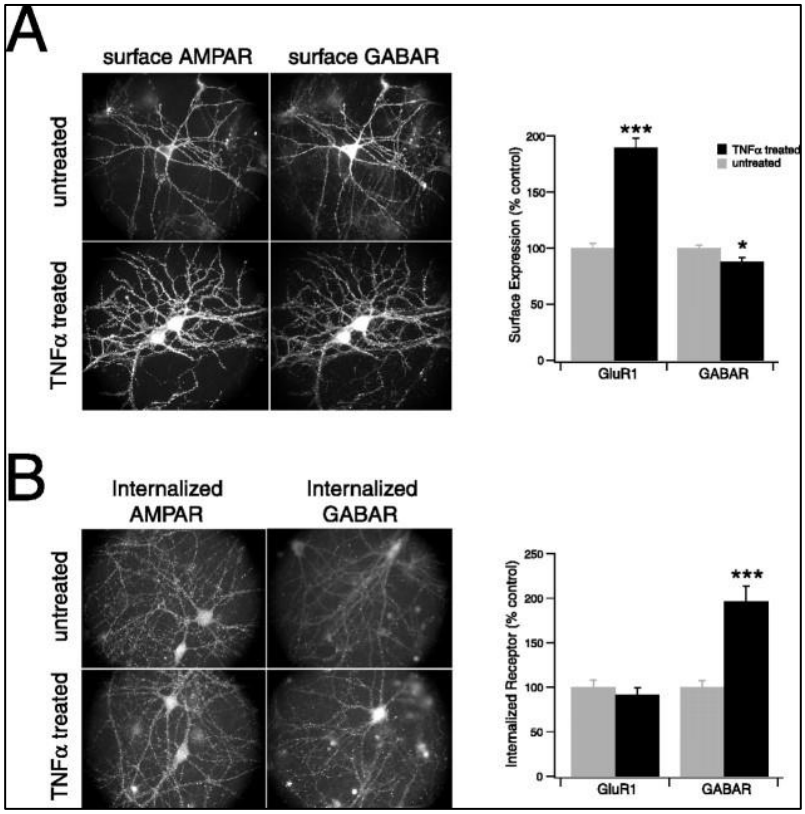

Figure I.5: TNFα decreases the surface expression of $GABA_A$ receptors. A) Representative micrographs and group data from cells double labeled for surface GluR1 and the β2/3 subunit of the $GABA_A$ receptors (GABAR). In cells showing a robust increase in GluR1 after TNFα treatment, there was a small but significant decrease in surface expression of GABAR compared with cells from untreated sister cultures. B) Sample images and composite data from cells labeled for endocytosed GluR1 or GABAR. TNF treatment (black bars) increased the endocytosis of GABAR but not GluR1 relative to cells from untreated cultures (gray bars). ***From Stellwagen et al (2007).***

Additionally, our lab has shown that blocking TLR4 at baseline reduces local field potential population spike amplitude in the hippocampal dentate network and increases kainic acid induced seizure susceptibility and severity (Korgaonkar, Li, et al., 2020; Li et al., 2015). These studies demonstrated that immune receptors may also play a role in maintaining network homeostasis under basal conditions, in the absence of an inflammatory insult. Furthermore, investigation into the underlying mechanism of how TLR4 modulates network excitability revealed that, unlike after brain injury, granule cell AMPA currents and receptor expression are not affected by blocking TLR4 at baseline (Korgaonkar, Li, et al., 2020). This emphasizes that though the same immune modulators may contribute to both constitutive and injury-induced modulation of network excitability, their underlying mechanisms are likely distinct.

Neuro-Immune Signaling Following Brain Injury

As previously mentioned, traumatic brain injuries are a result of primary mechanical and physical damage to cells within the brain as well as secondary inflammatory responses that may include the recruitment of macrophages and lymphocytes and activation of local microglia and astrocytes (Gyoneva & Ransohoff, 2015). These secondary effects of injury can lead to edema, network hyperexcitability, and additional cell death. Mechanical damage to cells also release endogenous factors that serve as DAMPs, and can include both protein DAMPs such as heat shock proteins or high-mobility group box 1 (HMGB1) proteins and non-protein DAMPs such as ATP, RNA, and DNA (Shi et al., 2019). TLRs that recognize these DAMPs have been shown to play an important role in mediating the

inflammatory responses following brain injury (Feldman et al., 2015). TLRs have been identified in different cell types within the brain including microglia, astrocytes, oligodendrocytes, neurons, and endothelial cells (Kleen & Holmes, 2010), and activation of these TLRs during injury may underlie the inflammatory responses after brain injury. In a study using RT-PCR, Hua et al (2011) found that mRNA levels of TLR1, TLR2, and TLR4 were upregulated in brain tissue 24 hours after TBI (Hua et al., 2011). Protein levels of TLR2 and TLR4 have also been shown to reach maximal at 24 hours after brain injury, reducing back to baseline levels after one to two weeks (Mao et al., 2012; Z. Zhang et al., 2012; Zhu et al., 2014). Furthermore, HMGB1 has been shown to stimulate the release of TNFα, MCP-1, IP-10, and MIP-1a through its interaction with TLR4, as release of these factors from administration of HMGB1 failed in TLR4 knockout animals (Kim et al., 2013).

Though many studies have focused on the release of cytokines and activation of immune cells following brain injury, relatively few have focused on how this immune response affects network excitability and the underlying mechanism that may lead to increased seizure susceptibility and the development of post traumatic epilepsy (PTE). Specifically, how TLR signaling pathways may be directly involved in regulating synaptic activity both before and after injury remains to be elucidated. Although protein levels of both TLR2 and TLR4 have been found to increase around the injured area following brain injury (Mao et al., 2012; Z. Zhang et al., 2012), the vast majority of trauma studies have focused on TLR4 signaling, potentially due to paucity of selective tools to study TLR2. TLR4, however, has been found to be expressed in hippocampal neurons and astrocytes (Feng et al., 2017).

Using western blot analyses of protein levels, our lab has shown a significant increase in TLR4 expression in the hippocampus as early as four hours after FPI, peaking at 24 hours, and returning to baseline levels within 7 days post injury (Li et al., 2015). Immunostaining studies have co-localized TLR4 expression with the neuronal marker, NeuN (Y. Li et al., 2015). This localization of TLR4 on neurons provides an exciting avenue to examine the potential effects of TLR4 on neuronal excitability and epileptogenesis.

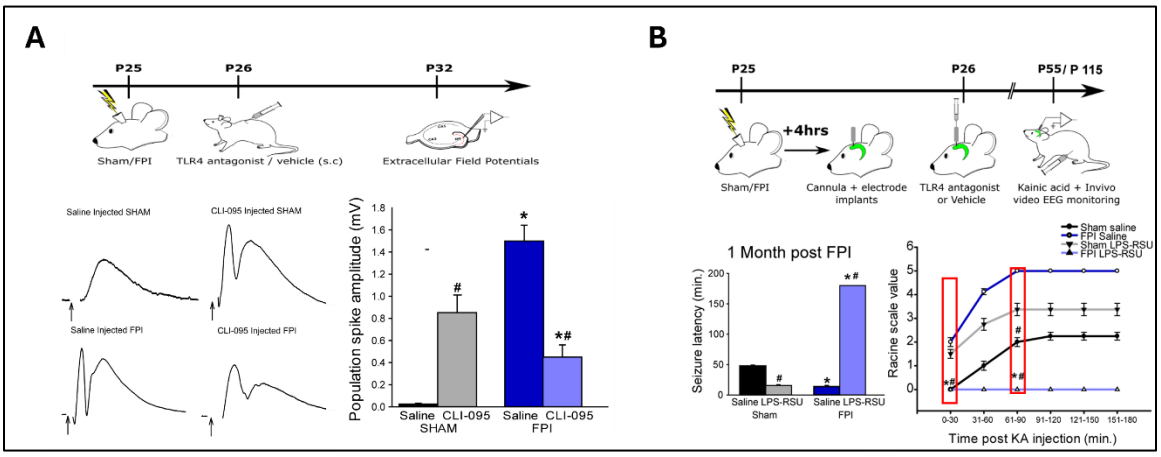

Figure I.6: TLR4 antagonism in vivo modulates dentate network excitability and seizure susceptibility. A) Dentate population responses and summary data evoked by a 4mA stimulus to the perforant path in slices from sham (above) and brain-injured (below) rats treated in vivo with saline (left) and CLI-095 (0.5mg/kg, right), demonstrating the effect of CLI-095 on perforant path–evoked GC population spike amplitude in slices. B) Summary of latency to kainic acid (KA; 5mg/kg)–induced seizures in sham and fluid percussion injury (FPI) rats 1 month post injury obtained using hippocampal depth electrodes. ***Adapted from Korgaonkar et al 2020.***

Initial studies in our lab found an increase in hippocampal dentate excitability both using local field potential recordings of population spike amplitude as well as in susceptibility to seizures following a chemoconvulsant challenge following fluid percussion injury (FPI) (Y. Li et al., 2015) (**Figure I.6**). Treatment with specific TLR4 antagonists, reduced dentate excitability in brain injured rats and prevented the development of seizures after kainic acid

injection, demonstrating a role of TLR4 signaling in modulating neuronal excitability following injury (**Figure I.6B)**. Studies in hippocampal cultures identified that TLR4 signaling enhances calcium entry through NMDA receptors (Balosso et al., 2014), leading to initial investigations isolating NMDA currents in dentate granule cells. Surprisingly, studies isolating NMDA currents by pharmacological blocking of AMPA/Kainate and GABA receptors revealed no TLR4-dependent changes in NMDA currents (Y. Li et al., 2015). Further studies in our lab isolated another ionotropic glutamate receptor, AMPA, and demonstrated an increase in overall granule cell excitation mediated by calcium permeable AMPA currents after FPI (Korgaonkar, Li, et al., 2020). These studies clearly indicate TLR4 signaling in increased dentate excitability and seizure susceptibility after injury, however whether TLR4 signaling also affects inhibitory networks within the dentate, show cell-type specific expression and function, and whether this TLR4 modulation of neuronal networks result in behavioral consequences in working memory and pattern separation has remained unanswered. Elucidating the role of TLR4 signaling in modulating dentate network circuits and its effect on memory and behavior, both at baseline and following concussive brain injury, is the focus of the following studies. Understanding the dual role of TLR4 signaling is critical not only in furthering the knowledge of immune modulation of neurophysiology in health and disease and may also lead to more specific therapeutic targets for treatments following brain injury if their underlying mechanisms prove to indeed be distinct.

CHAPTER ONE

Distinct cellular mediators drive the Janus Faces of Toll-like Receptor 4 regulation of network excitability which impacts working memory performance after brain injury.

Akshata A. Korgaonkar, PhD[1,*], **Susan Nguyen, MS**[2,#], Ying Li, PhD[1,#], Dipika Sekhar[1,2], Deepak Subramanian, PhD[1,2], Jenieve Guevarra, MS[1], Kevin C H Pang, PhD[1,3], Vijayalakshmi Santhakumar, PhD[1,2]

[1]Department of Pharmacology, Physiology and Neuroscience, Rutgers New Jersey Medical School, Newark, New Jersey 07103,
[2]Department of Molecular, Cell and Systems Biology, University of California Riverside, Riverside, California 92521
[3]Neurobehavioral Research Lab, Department of Veteran Affairs Medical Center–New Jersey Health Care System, East Orange, New Jersey

[#]Equal Contribution

Published in final edited form as:

Brain Behav Immun. 2020 August ; 88: 381–395. doi:10.1016/j.bbi.2020.03.035

Abstract

The mechanisms by which the neurophysiological and inflammatory responses to brain injury contribute to memory impairments are not fully understood. Recently, we reported that the innate immune receptor, toll-like receptor 4 (TLR4) enhances AMPA receptor (AMPAR) currents and excitability in the dentate gyrus after fluid percussion brain injury (FPI) while limiting excitability in controls. Here, we examine the cellular mediators underlying TLR4 regulation of dentate excitability and its impact on memory performance. In ex vivo slices, astrocytic and microglial metabolic inhibitors selectively abolished TLR4 antagonist modulation of excitability in controls, but not in rats after FPI, demonstrating that glial signaling contributes to TLR4 regulation of excitability in controls. In glia-depleted neuronal cultures from naïve mice, TLR4 ligands bidirectionally modulated AMPAR charge transfer consistent with neuronal TLR4 regulation of excitability, as observed after brain injury. In vivo TLR4 antagonism reduced early post-injury increases in mediators of MyD88-dependent and independent TLR4 signaling without altering expression in controls. Blocking TNFα, a downstream effector of TLR4, mimicked effects of TLR4 antagonist and occluded TLR4 agonist modulation of excitability in slices from both control and FPI rats. Functionally, transiently blocking TLR4 in vivo improved impairments in working memory observed one week and one month after FPI, while the same treatment impaired memory function in uninjured controls. Together these data identify that distinct cellular signaling mechanisms converge on TNFα to mediate TLR4 modulation of network excitability in the uninjured and injured brain and demonstrate a role for TLR4 in regulation of working memory function.

Introduction

A growing number of studies suggest that immune signaling can modulate nervous system function and plasticity (Pribiag & Stellwagen, 2014; Van Vliet et al., 2018). Activation of glial inflammatory signals, including TNFα and purinergic receptors, have been shown to impact synaptic plasticity and hippocampal memory function (Beattie et al., 2002; Belarbi et al., 2012; Pascual et al., 2012; Pribiag & Stellwagen, 2014). Increases in neuronal excitability and immune activation are hallmarks of traumatic brain injury and present a condition in which neuroimmune interactions are potentially accentuated (Chiu et al., 2016; Neuberger et al., 2017). While posttraumatic inflammatory responses are implicated in neurodegeneration, and immunosuppressants can improve neurological outcomes after brain injury (Saletti et al., 2019), mechanisms underlying immune regulation of neuronal function and behaviors are not fully understood. Among the immune pathways activated by brain injury, Toll-like receptor 4 (TLR4), an innate immune Pattern Recognition Receptor, has been shown to contribute to sterile inflammatory responses (Laird et al., 2014; Vezzani et al., 2011; Zhu et al., 2014). Although TLR4 is traditionally recruited in defense against microbial pathogens, it can be activated by endogenous ligands released from injured tissue and dying cells, making it a critical link between brain injury and the ensuing inflammatory response (Kielian, 2006). While TLR4 upregulation after brain injury is well documented (Ahmad et al., 2013; Laird et al., 2014; Ye et al., 2014), we recently demonstrated a preferential localization of TLR4 in hippocampal dentate granule cell layer and hilar neurons rather than in glia (Y. Li et al., 2015). Our results revealed that TLR4 signaling reduced excitability in ex vivo slices from sham injured animals while

enhancing excitability after brain injury (Y. Li et al., 2015). Moreover, we recently reported that brief in vivo antagonism of TLR4 reduced posttraumatic increases in seizure susceptibility one to three months after injury, while augmenting risk for seizures in controls (Korgaonkar, Li, et al., 2020), indicating that brain injury and changes in TLR4 signaling have lasting effects on dentate network excitability. The potential contribution of glial signaling and behavioral consequences of this differential TLR4 regulation of dentate network excitability are currently unknown.

TLR4 is known to be expressed in both neurons and glia (Okun et al., 2012). However, a majority of the established functional effects of TLR4 in the CNS involve glial signaling and little is known about the role of neuronal TLR4. Consequently, signaling downstream of TLR4 has been elucidated primarily in glia. Activation of microglial and astrocytic TLR4 is known to engage two distinct signaling cascades, the pathway dependent on the Myeloid Differentiation factor 88 (MyD88) and the MyD88independent pathway which activates the TIR-domain-containing adapter-inducing interferon-β (TRIF) (Kawai & Akira, 2007). Recruitment of the MyD88-dependent pathway in astrocytes and microglia leads to transcription of nuclear factor-kappa B (NF-κB) and production of the pro-inflammatory cytokine Tumor Necrosis Factor α (TNFα). Glia-derived TNFα has been shown to activate neuronal TNF receptor 1 (TNFR1) and mediate increases in NMDA receptor-dependent synaptic plasticity and AMPA receptor (AMPAR) surface expression (Stellwagen et al., 2005). The MyD88-independent pathway involves the recruitment of TRIF to activate Interferon regulatory factor 3 (IRF3), which in turn causes the production of interferon-β. Whether these or other signaling pathways are recruited by neuronal TLR4

remains unknown. A second aspect of interest concerns the functional consequences of TLR4 regulation in hippocampal dentate excitability. Sparse granule cell activity is critical for dentate spatial working memory function (Dengler & Coulter, 2016). Conditions that enhance dentate excitability or impair inhibition compromise memory function (Kahn et al., 2019). Indeed, brain injury leads to both increased dentate excitability and impairments in memory performance (Gupta et al., 2012; Hamm et al., 1996; Santhakumar et al., 2001; Semple et al., 2020). Several lines of evidence suggest a role for TLR4 in hippocampal memory processing. Mice lacking TLR4 show enhanced memory processing and mutations that alter TLR4 signaling impact hippocampal long-term potentiation and spatial reference memory (Costello et al., 2011; Okun et al., 2012). Changes in hippocampal memory processing in mice lacking TLR4 have been associated with increases in cells expressing the immediate early gene Arc, which is consistent with enhanced excitability. These findings suggest that TLR4 modulation of dentate excitability could impact memory performance (Jeltsch et al., 2001). The current study was conducted to determine the signaling mechanisms underlying TLR4 regulation of network excitability in the injured brain and its impact on behavioral outcomes.

Materials and Methods

All procedures were performed under protocols approved by the Institutional Animal Care and Use Committee of the Rutgers New Jersey Medical School, Newark, New Jersey and University of California, Riverside, California and are consistent with the ARRIVE guidelines.

Fluid percussion injury

Juvenile male Wistar rats (25–27 days old) were subject to moderate (2–2.2 atm) lateral fluid percussion injury (FPI) or sham-injury using standard methods (Y. Li et al., 2015; Neuberger et al., 2017). Studies were restricted to males to avoid confounds due to cyclical changes in immune responses and behavioral effects of injury in females(Potter et al., 2019; Roof & Hall, 2000). Briefly, under ketamine (80 mg/kg)-xylazine (10 mg/kg) anesthesia (i.p.), rats underwent stereotaxic craniotomy (3 mm dia, −3mm bregma, and 3.5 mm lateral to sagittal suture) to expose the dura and bond a Luer-Lock syringe hub. The next day, randomly selected animals received a brief (20 ms) impact on the intact dura using the FPI device (Virginia Commonwealth University, VA) under isoflurane anesthesia. Sham rats underwent all procedures except delivery of the pressure wave. Animals with implants dislodged during impact and those with < 10 sec apnea following injury or injuries in which the pressure waveforms were jagged were excluded.

Field electrophysiology

One week after FPI or sham-injury rats were euthanized under isoflurane and horizontal brain slices (400 μm for field recordings and 300 μm for patch recordings) were prepared in ice-cold sucrose-artificial cerebrospinal fluid (ACSF) containing (in mM) 85 NaCl, 75 sucrose, 24 NaHCO3, 25 glucose, 4 MgCl2, 2.5 KCl, 1.25 NaH2PO4, and 0.5 CaCl2 (Li et al., 2015; Yu et al., 2016). Recordings were restricted to the side of injury (ipsilateral). Field recordings were obtained in an interface recording chamber (BSC2, Automate Scientific, Berkeley, CA) perfused with ACSF containing (in mM) 126 NaCl, 2.5 KCl, 2 CaCl2, 2 MgCl2, 1.25 NaH2PO4, 26 NaHCO3 and 10 D-glucose at 32–33 °C. Granule cell

population responses were recorded using patch pipettes with ACSF, in response to stimuli delivered through bipolar tungsten stimulating electrodes in the perforant path. Population spike amplitude was measured as the amplitude of the first negative deflection overriding the field EPSP waveform, as described previously (Neuberger et al., 2014). In all drug incubation experiments, pre and post drug recordings were conducted in the same slices with a 45 min incubation between recordings. Slices were recorded in control ACSF and transferred to incubation chambers containing ACSF or one of the following drug cocktails (a) CLI-095, (b) CLI-095 + fluoroacetate + minocycline (c) fluoroacetate + minocycline (d) HMGB1 (e) anti-TNFα or (f) HMGB1 + anti-TNFα for 45 min before returning slices back to the recording chamber. The drugs were used at the following concentrations: CLI-095, 10 ng/ml; fluoroacetate, 1 mM; minocycline, 50 nM; HMGB1, 10 ng/ml and anti-TNFα, 1 μg/ml. The drugs and their concentrations are listed in Supplemental Table 1. Electrode positions were maintained during pre and post incubation recordings. Control incubations in ACSF between recordings confirmed that perforant path evoked dentate population spike amplitude was stable during experimental manipulations (Suppl. Fig. 1). All electrophysiology data were low pass filtered at 3 kHz, digitized using DigiData 1440A, acquired using pClamp10 at 10 kHz sampling frequency, and analyzed using ClampFit 10. In experiments in which the percent change in population spike was analyzed, data from recordings in which no population spikes were observed in ACSF were excluded from analysis. For whole cell patch clamp recordings, slices were visualized using infrared differential interference contrast techniques (IR-DIC) with a Nikon Eclipse FN-1 microscope and a 40X water-immersion objective. A MultiClamp 700B amplifier

(Molecular Devices) was used to perform voltage clamp recordings from granule cells at 32–33 °C using borosilicate microelectrodes (4–6 MΩ) containing (in mM) 140 CsMethanesulfonate, 10 HEPES, 2 MgCl2, 0.2 EGTA, 2Na-ATP, 0.5NaGTP, 10 phosphocreatine and 0.2% biocytin. Currents were evoked using a tungsten stimulating electrode located in the perforant path. Afferent evoked excitatory postsynaptic currents (eEPSCs) were recorded at −60 mV and data from slices incubated in ACSF or drugs were compared. Data were low pass filtered at 3 kHz, digitized using DigiData 1440A, and acquired using pClamp10 at 10 kHz sampling frequency. Recordings were rejected if the cell had more than a 20% change in series resistance over time. ClampFit 10 and Sigma Plot 12.3 were used to analyze the data.

Neuronal cultures

Primary hippocampal neurons were obtained from the hippocampi of E17–18 C57Bl/6J mouse embryos of both sexes. Hippocampi were transferred to 15 ml tissue culture tubes and the volume was adjusted to 10 ml with Hanks balanced salt solution (HBSS) and were then gently centrifuged at 1000 rpm for 1 min. HBSS was then removed from the tube and tissue was digested in 5 ml of 0.25% trypsin and 75 µl of DNase (200Units/mg) solution for 20 min at 37 °C. Trypsin/DNase mix was then removed from tissue and the tissue was washed with characterized fetal bovine serum. Tissue was transferred to Neurobasal plating media-A (NB-A) and mechanically dissociated by trituration with a Pasteur pipet. Cells were pelleted by centrifugation at 1500 rpm for 5 min. Cells were taken up in 20 µl of NB-A plating medium and counted in a hemocytometer. Approximately 0.5–1.0 × 106 cells per well were plated on Poly-D-Lysine (PDL) coated 15 mm coverslips in NB-A medium

containing B27 and L-glutamine and cultured at 37 °C in 5% C02/95% air. Medium was changed every 3–4 days. Ara-C was added to media on day 3 for complete removal of glia. Cultured coverslips were stained for GFAP and IBA-1 for confirmation of complete absence of glia. 11- to 13-day old cultures were used for physiological recordings. Recordings were obtained from independent culture plates obtained from embryos from 3 to 4 pregnant dams. Cultured neurons were visualized under IR-DIC using a Nikon Eclipse FN-1 microscope and a 40X, 0.8NA water-immersion objective. Whole cell recordings were obtained using MultiClamp 700B (Molecular Devices) at 32–33 °C. Voltage clamp recordings of AMPAR currents were performed using borosilicate microelectrodes (4–6 MΩ) containing (in mM) 140 Cs-gluconate, 10 HEPES, 2 MgCl2, 0.2 EGTA, 2Na-ATP, 0.5Na-GTP, 10 phosphocreatine and 0.2% biocytin in the presence of SR95531 (10 μM) to block GABAA receptors and D-APV (50 μM) to block NMDA receptors. Recordings were rejected if the cell had more than a 20% change in series resistance over time.

Drug administration

One day after injury, a randomly assigned cohort of FPI and sham rats received either vehicle (saline) or a synthetic TLR4 antagonist, CLI095 (0.5 mg/kg, s.c.) for 3 doses at 8–12 h intervals starting 8–12. after injury. A second group underwent stereotaxic injection (Hamilton syringe-26 G) of 5 μl of saline or the highly selective TLR4 antagonist LPSRS Ultrapure (LPS-RSU, 2 mg/ml) in the hippocampus on the side of injury. Injections were delivered through the implanted syringe hub (AP: 2.5–3.0 mm, ML: 2.5–3.5 mm, DV: 3–3.5 mm). Drugs were delivered one day after injury at a rate of 1 μl/5 mins under isoflurane anesthesia (2% in 95% O2, 5% CO2) delivered through a nose cone. 2.5. Western blotting

Western blots of protein from fresh hippocampal tissue were obtained from rats perfused with cold ACSF (4 °C) 3 days and 1 week after FPI or sham-injury as described previously(Y. Li et al., 2015) using antibodies listed in Table 1. Protein concentration of the sample lysates was measured using BCA assay (Santa Cruz). Equal amounts of protein samples were diluted at a ratio of 1:1 in Laemmli sample buffer (Sigma) and separated on pre-cast gel (4–12% Tris–glycineBio-Rad). Chemiluminescent detection was performed with ECL western blotting detection reagent (Westdura, Thermo Scientific) using FluoroChem 8800. Densitometric quantification was determined using Image-J software (NIH) and normalized to β-actin density.

Spatial working memory test

A delayed match to position working memory task was conducted using a Morris Water Maze (Pang et al., 2015). Rats were trained to locate a hidden escape platform (10 × 10 cm) located below the water surface in a pool (1.5 m diameter). The working memory procedure consisted of 6 trials in one day; each trial had a sample and a choice phase. During the sample phase, rats began from a predetermined location in a zone without the platform and had 60 sec to locate a randomly placed escape platform in the pool. Rats which failed to locate the platform were manually led to the platform. The choice phase commenced 60 s after the sample phase and was identical in procedure to the sample phase. Rats spent a minimum of 30 min in a holding cage between trials. In each session, the start and the escape platform locations were distributed to equally throughout the pool (3 zones X 2 trials each for a total of 6 trials). Swim paths were recorded for offline analysis of path efficiency (defined as ratio of the straight-line distance between the start and the escape

platform location and total distance traveled by a rat; a value of 1 indicates the most efficient path) using ANYmaze software. Rats were tested for spatial working memory performance prior to injury, rats with matched pre-injury path efficiency scores were assigned to either sham or FPI groups such that the average pre-injury path efficiency scores were not different between rats receiving sham or FPI. Rats in each stratum were randomly assigned to an injury group (Sham or FPI) and treatment (saline, LPS-RSU, CLI-095) groups. Rats had one session of testing at 1 week (early phase) and 1 month and/or 3 months (late phase) after injury.

Statistical analysis

Statistical analyses were performed using GraphPad Prism 8. A total of 140 rats and 6 mice (pregnant dams) were used in the study. All independent samples were tested for normality and homogeneity of variance in GraphPad Prism 8 using descriptive statistics from Levene's test. Post-hoc Tukey's test was used to assess statistical significance of between-group differences. In behavioral studies (**Figs. 1.7 and 1.8**), data from sample and choice phases were analyzed separately using mixeddesign ANOVA or two-way repeated measures ANOVA with time as repeated measure variable. Appropriate tests were selected depending upon the samples and their distribution for each experiment and on consultation with the Rutgers Biostatistics core. The significance level was set to $p < 0.05$. Data are shown as mean ± s.e.m. All data and statistical results are presented in Supplemental Tables 2 and 3 respectively.

Results

Differential contribution of glial signaling to TLR4 modulation of excitability in sham and injured rats.

The sterile inflammatory response after brain injury is known to enhance TLR4 signaling in the hippocampus (Ahmad et al., 2013; Laird et al., 2014). Brain injury results in dentate hilar neuronal loss and increases in expression of microglia and reactive astrocytes (Gupta et al., 2012; Y. Li et al., 2015; Neuberger et al., 2017). Our earlier studies identified that TLR4 is expressed in neurons in the hippocampal dentate gyrus and has divergent effects on hippocampal dentate excitability; reducing excitability in controls while enhancing excitability early after brain injury (Korgaonkar, Li, et al., 2020; Y. Li et al., 2015). However, prior studies have attributed TLR4 regulation of glutamatergic currents to recruitment of glial TLR4 signaling (Balosso et al., 2014). To specifically test the contribution of glial signaling to TLR4 modulation of dentate excitability in sham and FPI rats, we adopted a pharmacological cocktail of fluoroacetate (1mM) and minocycline (50nM) to acutely suppress astrocytes and microglia respectively. Fluoroacetate and its derivative flurocitrate are preferentially taken up by astrocytes and inhibit their metabolic function by blocking a critical Krebs cycle enzyme(Paulsen et al., 1987; Swanson & Graham, 1994). Minocycline, a tetracycline antibiotic and a potent inhibitor of microglial activation, has been shown to effectively suppress microglial TLR4 signaling (X. Li et al., 2014; Zhou et al., 2006). If glial signaling contributes to the effects of TLR4 on dentate excitability a cocktail of fluoroacetate (1 mM) and minocycline (50 nM), referred hereafter as glial metabolic inhibitors (GMI), should occlude TLR4 modulation of dentate afferent

evoked excitability. Alternatively, if neuronal TLR4 is solely responsible for modulating dentate excitability, glial metabolic inhibitors should not alter the TLR4 modulation. As in prior studies, we used two mechanistically distinct TLR4 antagonists CLI-095 (also known as TAK-242/Resatorvid, 10 ng/ml) and LPS-RS Ultrapure (LPS-RSU, 50 μg/ml) which have similar effects on dentate excitability (Korgaonkar, Li, et al., 2020; Y. Li et al., 2015). CLI-095 is a small molecule inhibitor of TLR4 signaling that acts on the intracellular domain to block both ligand dependent and independent TLR4 signaling and is approved for clinical trial in sepsis. LPSRSU is a competitive TLR4 antagonist acting on the extracellular binding site. As reported previously, CLI-095 increased granule cell population spike amplitude in slices from rats one week after sham injury (**Fig. 1.1A**, Note: the CLI-095 data, previously reported in Korgaonkar et al., 2020, are shown for comparison). In contrast, CLI095 failed to alter granule cell population spike amplitude when the slices from sham rats were incubated for 45 min in GMI (**Fig. 1.1B**, summarized in sham plots in **Fig. 1.1E**, population spike amplitude in mV in response to a 4 mA stimulation, sham in ACSF: 0.39 ± 0.08, n = 8 slices, 3 rats, and sham incubated in CLI-095 and GMI: 0.28 ± 0.06, n = 8 slices, 3 rats, $p > 0.05$ by two-way ANOVA followed by post-hoc Tukey's test; sham-CLI095: 1.04 ± 0.17, n = 5 slices, 3 rats, reported in Korgaonkar et. al., 2020). Similarly, LPS-RSU did not increase granule cell population spike amplitude in the presence of GMI (population spike amplitude in mV in response to a 4 mA stimulation, sham in ACSF: 0.33 ± 0.05; sham in LPS-RSU and GMI: 0.28 ± 0.08, n = 6 slices, 3 rats, $p > 0.05$ by two-way ANOVA followed by post-hoc Tukey's test).

These data indicate a critical role for glia in CLI-095 and LPS-RSU mediated increases in population spike amplitude in sham controls (**Fig. 1.1F**, sham plots).

One week after brain injury, CLI-095 reduced perforant path-evoked dentate population spike amplitude (**Fig. 1.1C**) indicating that TLR4 signaling enhances network excitability after FPI (Korgaonkar, Li, et al., 2020; Y. Li et al., 2015). Unlike the findings in sham controls, the reduction in population spike amplitude with CLI-095 treatment persisted in the presence of GMI (**Fig. 1.1D-E** FPI data, population spike amplitude in mV in response to a 4 mA stimulation, FPI in ACSF: 1.646 ± 0.12, n = 8 slices, 3 rats, and FPI in CLI-095 and GMI: 0.40 ± 0.13, n = 8 slices, 3 rats, $p > 0.05$ by two-way ANOVA followed by post-hoc Tukey's test; FPI-CLI095: 0.14 ± 0.11, n = 6 slices, 3 rats, reported in Korgaonkar et. al., 2020). Once again, effects of LPS-RSU paralleled those of CLI-095, with LPS-RSU reducing dentate population spike amplitude even in the presence of GMI (population spike amplitude in mV in response to a 4 mA stimulation, FPI in ACSF: 1.61 ± 0.30; FPI in LPS-RSU and GMI: 0.38 ± 0.14, n = 9 slices, 3 rats, $p > 0.05$ by two-way ANOVA followed by post-hoc Tukey's test). These data indicate glial signaling is unlikely to mediate TLR4 enhancement of dentate excitability after brain injury (**Fig. 1.1F**, FPI plots).

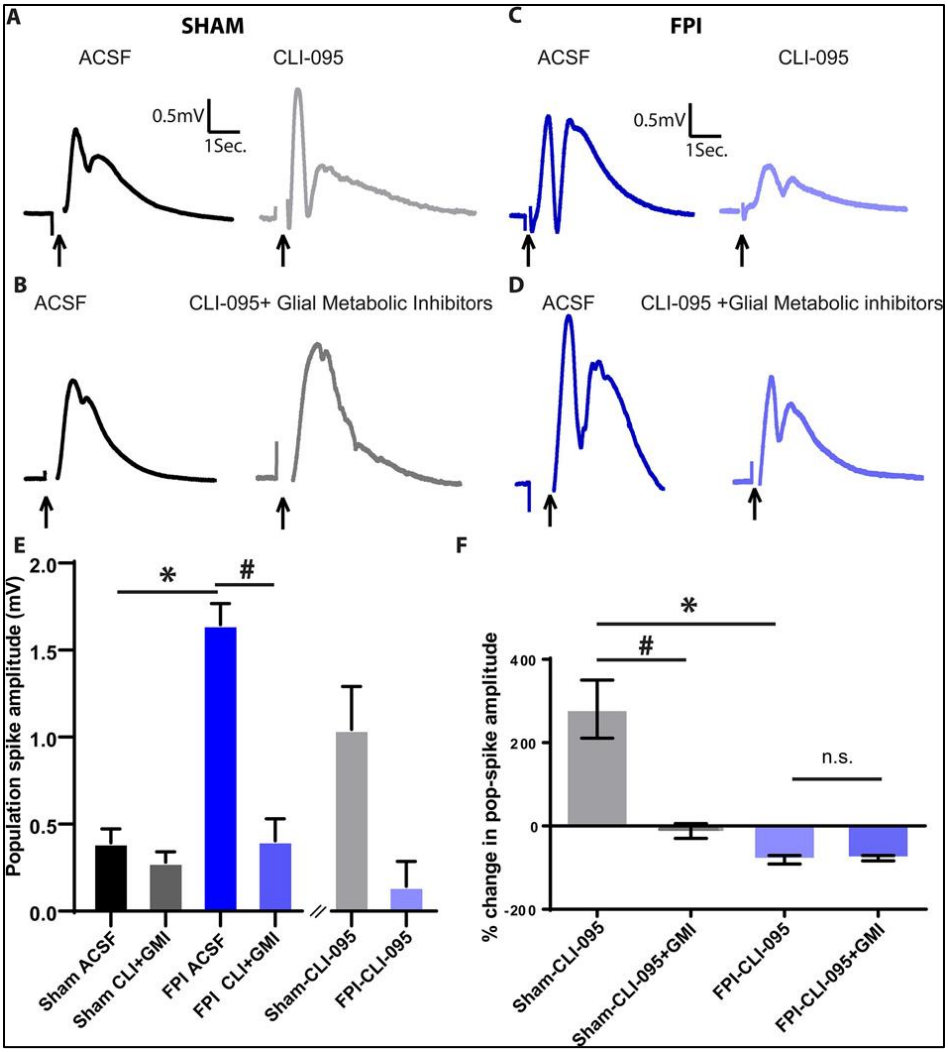

Figure 1.1. Differential role for glial signaling in TLR4 modulation of dentate excitability in sham and injured rats. (A-D). Granule cell population responses evoked by a 4mA stimulus to the perforant path in slices from sham rats before and after CLI-095 (10ng/ml) in A and before and after incubation in CLI-095+Fluororoacetate (1mM) +Minocycline (50nM) in B. Responses in slices from FPI rats before and after CLI-095 (10ng/ml) in C and before and after incubation in CLI-095+Fluororoacetate (1mM) +Minocycline (50nM) in D. Arrows indicate stimulus artifact. (E-F) Summary plots of population spike amplitude (E) and % change in population spike amplitude compared to corresponding ACSF treatment condition (F). *indicates $p<0.05$ compared to corresponding recordings in sham, # indicates $p<0.05$ and n.s. indicates $p>0.05$ for pairwise comparison with corresponding control drug incubation by TW-ANOVA followed by pairwise Tukey's test. Note: CLI-095 data in panel E was previously reported in Korgaonkar et al., 2020 and included for comparison with effect of GMI. (**Data generated by co-authors**)

Next we examined whether GMI could directly impact network excitability. While the population spike amplitude in slices from FPI rats was greater than in sham rats, treatment with GMI alone did not directly alter network excitability in slices from either sham or FPI rats (**Fig. 1.2A-C**, sham in ACSF: 0.29 ± 0.05; sham in GMI: 0.23 ± 0.06, −18.33 ± 12.11% change in n = 5 slices, 3 rats each; FPI in ACSF: 1.67 ± 0.13, and FPI in GMI: 1.68 ± 0.12, 1.30 ± 3.46% change, n = 5 slices, 3 rats each ; $p < 0.0001$ for effect of injury $F(1,8) = 101.8$).

We previously reported that TLR4 signaling enhances granule cell AMPA currents after FPI (Y. Li et al., 2015). To further verify whether glial signaling contributes to posttraumatic increase in granule cell EPSCs, we examine whether incubation in GMI altered perforant path evoked excitatory postsynaptic currents (eEPSCs) after FPI. Consistent with our prior data (Li et al., 2015), granule cell eEPSC amplitude was significantly increased one week after FPI (Amplitude in pA, sham-ACSF: 749.1 ± 139.5, n = 7 cells and FPI-acsf 1296 ± 146.2, n = 6 cells, $p < 0.05$ by t-test). We previously demonstrated that TLR4 antagonist selectively reduced post-injury increases in perforant path evoked granule cell eEPSCs one week after FPI without altering eEPSCs in sham injured controls (Li et al., 2015). Granule cell eEPSC amplitude in slices from sham rats showed a small increase following incubation in GMI which failed to reach statistical significance (**Fig. 1.2D**, Amplitude in pA, sham-ACSF: 749.1 ± 139.5, n = 7 cells and sham- GMI: 1044 ± 116.1, n = 6 cells, $p > 0.05$ by t-test). Importantly, in slices from FPI rats, eEPSC amplitude was not altered by incubation in GMI (FPI-ACSF: 1296 ± 146.2, n = 6 cells and FPI-GMI 920 ± 180.7, n = 8 cells, $p > 0.05$ by t-test) indicating the lack of

direct effect of GMI on granule cell eEPSCs amplitude after injury. These data further suggest that glial signaling does not underlie TLR4 regulation of eEPSC amplitude after FPI.

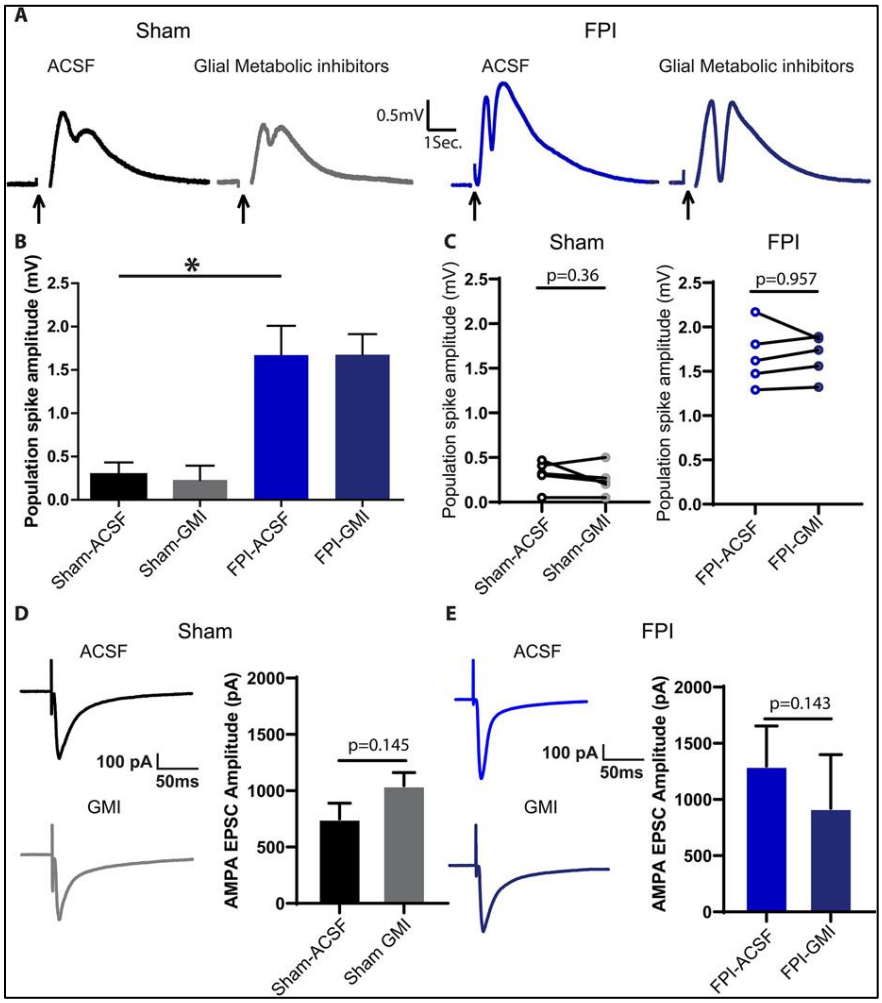

Figure 1.2. Effect of glial metabolic inhibitors on dentate excitability. (A). Granule cell population responses evoked by a 4mA stimulus to the perforant path in slices from the various experimental conditions. Arrows indicate stimulus artifact. (B-C) Summary plots of population spike amplitude (B) and pairwise comparison of population spike amplitude compared to corresponding ACSF treatment condition (C). *indicates $p<0.05$ by TW-ANOVA followed by pairwise Tukey's test. (D, E) Representative eEPSC traces from granule cells recorded following incubation (45 minute) in ACSF (above) or GMI (below). Responses were elicited by a 2mA stimulus to the perforant path in slices prepared one week after sham-injury (D) and FPI (E). Corresponding summary plots are presented in the panels to the right. (**Data generated by candidate**)

Neuronal signaling underlies TLR4 modulation of AMPAR currents.

To further examine the role for neuronal signaling in TLR4 modulation of excitability we established pure neuronal cultures from wildtype embryonic mouse hippocampi (**Fig. 1.3A**). Cultured cells were confirmed to be purely neuronal by the presence of the microtubule associate protein (MAP2) and absence astrocytic (GFAP) or microglial (Iba1) markers (**Fig. 1.3B**). In neuronal cultures, stimulation of neuropil evoked synaptic AMPAR currents, which were enhanced in cultures treated with the TLR4 agonist HMGB1 (10 ng/ml) (Fig. 3C-D, AMPAR charge transfer in pA.sec: ACSF: 152.3 ± 6.80, 7 cells from 4 different repeats, HMGB-1: 254.4 ± 15.57, 7 cells from 4 replicates, $p < 0.05$ by one-way ANOVA followed by a Tukey's multiple comparison test). The ability of TLR4 agonist to increase excitability is the opposite of what is observed in slices from control rats and similar to observations in ex vivo slices from the injured brain (Li et al., 2015). Similarly, when neuronal cultures in vitro were treated with the TLR4 antagonist LPSRSU (1 μg/ml) the AMPAR current charge transfer was reduced (**Fig. 1.3C-D**, AMPAR charge transfer in pA.sec: cultures incubated in LPSRSU: 93.4 ± 13.75, 6 cells from 4 replicates, $p < 0.05$ versus ACSF by one-way ANOVA followed by a Tukey's multiple comparison test) as reported in granule cells in ex vivo slices from brain injured rats (Li et al., 2015). Note that, since LPS-RSU and CLI-095 have similar effects on AMPA currents in hippocampal slices (Korgaonkar et al., 2020; Li et al., 2015), we restricted the in vitro analysis to a single TLR4 antagonist. Once again, these data show that the response of cultured neurons to TLR4 ligands is similar to that observed in granule cells from slices one week after FPI, suggesting that the trauma of dissociation may confer an injury-like phenotype to TLR4

effects in neuronal cultures. The ability of TLR4 ligands to bidirectionally modulate AMPAR currents in the absence of glia, and in a direction similar to that observed in slices after brain injury, is consistent with our finding (**Fig. 1.1**) that glial TLR4 signaling is not central to TLR4-dependent enhancement of excitability after brain injury.

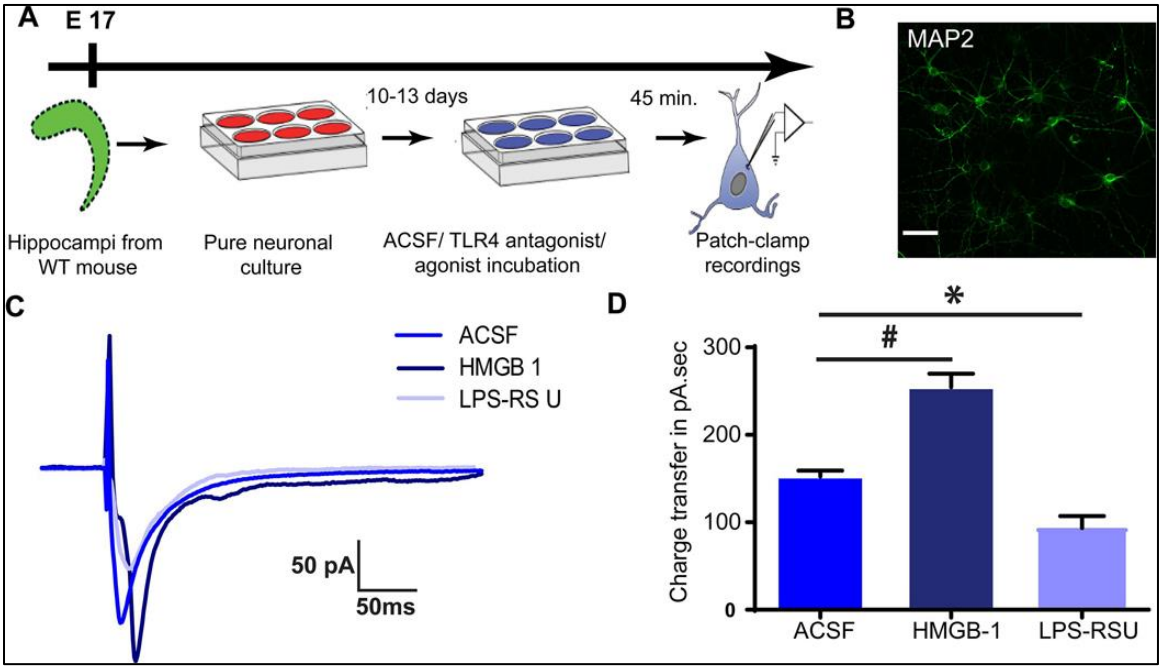

Figure 1.3. TLR4 modulation of AMPAR currents in hippocampal neurons in vitro. (A). Schematic of experimental design shows timeline for preparation of cultures followed by drug treatments and whole cell recordings. (B). Example maximum intensity projection of confocal image stacks from a hippocampal neuronal culture plated at embryonic day 17 and stained for MAP2 at 12 days in vitro (DIV) to reveal neurites. (C). Overlay of sample AMPAR current traces recorded in response to neuropil stimulation in neuronal cultures. Neurons were held at −60 mV to obtain recordings in ACSF, TLR4 agonist HMGB1 and TLR4 antagonist LPS-RSU. (D). Summary plot of AMPAR current charge transfer. * and # indicates $p<0.05$ compared to ACSF by One Way ANOVA followed by post-hoc Tukey's test. (**Data generated by co-authors**)

TLR4 antagonist treatment in vivo reduces post-injury increases in inflammatory signaling downstream of TLR4

Earlier studies have shown that anti-inflammatory agents can limit cell death after brain trauma by suppressing the inflammatory responses mediated downstream of TLR4 signaling (Dong et al., 2011). Our data show that TLR4 signaling reduces excitability in shams and increases excitability after brain injury. Moreover, we recently demonstrated that blocking TLR4 signaling in vivo reduced posttraumatic increases in hippocampal cellular inflammation observed three days after FPI without altering the inflammatory milieu in controls (Korgaonkar et al., 2020). However, whether blocking TLR4 signaling causes opposite changes in signaling pathways downstream of TLR4 in the uninjured and injured brain, which could contribute to the differing effects TLR4 signaling on excitability in sham and FPI rats, is not known. To test this possibility, we examined western blots from hippocampal tissue ipsilateral to injury for the endogenous TLR4 ligand, HMGB1, and downstream signaling elements of the MyD88-dependent and independent pathways. Fresh hippocampal tissue for western blot analysis was obtained from rats that had undergone sham or FPI followed by treatment with saline or CLI-095 treatment (0.5 mg/kg, 3 doses at 8–12 h intervals starting 8–12 hrs after injury). Since TLR4 expression peaks at 24 h, this dosing strategy was based on reported biological availability of CLI-095 in rat (Jinno et al., 2011) and was designed to antagonize the brief increase in TLR4 which peaks 24 h after injury.

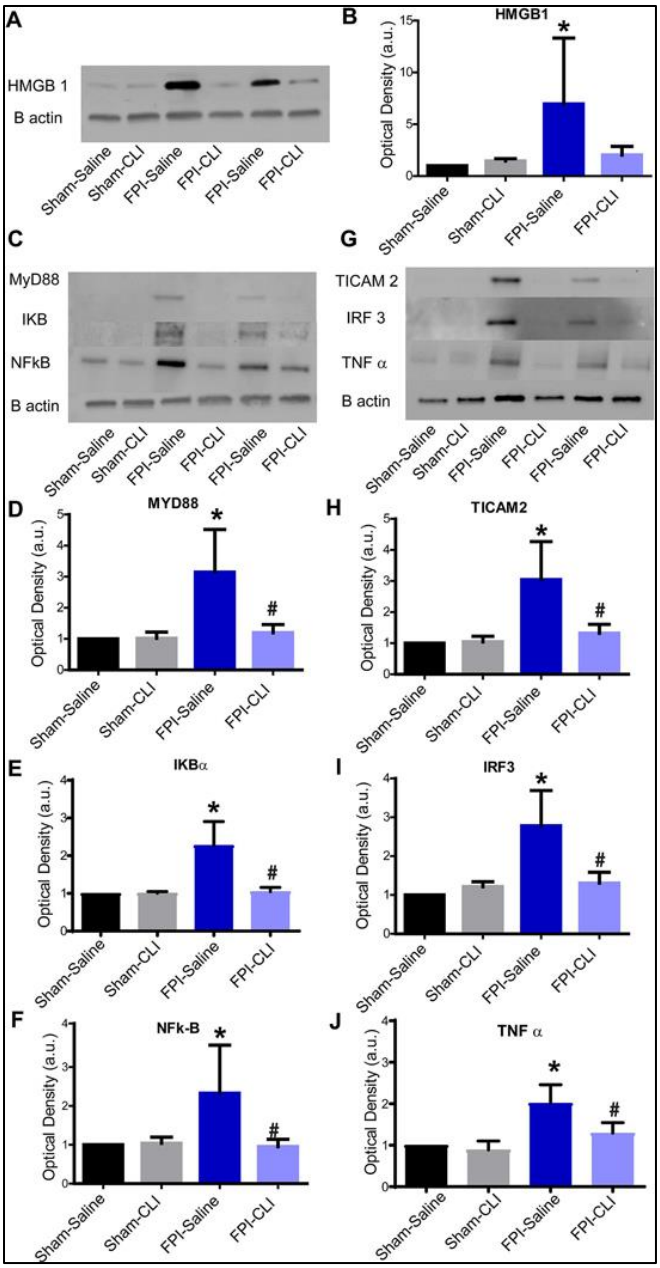

Figure 1.4. TLR4 antagonism in vivo suppresses increases in TLR4 signaling after brain injury. Representative western blots of HMGB1 (A) MyD88, IkBα, and NFκB, (C) and, TICAM2, IRF3 and TNFα (G) in hippocampal samples from the injured side obtained 3 days after vehicle/CLI-095 treatment. Treatments were started 24 hours after injury. Corresponding β-actin bands are illustrated. (A, C and G) Summary histograms of expression of HMGB1 (B), MyD88 (D), IkBα (E), NFκB (F), TICAM2 (H), IRF3 (I) and TNFα (J), normalized to the expression levels in sham-vehicle treated controls. * indicates $p<0.05$ compared to sham and # indicates $p<0.05$ compared to corresponding ACSF by TW ANOVA followed by post-hoc Tukey's test. (**Data generated by co-authors**)

In a cohort of rats examined one week after FPI or sham injury, hippocampal expression of TLR4 was not different between groups (Sham saline: 1.00 ± 0 , Sham-CLI095: 1.04 ± 0.10, FPI- Saline: 1.13 ± 0.12 and FPI-CLI095: 0.946 ± 0.083, n = 4 each, no group differences by TW-ANOVA) which is consistent with the recovery of TLR4 levels back to those observed in controls one week after injury (Li et al., 2015). Therefore we decided to evaluate TLR4 signaling in hippocampal tissue 3 days after FPI, a time point at which we have reported a significant post traumatic increase in TLR4 expression which is suppressed by CLI-095 treatment in vivo (Korgaonkar et al., 2020; Li et al., 2015). In saline treated rats, hippocampal expression of HMGB1 was significantly enhanced three days after FPI compared to sham rats (**Fig. 1.4A-B**, $p = 0.02$ by TW ANOVA test, followed by post-hoc pairwise Tukey's test). While CLI-095 treatment failed to enhance HMGB1 levels in sham controls ($p = 0.99$ for sham-saline vs. sham-CLI), HMGB1 levels in FPI rats treated with CLI095 trended towards a decrease when compared to saline-treated FPI rats ($p = 0.065$ for FPI-saline vs. FPI-CLI by pairwise Tukey's test) and was not different from saline-treated sham rats. Next we examined the pathways downstream of MyD88-dependent TLR4 signaling: MyD88, IkBα, and NFκB. Levels of the three proteins downstream of the MyD88-dependent TLR4 pathway were enhanced in saline-treated FPI rats compared to saline-treated sham rats. (**Fig. 1.4C-F**). Compared to saline, CLI-095 treatment reduced the level of all three proteins in FPI rats without altering their levels in sham (**Fig. 1.4C-F**). Similarly, proteins downstream of the MyD88-independent pathway, TICAM2 and IRF3 were also enhanced in saline-treated FPI rats than in sham controls (**Fig. 1.4G-I**;).

CLI-095 treatment returned TICAM2 and IRF3 levels in FPI rats back to levels comparable to sham controls without altering their levels in sham rats (**Fig. 1.4G-I**;). Moreover, TNFα, which is downstream of both MyD88 dependent and independent pathways was also enhanced in saline treated FPI rats and decreased to sham levels after CLI-095 treatment (**Fig. 1.4G, J**). However, CLI-095 did not alter TNFα levels in sham rats (**Fig. 1.4G, J**). Thus, in vivo CLI-095 treatment significantly reduced hippocampal expression of TLR4 effectors examined in the injured brain while the treatment failed to alter expression of any of the TLR4 effectors tested in sham rats. These findings confirm the ability of in vivo treatment with CLI-095 to reduce early injury-induced increases in TLR4 signaling in the hippocampus, possibly by reducing the activation glial and cellular inflammatory responses to brain injury (Korgaonkar et al., 2020), without altering inflammatory signaling in controls.

Role of TNF-α in TLR4 effects on network excitability

Since TNFα is a direct downstream effector of the MyD88-dependent pathway and is also recruited by MyD88-independent pathways (Akira & Takeda, 2004), we examined whether blocking basal TNFα signaling impacts network excitability in the absence of the TLR4 ligand. In ex vivo slices from sham rats, incubation in the TNFα antibody (anti-TNFα, 1 μg/ml, 1hr) increased dentate population spike amplitude (**Fig. 1.5A-B**, population spike amplitude evoked by a 4 mA stimulus, in mV, sham: before anti-TNFα 0.02 ± 0.01; after anti-TNFα: 0.33 ± 0.22, n = 8 slices from 4 rats, p = 0.028 by paired t-test). This increase in population spike amplitude in anti-TNFα is similar to what is observed in slices from

sham injured rats treated with TLR4 antagonist (**Fig. 1.1A** and Li et al., 2015). In contrast to findings from sham rats, incubation in anti-TNFα significantly reduced perforant path evoked population spike amplitude in slices from FPI rats (**Fig. 1.5C-D**, population spike amplitude in mV at 4 mA stimulation, FPI before anti-TNFα: 1.43 ± 0.22, FPI after anti-TNFα incubation: 0.422 ± 0.19, n = 14 slices from 5 rats, $p < 0.0001$ by paired t-test). Blocking TNFα which is elevated after brain injury (**Fig. 1.4J** and (Atkins et al., 2007; Sinha et al., 2017)), reduced network excitability, consistent with the effect of TLR4 antagonist application in slices from rats after FPI.

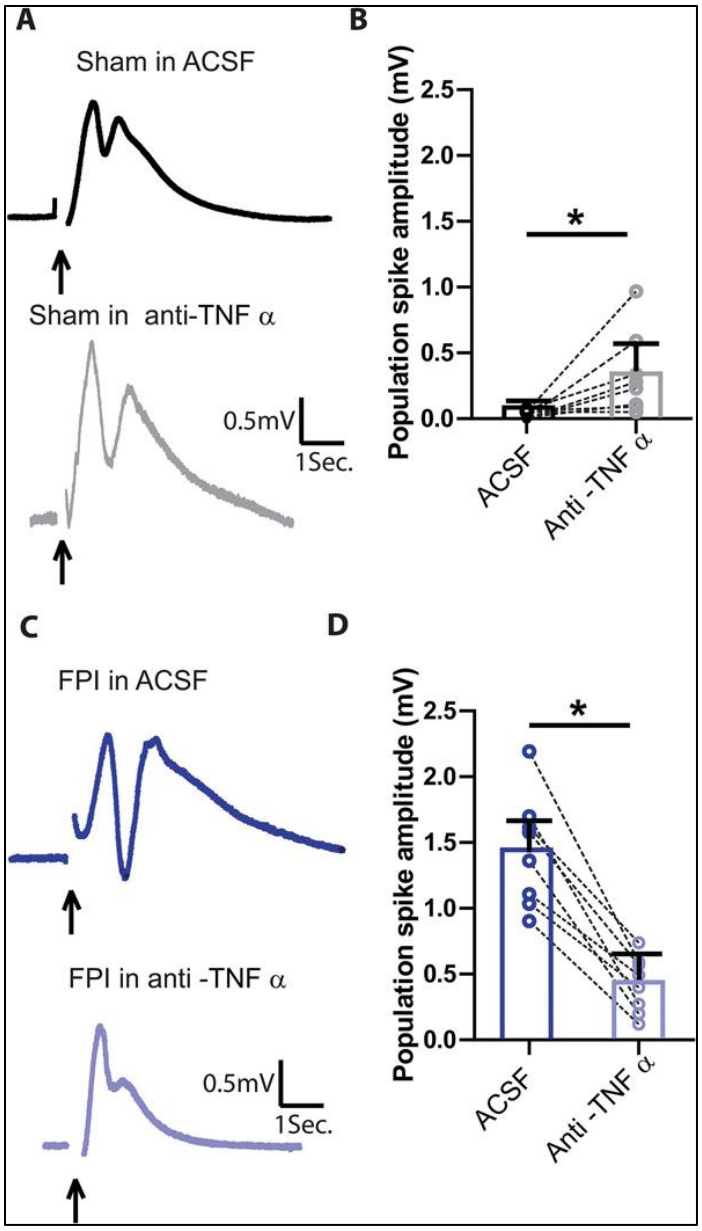

Figure 1.5. Effect TNFα signaling on network excitability in sham and injured rats. (A) Representative dentate population responses evoked by a 4mA stimulus to the perforant path in a slice from a sham rat before (above) and after (below) incubation in anti-TNFα (1μg/ml). Arrows indicate stimulus artifact. (B) Summary data of effect of anti-TNFα (1μg/ml) on perforant path-evoked granule cell population spike amplitude in slices from sham rats. (C) Example dentate population responses perforant path stimulation at 4 mA in slices from FPI rats before (above) and after (below) incubation in anti-TNFα (1μg/ml). Arrows indicate stimulus artifact. (D) Summary data of effect of anti-TNFα (1μg/ml) on perforant path-evoked granule cell population spike amplitude in slices from sham rats. *indicates $p<0.05$ by paired Student's t-test. (**Data generated by co-authors**)

Since the effects of anti-TNFα on excitability paralleled that of TLR4 antagonists, we examined the potential ability of anti-TNFα to occlude the effects of the TLR4 agonist HMGB1. We previously reported that HMGB1 (10 ng/ml) reduced dentate population spike amplitude in slices from sham rats (**Fig. 1.6A-B**, Li et al., 2015, HMGB1 data from prior study were used to determine % change data in **Fig. 1.6A-B**). The ability of HMGB1 to reduce dentate population spike amplitude in slices from sham rats was decreased in the presence of anti-TNFα (1 μg/ml) (**Fig. 1.6A-B**, % change in population spike amplitude compared to corresponding ACSF, sham-HMGB1: −55.01 ± 9.45 and sham HMGB1 + anti-TNFα: −27.81 ± 2.59, n = 8 slices from 3 rats, p = 0.045 by Students t-test). In contrast to the increase in dentate population spike amplitude following HMGB1 treatment reported in slices from FPI rats (**Fig. 1.6C-D**, Li et al., 2015, HMGB1 data from prior study were used to determine % change data in **Fig. 1.6C-D**), co-treatment with anti-TNFα and HMGB1 decreased dentate population spike amplitude in slices from FPI rats (**Fig. 1.6c**, % change in population spike amplitude compared to ACSF, FPI-HMGB1: 77.32 ± 21.59 and FPI HMGB1 + anti-TNFα: −47.51 ± 3.89 , n = 11 slices from 4 rats, p = 0.001 by Students t-test). These results suggest that, in spite of the opposite functional effects and differential neuro-glial involvement in TLR4 signaling in sham and FPI rats, TNFα signaling contributes to TLR4 regulation of excitability in both the uninjured brain and after brain injury.

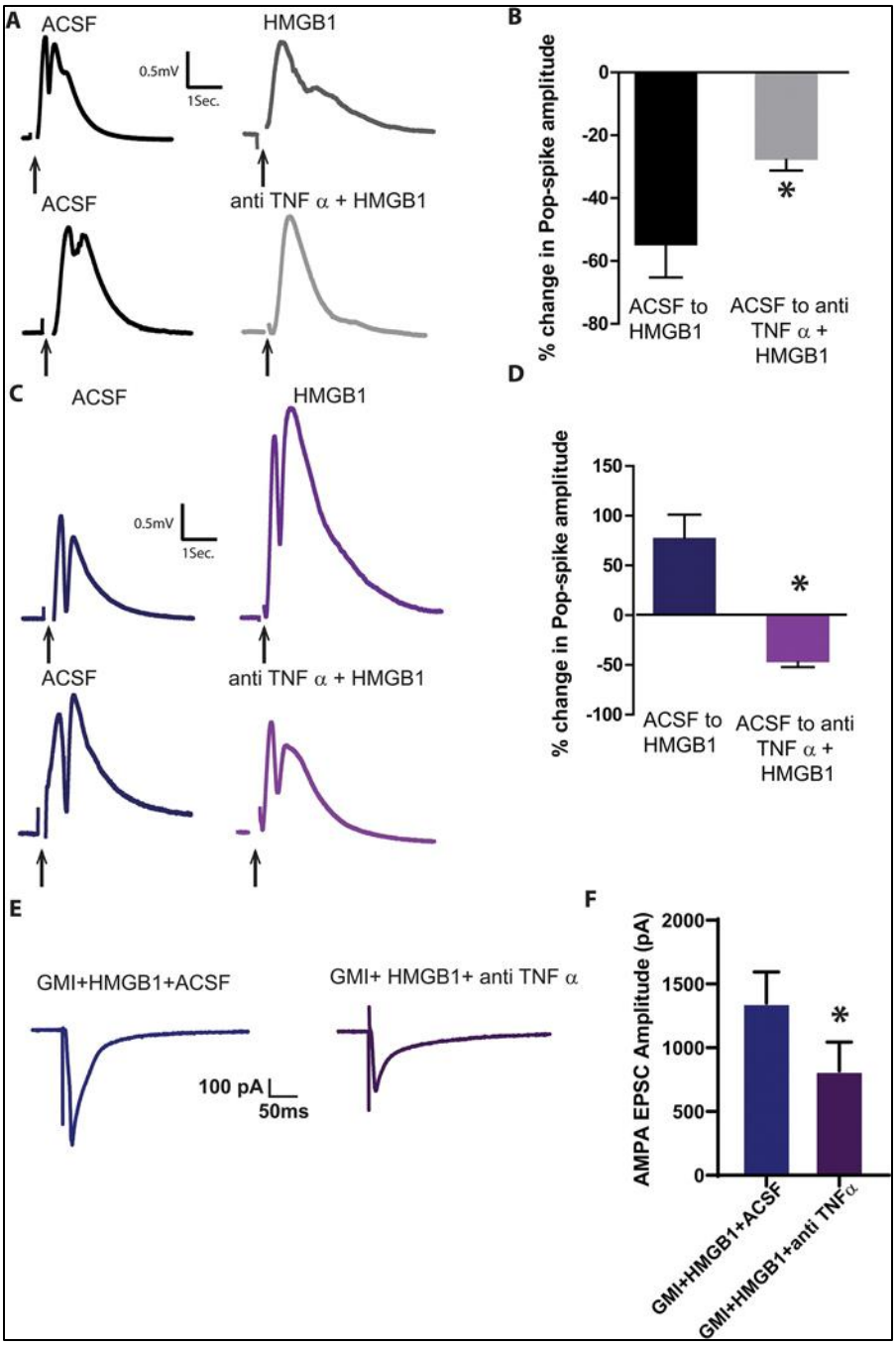
A
ACSF
HMGB1
0.5mV
1Sec.
ACSF
anti TNF α + HMGB1
B
% change in Pop-spike amplitude
0
-20
-40
-60
-80
*
ACSF to HMGB1
ACSF to anti TNF α + HMGB1
C
ACSF
HMGB1
0.5mV
1Sec.
ACSF
anti TNF α + HMGB1
D
% change in Pop-spike amplitude
150
100
50
0
-50
-100
*
ACSF to HMGB1
ACSF to anti TNF α + HMGB1
E
GMI+HMGB1+ACSF
GMI+ HMGB1+ anti TNF α
100 pA
50ms
F
AMPA EPSC Amplitude (pA)
2000
1500
1000
500
0
*
GMI+HMGB1+ACSF
GMI+HMGB1+anti TNFα

Figure 1.6. Contribution of TNFα signaling toTLR4 effects on network excitability in sham and injured rats. (A) Representative dentate population responses evoked by a 4mA stimulus to the perforant path in slices from sham rats before and after HMGB1 (10ng/ml) in upper panel and before and after incubation in HMGB1+ anti-TNFα (1μg/ml) in lower panel. Arrows indicate stimulus artifact. (B) Summary of % change in population spike amplitude in the drug(s) compared to corresponding ACSF treatment condition in slices from sham rats (C) Dentate population spike traces evoked by a 4mA stimulus to the perforant path in slices from FPI rats before and after HMGB1 in upper panel and before and after incubation in HMGB1+ anti-TNFα) in lower panel. (D) Summary of % change in population spike amplitude in the drug(s) compared to corresponding ACSF treatment condition in slices from sham rats. Error bars indicate s.e.m. * indicates $p<0.05$ by unpaired Student's t-test. (E) Representative eEPSC traces from granule cells from FPI rats recorded following incubation (45 minute) in HMGB1 and GMI with and without anti-TNFα. Responses were elicited by a 2mA stimulus to the performant path in slices prepared one week. (F) Summary plot of granule cell eEPSC peak amplitude in rats one week after FPI under various recording conditions. (**Panels E and F generated by candidate**)

To further examine the involvement of glial signaling in TNFα modulation of granule cell eEPSCs after FPI, we incubated hippocampal slices from rats one week after FPI in GMI and HMGB1 (10 ng/ml, 45 min) and examined the effect of anti-TNFα on eEPSC amplitude. Even in the presence of GMI, anti-TNFα (1 μg/ml) significantly reduced the peak amplitude of granule cell eEPSCs recorded in the presence of HMGB1 (**Fig. 1.6E-F**). These findings support a role for neuronal TNFα in mediating TLR4 induced increases in eEPSC amplitude.

TLR4 modulation of network excitability alters working memory function.

Recent studies have identified that optimal activity in the dentate is crucial for its role in memory processing and that both increases and decreases in excitability can impair memory function (Kahn et al., 2019). Brain injury is associated with early increase in dentate excitability (Gupta et al., 2012; Neuberger et al., 2017) and is known to affect dentate and hippocampus-dependent memory function (D'Ambrosio et al., 1998; Hamm et al., 1996; Pang et al., 2015; Smith et al., 2015). Moreover, there is persistent enhancement in seizure susceptibility and development of epilepsy several months after FPI which is consistent with a chronic increase in network excitability (Kharatishvili et al., 2006; Korgaonkar, Li, et al., 2020; Neuberger et al., 2017; Santhakumar et al., 2001). Interestingly, TLR4 antagonist treatment leads to opposing changes in early dentate excitability in injured and uninjured rats which influences long-term seizure susceptibility (Korgaonkar et al., 2020). Moreover, in vivo treatment with TLR4 antagonist induces hilar neuronal loss in sham injured rats while reducing loss of hilar neurons after FPI (Korgaonkar et al., 2020). Therefore, we reasoned that blocking TLR4 signaling would

differentially impact memory processing in the uninjured and injured brain. We focused on a short-term spatial working memory task dependent on dentate function to examine whether FPI, and the associated network alterations, impairs memory processing. Rats were assessed for spatial working memory on a modified Morris Water Maze (MWM) task before injury, at 1 week (Early phase), and at 1 and 3 months (Late phase) after injury. Path efficiency (**Fig. 1.7A**, see methods), a measure independent of distances between start and escape platform locations and swimming speed of rats, was used to quantify performance (Pang et al., 2015). Rats with matched pre-injury path efficiency scores were assigned to either sham or FPI groups such that the average pre-injury path efficiency scores were not different between rats receiving sham or FPI. Path efficiency on the sample phase increased as training proceeded, but did not show any significant differences between FPI and sham rats (**Fig. 1.7B-C**, path efficiency, sham: pre:0.16 ± 0.01; 1 week: 0.166 ± 0.02; 1 month: 0.21 ± 0.03; 3 month: 0.25 ± 0.03; FPI: pre: 0.17 ± 0.01; 1 week: 0.151 ± 0.02; 1 month: 0.22 ± 0.03; 3 month: 0.21 ± 0.02, n = 8 rats each, $F(1,14) = 0.026$ and $p = 0.87$ for effect of Injury; $F(3,14) = 3.15$ and $p = 0.057$ for effect time and $F(3,14) = 0.215$ and $p = 0.8$ for interaction by Mixed design ANOVA). Path efficiency during the choice phase after a 60 sec retention interval was not different between sham and FPI rats prior to injury (**Fig. 1.7C**, pre-injury path efficiency, sham: 0.310 ± 0.04, FPI: 0.312 ± 0.03, n = 8 rats, $p = 0.96$ by Mixed design ANOVA followed by post hoc Tukey's test). However, injured rats demonstrated a significant reduction in path efficiency 1 week and 1 month (**Fig. 1.7B-C**, path efficiency, sham-1wk: 0.41 ± 0.03; FPI-1wk: 0.183 ± 0.028; sham-1mo: 0.40 ± 0.04; FPI-1mo: 0.21 ± 0.01, n = 8 rats/group, $p < 0.001$ for FPI vs. sham at same time point by

Mixed design ANOVA followed by post hoc Tukey's test) which recovered by 3 months (**Fig. 1.7C**. Sham 3mo; 0.364 ± 0.05, n = 4 rats; FPI-3mo 0.34 ± 0.04, n = 4 rats, p > 0.99 by Mixed design ANOVA followed by post hoc Tukey's test). These data identify a transient deficit in memory function 1 week and 1 month after FPI.

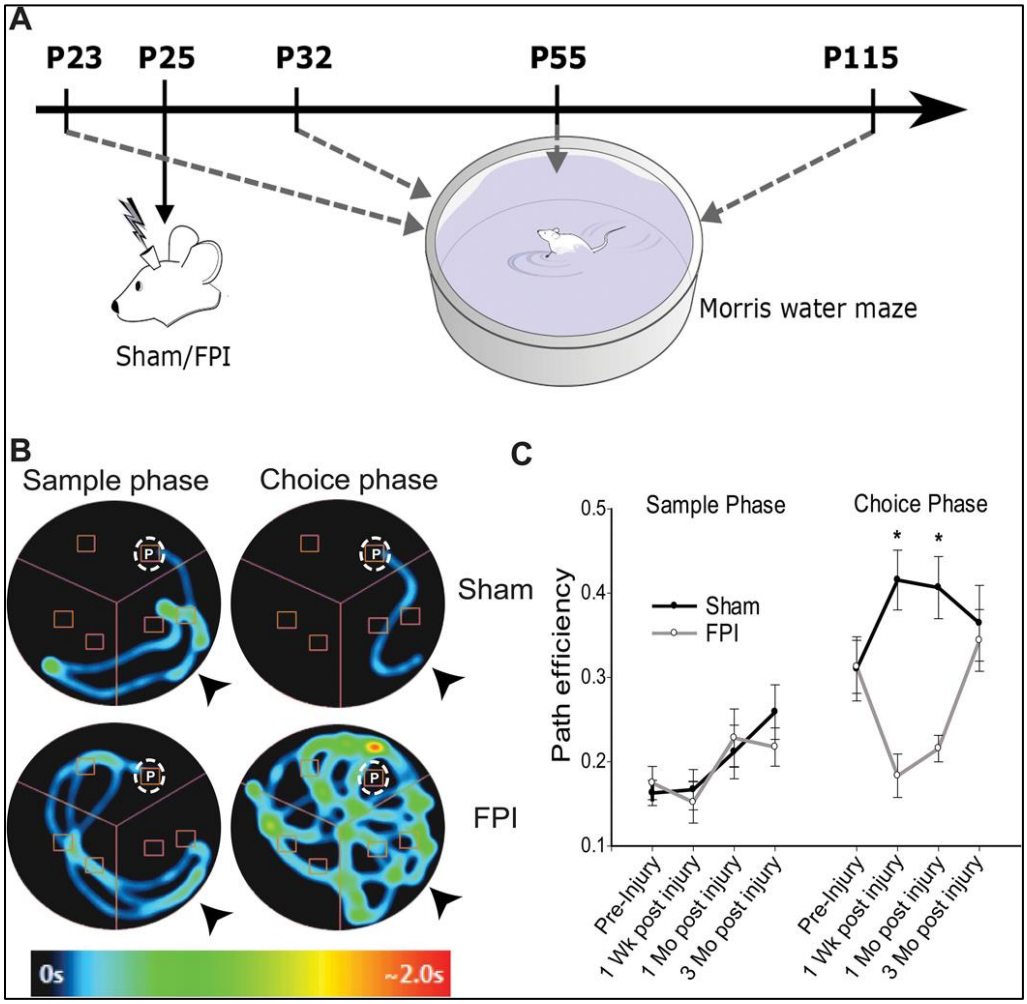

Figure 1.7. Brain injury impairs working memory function. (A). Schematic of experimental design shows timeline for working memory testing pre and post injury using Morris Water Maze. (B) Representative heatmaps of time spent at each location as the rat traced the path to the platform during sample and choice phase of a delayed match to position task in sham and FPI rats 1 week, after injury. Arrows indicate insertion point in pool. (C) Summary of path efficiency during sample and choice phases, *p<0.05 by mixed design ANOVA followed by pairwise Tukey's test. (**Data generated by co-authors**)

Next, we examined whether treatment with a TLR4 antagonist could improve deficits in working memory performance in brain injured rats. Based on the initial findings (**Fig. 1.7**), we chose to focus on one week and one month after injury to test the effects of pharmacologic treatment (Schematic in **Fig. 1.8A**). As before, rats were matched and stratified within the four experimental groups based on pre-injury path efficiency scores. Path efficiency on the sample phase did not show any significant effect of injury/drug or time (**Fig. 1.8B**, n = 9 rats per group, $F(3,32) = 0.36$ and $p = 0.78$ for effect of Injury/Drug; $F(2,32) = 0.3$ and $p = 0.74$ for effect time and $F(6,32) = 0.23$ and $p = 0.95$ for interaction by TW RM ANOVA). In pre-injury trials, path efficiency during choice phase following a 60 sec retention interval was not different between groups (**Fig. 1.8B**, n = 9 rats per group, $p > 0.99$ by TW RM ANOVA followed by post-hoc pairwise Tukey's test). As expected, saline-treated brain injured rats showed an impairment in path efficiency during choice phase compared to sham-saline rats one week and one month after FPI. Consistent with our prediction based on changes in dentate excitability, CLI-095-treatment improved path efficiency in FPI rats compared to saline treated counterparts both one week and one month after injury (**Fig. 1.8B**, FPI-saline: 1 week after injury 0.152 ± 0.008 and FPI-CLI-095: 1 week after injury 0.41 ± 0.03, n = 9 rats, $p < 0.001$ and FPI-saline: 1 month after injury 0.24 ± 0.020, n = 9 rats and FPICLI-095 1 month after injury 0.49 ± 0.014, n = 9 rats, $p < 0.005$ by TW-RM ANOVA followed by pairwise Tukey's test). In contrast, sham rats treated with systemic CLI-095 showed a reduction in path efficiency compared to sham-saline rats one week and one month after sham-injury/treatment (**Fig. 1.8B** sham-saline: 1 week after injury 0.44 ± 0.04 and Sham-CLI-095: 1 week after injury 0.332 ± 0.007n = 9

rats, $p = 0.04$ by post hoc Tukey's test and sham-saline: 1 month after injury 0.60 ± 0.029, $n = 9$ rats and Sham-CLI-095 1 month after injury 0.349 ± 0.03, $n = 9$ rats, $p < 0.005$ by TW-RM ANOVA followed by pairwise Tukey's test). While the impairment in memory performance following TLR4 antagonist treatment in uninjured rats is surprising, it is consistent with the ability of CLI-095 to enhance network excitability which would impair dentate memory function.

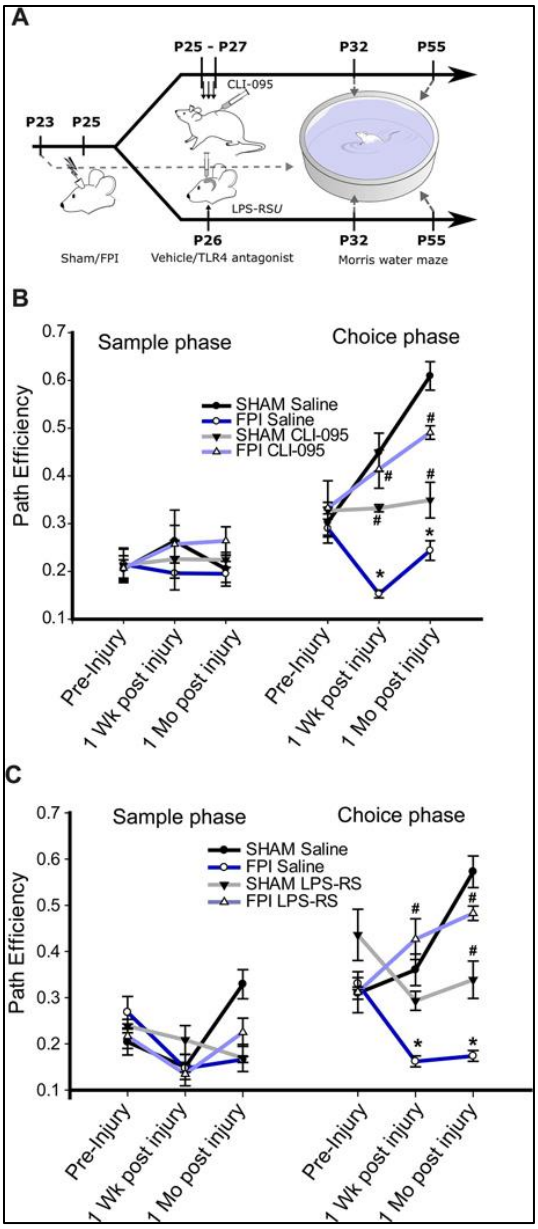

Figure 1.8. TLR4 antagonist treatment early after FPI improves working memory function. (A) Schematic of experimental design shows timeline for working memory testing pre and post injury using Morris Water Maze. (B) Summary of path efficiency during sample and choice phases of a delayed match to position task in vehicle or CLI-095 treated (systemic) sham and preinjury, 1 week and 1 month after FPI. (C) Summary of path efficiency during sample and choice phases of a delayed match to position task in vehicle or LPS-RSU treated (systemic) sham and pre-injury, 1 week and 1 month after FPI. *indicates $p<0.05$ compared to sham and # indicates $p<0.05$ compared to corresponding vehicle treatment by TW-RM ANOVA followed by pairwise Tukey's test, n= 9 rats each group (**Data generated by co-authors**)

Focal and transient hippocampal TLR4 antagonism alters working memory function.

Systemic administration of CLI-095 can potentially alter central and peripheral immune responses, which raises the possibility that the suppression of global immune responses may underlie the efficacy of TLR4 modulation on neurobehavioral outcomes after FPI. To limit the potential contribution of systemic effects of TLR4 antagonism, we examined whether local, unilateral hippocampal injection of LPS-RSU (5 µl of a 2 mg/ml solution, intrahippocampal injection 24 hrs after FPI/sham) on the injured side would reduce the working memory impairment following FPI, as observed after systemic treatment. Similar to what was observed after systemic CLI-095 treatment, path efficiency on the sample phase and during pre-injury trials did not show any significant effect of injury/drug or time (**Fig. 1.8C**). Focal TLR4 antagonist treatment reduced path efficiency in uninjured controls at one month (**Fig. 1.8C**, sham-saline: 1 month after injury 0.57 ± 0.034, n = 9 rats and Sham-LPS-RSU 1 month after injury 0.338 ± 0.04, n = 9 rats, p = 0.028 by TW-RM ANOVA followed by pairwise Tukey's test). Additionally, there was a trend for the treatment to decrease path efficiency one week after sham injury which did not reach statistical significance (**Fig. 1.8C** sham-saline: 1 week after injury 0.36 ± 0.033 and Sham-LPS-RSU: 1 week after injury 0.29 ± 0.020 n = 9 rats, p = 0.074 by TW-RM ANOVA followed by pairwise Tukey's test). In contrast, LPS-RSU-treatment improved path efficiency in brain injured FPI rats compared to saline treated counterparts both one week and one month after injury (**Fig. 1.8C**, FPI-saline: 1 week after injury 0.162 ± 0.008 and FPI-LPS-RSU: 1 week after injury 0.426 ± 0.04n = 9 rats, p < 0.001 and FPI-saline: 1 month after injury 0.173 ± 0.011, n = 9 rats and FPI-LPS-RSU 1 month after injury 0.482

± 0.015, n = 9 rats, $p < 0.005$ by TW-RM ANOVA followed by pairwise Tukey's test). Thus, as with systemic CLI-095, focal LPS-RSU improved memory performance one week and one month after FPI while impairing path efficiency at the one-month time point in sham controls (**Fig. 1.8C**). Together, these data support our hypothesis that early changes in dentate excitability and TLR4 modulation of dentate excitability contribute to neurological deficits including impaired working memory performance after brain injury.

Discussion

Janus faced effects of TLR4 signaling on excitability and memory function.

This study identifies that distinct cellular mediators contribute to the divergent effects of TLR4 on dentate excitability in the normal and injured brain which have a lasting impact on behavioral outcomes. The data show that the 'Janus faced' effects of TLR4 on excitability are likely determined by differential recruitment of glial versus neuronal TLR4 signaling. It has long been recognized that sparse firing is an essential functional feature of the dentate gyrus and its ability to 'gate' activity is critical for memory processing and for limiting pathology (Acsady and Kali, 2007; Dengler and Coulter, 2016; Kahn et al., 2019; Lothman et al., 1992). TLR4 activation enhances dentate network excitability after brain injury (Korgaonkar et al., 2020; Li et al., 2015) which would compromise the dentate gate. Consequently, TLR4 antagonists reduce dentate excitability after brain injury and improve working memory function in vivo. Simultaneously, TLR4 antagonist treatment in vivo reduces injury-induced increases in molecular signals associated with both the MyD88-dependent and MyD88-independant pathways effectively suppressing TLR4-dependent

immune response early after brain injury. Following brain injury, TLR4 antagonists reduced dentate excitability in ex vivo slices even in the presence of glial metabolic inhibitors. Moreover, AMPAR currents in neuronal cultures depleted of glia were enhanced by HMGB1, a TLR4 agonist, and reduced by LPSRSU, a selective TLR4 antagonist. These results using both pharmacological and neuronal culture systems strongly support a role for neuronal TLR4 signaling in augmenting excitability in the injured brain. Interestingly, blocking TNFα, a proinflammatory cytokine downstream of MyD88-dependent TLR4 signaling, reduced dentate excitability, reduced granule cell eEPSC amplitude even in the presence of GMI and occluded the ability of HMGB1 to increase excitability indicating that TLR4 signaling acts through TNFα to enhance excitability after brain injury. In contrast, TLR4 signaling appears to reinforce the dentate gate in the uninjured brain, where TLR4 signaling limits dentate network excitability during afferent stimulation (Li et al., 2015). Consistently, blocking basal TLR4 signaling enhances dentate excitability in response to input activation in ex vivo slices and compromises working memory function in vivo, demonstrating that basal TLR4 signaling regulates memory processing. Distinct from the effects on excitability, in vivo treatment with TLR4 antagonist failed to alter effectors downstream of the MyD88-dependent and MyD88-indepandant pathways in controls, indicating that antagonists did not have paradoxical effects on inflammatory signaling. Unlike after injury, glial metabolic inhibitors blocked TLR4 antagonist enhancement of dentate excitability in slices from sham rats indicating involvement of glial signaling in TLR4 modulation of excitability in controls. Blocking TNFα tended to enhance excitability suggesting a role for basal TNFα signaling in limiting network

excitability. Anti-TNFα reduced the ability of a TLR4 agonist to decrease excitability indicating that TNFα is downstream of TLR4 signaling in controls. These findings coupled with the ability of GMI to block effects of TLR4 modulation in sham rats suggest that TLR4 recruitment of signaling pathways in glia and glia-derived TNFα contribute to suppression of basal excitability in the uninjured dentate gyrus. Thus, the Janus faces of TLR4 signaling in the brain are distinguished by recruitment of glial metabolic processes and TNFα to limit excitability which supports working memory function in the uninjured brain. On the other hand, our data support a role for neuronal TLR4 and TNFα in increasing network excitability and contributing to deficits in working memory function after brain injury.

Immune signaling and memory function.

Several lines of evidence point to multiple roles for molecules, once thought to be confined to the peripheral immune system, in regulating normal function in healthy brains and in neurological disorders (Pickering and O'Connor, 2007; Williamson and Bilbo, 2013). Basal levels of neuroimmune signaling through specific cytokines such as TNFα have been shown to contribute to synaptic plasticity and memory processing (Avital et al., 2003; Balschun et al., 2004; Ben Menachem-Zidon et al., 2011; Goshen et al., 2007). Studies in transgenic mice lacking specific immune receptors, including TLR4, have identified memory and cognitive changes underscoring the importance of neuroimmune interactions in shaping brain function (Okun et al., 2012; Potter et al., 2019). Since neuro-immune interplay is critical for the developmental establishment of circuits (Szepesi et al., 2018),

use of germline knockouts confounds the ability to distinguish between immune regulation of circuit development and basal neuroimmune signaling in behaviors. Here we show that even a brief and transient block of basal TLR4 signaling, which increases network excitability, leads to prolonged impairments in working memory function for up to a month after treatment. Moreover, two mechanistically distinct TLR4 antagonists administered either focally in the hippocampus (LPS-RSU) or systemically (CLI-095) had similar effects in impairing working memory function, reducing the potential for off target effects. Curiously, an earlier study in mice reported impaired memory performance one week after a single treatment with the exogenous TLR4 agonist LPS and showed that TLR4 antagonist treatment abolished LPS induced memory impairments and suppressed the associated inflammatory response(J. Zhang et al., 2018). These findings contrast with what we would expect based on results demonstrating that TLR4 antagonist impairs memory function in uninjured rats (**Fig. 1.8**). However, it should be noted that LPS treatment in Zhang et al. (2018) enhanced inflammatory cytokines and TLR4 mediated signaling and may better reflect the neuroimmune environment present in the injured brain in our study. We find that TLR4 antagonist treatment reduced network excitability, neuronal loss and seizure susceptibility after FPI (Korgaonkar et al., 2020) and improved working memory after brain injury. The behavioral outcomes paralleled the opposing effect of TLR4 ligands on excitability, rather than the effects on inflammatory signaling which were unchanged in controls. Moreover, TLR4 expression returned to control levels and was unchanged by antagonist treatment one week (current study) after FPI. Similarly both GFAP and TLR4 expression were not different between vehicle and drug treated sham and FPI groups one

month after FPI (Korgaonkar et al., 2020). Thus, it is reasonable to propose that, while TLR4 antagonism after FPI reduces glial activation and may thereby reduce inflammatory signaling, the changes in excitability underlie the effects on memory function. Indeed, in controls, TLR4 antagonists enhanced excitability (Korgaonkar et al., 2020) which would be expected to compromise sparse neuronal activity and impair working memory performance (Kahn et al., 2019; Madar et al., 2019b; Scharfman & Bernstein, 2015; Wixted et al., 2014). In contrast, when neuronal excitability and the glutamate receptor subtype GluA1 are increased following brain injury, TLR4 antagonists reduced excitability (Korgaonkar et al., 2020), potentially aiding in maintaining sparse neuronal activity, which improved working memory. These data suggest that there may be an optimal range for TLR4 signaling to maintain physiological levels of excitability; both blocking basal levels, as with TLR4 antagonism in controls, as well as enhanced TLR4 signaling, as occurs after injury, can be pathological. Our findings are in line with the ability of innate immune signals to regulate the immediate early gene Arc and reports that Arc expression both above and below the optimal range can impair synaptic plasticity and cognitive function (Pickering and O'Connor, 2007; Rosi, 2011). Curiously, anti-TNFα mimics the effects TLR4 antagonists in slices from both the control and injured brains. Moreover, TLR4 mediated decrease in excitability in controls and increase in excitability after FPI appear to involve TNFα signaling suggesting that there may be a physiological range for TNFα that regulates excitability and synaptic plasticity at optimal levels. Our findings are consistent with the ability of exogenous TNFα to modulate synaptic excitability and plasticity (Belarbi et al., 2012; Maggio & Vlachos, 2018; Stellwagen et al., 2005) However, HMGB1

effects on dentate excitability in controls were reduced but not eliminated in anti-TNFα. It is possible HMGB1 may recruit additional receptor and or downstream pathways to impact network excitability. Traumatic brain injury is known to impair memory and cognitive function (Azouvi et al., 2017; Hamm et al., 1996; Lyeth et al., 1990; Titus et al., 2016; Vallat-Azouvi et al., 2007) and lead to persistent deficits in hippocampal long-term potentiation (Sanders et al., 2000). In earlier studies, mild lateral FPI (1.2 atm) was shown to contribute to transient working memory deficits which recovered by 3 weeks(Pang et al., 2015) . At the moderate injury strength (2–2.2 atm) used in the current study working memory deficits persist 4 weeks after injury and recover by 3 months, which is consistent with increasing neuropathology with injury severity. There is considerable evidence for the ability of non-specific immune modulators to limit post-traumatic inflammatory responses including TLR4 expression and improve neurological outcomes (Mao et al., 2012; C. Wang et al., 2015; W.-H. Yu et al., 2012). Our study using both local and systemic administration of specific TLR4 antagonists clearly demonstrates that suppression of TLR4 is beneficial following experimental brain injury in rats. The paradoxical detrimental effects of TLR4 antagonist treatment in the uninjured brain, interestingly, are coupled to both early and persistent increase in network excitability (Korgaonkar et al., 2020; Li et al., 2015) by mechanisms that are currently unknown. However, our data indicate that TLR4 does not modulate AMPA and NMDA receptor currents in slices from uninjured rats (Li et al., 2015), suggesting that modulation of GABA currents or intrinsic neuronal excitability need to be examined in future studies. Regardless of the underlying mechanisms, the effects of

TLR4 antagonists on excitability and memory function in uninjured brain warrants caution while proposing to use TLR4 antagonists for therapeutics.

Post-injury switch in cellular mediators of TLR4 effects on excitability.

We previously identified that post-traumatic increase in TLR4 expression is predominantly neuronal (Li et al., 2015). However, activation of glial purinergic signaling by TLR4 is known to acutely increase excitatory synaptic drive to CA1 neurons by modulating metabotropic glutamate receptors (Pascual et al., 2012). Additionally, LPS induced neurotoxicity in cortical cultures was found to be mediated through glia(Lehnardt et al., 2003). Moreover, glial TLR4 signaling through endogenous TLR4 ligands such as HMGB1, can enhance proinflammatory cytokines such as IL-1β and TNFα in immune cells including microglia and promote excitability (Maroso et al., 2010). While we acknowledge that fluoroacetate and minocycline may have nonspecific effects, our studies using complementary strategies of pharmacological glial metabolic inhibitors and isolated neuronal cultures, indicate that TLR4 modulation of AMPAR currents is independent of glia. It is possible that the lack of TLR4 in cortical neurons (Lehnardt et al., 2003) or use of LPS, which activates a broader immune response, contributes to the glial dependence of TLR4 signaling in prior studies. Future studies using cell specific deletion of TLR4 could further validate the role for neuronal TLR4 in modulating AMPA currents after brain injury. It is notable that our data in control slices demonstrate that glial signaling is necessary for maintaining basal levels of excitability and TLR4 modulation of excitability in the uninjured brain. Our findings suggest two distinct cellular and signaling pathways

for TLR4 function depending on whether there is injury to the brain. Classically, TLR4 signaling in glia is mediated by MyD88-TNFα dependent pathway and MyD88-independent pathway. TLR4 activation induces a MyD88-dependent increase in TNFα (Gao et al., 2009) and is proposed to enhance NMDA current s(Balosso et al., 2014; Maroso et al., 2010) and recruit glial purinergic receptors (Pascual et al., 2012). However, the post-traumatic increase in dentate excitability is mediated by enhancement of polysynaptic AMPAR currents with no change in NMDAR currents (Santhakumar et al., 2000). Consistent with this data, TLR4 enhances granule cell AMPAR, specifically, calcium permeable AMPARs (CP-AMPARs), and not NMDAR currents after FPI (Korgaonkar et al., 2020; Li et al., 2015). Interestingly, glial TNFα has been shown to recruit CP-AMPARs to the synapse (Pickering et al., 2005; Pribiag and Stellwagen, 2014; Stellwagen and Malenka, 2006). Since our results with glial metabolic inhibitors and neuronal cultures indicate that TLR4-mediated increases in excitability after injury does not involve glial signaling, it is possible that TLR4 activation after brain injury recruits "neuronal" TNF-α signaling. This would constitute a novel function for neuronal TNFα. TNFα is a likely candidate for the neuropathological effects of TLR4 after brain injury since it is known to contribute to excitotoxicity (Pickering et al., 2005; Stellwagen, 2011). Indeed, an inhibitor of TNFα synthesis has been shown to reverse cognitive deficits induced by chronic neuroinflammation(Belarbi et al., 2012). Unlike after injury, our data suggest that classical glial-TNFα signaling may reduce excitability in the uninjured hippocampus by mechanisms of which are currently under investigation.

Basal TLR4 modulation of network function and behaviors.

A particularly interesting finding is the ability of transient TLR4 antagonism to increase excitability and impair working memory performance in control, uninjured animals. These data suggest a critical neurophysiological function for the low levels of TLR4 signaling observed in the uninjured brain. Moreover, the lack of change in immune signaling alongside changes in excitability observed after TLR4 antagonism in the controls suggests that non-immune responses underlie this effect. Yet, blocking glial signaling eliminated the ability of CLI-095 to increase excitability in controls suggesting that glia are necessary intermediaries for this process. We demonstrate changes in memory function following acute and transient modulation of TLR4. These results extend prior works demonstrating a developmental role for TLR4 in learning and memory function in mice with constitutive TLR4 knockout (Okun et al., 2012). It remains to be seen whether TLR4 can modulate glial glutamate uptake and glutamate-glutamine cycling in the brain as has been shown in spinal circuits during LPS challenge (Yan et al., 2015). Regardless, the basal role for TLR4 in modulating dentate excitability and its impact on memory function need to be considered while proposing TLR4 modulators for use in therapies (Gnjatic et al., 2010; Hanke & Kielian, 2011).

Conclusions

Our data indicate that TLR4 signaling in neurons contributes to pathological increase in excitability after brain injury by enhancing AMPAR currents through a mechanism that involves TNFα. Blocking TLR4 signaling early after brain injury reduces injury-induced

decreases in hippocampal working memory function. However, we find that blocking basal TLR4 signaling in the uninjured brain augments dentate excitability through recruitment of glial signaling and TLR4 demonstrating a role for basal TLR4 signaling in maintaining sparse dentate activity. Thus, blocking the basal TLR4 signaling impairs working memory function. Taken together, the potential therapeutic effect of TLR4 antagonists may be better harnessed by isolating and selectively targeting the distinct pathological signaling downstream of neuronal TLR4.

Declaration of Competing Interest

The authors declare that they have no known competing financial interests or personal relationships that could have appeared to influence the work reported in this paper.

Acknowledgement

We thank Drs. Roman Shirakov, Stella Elkabes and Martin Riccomagno for help with culture studies. We thank Dr. Kelly Hamilton for discussions.

Funding

The project was supported by CURE Foundation CF 259051, NJCBIR CBIR14RG024, NIH/NINDS R01 NS069861 and R01NS097750 to V.S. and NJCBIR CBIR15FEL011 to A.K.

CHAPTER TWO

Early Deficits in Dentate Circuit and Behavioral Pattern Separation after Concussive Brain Injury

Lucas Corrubia[1,2,*], Andrew Huang[2,*], **Susan Nguyen**[2,*], Michael W. Shiflett[3], Mathew V. Jones[4], Laura A. Ewell[5], Vijayalakshmi Santhakumar[1,2]

[1]Department of Pharmacology, Physiology and Neuroscience, Rutgers New Jersey Medical
School, Newark, New Jersey 07103,
[2]Department of Molecular, Cell and Systems Biology, University of California Riverside, Riverside,
California 92521.
[3]Department of Psychology, Rutgers University, Newark, NJ 07102.
[4]Department of Neuroscience, University of Wisconsin, Madison, WI, 53705.
[5]Department of Anatomy and Neurobiology, University of California Irvine, Irvine, California
92697

*Authors Contributed Equally

Published in final edited form as:

Exp Neurol. 2023 December ; 370: 114578. doi:10.1016/j.expneurol.2023.114578.

Abstract

Traumatic brain injury leads to cellular and circuit changes in the dentate gyrus, a gateway to hippocampal information processing. Intrinsic granule cell firing properties and strong feedback inhibition in the dentate are proposed as critical to its ability to generate unique representation of similar inputs by a process known as pattern separation. Here we evaluate the impact of brain injury on cellular decorrelation of temporally patterned inputs in slices and behavioral discrimination of spatial locations in vivo one week after concussive lateral fluid percussion injury (FPI) in mice. Despite posttraumatic increases in perforant path evoked excitatory drive to granule cells and enhanced ΔFosB labeling, indicating sustained increase in excitability, the reliability of granule cell spiking was not compromised after FPI. Although granule cells continued to effectively decorrelate output spike trains recorded in response to similar temporally patterned input sets after FPI, their ability to decorrelate highly similar input patterns was reduced. In parallel, encoding of similar spatial locations in a novel object location task that involves the dentate inhibitory circuits was impaired one week after FPI. Injury induced changes in pattern separation were accompanied by loss of somatostatin expressing inhibitory neurons in the hilus. Together, these data suggest that the early posttraumatic changes in the dentate circuit undermine dentate circuit decorrelation of temporal input patterns as well as behavioral discrimination of similar spatial locations, both of which could contribute to deficits in episodic memory.

Introduction

Traumatic brain injury (TBI) is a growing epidemic (Rusnak, 2013; Vaishnavi et al., 2009) with an annual global incidence of over 60 million patients (McAllister, 1992) who are at risk for a variety of neuropsychological sequelae (Rao & Lyketsos, 2000). While neurological complications of TBI increase with injury severity (Annegers & Coan, 2000), even mild to moderate concussive brain injuries can lead to early and long term deficits in memory function (Alosco et al., 2023; Arciniega et al., 2021; Kumar et al., 2013). The dentate gyrus, a critical node in memory processing, receives extensive inputs from the entorhinal cortex and develops discrete sparse representations for downstream processing in hippocampal circuits (Leutgeb et al., 2007; Neunuebel & Knierim, 2014). The dentate gyrus is also the focus of neuronal loss and circuit reorganization early after human and experimental concussive brain injury (Folweiler et al., 2020; Leh et al., 2017; Lowenstein et al., 1992; Meier et al., 2016; Neuberger et al., 2017; Santhakumar et al., 2000), suggesting that dentate dependent memory functions are likely compromised after brain injury.

In particular, the dentate gyrus has been shown to be essential for distinguishing between similar memory episodes by encoding partially overlapping memories into discrete neuronal representations (Cayco-Gajic & Silver, 2019; Gilbert et al., 2001; T. J. McHugh et al., 2007; Yassa & Stark, 2011). At the circuit level, this is proposed to be achieved by pattern separation, a process of minimizing interference by segregating similar input patterns into discrete neuronal activity patterns. Whereas behaviorally relevant inputs and the resulting neuronal input patterns occur in space and time (Hainmueller & Bartos, 2020),

their neuronal representations have been evaluated mostly in the spatial domain as changes in firing or activity rates in spatially discrete neuronal groups or ensembles (GoodSmith et al., 2017; Larimer & Strowbridge, 2010; Leutgeb et al., 2007). However, whether brain injury impairs the ability of the dentate circuit to faithfully represent inputs and disambiguate similar neuronal input patterns remains unknown.

Most behavioral studies have focused on discrimination of spatial and contextual patterns to evaluate mechanisms of dentate pattern separation and assess the impact of disease (Bekinschtein et al., 2013; Kahn et al., 2019; T. J. McHugh et al., 2007; Morris et al., 2012). Studies in the fluid percussion injury (FPI) model of concussive brain injury have revealed early deficits in sequential spatial navigation in a dentate-dependent radial arm maze task, indicating that concussive brain injury compromises the ability to process and recall subtle spatial differences (Correll et al., 2021). Similarly, brain injury is also known to compromise working memory function (Korgaonkar, Li, et al., 2020; Smith et al., 2015). Still, whether episodic processing of spatial novelty by behavioral discrimination of spatial location is altered after brain injury remains to be determined.

In an approach complementary to behavioral studies, computational analyses of mechanisms for disambiguating overlapping memories have adopted spatially and temporally patterned inputs to assess "pattern separation". In this approach, model networks are activated by inputs with various degrees of similarity in spike timing and/or activated cell ensembles and the ability of the network to generate distinct spatio-temporal firing patterns is used as a measure of pattern separation (Braganza et al., 2020; Madar et al., 2019b; Myers & Scharfman, 2011; Rolls & Kesner, 2006). These studies have shown

that dentate granule cells (GCs) decorrelate input patterns both in terms of the active ensembles recruited as well as the pattern of firing in the active neurons (Myers & Scharfman, 2009; Yim et al., 2015). However, few experimental studies have evaluated the ability of the dentate circuit to decorrelate spatially and temporally patterned inputs (Larimer & Strowbridge, 2010; Madar et al., 2019a). Recently, Madar et al. (2019a) adopted an experimental paradigm in hippocampal slices to demonstrate that GCs could undertake input decorrelation at the level of individual neurons. These studies identified a role for inhibition in supporting temporal pattern separation in GCs and revealed cell-type specific and disease related changes in input decorrelation by dentate neurons (Madar et al., 2019a, 2021). These findings are consistent with predictions of simulations (Braganza et al., 2020) and with behavioral deficits in discrimination of novel spatial location in mice during suppression of dentate somatostatin interneuron activity in vivo (Morales et al., 2020). Since experimental concussive brain injury has been shown to result in early loss of dentate inhibitory neuron subtypes (Folweiler et al., 2020; Lowenstein et al., 1992; Santhakumar et al., 2001; Toth et al., 1997), we examined whether the resulting changes in inhibition (Folweiler et al., 2020; Gupta et al., 2020, 2022) could alter dentate dependent pattern separation in the temporal and spatial domains one week after brain injury. Because the relationship between neuronal spike train timing and behavioral spatial information is currently unclear, we will denote GC pattern separation of temporally patterned inputs in slice as “decorrelation” and behavioral spatial pattern separation in vivo as “spatial discrimination.”

Materials and Methods

All experiments were performed in accordance with IACUC protocols approved by the University of California, Riverside, CA in keeping with the ARRIVE guidelines.

Fluid Percussion Injury:

Randomly selected 8 to 10-week-old littermate male and female C57BL6/J mice were subjected to lateral fluid percussion injury (FPI) or sham injury. Briefly, mice were placed in a stereotaxic frame under isoflurane anesthesia and administered the local anesthetic 0.25% bupivacaine (subcutaneous). A 2.7 mm hole was trephined on the left side of the skull 2 mm caudal to bregma and 1 mm lateral from the sagittal suture. A Luer-Lok syringe hub with a 3 mm inner diameter was placed over the exposed dura and bonded to the skull with cyanoacrylate adhesive. The animals were returned to their home cage following recovery. One day later, animals were anesthetized with isoflurane and attached to a fluid percussion injury device (Virginia Commonwealth University, Richmond, VA, Model 01-B) directly at the metal nozzle. A pendulum was dropped to deliver a brief (20 ms) 1.5–1.7 atm impact on the intact dura. For sham injury, the animals underwent surgical implantation of the hub and were anesthetized and attached to the FPI device, but the pendulum was not dropped (Gupta et al., 2022; Smith et al., 2012).

Slice Preparation:

Naive C57BL6/J mice and mice one week after FPI or sham injury were anesthetized with isoflurane and decapitated for slice preparation using established protocols (Afrasiabi et al., 2022; Korgaonkar, Nguyen, et al., 2020). Horizontal brain slices (300 μm) were prepared in ice-cold sucrose artificial CSF (sucrose-aCSF) containing the following (in

mM): 85 NaCl, 75 sucrose, 24 NaHCO3, 25 glucose, 4 MgCl2, 2.5 KCl, 1.25 NaH2PO4, and 0.5 CaCl2 using a Leica VT1200S Vibratome (Wetzlar, Germany). Slices were incubated at 34°C for 30 min in an interface holding chamber containing an equal volume of sucrose-aCSF and recording aCSF, and subsequently were held at room temperature. The recording aCSF contained the following (in mM): 126 NaCl, 2.5 KCl, 2 CaCl2, 2 MgCl2, 1.25 NaH2PO4, 26 NaHCO3, and 10 D-glucose. All solutions were saturated with 95% O2 and 5% CO2 and maintained at a pH of 7.4 for 1– 6 h. Only sections on the side of injury were used in experiments.

Physiological Recordings

Voltage clamp recordings of perforant path evoked excitatory postsynaptic currents (eEPSCs) were obtained from dentate GCs using recording electrodes (3 – 6 MΩ) containing a Cs-Methanesulfonate Internal (in mM): 140 Cs-Methane sulfonate, 5 NaCl, 10 HEPES, 0.2 EGTA, 4 Mg-ATP, 0.2 Na-GTP, 5 Qx-314 with 0.2% biocytin. GCs were held at −70 mV, close to reversal potential for GABA, to isolate EPSCs (Andreasen & Hablitz, 1994). Evoked EPSCs were recorded in response to 0.1 to 2.0 mA stimuli, applied in 100 pA steps, through a concentric stimulus electrode positioned at the perforant path on the other side of the fissure from the dentate molecular layer. Peak amplitude of eEPSC was measured from the average of 3 to 5 responses at each step using ClampFit 10. A subset of recordings were obtained in a saturating concentration of gabazine (10 μM) to block both synaptic and extrasynaptic GABAA receptors.

Current clamp recordings to assess GC pattern separation were obtained using filamented borosilicate glass electrodes (3 – 6 MΩ) containing (in mM): 126 K-gluconate, 4 KCl, 10

HEPES, 4 Mg-ATP, 0.3 Na-GTP, 10 PO-creatinine with 0.2% biocytin. To assess cell health, GCs were held at −70 mV and responses to 1500 ms current steps from −200 pA to threshold positive current injection in 40 pA steps were recorded. Cells with resting membrane potential positive to −55 mV were excluded from analysis.

Pattern Separation Paradigm and Analysis

To assess GC pattern separation, input trains of varying correlations were adopted from Madar et al. (2019a). Each input correlation set included 5 temporally distinct trains at 10 Hz with an overall mean Pearson's correlation coefficient (Rin) of 0.25, 0.50, 0.75, or 0.95, designated henceforth as R25, R50, R75 and R95. The individual input trains (#1-#5) within an input correlation set were each 2 seconds long and were delivered at 2 second intervals. The 5 distinct input trains were delivered in sequence and the set was repeated 10 times for a total of 50 recorded trains (Madar et al., 2019a, 2021). Note that the average frequency of each input train was maintained at 10 Hz while in each set of 5 trains the timing of stimuli was varied to generate trains with different correlations.

GCs were held at −70 mV in whole cell configuration and stimuli were delivered through a concentric stimulating electrode (10 μm tip diameter) placed in the outer molecular layer to activate perforant path fibers. Stimulus trains were delivered with intensity ranging from 0.1–2 mA at 0.5 Hz so as to elicit action potentials in response to approximately 50% of stimuli. Once stimulus intensity was set, it was maintained constant for all input sets recorded. Cell resting membrane potential and access resistance were assessed between input sets and recordings were terminated if access resistance increased over 20% or membrane depolarized beyond −55 mV. To assess the role of inhibition in temporal pattern

separation, GCs were recorded and stimulated with input correlations of R75 in aCSF and then perfused with a sub-saturating concentration of gabazine (SR95531, 100nM), a GABAA receptor antagonist as described in earlier studies (Madar et al., 2019b), and to avoid burst firing (not shown) that occurred in pilot studies using saturating gabazine (10 μM).

For quantification of GC pattern separation function, Pearson's R correlation was calculated on output spike train rasters as previously defined in Madar et al. (2019a) using custom MATLAB code modified from: https://github.com/antoinemadar/PatSepSpikeTrains. Unless indicated otherwise, data were binned at 10 ms. For validation of pattern separation paradigm in naïve mice, pairwise correlation of each GC spike output train (Rout) was plotted against the predetermined correlation in the corresponding pairwise input spike trains. The five distinct input spike trains and their corresponding output spike trains are compared in a pairwise manner to assess correlation. Thus, the five input patterns yield 10 distinct Rin values centered around the target Rin and correspondingly, 10 Rout values. These Rin-Rout sets were used to compare data between GCs from sham and FPI mice.

To assess the reliability of GC input-output coupling between experimental groups, we evaluated spike train reliability (Rw) as a measure of the cell's ability to faithfully respond to multiple presentations of the same input train (effectively Rin=1). Rw was calculated as the average correlation of output of a given GC in response to 10 presentations of the same input pattern in the R95 input set and then averaged across the 5 patterns.

Novel Object Location Task and Analysis

To assess behavioral pattern separation, we implemented a novel object location task to test spatial discrimination (Bekinschtein et al., 2013; Morales et al., 2020) in mice one week post FPI or sham injury. The task consisted of a circular arena 50 cm in diameter and 47 cm high with laboratory tape in varying patterns in four distinct locations on the white opaque arena walls serving as spatial visual cues. The experimenter room was separated from the testing room with the test arena by a closed door. The testing room was dimly lit with overhead lights using dimmer switch on lowest setting. Mice underwent four days of habituation for 10 minutes each followed by a sample and choice phase on day five. The testing arena and objects were cleaned with 70% ethanol in between each animal throughout the entire experiment. During habituation, mice were brought to the testing room from the vivarium, handled by the experimenter, and exposed to the testing arena for 10 min each day where they were allowed to explore freely. On test day, mice were first exposed to a sample phase for 10 min, with three identical objects placed 120 degrees and approximately 16 cm apart and allowed to freely explore the objects. Mice were then returned to their home cage for 30 min before the choice phase. During the choice phase, one object was placed in its original (familiar) location, one object was removed, and the last object was shifted by 60° to a novel (unfamiliar) location. The mice were placed into the arena and allowed to explore the objects for five minutes. Videos were manually coded and analyzed by an experimenter blinded to animal injury status. Object exploration was counted as the number of times the animal's nose was within 0.5 cm of the object, with each continuous second counted as an additional exploration. Discrimination ratio was

calculated as [Exploration of Object in Unfamiliar Location – Exploration of Object in Familiar Location] / [Total Exploration]. Total exploration was also compared between groups.

Immunohistochemistry

Immunohistochemistry for ΔFosB, somatostatin (SST), and parvalbumin (PV) was used to evaluate persistent neuronal activity (You et al., 2017) and interneuron loss. Immediately following the novel object location task, mice were perfused transcardially with ice cold PBS followed by 4% PFA. Brains were excised and incubated in 4% PFA overnight and transferred to 30% sucrose for 2–3 days or until tissue sank. Brains were then flash frozen in OCT using liquid nitrogen and stored at −80°C prior to cryosectioning. 20μm serial sections were collected and mounted on SuperFrost slides and stored at −80°C prior to staining. Slides were stained for ΔFosB, SST, or PV following standard procedures (Neuberger et al., 2017a; Korgaonkar et al., 2020b). Briefly, slides were allowed to thaw to room temperature (RT) for 10 min, washed with 1xPBS 3×5min to wash off residual OCT. Slides were blocked in 10% normal goat serum in PBS + 0.3% Triton-X for one hour at RT, then incubated in anti- ΔFosB, SST, or PV antibody (1:500, Cell Signaling D3S8R; SST: 1:100, Millipore MA5–16987; PV: 1:1000, Swant GP72) overnight at 4°C. Slides were then washed 3×10 min with PBS and then incubated in goat anti-rabbit AF594 secondary antibody (1:1000, Invitrogen A11012) for ΔFosB, goat anti-rat AF647 antibody (1:1000, Invitrogen A-21247) for SST goat anti-guinea pig AF647 antibody (1:1000, Invitrogen, A-21450) for PV for 1.5 hours at RT, washed 3×10 min with PBS, and coverslipped using VectaShield with DAPI mounting media. Slides were imaged using

Zeiss Axioscope Epifluorescence Microscope as single optical sections at 10x and 20x for analysis. Blinded analysis was performed using Cell Detection settings in QuPath 0.4.2 (https://qupath.github.io) with files coded without injury status. Briefly, for ΔFosB and SST analysis, a ROI was drawn to outline the granule cell layer (GCL) using DAPI labeling to detect ΔFosB positive cells and in the hilus to detect SST neurons. Detection parameters were kept consistent between sections, and 3 to 6 level matched sections were averaged in each mouse for analysis, depending on slice and image quality. Robust and sparse PV immunolabeled neuronal somata were counted manually on QuPath for full dentate region to include both hilar, GCL, and molecular layer PV interneurons. SST cell counts were normalized to total hilar area (in mm2). The hilar area averaged across sections was not different between sections from sham and FPI mice (area in mm2, sham: 1.11±0.06 in 8 mice, FPI: 1.20±0.09 in 6 mice, p=0.38 by Student's t-test).

Statistical Analysis:

Statistical analyses were conducted in GraphPad Prism 9. The Shapiro-Wilk test was used to test for normality, and appropriate parametric or non-parametric statistical analyses were conducted. F-test to compare variances was used to assess whether both sample groups undergoing statistical comparisons have equal standard deviations. All statistical comparisons were conducted at an alpha level of $\alpha = 0.05$. Two-way repeated measures ANOVA (TW-RM ANOVA), paired and unpaired Student's or Welch's t-test, Mann-Whitney U test and Kolmogorov-Smirnov (K-S) test were used where appropriate.

Results

Dentate gyrus excitability is increased one week after concussive brain injury in mice.

Previous studies have identified an early increase in dentate network excitability after concussive brain injury in rat (Santhakumar et al., 2001; Neuberger et al., 2017a; Korgaonkar et al., 2020b) and mice (Folweiler et al., 2018, 2020; Smith et al., 2012; Witgen et al., 2005). To determine if afferent input drive to GCs is enhanced after FPI in mice, we recorded granule cell current responses to stimulation of the perforant path fibers using an electrode placed outside the fissure in mice one week after FPI or sham injury. As illustrated by the IR-DIC images (**Fig. 2.1A**) and the lack of change in average cross-sectional area of the hilus (see methods), the moderate FPI used in this study did not result in gross anatomical distortions of the dentate gyrus. Recordings were obtained from a holding potential of −70 mV to isolate glutamatergic currents in the absence of synaptic blockers. As reported following FPI in rat (Korgaonkar et al., 2020b), perforant path-evoked excitatory post-synaptic current (eEPSC) amplitudes in response to increasing current injection, was significantly enhanced in mice one week after FPI compared to sham injured controls (**Figure 2.1B–C**, n = 14 cells from 5 sham mice and 8 cells from 4 FPI mice, $F(1, 176)=31.25$, $p<0.0001$ for effect of injury by TW-RM ANOVA). In light of the extensive changes in dentate inhibition after FPI (Gupta et al., 2012; Gupta et al., 2022), we isolated eEPSCs in the presence of saturating concentration of the ionotropic GABAAR antagonist gabazine (10μM). Granule cell eEPSC amplitude recorded in gabazine was also increased after FPI (**Figure 2.1D–E**, n = 11 cells/4 sham mice and 10 cells/4 FPI mice, $F(1, 19)=15.49$, $p<0.0009$ for effect of treatment by TW-RM ANOVA). Note that the

prolonged eEPSC depolarization is consistent with polysynaptic activation previously reported after FPI in rat (Santhakumar et al., 2000). Analysis of the resting membrane potential (in mV, sham: −65.63±2.95 in 12 cells, FPI: −64.7±1.92 in 10 cells, p=0.9 by t-test) and access resistance (in MΩ, sham: 14.1±1.4 in 12 cells, FPI: 15.3±1.5 in 10 cells, p=0.56 by t-test) failed to reveal systematic differences between groups. To assess whether FPI results in sustained increase in excitability one week after injury, we examined dentate sections for expression of ΔFosB, a uniquely stable activity-dependent immediate early gene product shown to be persistently enhanced in epilepsy (You et al., 2017). Immunohistochemical staining of sections from a cohort of sham and FPI mice sacrificed one week after FPI identified an increase in the number of ΔFosB expressing putative GCs in the granule cell layer compared to that in sham mice (**Fig 2.1 F–G**, number of ΔFosB + GCs: sham: 24.11±5.98, n = 8 mice FPI: 52.51±15.25, n = 7 mice, p=0.02 by Mann-Whitney U test), which is consistent with sustained enhancement of dentate excitability. There was an increase in variance in the number of ΔFosB expressing GCs after brain injury ($F_{6,7} = 5.6$, p=0.04) indicative of individual differences in dentate hyperexcitability. Together, these data establish that the mouse model of moderate FPI used in our study results in both an increase in excitatory drive to GCs and an overall sustained increase in dentate excitability one week after injury.

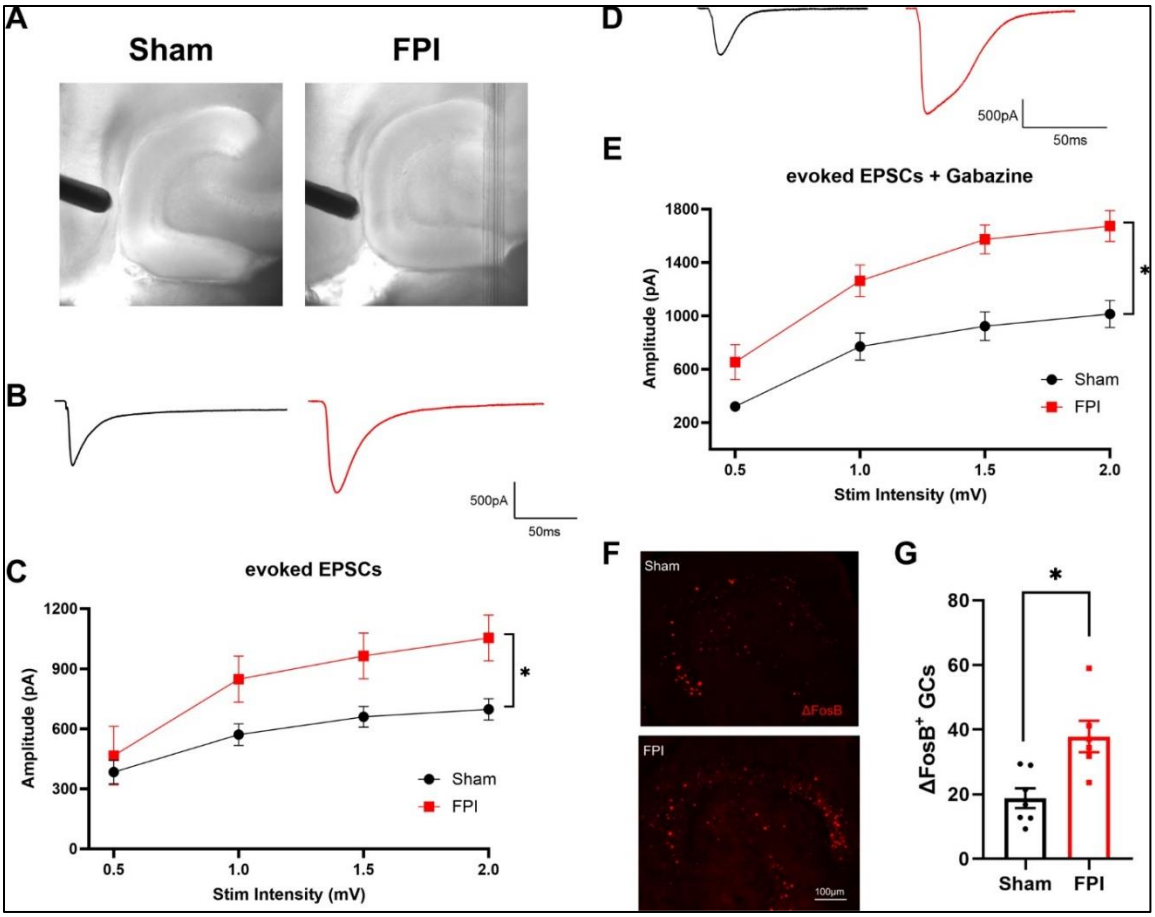

Figure 2.1. Enhanced dentate excitability one week after brain injury. (A) Representative IR-DIC images illustrating stimulating electrode positioning in slices from sham and FPI mice. (B) Representative eEPSC traces from dentate granule cells in sham (black) and FPI (red). (C) Plot of eEPSC peak amplitude in granule cells recorded in responses to increasing stimulus intensities. (D) Representative traces of pharmacologically isolated eEPSCs from dentate granule cells in sham (black) and FPI (red) recorded in 10 μM gabazine. (E) Summary plot of granule cell eEPSC peak amplitude in responses to increasing stimulus intensities recorded in 10 μM gabazine. (F) Representative images of staining for ΔFosB in sections (20 μm) from mice one week after sham and FPI. Scale bar=100μm. (G) Histogram showing average number of ΔFosB-positive cells in GCL of sham and FPI mice. (**Data generated by candidate**)

Inhibition is critical for granule cell decorrelation of temporal spike train patterns.

The characteristic low GC excitability and robust inhibition are critical for maintaining sparse GC firing and pattern separation. To determine if temporal input decorrelation by

GCs is impacted by FPI, we implemented an ex-vivo temporal pattern separation paradigm (Madar et al., 2019a; Madar et al., 2021) to assess the ability of GCs, within the local dentate microcircuit, to disambiguate temporally patterned inputs. GC firing was recorded in response to stimulation of perforant path fibers in the outer molecular layer, using sets of stimulus patterns with known degrees of similarity, to quantify similarity between output spikes. For initial validation, four sets of Poisson input stimulus patterns with 10 Hz average frequency and input correlations of R25, R50, R75, or R95 were used to elicit GC responses (**Fig 2.2A**). Similarity indices of the GC "output" spike trains (Rout) were computed as the pairwise Pearson's correlation coefficient on output spike train data binned at 10, 20 and 100 ms to assess the effect of bin-width on Rout (Fig 2B). Consistent with Madar et al. (2019a), GC output similarity was consistently lower than the corresponding pairwise input similarity (**Fig 2.2B**, Rin vs. Rout, n =4 cells / 3 mice). Since the reduction in output similarity was most robust when spike data were binned over 10 ms (**Fig. 2.2B**), a bin width of 10 ms was adopted in subsequent experiments. We then examined the potential contribution of the local inhibitory circuit to GC temporal pattern separation by partially decreasing GABAergic inhibition. To compare similarity indices before and after partial inhibitory block within the same cell, we restricted the inputs to a set of 5 stimuli with R75, reflecting a 75% similarity of across the inputs. GC responses were recorded first in aCSF and then in a non-saturating concentration of gabazine (100 nM). Under both recording conditions, GC output correlation remained consistently lower than the input correlation of 0.75 suggesting contributions from cell intrinsic and/or afferent synaptic characteristics in mediating GC temporal pattern separation. However,

pairwise comparison of Rout within the same cell and pattern in aCSF versus gabazine revealed a significant increase in GC output correlation (**Fig. 2.2 C–E**, Mean pairwise Rout, aCSF: 0.20±0.02, Gabazine: 0.30±0.01, n = 4 cells/3 mice; $p < 0.0001$ by Paired t-test, Cohen's D =1.7). These results validate the role for inhibition in the ability of GCs to decorrelate temporally patterned inputs as reported previously (Madar et al., 2019a).

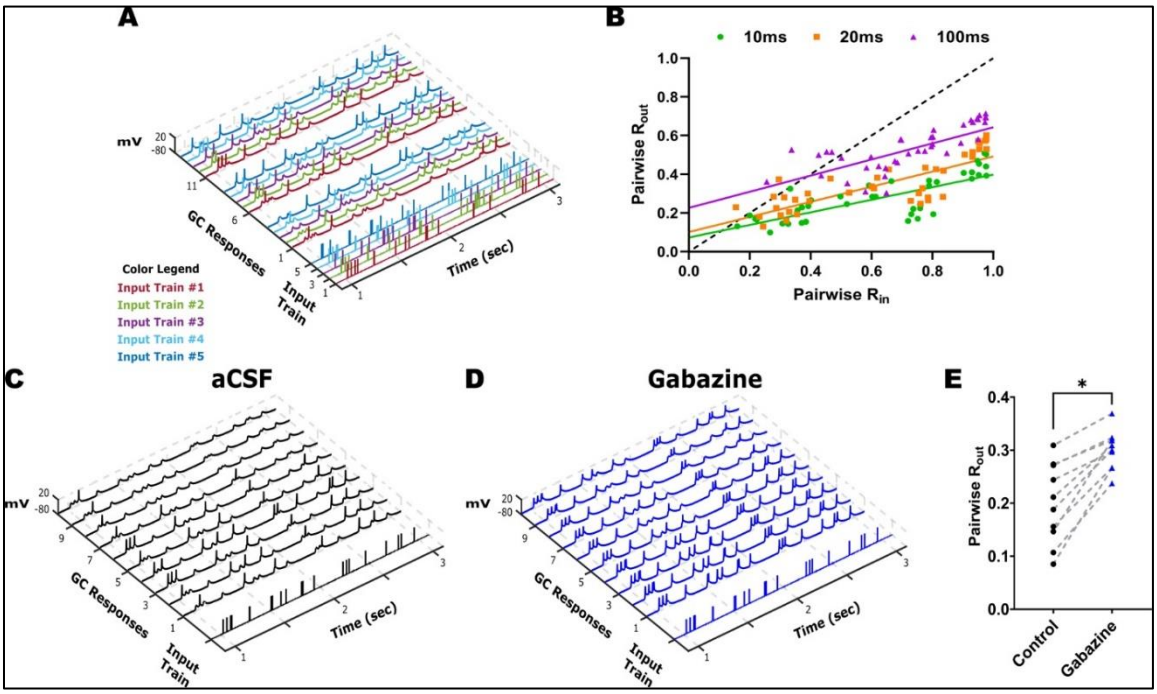

Figure 2.2. Robust temporal pattern separation by dentate granule cells. (A) Representative input spike trains from the R75 input set are illustrated with each pattern (input trains #1–5) in a distinct color. The GC firing evoked by three (of 10) repetitions of each input set is illustrated with output trace color matched to corresponding input spike train. (B) Rout vs Rin plots calculated with bin widths for correlation set to 10, 20, and 100 ms. Responses were elicited by input sets with similarity indices ranging from R25 to R95. (C-D) Example traces of GC firing responses elicited during 10 repetitions of the same representative (R75, pattern #4) input spike train recorded in aCSF (C) and in 100 nM gabazine (D). (E) Summary of pairwise R comparisons in aCSF and 100 nM gabazine (n = 4 cells). * Indicates $p < 0.05$ by Paired t-test. (**Data generated by co-authors**)

Reliability of dentate granule cell spiking is not altered early after FPI.

After validating the experimental brain injury model in mouse (**Fig. 2.1**) and establishing the temporal pattern separation paradigm in slice recordings (**Fig. 2.2**), we examined GCs in mice one week after sham or FPI for their ability to decorrelate input spike train sets with 25% and 95% similarity. To ensure that there were no systematic differences in GC recordings between sham and FPI, we confirmed that the access resistance was not different between recordings from the two experimental groups (in MΩ, sham: 13.98±1.38, FPI: 15.57±1.97, p=0.54 by Student's t-test). Additionally, examination of the GC intrinsic parameters failed to reveal differences in resting membrane potential (Fig. 3A–C, in mV, sham: −72.18±1.14, , FPI: −75.86±2.06, p=0.16 by Student's t-test) and input resistance (in MΩ, sham: 102.3±8.61, FPI: 121.1±13.34, p=0.28 by Student's t-test, based on 11 cells/3 sham mice and 14 cells/4 FPI mice. In GCs that reached threshold with a +160 pA current injection, firing frequency was unchanged after FPI (in Hz, sham: 6.67±2.46 in 7 cells, FPI: 6.74±1.54 in 9 cells, p=0.98 by unpaired Student's t-test). Similarly, action potential threshold measured at rheobase current injection was not different between groups (**Fig. 2.3B-C**, in mV, sham: −31.49±2.13, FPI: −32.15±1.78, p=0.81 by unpaired Student's t-test).

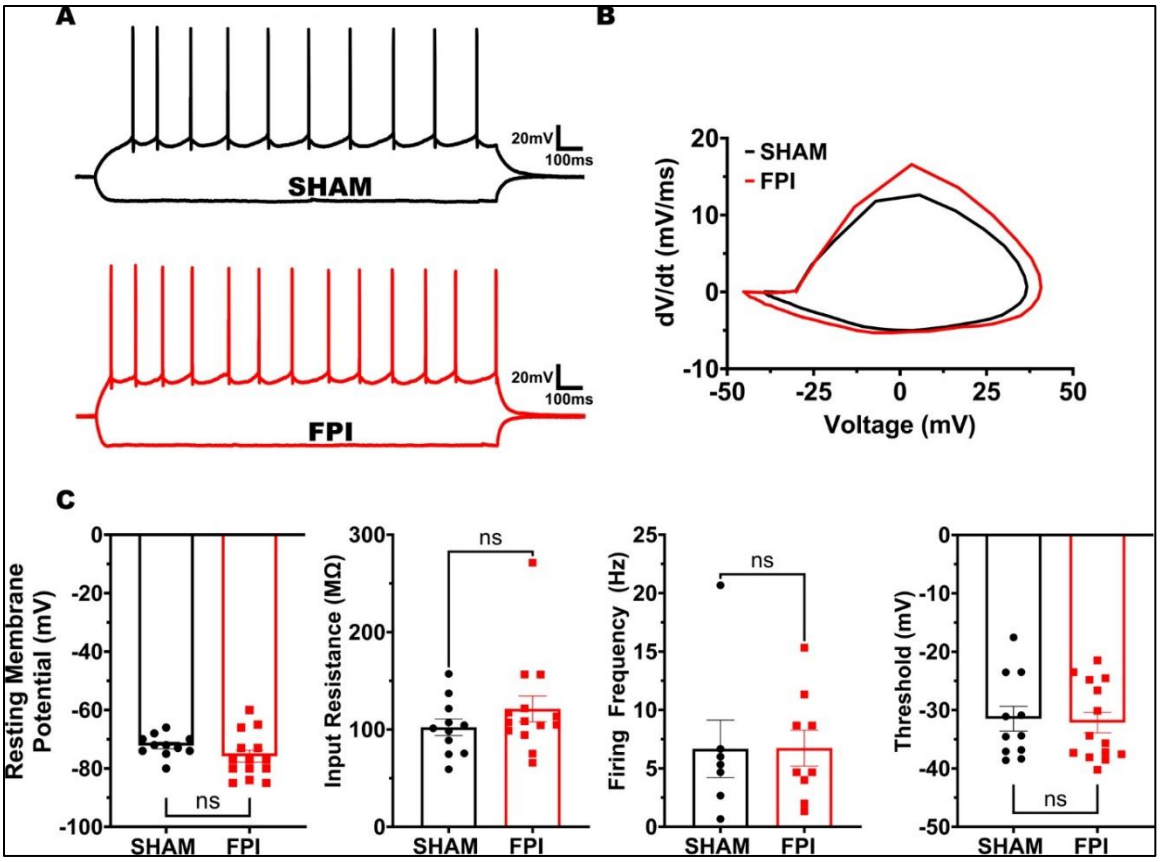

Figure 2.3. Granule cell intrinsic physiology is not altered FPI (A) Representative granule cell membrane voltage traces in response to −200 pA and +160 pA current injections. (B) Representative action potential phase plots obtained from the first action potential in granule cells sham (black) and FPI (red) mice. (C) Summary plots of resting membrane potential, input resistance, firing frequency at +160pA i-inj and action potential threshold. Note that only cells that reached threshold at +160pA were included in analysis of firing frequency. (**Data generated by co-authors**)

Given the neuronal loss and circuit alterations after FPI (Bonislawski et al., 2007; Folweiler et al., 2020; Gupta et al., 2020, p. 20; Neuberger et al., 2017), we examined whether the fidelity of GC response to a given input train is fundamentally altered by injury. Under optimal conditions, if a local dentate network receives identical inputs, a given GC within the receiving network should maintain indistinguishable output responses. To determine if injury alters the ability of the GC network to reliably respond to a given input train, we

calculated spike train reliability (Rw) as the average Rout of a given GC in response to identical input pattern using the R95 input set (**Fig 2.4A, B**). Note that because stimulus intensity was set to achieve a 50% spike success in each cell, the enhanced eEPSC (Fig. 1) should not impact evaluation of spike train reliability. Indeed, the average firing rate elicited by the input spike trains was not different between GCs from sham and FPI (**Fig. 2.4C**, average firing frequency in Hz, sham: 3.55±0.38, FPI: 2.99±0.19, p=0.17 by unpaired Student's t-test). Interestingly, the variance of the firing frequency trended towards a reduction after FPI ($F_{10,13}$= 3.10, p = 0.06, F-test for variance) suggesting a potential decrease in a source of input decorrelation after FPI. Despite the dentate circuit changes and enhanced ΔFosB labeling in GCs after FPI, spike train reliability was not different between the GCs from sham and FPI mice (**Fig. 2.4C**, average spike train reliability: sham: 0.47±0.05, FPI: 0.51±0.03, p=0.44 by unpaired Student's t-test; variance ($F_{10,13}$= 1.92, p = 0.27 by F-test for variance).

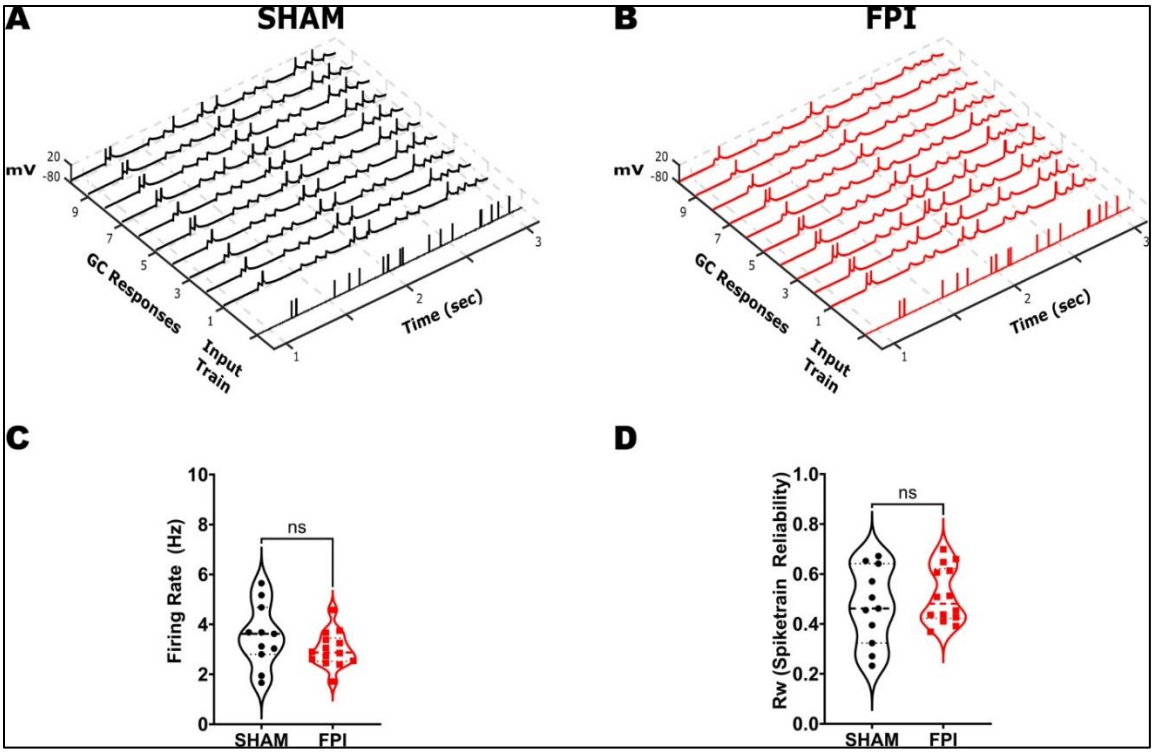

Figure 2.4. Assessment of GC firing fidelity after FPI. (A-B) Example of a single input spike train at R95 and the corresponding membrane voltage traces recorded in GC during 10 repetitions of the same stimulus in sham (A) and FPI (B) mice. (C-D) Summary plot of GC firing frequency (C) and reliability index (D) of GC firing during R95 inputs in sham (n = 11 cells from 3 mice) and FPI (n = 14 cells from 3 mice). (**Data generated by co-authors**)

Granule cell decorrelation of temporal patterned inputs is reduced after FPI.

To compare temporal pattern separation between GCs from sham and FPI mice, GCs were stimulated using input stimulus train sets with 25% and 95% similarity (**Fig. 2.5A–B**). Plots of averaged pairwise Rout values against Rin, for each input set showed that the GCs from both sham and FPI mice were still able to decorrelate inputs (Rout < Rin) (**Fig. 2.5C–E**). Note that the input trains each average Rin generate 10 distinct pairwise Rin values, reflecting correlation between 2 input trains, with corresponding 10 pairwise Rout values

for each cell (**Fig. 2.5D, E**). Comparison of the Rout values obtained in response to the 20 Rin values (10 each at R25 and R95) in GCs from sham and FPI mice revealed a significant effect of injury ($F(1,18) = 6.57$, $p<0.02$ by TW-RM ANOVA, based on 9 Sham cells from 3 mice and 11 FPI cells from 4 mice each where all input trains were recorded). However, the Rout within each cell averaged across the 10 Rin values at R25 (Sham: 0.13±0.01 in 9 cells/3 mice, FPI: 0.12±0.01 in 11 cells/4 mice, $p=0.36$) and R95 (Sham: 0.47±0.04 in 11 cells/3 mice, FPI: 0.49±0.01 in 14 cells/4 mice, $p=0.49$) showed no apparent difference (**Fig 2.5 F, G**, note that a few cells in which only R95 stimulus trains were recorded were included in this analysis). We reasoned that this was because averaging across multiple Rin values fails to capture the differences between Rin values and corresponding Rout (**Fig. 2.5D, E**). We generated cumulative probability distributions of the Rout data corresponding to each average Rin value to better assess changes in decorrelation. The cumulative probability distribution of all Rout values for Rin values centered around R25 was not different between GCs from sham and FPI (**Fig. 2.5H**, $p=0.8$ by K-S test). However, the distribution of all Rout values in response to inputs centered around R95 was significantly different between groups (Fig. 5I, $p=0.0005$ by K-S test) with a preferential reduction in the ability of GCs to support greater decorrelation after FPI. These findings are consistent with a subtle reduction in the ability of the dentate circuit to decorrelate highly similar inputs after injury. These data show that although GCs are continuing to disambiguate similar spike train inputs early after injury, their critical ability to do so when inputs are highly similar is compromised after injury.

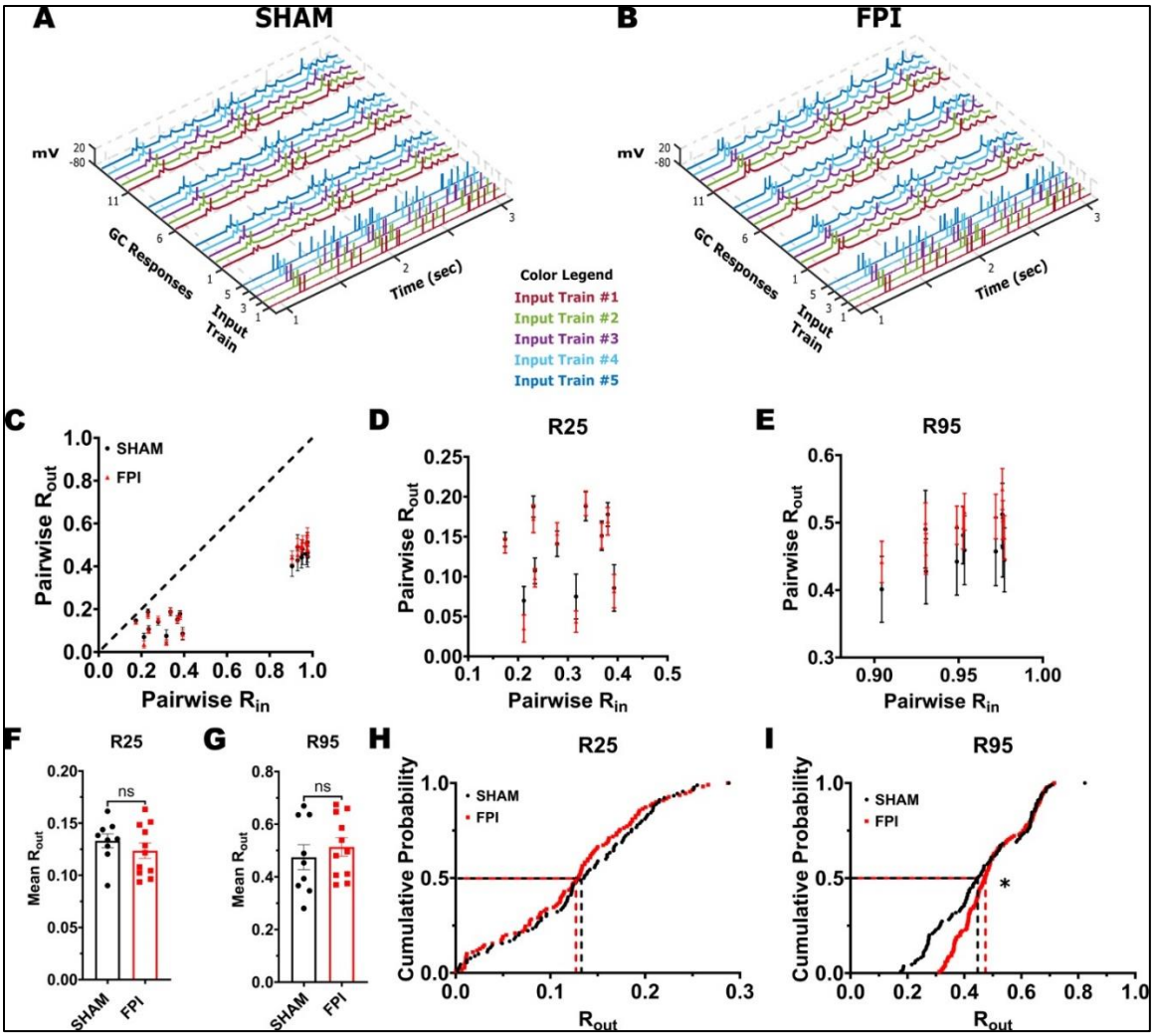

Figure 2.5. GC temporal pattern decorrelation is maintained after brain injury. (A-B) Representative input spike trains from the R95 input set are illustrated with each pattern (input trains #1–5) in a distinct color. GC firing evoked by three repetitions of each input set in sham (A) and FPI (B). Each membrane voltage trace is color matched to corresponding input spike train. (C) Summary plot of Rout vs Rin recorded during presentation of stimulus sets with R25 and R95 similarity indices in GCs from sham (black) and FPI (red) mice. (D-E) Pairwise Rout/Rin in GCs from sham and FPI mice for 10 distinct Rin values each centered around R=0.25 (D) and R=95 (E). Note that these are the same data as in Fig 5C presented at a different scale. (F-G) Summary plots of average Rout in each cell averaged across all Rin values centered around R25 (F) and R95 (G). (H-I) Cumulative probability distributions of pairwise Rout in GCs from sham and FPI mice during presentation of input sets with average Rin=R25 (H, recordings from 9 cells in 3 sham mice and 11 cells in 3 FPI mice) and R95 (I, 11 cells in 3 sham mice and 14 cells in 3 FPI mice) * Indicates $p < 0.05$ by K-S test. (**Data generated by co-authors**)

Behavioral spatial pattern separation is degraded early after FPI.

To determine whether the reduction in the ability of the dentate circuit to decorrelate input patterns after injury was accompanied by deficits in behavioral spatial discrimination, we adopted a novel object location task, which relies on dentate function and tests for episodic rather than sequential memory (Morales et al., 2021). Mice one week after FPI or sham surgery were assessed in the novel object location task following appropriate habituation (**Fig. 2.6A**). The mice were exposed to three identical objects in the sample phase followed, 30 minutes later, by a choice phase in which one object was removed and one of the remaining objects was moved to a novel location (**Fig. 2.6A–B**). Compared to sham mice, which showed significantly greater interaction with the object in the novel location ($p=0.0002$ by one sample t-test), FPI mice failed to show preference for the object in the novel location ($p=0.67$ by one sample t-test). Consistently, the discrimination ratio, defined as the difference between number of interactions with the object in the novel location and the familiar location divided by the total interaction with both objects, was lower in FPI mice (**Fig. 2.6C**, discrimination ratio: sham: 0.28±0.04, FPI: 0.04±0.08, n = 8 mice/group, $p=0.02$ by unpaired Student's t-test). However, the total exploration assessed as the number of contacts with objects in the 5-minute exploration period was not different between groups (**Fig. 2.6D**, number of contacts: sham: 39.25±5.58, FPI: 41.13±6.6, n = 8 mice each, $p=0.83$ by unpaired Student's t-test) indicating no difference in exploration between sham and FPI mice.

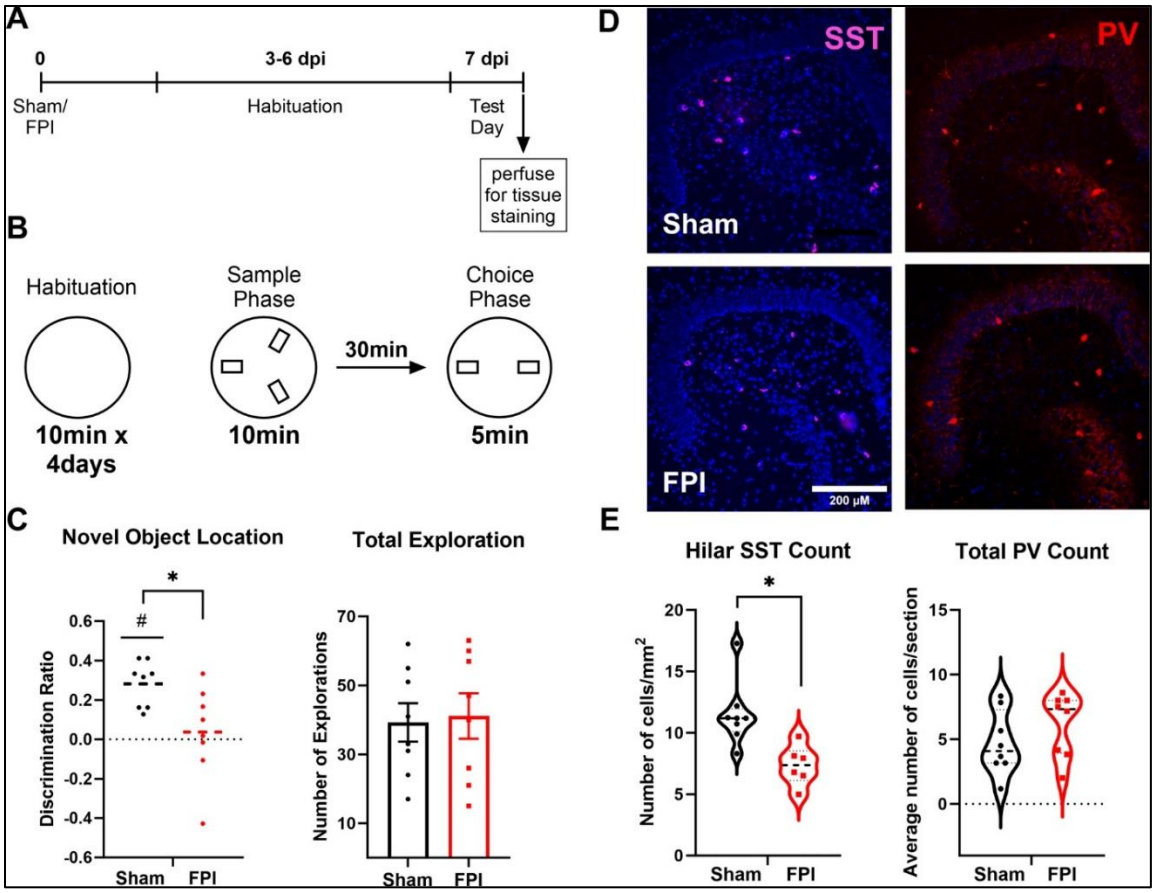

Figure 2.6. Spatial recognition memory is impaired following FPI (A) Timeline of behavioral task and tissue processing for histological staining. (B) Schematic representation of the novel object location task performed one week post injury showing 4-day habituation in open chamber and test day timeline and location of objects in sample and choice phases. (C) Summary plot of discrimination ratio (left) and total duration of exploration (right) in sham (n = 8) and FPI (n=8) mice. (D) Representative images of dentate sections immunostained for somatostatin (left) and PV (right) illustrates reduction in hilar somatostatin neurons one week after FPI, scale bar=100µm. (E) Summary histogram of somatostatin (left) and PV (right) cell counts in sections from the dentate hilus in sham and FPI mice. (**Data generated by candidate**)

Finally, because, previous studies have identified a role for dentate somatostatin interneurons in performance of the novel object location task (Morales et al., 2021) and somatostatin neurons are vulnerable to brain injury (Lowenstein et al., 1992; Santhakumar

et al., 2000; Frankowski et al., 2019), we examined whether there was a loss of somatostatin neurons in the FPI mice that performed the behavioral task. Staining for somatostatin revealed a significant reduction of labeled neurons in the dentate hilus one week after FPI (**Fig 2.6D–E**, cells/mm2, sham: 11.50±0.92, FPI: 7.337±0.66, based on within animal averages of level matched sections from 8 sham and 6 FPI mice, p=0.005 by unpaired Student's t-test). In contrast immunostaining for PV failed to reveal changes in PV neuron density after FPI (**Fig 2.6D–E**, cells/section, sham: 4.52±0.86, FPI: 5.22±0.70, based on within animal averages of level matched sections from 8 sham and 8 FPI mice, p>0.05 by unpaired Student's t-test). These data suggest that injury-induced selective loss of dentate somatostatin interneurons could contribute to the observed impairment in location discrimination in mice early after brain injury.

Discussion

Changes in episodic memory are a major neurocognitive consequence of traumatic brain injury with early and persistent deficits observed in patients and in animal models (Alosco et al., 2023; Hamm et al., 1996; Korgaonkar, Li, et al., 2020; Kumar et al., 2013; T. McHugh et al., 2006; Smith et al., 2015; Tsirka et al., 2010). Although the dentate gyrus is known to play an essential role in encoding and disambiguating spatial memories, the underlying circuit mechanisms are not fully understood (Cayco-Gajic & Silver, 2019; Kesner, 2013; Morris et al., 2012; Rolls & Kesner, 2006). Here we implemented parallel circuit and behavioral assays of pattern separation in mice one week after concussive brain injury. Interestingly, we find that the reliability of GC firing is not altered after brain injury.

Moreover, the GC output correlation was consistently lower than input spike train correlation in cells from both control and injured mice, indicating that temporal pattern separation at the cellular level continued to occur after brain injury. However, the critical ability of dentate GCs to decorrelate highly similar input patterns was reduced after brain injury. These results are analogous to the effect of partial GABAA receptor antagonism where GC output correlation is higher than in aCSF, yet, remains lower than input correlation indicating deficits in decorrelation of inputs by GCs (**Fig. 2.2** and Madar et al., 2019a). Despite the limited decrease in GC cellular temporal pattern decorrelation after injury, behavioral discrimination of spatial location in an episodic memory test was severely compromised. It is possible that the posttraumatic increase in the number of GCs showing sustained increase in excitability, identified by ΔFosB labeling, degrades sparse coding in the dentate and contributes to decline in spatial location discrimination. Furthermore, we demonstrate a decrease in dentate hilar somatostatin neurons in brain injured mice that showed deficits in spatial discrimination. Since somatostatin neurons have been shown to contribute to the novel object location task (Morales et al., 2021) used in our study, posttraumatic somatostatin neuron loss could contribute to deficits in behavioral spatial discrimination. Together these findings identify early changes in dentate inhibition and an increase in GC activity that could compromise the ability of the dentate to effectively decorrelate spike trains and engage distinct GC ensembles, likely contributing to deficits in encoding episodic memories.

Posttraumatic changes in dentate circuit impact temporal decorrelation of input patterns. There is considerable evidence for the dentate gyrus playing a critical role in distinguishing context and spatial locations (Kesner, 2013; Leutgeb et al., 2007; T. J. McHugh et al., 2007; Senzai & Buzsáki, 2017). Because events occur in space and time, patterned neuronal firing can be essential for encoding spatial and temporal information (Buzsáki, 2010; Eichenbaum, 2013; Kobayashi & Poo, 2004; Tort et al., 2011). Experimental and computational studies examining dentate gyrus processing of temporally patterned inputs have identified that individual GCs can effectively orthogonalize temporal patterns in input spike trains. The ability of GCs to decorrelate temporal patterns likely depends on a combination of their intrinsic properties, local circuit inhibition, probabilistic synaptic release and spike-timing history resulting from short-term synaptic dynamics (Madar et al., 2019a, 2019b; Yim et al., 2015). By adopting a temporal pattern separation paradigm, we confirmed that GCs effectively decorrelate input patterns, particularly those with high similarity (**Fig. 2.2**). Additionally, we show that even low dose gabazine (100 nM), resulting in partial block of inhibition, contributed to input decorrelation (**Fig. 2.2**) demonstrating a role for inhibition in decorrelation of input patterns. It is possible that, in addition to inhibition, perforant path synaptic dynamics and GC intrinsic physiology also contribute to temporal pattern separation in GCs.

In mice one week after concussive brain injury, we demonstrated an increase in perforant path evoked excitatory drive (**Fig 2.1**) which is consistent with our prior studies identifying an immune receptor mediated increase in AMPA currents one week after FPI in rat (Li et al., 2015; Korgaonkar et al., 2020b). These results and the lack of changes in GC intrinsic

physiology (Fig. 3) and loss of hilar somatostatin neurons early after FPI are consistent with earlier studies in rats (Lowenstein et al., 1992; Santhakumar et al., 2000; Korgaonkar et al., 2020b). Moreover, labeling for ΔFosB, which indicates sustained increases in excitability (You et al., 2017), is increased one week after FPI. Therefore, it may seem surprising that the reliability and average firing frequency of GC responses to temporally patterned inputs remains unchanged after brain injury (**Fig 2.4**). Indeed, spike train reliability, a measure of the output correlation in response to identical inputs, is consistently lower than unity due to contributions from network noise and probabilistic transmitter release. A possible reason for maintenance of GC reliability despite the posttraumatic increase in afferent drive (**Fig. 2.1**) could be because, in the absence of post-injury changes in GC intrinsic physiology, setting the input stimulus intensity to elicit response in 50% of trials limited the effect of the increased excitatory input. Additionally, despite the loss of interneuron populations (Santhakumar et al., 2000; Folweiler et al., 2020), dentate inhibitory circuits undergo reorganization including increase in granule cell tonic GABA currents (Gupta et al., 2012; Gupta et al., 2022) which could help maintain GC activity levels. Moreover, GCs continue to effectively decorrelate input spike patterns as demonstrated by the consistent observation that output correlation remains lower than the input correlation even after brain injury (**Fig 2.5C–E**). Our finding that GCs continue to decorrelate input patterns early after brain injury is also consistent with recent findings in computational and experimental models of temporal lobe epilepsy (Yim et al., 2015; Madar et al., 2021). However, our results reveal a significant decrease in temporal pattern separation in response to input trains with high degrees of similarity, which suggests that

the network level changes including a partial loss of hilar somatostatin neurons do impact decorrelation of input information. Because suppressing dentate inhibition with saturating concentrations of gabazine leads to burst firing in GCs (not shown), complete disinhibition is unlikely to yield meaningful analysis of decorrelation. Future studies adopting opto- or chemogenetic suppression of specific neuronal subtypes could provide additional insights into the contribution of specific interneuron subtypes to GC input decorrelation. Although injury did not decrease GC spike reliability, the variance in firing frequency in response to identical input trains trended to decrease after injury. It is interesting to speculate that the mechanisms contributing to reduced variance in GC firing after injury could also reduce GC decorrelation of highly similar inputs.

Distinguishing between cellular decorrelation of spike timing and behavioral discrimination of temporally ordered memories.

It must be noted that the temporal pattern separation paradigm used in this study focused on timing of spike trains and does not directly correspond to the encoding of temporal sequences of events. Indeed, it is unclear whether the dentate gyrus is involved in distinguishing the temporal order of sequential events occurring over a span of minutes to days (Gilbert et al., 2001). However, the dentate gyrus, and particularly the ongoing generation of adult-born neurons in the dentate, has been shown to play a role in stratification of memories over the time course of weeks (Aimone et al., 2011; Clelland et al., 2009; Miller & Sahay, 2019; Nakashiba et al., 2012; Rangel et al., 2014). Interestingly, adult neurogenesis is altered after brain injury with early increase at one week followed by

a progressive decline at one month (Clark et al., 2020; Kernie & Parent, 2010; Neuberger et al., 2017; Ngwenya & Danzer, 2019; Shapiro, 2017; T.-S. Yu et al., 2008). Whether injury induced changes in neurogenesis alter stratification or timestamping of contemporary memories and/or compromise spatial and contextual pattern separation at later time points after injury remains to be examined. In this study we focused on the early time point, one week after injury, when the injury-induced neurons are believed to be immature and unlikely to contribute to local dentate feedback inhibition (Miller & Sahay, 2019; Overstreet-Wadiche & Westbrook, 2006; Temprana et al., 2015). Additionally, we recorded GCs in the middle and outer third of the granule cell layer so as to avoid immature adult-born neurons, typically located in the inner third of the granule cell layer (Kerloch et al., 2019; Save et al., 2019). Crucially, all GCs included in analysis had input resistance less than 300 MΩ consistent with mature GC phenotype. Thus, our results identify that, at the level of individual putative mature dentate GCs, spike reliability and ability to decorrelate spike train patterns persist despite the early circuit changes after brain injury. Still, considering that temporal correlations between dentate neurons at the sub-second time scale are important for spatial memory discrimination (Van Dijk & Fenton, 2018), our slice physiology data suggest that the dentate's ability to encode input timing is largely retained early after brain injury. Because the dentate gyrus is particularly important for disambiguating highly similar patterns, the posttraumatic reduction in GC ability to decorrelate highly similar inputs could contribute to deficits in pattern separation after brain injury.

Mechanisms underlying altered behavioral pattern separation after brain injury.

In contrast to GC temporal pattern separation, we find that the ability to encode and discriminate subtle differences in spatial location is profoundly compromised one week after brain injury (**Fig. 2.6**). Our results complement a previous study which showed that mice one week after mild to moderate concussive brain injury are impaired in a sequential location discrimination task using the radial arms maze (Correll et al., 2021). Unlike the radial arm maze, the novel object location adopted in our study examines episodic memory and does not rely on repetition of discrete trial procedures (Bekinschtein et al., 2013; Morales et al., 2020). At the medium difficulty level (60° relocation) adopted in our study, the task has been shown to rely on dentate processing and is compromised by selective suppression of dentate somatostatin neurons. Consistently, we find that the behavioral deficit in novel object location one week after brain injury is accompanied by selective loss of hilar somatostatin neurons suggesting that interneuron loss may drive deficits in spatial pattern separation. Our data showing lack of change in PV neurons one week after FPI, when quantified across all dentate subregions, is consistent with Folweiler et al. (2020). However previous studies have identified post-FPI loss of PV neurons restricted to the dentate hilus and altered inhibition after FPI (Santhakumar et al., 2000; Folweiler et al., 2020). Whereas loss of immature and highly excitable adult born neurons born prior to injury could contribute to deficits in encoding novel object location, studies using the cortical impact injury have reported no loss of GCs born prior to injury (Kang et al., 2022). Rather, these neurons support enhanced feedback inhibition 8–10 weeks after injury. Moreover, it should be noted that neurogenesis is increased rather than decreased one week

after injury (Clark et al., 2020; Correll et al., 2021; Neuberger et al., 2017; Shapiro, 2017) and adult born neurons support local circuit feedback inhibition of mature GCs 4–6 weeks into development (Miller & Sahay, 2019; Temprana et al., 2015). Taken together, it is unlikely that injury induced changes in dentate neurogenesis underlie deficits in spatial pattern separation observed one week after injury. Instead, post-injury reduction of feedback inhibition, due to loss of somatostatin neurons, and increases in basal activity of GCs, revealed by the enhanced ΔFosB staining, likely impair the ability of the dentate circuit to effectively decorrelate entorhinal inputs into discrete active GC ensembles and firing patterns.

Reconciling the modest loss in cellular temporal decorrelation with profound impairment in behavioral spatial discrimination.

The apparent divergence in effect of brain injury on decorrelation of spike trains at the cellular level and discrimination of spatial location at a behavioral level indicate that disambiguation of information likely involves activation of distinct neuronal ensembles by input patterns. This is consistent with findings in computational models (Myers & Scharfman, 2009, 2011). Experimentally, due to the time for genetically encoded reporters to express (Cj et al., 2013; Ramirez et al., 2013), it may be challenging to identify neurons activated by two distinct and recent spatial inputs. However, there is some evidence for sparse but shared activation of neurons by different spatial experiences (Tashiro et al., 2007). The basal increase in neuronal excitability, identified by increase in ΔFosB labeled GCs after brain injury, could corrupt this sparse and selective activity necessary for

discrimination of spatial memories. A potential caveat is that, whereas the circuit experiments focused on the outer molecular layer, which receives the lateral entorhinal cortical fibers carrying contextual information, the spatial information examined in the behavioral spatial discrimination study is thought to be carried by inputs from the medial entorhinal cortex. Future studies examining decorrelation of medial perforant path inputs and behavioral analysis of context encoding could resolve whether the differences identified here are pathway specific. Analysis of spatiotemporal activity patterns of neuronal ensembles during behaviors or imaging circuit activity in vitro in response to spatiotemporal input patterns would help resolve how the dentate disambiguates input patterns.

In summary, our study identifies that early posttraumatic changes, including persistent increase in excitability and loss of somatostatin interneurons, reduce temporal pattern separation by dentate GCs and degrade the ability to discriminate between similar spatial locations. These changes likely contribute to working memory deficits after brain injury.

Acknowledgements

We thank Dr. Krista Marrero for thoughtful comments and discussion.

Funding

The project was supported by National Institutes of Health (NIH) NINDS R01 NS069861, R01NS097750 to V.S., NIH/NINDS F31NS110220 to L.C, American Epilepsy Society (AES) # 695548 and F31NS120620 to S.N, and AES #957615 and NIH F31NS131052 to A.H.

CHAPTER THREE

Altered Toll-Like Receptor 4 Modulation of Somatostatin Interneuron Inhibition Contributes to Pattern Separation Deficits after Brain Injury

Susan Nguyen[1,2], Chia-Wei Yeh[1,2], Erick Contreras[2], Ashley Dawson[2], and Vijayalakshmi Santhakumar[1,2]

Neuroscience Graduate Program[1], Department of Molecular, Cell and Systems Biology[2], University of California Riverside, Riverside, California 92521.

Manuscript in prep

Abstract

Neuroimmune signals within the brain play a pivotal role in synaptic physiology and plasticity both constitutively and in response to injury and infection. Current literature focuses on glial-based immune modulation of neuronal excitatory synapses, however neuronal expression of immune modulators and their impact specifically on inhibitory synapse function are still unclear. This study provides evidence that the innate immune receptor, Toll-Like Receptor 4 (TLR4), differentially modulates cell-type specific GABAergic inhibition within the hippocampal dentate circuit constitutively and after fluid percussion injury (FPI). Using whole-cell recordings from dentate granule cells, we identify that perforant-path evoked inhibitory postsynaptic current (IPSC) amplitude is reduced after brain injury. TLR4 antagonism resulted in opposing modulation of evoked IPSC amplitude, decreasing it in sham controls and enhancing it back to control levels in and injured mice, demonstrating a unique and plastic TLR4 mediated regulation of dentate inhibition. Fluorescent in-situ analysis identified TLR4 mRNA in somatostatin (SST), but not parvalbumin (PV) interneurons. Consistently, blocking TLR4 selectively modulated granule cell IPSCs evoked by optical activation of SST interneurons. Notably, acutely blocking TLR4 impaired behavioral pattern separation in a novel object location task in controls and improved performance after injury. Although cell specific deletion of TLR4 in SST neurons did not alter IPSC amplitude or pattern separation in uninjured mice, SST-neuron specific TLR4 deletion after brain injury prevented posttraumatic decrease in evoked IPSC amplitude and deficits in behavioral pattern separation. Our results identify a central role for TLR4 signaling in regulating inhibition which diverge in the normal and

injured brain and impact behavioral function. These findings identify a role for cell-type specific TLR4 signaling in SST neurons in circuit and behavioral dysfunction after brain injury, opening avenues for targeted neuro-immune therapies to improve posttraumatic neurological outcomes.

Introduction

Studies within recent decades have demonstrated a crucial interplay between the immune system and neurophysiology (Yang et al., 2023). Immune signals within the brain are not only involved in the body's defenses, but also play a pivotal role in functional and structural homeostasis of neurons, glia, and endothelial cells (Beattie et al., 2002; Pribiag & Stellwagen, 2014). In fact, studies have demonstrated that cytokines, such as tumor necrosis factor alpha (TNFα), are constitutively expressed in low levels in the brain and are important in synaptic physiology and plasticity (Stellwagen & Malenka, 2006). Innate immune receptors and their signaling pathways, in this sense, may play a dual role in initiating and mediating immunomodulatory activity in response to injury and infection as well as regulating developmental and homeostatic neuronal processes. As such, disruptions in neuroimmune systems may impact neurological network function with behavioral consequences. Current evidence mostly attributes neuroinflammatory modulation of network excitability to glial effects (Villasana-Salazar & Vezzani, 2023), and neuronal expression of immune mediators and its functional consequences have received little attention. In previous studies, we demonstrated that mild to moderate brain injury leads to acute increase in the innate immune receptor toll-like receptor 4 (TLR4) expression in hippocampal dentate gyrus neurons, which enhanced glutamatergic currents and contributed to impaired working memory (Korgaonkar, Li, et al., 2020; Korgaonkar, Nguyen, et al., 2020; Y. Li et al., 2015). Here we identify a novel role for TLR4 signaling in modulating synaptic inhibition in uninjured and injured dentate gyrus.

The dentate gyrus is typified by low excitability and strong GABAergic inhibition of granule cells (Piatti, Ewell, et al., 2013). Optimal levels of granule cell excitability and inhibition have been shown to be crucial for the key function of dentate gyrus known as pattern separation (Coulter & Carlson, 2007; Morales et al., 2020). Pattern separation is the ability to discriminate between similar spatial or temporal patterns or detect subtle differences in the environment and is thought to derive from circuit processes by which overlapping patterns of neuronal activity are minimized (Yassa & Stark, 2011). SST interneurons, specifically, have been shown to be crucial for performance on the novel object location task, a behavioral measure of pattern separation (Morales et al., 2020). In previous studies, we demonstrated that there is a differential loss in hilar SST interneurons compared to PV neurons (Corrubia et al., 2023). However, the changes in cell-type specific contribution to inhibition after brain injury and whether TLR4 regulates synaptic inhibition mediated by interneuron subtypes is not known. Dentate excitability and inhibition are altered in disease states including brain injury and epilepsy, which are associated with deficits in dentate-dependent memory function (Gupta et al., 2022; Korgaonkar, Li, et al., 2020; Korgaonkar, Nguyen, et al., 2020; Y. Li et al., 2015). However, the mechanisms linking injury to altered excitability and memory deficits remain poorly understood.

Previously, we demonstrated that excitatory currents are modulated by TLR4 signaling both before and after injury, leading to deficits in spatial working memory (Korgaonkar, Li, et al., 2020; Korgaonkar, Nguyen, et al., 2020). We also recently showed that granule cell temporal pattern separation and behavioral spatial pattern separation are impaired one week after FPI and are correlated with hilar somatostatin cell loss (Corrubia et al., 2023).

The effect of TLR4 and immune regulation of inhibition and interneuron subtypes, however, has not yet been examined. In these studies, we focus on dentate synaptic inhibition, and demonstrate that inhibitory currents are reduced following moderate fluid percussion injury (FPI) and are modulated by cell-type specific TLR4 signaling. Blocking TLR4 after injury mitigates injury-induced decreases in evoked inhibitory post synaptic currents (eIPSCs), while, paradoxically, reducing eIPSCs in control mice. Correspondingly, performance on the Novel Object Location (NOL) test for spatial pattern separation also shows opposing modulation by TLR4 treatment in uninjured and brain injured mice. Interestingly, cell-type specific deletion of TLR4 selectively in somatostatin (SST) interneurons improved loss of inhibition and NOL performance in brain injured mice, while having no effect in sham control mice. These results demonstrate that TLR4 modulates granule cell synaptic inhibition in an input cell-type specific manner. The findings identify that expression of TLR4 on distinct somatostatin neurons selectively alters dentate disinhibitory circuits after brain injury and contributes to impaired behavioral outcomes.

MATERIALS AND METHODS

Key Resources Table

REAGENT or RESOURCE	SOURCE	IDENTIFIER
Chemicals, Peptides, etc.		
CLI-095	InvivoGen	Cat # tlrl-cli95
Rat anti-somatostatin	Millipore	Cat # MA5-16987
Guinea Pig anti-parvalbumin	Swant	Cat # GP72
Rabbit anti-ΔFosB	Cell Signaling	Cat # D3S8R
goat anti-rabbit AF 594	Invitrogen	Cat # A11012
goat anti-rat AF647	Invitrogen	Cat # A-21247
goat anti-guinea pig AF647	Invitrogen	Cat # A-21450
RNAscope® Probe-Mm-TLR4	Advanced Cell Diagnostics	Cat # 316801
RNAscope® Probe- Mm-Sst-C3	Advanced Cell Diagnostics	Cat # 404631-C3
RNAscope® Probe- Mm-Pvalb-C2	Advanced Cell Diagnostics	Cat # 421931-C2
Critical Commercial Kits		
RNAscope® Multiplex Fluorescent Reagent Kit v2	Advanced Cell Diagnostics	Cat. #323100
Experimental Models: Organisms/Strains		
B6 mouse: C57BL/6J	The Jackston Laboratory	JAX # 000664
SST-CreERT2	The Jackston Laboratory	JAX # 010708
SST-IRES-Cre	The Jackston Laboratory	JAX # 013044
PV-Cre	The Jackston Laboratory	JAX # 029721
ChR2-YFP $^{fl/fl}$	The Jackston Laboratory	JAX # 012569
TLR4$^{fl/fl}$	The Jackston Laboratory	JAX # 024872
Software		
Prism 10.1.2	GraphPad	
pCLAMP 11.3	Molecular Devices	
QuPath v0.5.0	General Public License	
FIJI, ImageJ		

Experimental Model and Subject Details

Animals

All experiments were performed in accordance with IACUC protocols approved by the University of California, Riverside, CA and conform to the ARRIVE guidelines.

Mice were group housed in standard cages on a 12h:12h light/dark cycle. 8–12-week-old mice of either sex were used for all studies. All mice were bred in-house. For optogenetic experiments, mice specifically expressing ChR2-eYFP in somatostatin interneurons were generated by crossing SST-IRES-Cre mice ($Sst^{tm2.1(cre)Zjh}$/J, Jackson Labs, 013044) with ChR2-eYFP mice (B6;129S-Gt(ROSA)26$Sor^{tm32(CAG-COP4*H134R/EYFP)Hze}$/J, Jackson Labs, 012569). For mice expressing ChR2-eYFP in parvalbumin interneurons, the ChR2-eYFP line was crossed with PV-IRES-Cre (B6.Cg-$Pvalb^{tm1(cre)Arbr}$ $Fxn^{em2Lutzy}$ $Fxn^{em2.1Lutzy}$/J, Jackson Labs, 029721) mice.

To knock down TLR4 specifically in somatostatin interneurons without potential developmental effects, we crossed the inducible SST-Cre-ERT2 mouse line (B6(Cg)-$Sst^{tm1(cre/ERT2)Zjh}$/J, Jackson Labs, 010708) with $TLR4^{fl}$ (B6(Cg)-$Tlr4^{tm1.1Karp}$/J, Jackson Labs, 024872) mice to generate $SSTcre^{ERT2}$-$TLR4^{-/-}$ mice using the breeding strategy outlined in **Figure 3.6A**. Briefly, heterozygous SST-CreERT2 mice were paired with a homozygous $TLR4^{fl/fl}$ mouse to yield F1 offspring with SST-CreERT2+/-; TLR4fl-/fl+ genotype. These mice were then paired with another homozygous $TLR4^{fl/fl}$ mouse to yield F2 offspring with heterozygous SST-CreERT2;homozygous $TLR4^{fl/fl}$ (Cre+ mice used for experiments, Figure 3.6A green box) and SST-CreERT2-/- (Cre- mice used as controls,

Figure 3.6A blue box). Experimental SST-Cre+-TLR4fl/fl and Cre negative (Cre-) littermates were administered 150mg/kg tamoxifen via oral gavage for 3 days, , as described below, to induce timed cre-recombinase after FPI/sham. Whenever possible in each experiment, littermates were distributed across experimental groups.

Fluid Percussion Injury

Randomly selected 8 to 10-week-old littermate male and female C57BL6/J, PV- or SST-ChR2-eYFP, and Cre^{+} and Cre^{-} heterozygous SST-creERT2- crossed with $TLR4^{fl/fl}$ mice to generate $SSTcre^{ERT2}$-$TLR4^{-/-}$ mice were subjected to lateral fluid percussion injury (FPI) or sham injury. Briefly, mice were placed in a stereotaxic frame under isoflurane anesthesia and administered 0.25% bupivacaine (subcutaneous) as a local anesthetic. A 2.7 mm hole was trephined on the left side of the skull 2 mm caudal to bregma and 1 mm lateral from the sagittal suture. A Luer-Lok syringe hub with a 3 mm inner diameter was placed over the exposed dura and bonded to the skull with cyanoacrylate adhesive. The animals were returned to their home cage following recovery. One day later, animals were anesthetized with isoflurane and attached to a fluid percussion injury device (Virginia Commonwealth University, Richmond, VA, Model 01-B) directly at the metal nozzle. A pendulum was dropped to deliver a brief (20 ms) 1.5–1.7 atm impact on the intact dura. For sham injury, the animals underwent surgical implantation of the hub and were anesthetized and attached to the FPI device, but the pendulum was not dropped (Gupta et al., 2022; Smith et al., 2012). For Cre^{+} and Cre^{-} SST-$TLR4^{fl/fl}$ studies, mice were administered 175mg/kg tamoxifen dissolved in 10% ethanol and 90% corn oil via oral gavage for 3 days: day 1: 1 hr prior to craniectomy, day 2: 1 hr prior to sham/FPI, and day 3: 24hrs post injury.

Slice Preparation

Mice one week after FPI or sham injury were anesthetized with isoflurane and decapitated for slice preparation using established protocols (Afrasiabi et al., 2022; Korgaonkar, Li, et al., 2020). Horizontal brain slices (300-350 µm) were prepared in ice-cold sucrose artificial CSF (sucrose-aCSF) containing the following (in mM): 85 NaCl, 75 sucrose, 24 $NaHCO_3$, 25 glucose, 4 $MgCl_2$, 2.5 KCl, 1.25 NaH_2PO_4, and 0.5 $CaCl_2$ using a Leica VT1200S Vibratome (Wetzlar, Germany). Slices were incubated at 34°C for 30 min in an interface holding chamber containing an equal volume of sucrose-aCSF and recording aCSF, and subsequently were held at room temperature. The recording aCSF contained the following (in mM): 126 NaCl, 2.5 KCl, 2 $CaCl_2$, 2 $MgCl_2$, 1.25 NaH_2PO_4, 26 $NaHCO_3$, and 10 D-glucose. All solutions were saturated with 95% O_2 and 5% CO_2 and maintained at a pH of 7.4 for 1– 6 h. Only sections on the ipsilateral side of injury were used in experiments.

Physiological Recordings

For patch clamp recordings, slices were transferred to a submerged recording chamber and perfused with oxygenated aCSF at 33 ± 1°C. Visualization of slices and cells was done using IR-DIC with a Nikon AR microscope with a 40X water-immersion objective. Recordings were obtained using Axon Instruments MultiClamp 700B (Molecular Devices, Sunnyvale, CA). Data were low pass filtered at 2 kHz, digitized using DigiData 1440A and acquired using pClamp10 at 10 kHz sampling frequency. Voltage clamp recordings of perforant path evoked inhibitory postsynaptic currents (eIPSCs) were obtained from dentate GCs using recording electrodes (3 - 6 MΩ) containing a Cs-Methanesulfonate Internal (in mM): 140 Cs-Methane sulfonate, 5 NaCl, 10 HEPES, 0.2 EGTA, 4 Mg-ATP,

0.2 Na-GTP, 5 Qx-314 with 0.2% biocytin. For CLI-treatment, slices were incubated in 10ng/ml of CLI-095 or DMSO vehicle control for 30-45min prior to recordings. GCs were held at 0 mV, close to reversal potential for glutamatergic ions, to isolate IPSCs. Evoked IPSCs were recorded in response to 0.1 to 2.0 mA stimuli, applied in 100-500 pA steps, through a concentric stimulus electrode positioned at the perforant path on the other side of the fissure from the dentate molecular layer. Peak amplitude of eIPSC was measured from the average of 3 responses at each step using ClampFit 10. To assess cell health, GCs were held at -70 mV and responses to 1500 ms current steps from -200 pA to threshold positive current injection in 40 pA steps. Cells with resting membrane potential positive to -55 mV and access resistance over 20MΩ were excluded from analysis.

Optogenetic stimulation

For optogenetic experiments, SST(IRES-Cre)-ChR2-YFP and PV-ChR2-YFP mice underwent FPI/sham injury and slice preparation as described previously, with slices kept under opaque lid to avoid potential effects of overhead lighting on slices. Slices from sham and FPI mice were incubated for 45min in the TLR4 antagonist, CLI-095 (5ng/ml) or a vehicle control prior to voltage-clamp recordings. Internal pipette solution constituted of a 50/50 KCl-Kgluc mixture containing (in mM): KCl: 125 KCl , 10 K-gluc, 2 MgCl, 10 HEPES, 0.2 EGTA, 2 Mg-ATP, 0.5 Na-GTP, 10 PO Creatinine, 5 Qx-314 and K-gluc: 126 K-gluc, 4 KCl, 10 HEPES, 4 Mg-ATP, 0.3 Na-GTP, 10 PO Creatinine with 0.2% biocytin. GCs were held at resting potential of -70mV. Optical stimulation of presynaptic ChR2 expressing cells was provided using a Digital Mirror Device (DMD)-based pattern illuminator (Mightex Polygon 400), coupled to 473nm blue LED (AURA light source),

and controlled via TTL based input from pClamp. Full-field stimulation at 9% light intensity resulting in optical recording of 0.395µW was used to provide a 3ms pulse at 20Hz for 500ms onto the slices to elicit a response without doublets. Optically evoked inhibitory post synaptic currents (oeIPSCs) from dentate GCs were recorded following light stimulation and oeIPSC amplitudes from an average of 5 sweeps were used for analyses.

Novel Object Location Task and Analysis

To assess behavioral pattern separation, we implemented a novel object location task to test spatial discrimination (Bekinschtein et al., 2013; Corrubia et al., 2023; Morales et al., 2020) in mice one week post FPI or sham injury. The task consisted of a circular arena 50 cm in diameter and 47 cm high with laboratory tape in varying patterns in four distinct locations on the white opaque arena walls serving as spatial visual cues. The experimenter room was separated from the testing room with the test arena by a closed door. The testing room was dimly lit with overhead lights using dimmer switch on lowest setting. Mice underwent four days of habituation for 10 minutes each followed by a sample and choice phase on day five. The testing arena and objects were cleaned with 70% ethanol in between each animal throughout the entire experiment. During habituation, mice were brought to the testing room from the vivarium, handled by the experimenter, and exposed to the testing arena for 10 min each day where they were allowed to explore freely. For studies with acute CLI-095 treatment, mice were also handled and injected with 50ul saline 1hr before exploring the testing arena each day leading up to the test day, where they were treated with 0.5mg/kg dose of CLI-095 or vehicle i.p. injection 1 hr prior to behavioral testing.

Cre^+ and Cre^- SST-$TLR4^{fl/fl}$ mice were administered tamoxifen for 3 days as described previously and habituated as detailed above. On test day, mice were first exposed to a sample phase for 10 min, with three identical objects placed 120 degrees and approximately 16 cm apart and allowed to freely explore the objects. Mice were then returned to their home cage for 30 min before the choice phase. During the choice phase, one object was placed in its original (familiar) location, one object was removed, and the last object was shifted by 60° to a novel (unfamiliar) location. The mice were placed into the arena and allowed to explore the objects for five minutes. Videos were manually coded and analyzed by an experimenter blinded to animal injury status. Object exploration was counted as the number of times the animal's nose was within 0.5 cm of the object, with each continuous second counted as an additional exploration. Discrimination ratio was calculated as [Exploration of Object in Unfamiliar Location – Exploration of Object in Familiar Location] / [Total Exploration]. Total exploration was also compared between groups.

Immunohistochemistry:

Immunohistochemistry for somatostatin (SST) and parvalbumin (PV) was used to evaluate interneuron loss. Immediately following the novel object location task, mice were perfused transcardially with ice cold PBS followed by 4% PFA. Brains were excised and incubated in 4% PFA overnight and transferred to 30% sucrose for 2-3 days or until tissue sank. Brains were then flash frozen in OCT using liquid nitrogen and stored at -80°C prior to cryosectioning. 20 µm serial sections were collected and mounted on SuperFrost slides and stored at -80°C prior to staining. Slides were stained for SST, or PV following standard procedures (Korgaonkar, Li, et al., 2020; Neuberger et al., 2017). Briefly, slides were

allowed to thaw to room temperature (RT) for 10 min, washed with 1xPBS 3x5min to wash off residual OCT. Slides were blocked in 10% normal goat serum in PBS + 0.3% Triton-X for one hour at RT, then incubated in anti- SST or PV antibody (SST: 1:100, Millipore MA5-16987; PV: 1:1000, Swant GP72) overnight at 4°C. Slides were then washed 3x10 min with PBS and then incubated in goat anti-rat AF647 antibody (1:1000, Invitrogen A-21247) for SST goat anti-guinea pig AF647 antibody (1:1000, Invitrogen, A-21450) for PV for 1.5 hours at RT, washed 3x10 min with PBS, and coverslipped using VectaShield mounting media. Slides were imaged using Zeiss Axioscope Epifluorescence Microscope as a single plane at 10x and 20x for analysis. Blinded analysis was performed using Cell Detection settings in QuPath 0.5.0 (https://qupath.github.io) with files coded without injury status. For SST analysis, a ROI was drawn to outline the hilus using DAPI labeling to detect SST+ cells. Detection parameters were kept consistent between sections, and 3 to 6 level matched sections were averaged in each mouse for analysis, depending on slice and image quality. Robust and sparse PV immunolabeled neuronal somata were counted manually on QuPath for hilar, GCL, molecular layer regions as well as total PV interneurons, which include axo-axonic cells (Proddutur et al., 2023).

To visualize TLR4 and SST colocalization, we used RNAscope *Multiplex Fluorescent In situ hybridization* (*m-FISH*) on cryosectioned (50 µm) tissue from control and mice one-week post-FPI. RNAscope Multiplex Fluorescent Reagent Kit v2 Assay was used following the protocol for fixed frozen tissue. The following kits and probes were used for this study: RNAscope® Multiplex Fluorescent Reagent Kit (Cat. #323100), RNAscope® Probe-Mm-TLR4 (Cat. No. 316801), and RNAscope® Probe- Mm-Sst-C3 (Cat No.

404631-C3). Slides were coverslipped using DABCO with DAPI mounting media and imaged using a Zeiss Axioscope and analyzed using Stereo Investigator (Microbrightfield).

Statistical Analysis

Statistical analyses were conducted in GraphPad Prism 10. The Shapiro-Wilk test was used to test for normality, and appropriate parametric or non-parametric statistical analyses were conducted. F-test to compare variances was used to assess whether both sample groups undergoing statistical comparisons have equal standard deviations. All statistical comparisons were conducted at an alpha level of $\alpha = 0.05$. Two-way repeated measures ANOVA (TW-RM ANOVA), one-sample, paired and unpaired Student's or Welch's t-test, Mann-Whitney U test and Kolmogorov-Smirnov (K-S) test were used where appropriate.

RESULTS

Acute TLR4 regulation of synaptic inhibition in the dentate gyrus

We previously identified a novel role of TLR4 in regulating dentate network physiology with opposing changes in excitability between uninjured/control and brain injured mice and a corresponding divergent effect on working memory performance (Korgaonkar, Li, et al., 2020; Korgaonkar, Nguyen, et al., 2020; Y. Li et al., 2015). Although we identified that TLR4 signaling selectively enhances AMPA currents in dentate granule cells (GCs) after concussive brain injury, mechanisms underlying the differential TLR4 regulation of network excitability remain unknown. To determine whether afferent evoked inhibition is differentially modulated by TLR4 signaling in the control and injured dentate gyrus, we

examined TLR4 regulation of GC inhibitory current responses to perforant path stimulation in mice one week after concussive brain injury using FPI model or sham injury. Granule cells were held in voltage clamp at 0mV, the reversal potential for glutamatergic currents, to isolate inhibitory currents. In contrast to the previously reported increase in afferent evoked AMPA currents (Corrubia et al., 2023; Korgaonkar, Li, et al., 2020; Y. Li et al., 2015) and spontaneous inhibitory post synaptic currents (sIPSCs) after injury (Gupta et al., 2012; Santhakumar et al., 2000, 2001), mice one week after FPI exhibited a significant decrease in evoked IPSCs (eIPSCs) compared to sham injured controls (**Fig 3.1B-D**, n=8 cells from 4 sham mice and 8 cells from 4 FPI mice, $p < 0.05$ by Two-Way ANOVA with Multiple Comparisons). Importantly, acute incubation of the slices in CLI-095 (10ng/ml), a specific TLR4 antagonist, significantly altered eIPSCs in both sham and FPI mice in different directions. Notably, in slices from sham mice, CLI-095 treatment decreased eIPSC amplitudes, demonstrating a basal TLR4 signaling tone in the uninjured brain which augments synaptic inhibition (n=6 cells from 4 mice, $p<0.05$ by TW-MC ANOVA). In contrast, following FPI, TLR4 antagonist treatment enhanced eIPSC amplitude (**Fig 3.1B-D**, n = 8 cells from 4 mice, $p < 0.05$ by TW-MC ANOVA), thereby attenuating the injury-induced decreases in eIPSC amplitude. These results demonstrate a novel neurophysiological role of TLR4 in modulating synaptic inhibition both constitutively and following injury. The effects observed in sham mice demonstrate a role of TLR4 in supporting baseline network inhibition. In contrast, the neuroinflammatory response mediated by TLR4 signaling following injury not only increases excitatory currents as observed previously (Korgaonkar, Li, et al., 2020; Y. Li et al., 2015), but additionally

decreases inhibition, potentially shifting excitation-inhibition balance towards increased excitation.

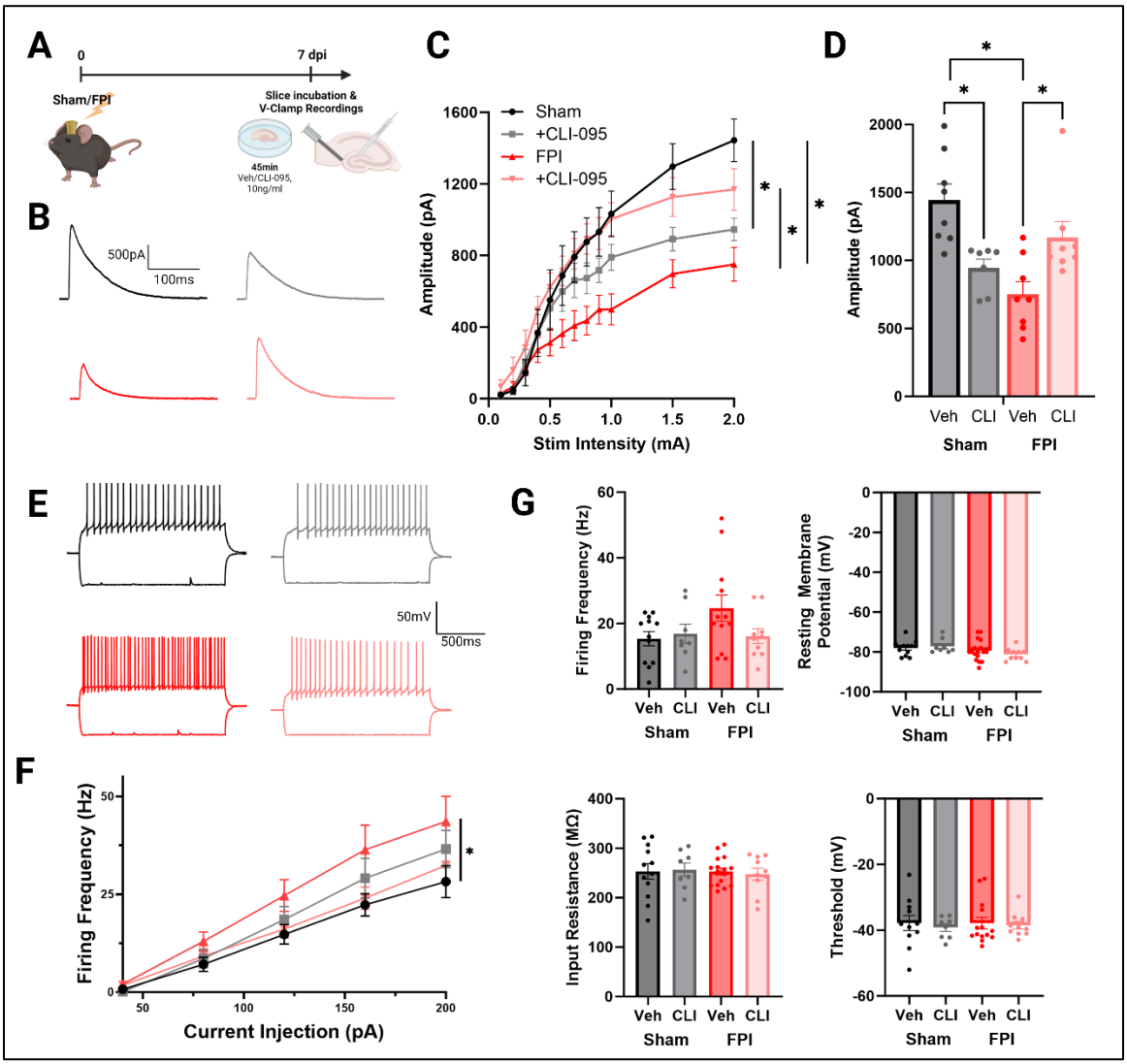

Figure 3.1. **Dentate inhibition is impaired one week after injury and is modulated by TLR4 signaling**. (A) Schematic of timeline for acute slice incubations in vehicle or CLI-095 (10ng/ml) for v-clamp experiments one week after FPI. (B) Representative eIPSC traces from dentate granule cells in sham (black), FPI (red), and with CLI-095 treated slices (lightened). (C) Plot of eIPSC peak amplitude in GCs recorded in responses to increasing stimulus intensities. (D) Summary plot of GC eIPSC peak amplitude at 2.0mA stimulation. (E) Representative GC membrane voltage traces in response to -200 pA and +120 pA current injections. (F) GC Current-Frequency plot at increasing current injections (G)

Summary plots of GC firing frequency at +120 pA current injection, input resistance, resting membrane potential, and firing threshold.

We examined if TLR4 modulation of granule cell intrinsic physiology, including input resistance, could contribute to the observed changes in eIPSC amplitudes. Analysis of the current-frequency (IF) curve demonstrated an increase in GC firing frequency after FPI (**Figure 3.1E-G**, p=0.03 by 2W ANOVA). However, as reported previously (Corrubia et al., 2023), passive properties including resting membrane potential and input resistance were not different between granule cells from sham and FPI mice (**Figure 31E-G**). Moreover, GC passive properties were not modulated by TLR4 antagonist treatment (**Figure 3.1E-G**).

Posttraumatic increase but no TLR4 modulation of PV input onto GCs

Brain injury leads to loss of interneuron subtypes in the dentate gyrus (Corrubia et al., 2023; Folweiler et al., 2020; Frankowski et al., 2019; Lowenstein et al., 1992; Toth et al., 1997) which may contribute to the decrease in eIPSC amplitude we observed. As observed in previous studies (Corrubia et al., 2023), immunostaining for PV interneurons in ventral slices from mice one week after FPI revealed no changes in either hilar or molecular layer PV+ neuron counts (**Figure 3.2A-B**, n=14 sham, n=14 FPI, p=0.63 Hilar, p=0.77 Molecular Layer, p=0.08 Total).

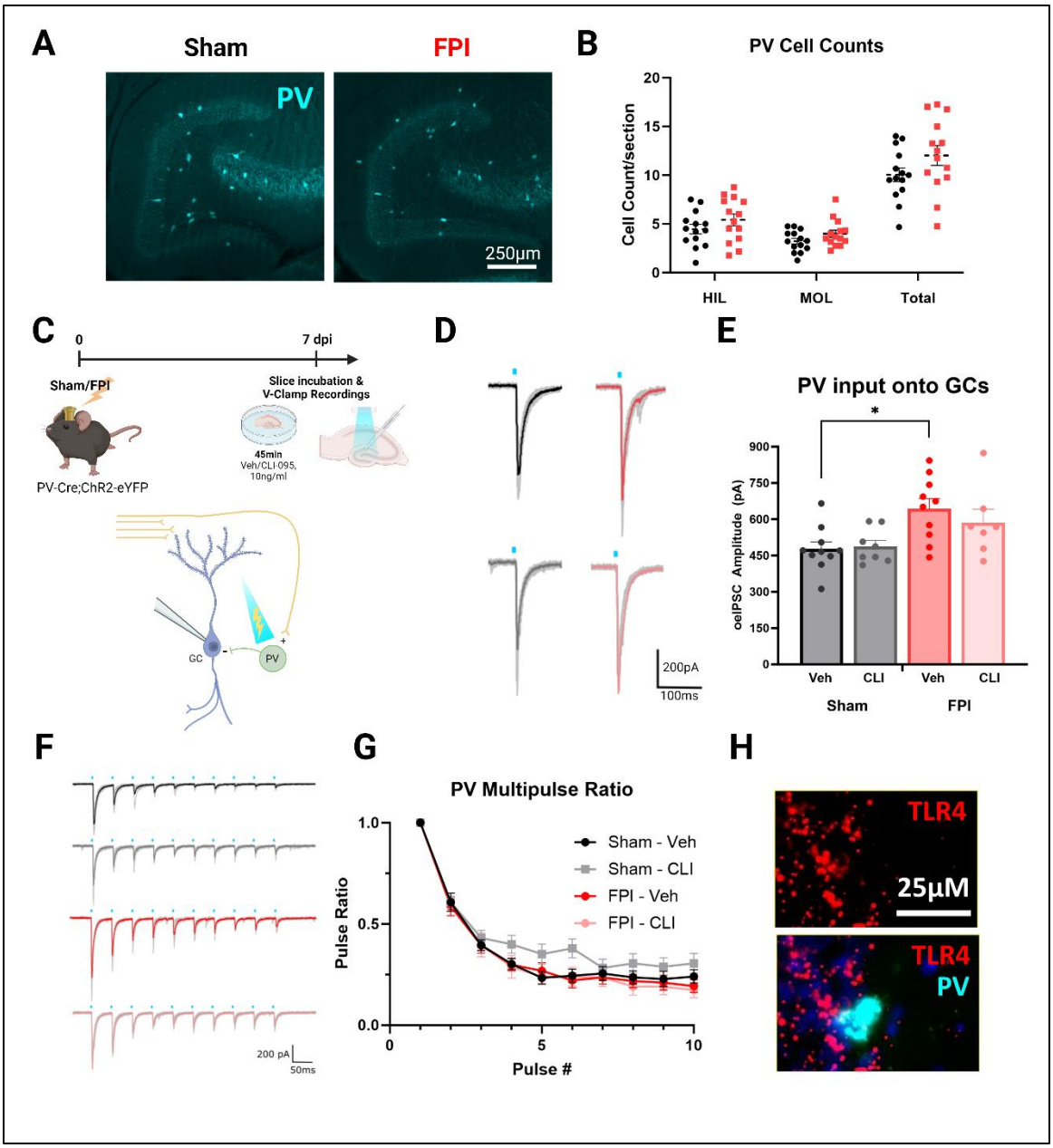
A
Sham
FPI
PV
250µm
B
PV Cell Counts
Cell Count/section
HIL
MOL
Total
C
0
7 dpi
Sham/FPI
PV-Cre;ChR2-eYFP
Slice incubation &
V-Clamp Recordings
45min
Veh/CLI-095,
10ng/ml
GC
PV
D
200pA
100ms
E
PV input onto GCs
oeIPSC Amplitude (pA)
Veh
CLI
Veh
CLI
Sham
FPI
F
200 pA
50ms
G
PV Multipulse Ratio
Sham - Veh
Sham - CLI
FPI - Veh
FPI - CLI
Pulse Ratio
Pulse #
H
TLR4
25µM
TLR4
PV

Figure 3.2. **PV input onto dentate granule cells is increased one week after brain injury but not mediated by TLR4**. (A) Representative images of dentate sections immunostained for parvalbumin (PV) in sham and FPI mice, scale bar = 100μm. (B) Summary plot of PV cell counts in hilus, molecular layer, and total dentate subregion in sections from sham and FPI mice. (C) Timeline and schematic for sham/FPI, followed one week later by acute drug incubation and optogenetic experiments showing optical activation of PV neurons using blue light in slices from PV-ChR2 mice and recordings from GCs. (D) Representative traces from PV-driven oeIPSC recordings in GCs in sham (black), FPI (red), and CLI-095 incubations (lightened). (E) Summary histogram of oeIPSC peak amplitudes in GCs from PV neurons (F) Representative traces of GC IPSCs following optical stimulation of PV neurons at 3ms at 20Hz (G) Summary plot of multipulse ratio of each peak compared to amplitude of first peak. (H) Representative images from RNAscope sm-FISH showing no colocalization of TLR4 mRNA with PV.

To test whether cell-type specific inhibitory input onto dentate granule cells is affected after FPI and differentially modulated by TLR4, we examined PV-Cre:ChR2/eYFP mice in which the excitatory opsin, channelrhodopsin (ChR2) is expressed exclusively in PV interneurons. Voltage clamp recordings were obtained from dentate GCs in response to optical activation of PV interneurons using blue light (full-field stimulation under a 40X objective at 0.395mW intensity and 3ms pulse duration at 20Hz for 500ms) in slices from sham and FPI mice (**Figure 3.2C**). Slices were incubated for 45min in the TLR4 antagonist, CLI-095 (5ng/ml) or a vehicle control prior to recordings. Amplitude of the optically evoked IPSCs (oeIPSCs) from PV neurons was compared across treatment groups. Interestingly, the amplitude of PV driven IPSCs onto GCs was increased one week after FPI (**Figure 3.2D-E**, n=7 sham, n=10 FPI, p=0.002 by TW-MC ANOVA), suggesting that PV neurons may compensate for potential loss of other interneuron populations. However, TLR4 antagonism failed to modulate PV-evoked IPSC amplitude in both sham or FPI mice (**Figure 3.2D-E**, n= 8 Sham-CLI, n=7 FPI-CLI, p=0.84 Sham, p=0.31 FPI, by TW-MC ANOVA). Analysis of multi-pulse depression of the 20Hz train revealed no significant differences between groups (**Figure 3.2F-G**) suggesting no change in release probability. Consistent with the lack of TLR4 effect on PV-evoked IPSCs, *RNAscope/m-FISH* failed to reveal TLR4 mRNA in PV interneurons (**Figure 3.2H**).

TLR4 signaling selectively enhances SST-driven IPSCs to granule cells after FPI

Unlike PV neurons, immunostaining for somatostatin (SST) showed a significant reduction of SST^+ neurons in the hilus in the ventral DG one week after FPI (**Figure 3.3A-B**, n=14

sham, n=15 FPI, p=0.004 by unpaired t-test). To assess changes in SST input onto GCs, we examined SST-IRES-CreChR2/eYFP mice expressing ChR2 in somatostatin interneurons for optically evoked IPSCs in granule cells from sham and FPI mice. Despite loss of SST neurons (**Figure 3.3A-B**), SST neuron driven oeIPSC peak amplitude in granule cells remained unchanged one week after injury (**Figure 3.3D-E**, n=7 sham, n=8 FPI, p=0.75). Additionally, incubation in the TLR4 antagonist resulted in no change in SST-evoked IPSC in sham slices (**Figure 3.3D-E**, n=6 Sham-CLI, p=0.45 by TW-MC ANOVA). Unexpectedly, we observed a *decrease* in SST evoked IPSCs when slices were incubated in the TLR4 antagonist after FPI (**Fig 3.3D-E**, n= 8 FPI-CLI, p=0.007 by TW-MC ANOVA). These results were surprising, given the previous findings that blocking TLR4 *increased* overall eIPSCs after injury (**Figure 3.1C-D**). Analysis of multi-pulse depression of the 20Hz train revealed no significant differences between groups (**Figure 3.3F-G**). In contrast to findings in PV neurons, RNAscope/mFISH identified colocalization of TLR4 mRNA in SST interneurons (**Figure 3.3H**). These results suggest that TLR4 selectively modulates SST synapses on to GCs after injury, but likely affects basal inhibition through different mechanisms. The contrasting effects of TLR4 antagonism on perforant path eIPSC and SST-driven oeIPSCs suggest that SST neurons may contribute to disinhibition of DG interneurons (Estarellas et al., 2023; Nolan et al., 2022; Ogando et al., 2021).

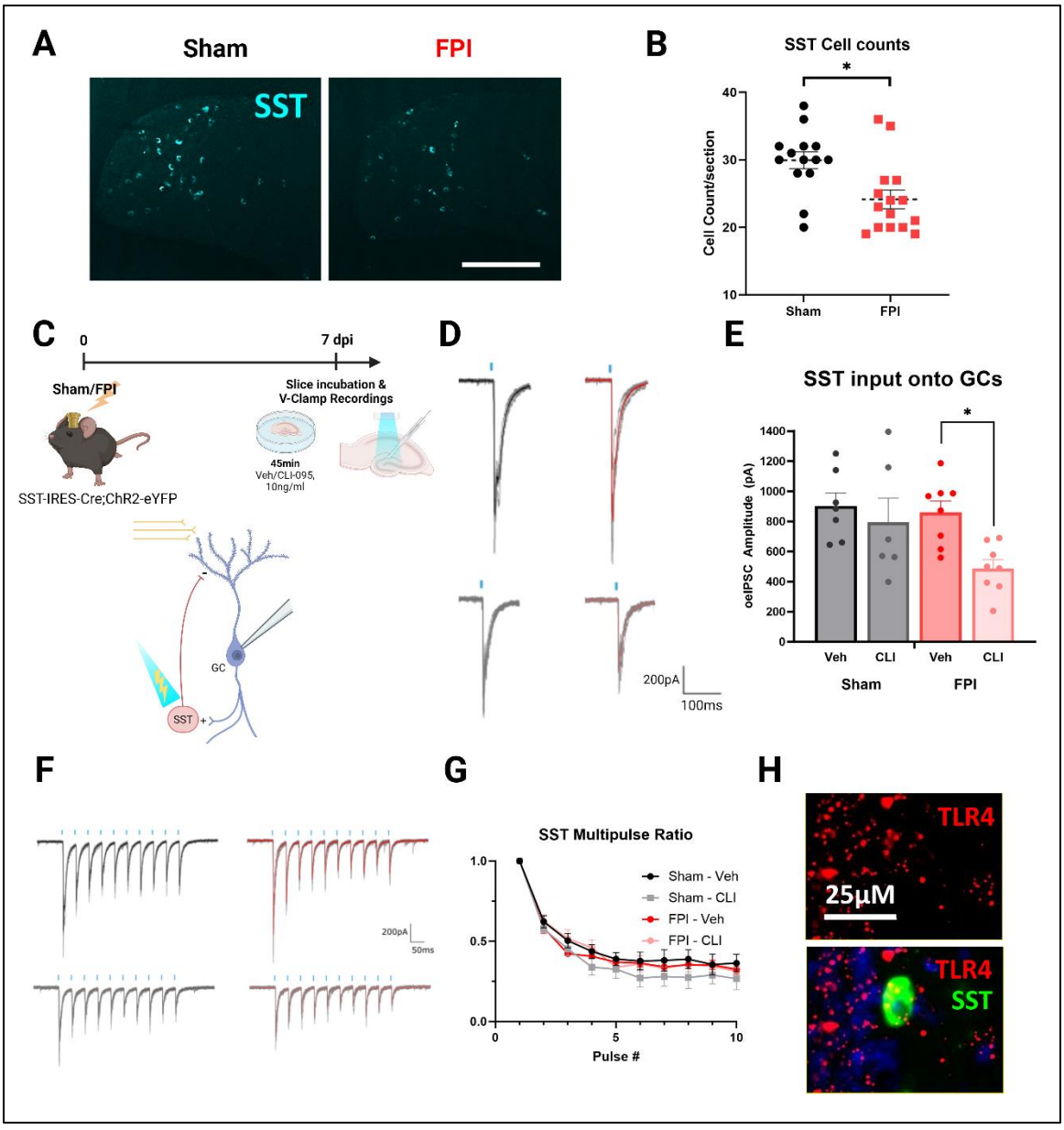
A
Sham
FPI
SST
B
SST Cell counts
Cell Count/section
Sham
FPI
C
0
7 dpi
Sham/FPI
Slice incubation &
V-Clamp Recordings
45min
Veh/CLI-095,
10ng/ml
SST-IRES-Cre;ChR2-eYFP
GC
SST
D
200pA
100ms
E
SST input onto GCs
oeIPSC Amplitude (pA)
Veh
CLI
Veh
CLI
Sham
FPI
F
200pA
50ms
G
SST Multipulse Ratio
Sham - Veh
Sham - CLI
FPI - Veh
FPI - CLI
Pulse #
H
TLR4
25μM
TLR4
SST

Figure 3.3. **TLR4 specifically modulates SST input onto dentate granule cells after injury**. (A) Representative images of dentate sections immunostained for Somatostatin (SST) in sham and FPI mice, scale bar = 100um. (B) Summary plot of SST cell counts in sections from dentate hilus in sham and FPI mice. (C) Timeline and schematic for sham/FPI, followed one week later by acute drug incubation and optogenetic experiments showing optical activation of SST neurons using blue light in slices from congenital SST-ChR2 mice and recordings from GCs. (D) Representative traces from SST-oeIPSC recordings in GCs in sham (black), FPI (red), and CLI-095 incubations (lightened). (E) Summary histogram of oeIPSC peak amplitudes in GCs from SST neurons (F) Representative traces of GC IPSCs following optical stimulation of SST neurons at 3ms at 20Hz (G) Summary plot of multipulse ratio of each peak compared to amplitude of first peak. (H) Representative images from RNAscope sm-FISH showing colocalization of TLR4 mRNA with SST neurons.

SST contribution to evoked IPSCs is modulated by TLR4 signaling

The changes we observed in PV and SST input onto GCs failed to account for either the posttraumatic decrease in eIPSC or the bidirectional effect of TLR4 signaling on perforant path evoked IPSCs in the uninjured and injured brain. Since optical activation of the neurons allows for cell specificity and cannot determine recruitment of the interneurons during afferent activation, we sought to suppress the neurons and identify their circuit contributions. Since we previously reported that optogenetic suppression of parvalbumin neurons does not reduce perforant path evoked IPSCs in the DG, likely due to the inability of limited hyperpolarization to suppress afferent evoked responses, we adopted a strategy of depleting synaptic output in specific cell types to examine their relative contribution to eIPSC amplitude. To accomplish this, we optically stimulated either parvalbumin or somatostatin neurons, using PV- or SST-ChR2/eYFP mouse lines, at a high frequency (3ms at 50-75Hz) to achieve short term synaptic depression. Comparison of amplitude of the last oeIPSC in the train to the first oeIPSC confirmed that the stimulation reduced both PV and SST driven IPSCs by over 90% in both PV and SST neurons (**Figure 3.4B**, n=20 PV, n=21 SST). Using this strategy, we were able to depress the PV and SST oeIPSC amplitude to evaluate the contribution of the interneuron subtype specific currents to the overall evoked IPSC.

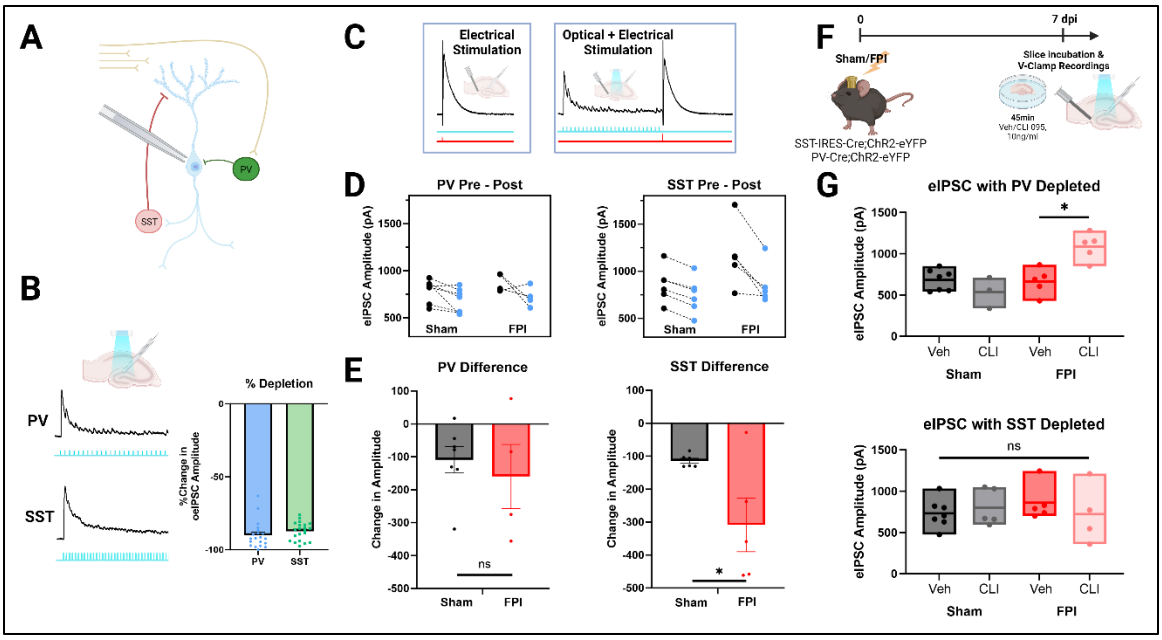

Figure 3.4. **SST neurons contribute more to overall eIPSC than PV** (A) Schematic of dendritic SST and perisomatic PV inhibition onto GCs (B) Representative oeIPSC traces from GCs in response to PV (top) and SST (bottom) stimulation at high frequencies showing depletion of synaptic response following prolonged simulation. (C) Schematic of experimental paradigm showing electrical stimulation of perforant path (PP) (left), and optical stimulation combined with immediate electrical PP stimulation (right). Subtraction of peak amplitude from IN-depleted eIPSC from initial PP-stimulated eIPSC results in IN contribution towards overall eIPSC amplitude. (D) Summary plot comparing evoked responses from PV- (left) and SST- (right) synaptic depletion on overall eIPSC before suppression (black) and post suppression (blue). (E) Summary histogram of difference in eIPSC amplitude following PV (left) and SST (right) synaptic depression in sham and FPI. (F) Experimental timeline and paradigm for CLI-095 incubation and recordings. (G) Summary plots showing eIPSC amplitudes in each condition following suppression of PV synapses (top) and SST synapses (bottom).

Comparing the perforant path evoked eIPSC amplitude before and following optical depression of PV synapses identified a small reduction in eIPSC amplitude which remained unchanged after FPI (**Figure 3.4D-E**, n=7 sham, n=4 FPI, p=0.58 by unpaired t-test), despite an increase in optically evoked PV IPSCs onto GCs **(Figure 3.2**). The unexpectedly small reduction in IPSC amplitude following depletion of PV synaptic release could indicate a potential circuit-level compensation during suppression of PV neuron mediated

inhibition. Similarly, optical depletion of SST synapses consistently decreased eIPSC amplitude in controls. However, the contribution of SST inputs to granule cell eIPSC amplitude was increased after FPI (**Figure 3.4D-E**, n=6 sham, n=5 FPI, p=0.03 by unpaired t-test). These data demonstrate that SST neurons have a greater influence on overall eIPSC amplitude after FPI, despite the lack of change in SST-driven oeIPSC onto GCs after injury (**Figure 3.3D-E**). These results demonstrate that SST mediated eIPSCs are not reduced after brain injury, rather, they suggest that loss or inhibition of additional interneuron subtypes may contribute to the post-injury decrease in eIPSC amplitude.

Next we examined whether TLR4 modulation of eIPSC required the contribution of PV or SST neurons by comparing the effect of TLR4 antagonist on eIPSC amplitude when PV or SST neuron release was suppressed. In slices from sham injured PV-ChR2/eYFP mice, the eIPSC amplitude following suppression of PV neuron synaptic release was unchanged between slices treated with TLR4 antagonist (CLI-095) and vehicle treated slices (**Figure 3.4G**, n=7 Veh, n=3 CLI, p=0.52). Similarly, slices treated with TLR4 antagonist failed to show a reduction in eIPSC amplitude following suppression of SST neuron synaptic release (**Figure 3.4G**, n=7 Veh, n=5 CLI, p=0.96). The inability of TLR4 antagonist to modulate eIPSC amplitude when either PV or SST synapses are suppressed suggests contribution of both PV and SST neurons in TLR4 regulation of eIPSC amplitude in uninjured mice. Interestingly, TLR4 antagonist continued to increase eIPSC amplitude in slices from brain injured PV-ChR2/eYFP mice even when PV neuron synaptic release was suppressed (**Figure 3.4G**, n=5 Veh, n=5 CLI, p=0.002 from OW-ANOVA with Multiple Comparisons). However, TLR4 antagonist failed to enhance eIPSC amplitude in slices

from brain injured mice following suppression of SST neuron synaptic release (**Figure 3.4G**, n=5 Veh, n=3 CLI, p=0.83), identifying a role for SST neurons in TLR4 regulation of eIPSC amplitude after brain injury. Since we show TLR4 inhibition suppresses SST-driven IPSC, these data suggest a potential role for SST neurons in disinhibiting additional interneurons. Since suppressing PV synaptic release does not impact TLR4 regulation of eIPSC, it is unlikely that SST neuron suppression of PV neurons underlies the decrease in eIPSC during TLR4 block. Rather, our data suggest that TLR4 regulation of SST-driven inhibition likely mediates its effect on eIPSC amplitude by disinhibition of additional non-PV dentate interneuron subtypes.

TLR4 signaling regulates behavioral pattern separation

TLR4 signaling has previously been shown to affect spatial working memory performance in rats (Korgaonkar, Nguyen, et al., 2020). Additionally, we recently demonstrated that spatial pattern separation in a novel object location task, a dentate specific task dependent on intact somatostatin interneuron activity (Morales et al., 2020), is impaired one week after brain injury in mice (Corrubia et al., 2023). Using the novel object location task, we assessed whether acute modulation of TLR4 affects episodic spatial pattern separation behavior. Mice were injected mice with 0.5mg/kg CLI-095 or vehicle intraperitoneally (i.p.) one hour before the start of the sample phase on the test day, one week post FPI (**Figure 3.5A**). CLI-095 readily crosses the blood brain barrier, with levels detected as early as 30 min post i.p. injection (Y.-C. Wang et al., 2013). Mice were habituated for four days prior to the test day, including being injected with 0.1ml saline i.p. one hour prior to

being exposed to an empty testing chamber for 10 min. On test day, 1 hour after TLR4 antagonist or vehicle injection, mice were exposed to the testing chamber and allowed to explore three identical objects spatially oriented 120° apart for 10 min during the sample phase before being returned to their home cage for 30 min before starting the choice phase. During the choice phase, one object was removed, and another object was shifted to a novel location (**Figure 3.5A**). Mice explored the chamber with the two remaining objects for 5 min, and the discrimination index was calculated as the difference between the number of explorations of the displaced object and the undisplaced object divided by the total number of explorations for both objects. Vehicle treated control mice explored the displaced object significantly more than the undisplaced object (**Figure 3.5B-C**, n=9, p=0.007 by one sample t-test). Interestingly, acute TLR4 antagonist treatment resulted in impaired performance on the NOL task in sham mice (**Figure 3.5B-C**, n=7, p=0.94), paralleling the decrease in eIPSC amplitude observed in physiology experiments (**Figure 31B-D**). As reported previously (Corrubia et al., 2023), vehicle-treated mice one week after FPI were impaired in their ability to discriminate the novel object location (**Figure 3.5B-C**, n=6, p=0.12 by one-sample t-test). Notably, FPI mice treated with TLR4 antagonist demonstrated improved discrimination (**Figure 3.5B-C**, n=9, p=0.03 by one sample t-test). The total number of explorations was not different between groups (**Figure 3.5D**, n=7-9 per group, p>0.05 by TW-MC ANOVA), demonstrating that the results are likely due to TLR4 antagonist treatment, rather than any effects of protocol or injury.

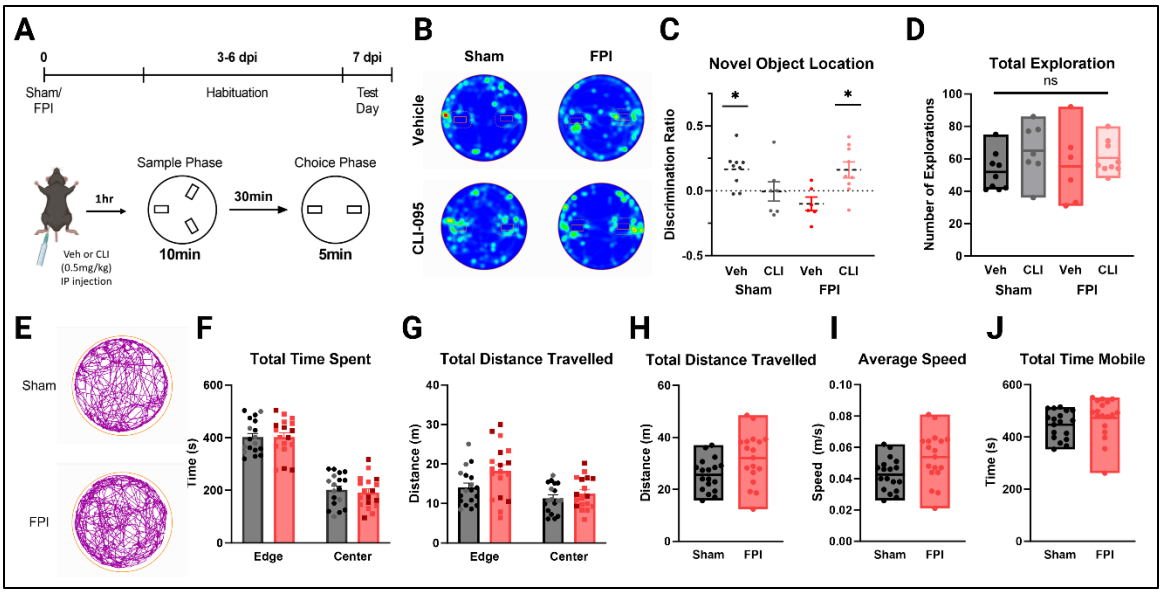

Figure 3.5. **TLR4 signaling modulates behavioral pattern separation before and after injury**. (A) Experimental timeline and schematic for behavioral test. (B) Representative heat maps depicting relative time spent and location within the testing chamber. (C) Summary plot of discrimination ratio for each group (*p<0.05 by one-sample t-test). (D) Histogram of total number of explorations in each experimental group. € Representative track plot of Sham and FPI mice in open chamber during first day of habituation. (F-G) Summary histogram showing total time and distance traveled in outer edge and center of open chamber during initial habituation. (H-J) Summary histogram showing total distance traveled, average speed, and total time mobile were not different between sham and FPI mice.

Additionally, since mice were allowed to explore an empty chamber during habituation, we analyzed the open field exploration behavior of mice on the first day of habituation (3 days post injury) prior to drug treatments (**Figure 3.5E-K**). The time spent and distance traveled along the outer edge or center of the chamber were not different between sham and FPI mice (**Figure 3.5E-H**), demonstrating no change in thigmotaxis due to injury. Mobility measures including total distance traveled, average speed, and total time mobile were also similar between sham and FPI mice (**Figure 3.5I-J**). These results demonstrate that even acute treatment with the TLR4 antagonist one week post injury can have

beneficial effects on behavioral performance in the injured brain. However, the bidirectional impact of TLR4 treatment in control mice compared to FPI further illustrates that TLR4 may have differential roles in the uninjured brain compared to the injured brain.

TLR4 expression in SST neurons regulates granule cell inhibition in the injured brain

To test whether the TLR4 expression in SST neurons underlies TLR4 regulation of eIPSC amplitude, we selectively deleted TLR4 in SST neurons after brain injury by crossing SST-CreERT2 mice with $TLR4^{fl/fl}$ to create an F2 generation inducible mouse line where TLR4 could selectively be deleted in SST neurons following tamoxifen induction (**Figure 3.6A**, green box used as Cre+ experimental mice, blue Cre- littermates used as controls). Using this line, we can temporally target TLR4 deletion after FPI/sham injury while avoiding germline deletion of TLR4 in SST interneurons and potential developmental consequences or compensation. Littermate Cre- mice treated with tamoxifen were used as controls. Cre+ and Cre- SST-creERT2-$TLR4^{fl/fl}$ mice underwent FPI or sham injury and received tamoxifen (150mg/kg daily for 3 days by oral gavage, starting 1hr before hub implantation, **Figure 3.6B**). *RNAscope/m-FISH* demonstrated a significant decrease in the number of SST interneurons localizing TLR4 compared to Cre- mice (Figure 6C-D, n=7 Cre-, n=7 Cre+, $p<0.05$ by student's t-test) validating the approach.

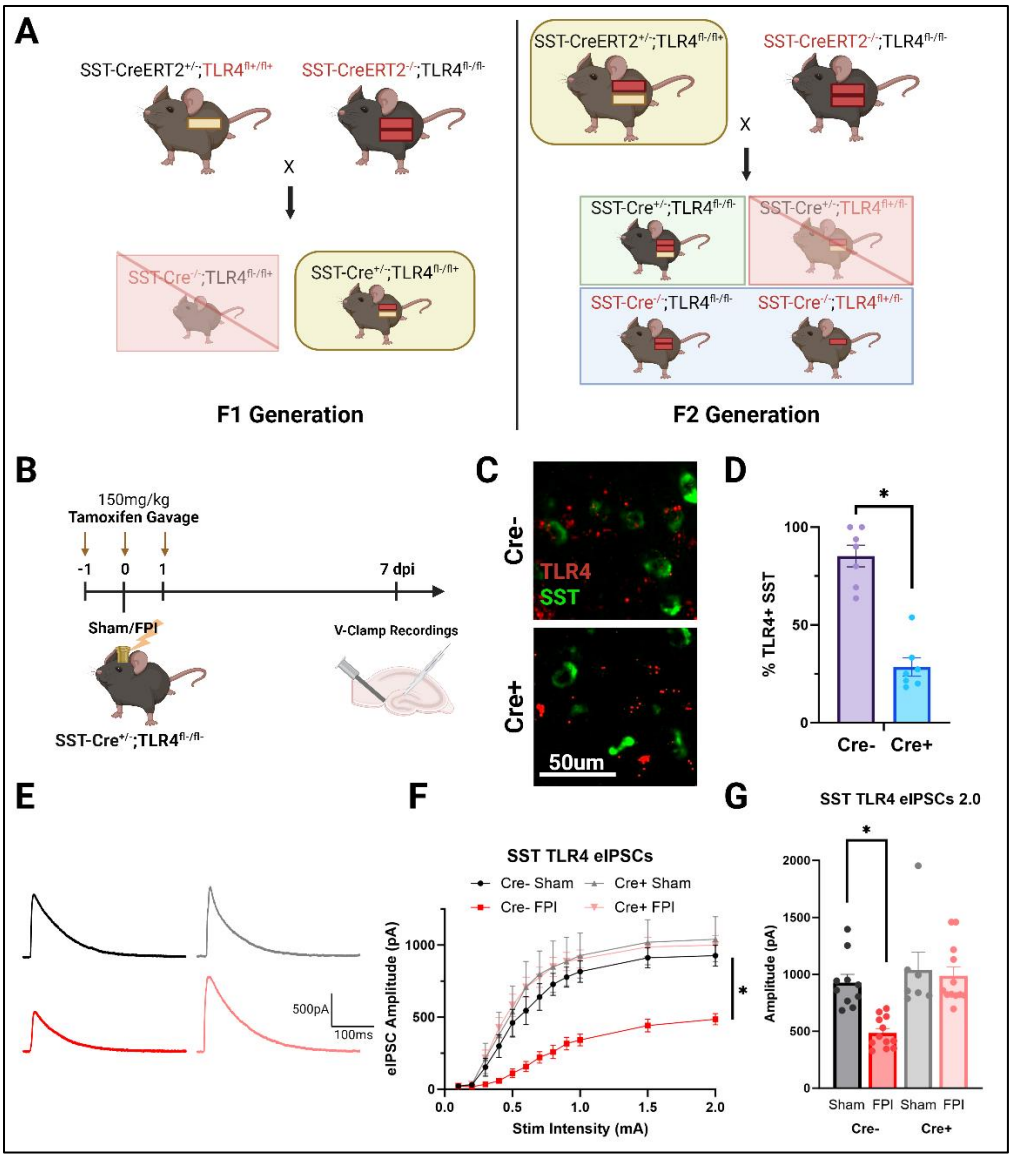

Figure 3.6. **SST-specific TLR4 modulates inhibition after FPI, but not at baseline**. (A) Schematic depicting breeding strategy to yield SST-CreERT2; TLR4fl/fl mice in which TLR4 is deleted specifically from SST neurons after tamoxifen induction. SST-Cre+ mice with homozygous TLR4fl-/fl- (green box) were used to experimentally delete TLR4 from SST neurons, and SST-Cre- controls (blue box) were used as littermate controls. (B) Experimental timeline of tamoxifen induction and v-clamp recordings. (C) Representative images showing decrease in TLR4 mRNA puncta in Cre+ mice following tamoxifen induction compared to Cre- controls. (D) Summary plot of percentage of total SST neurons colocalized with TLR4 mRNA. (E) Representative eIPSC traces from GCs in Cre- sham (black), Cre- FPI (red), and Cre+ SST-TLR4 deletions (lightened). (F) Summary plot of eIPSC peak amplitudes in responses to increasing stimulus intensities. (G) Histogram of GC eIPSC peak amplitude at 2.0mA stimulation for each experimental group.

Cre- sham injured control mice had similar perforant path evoked IPSC amplitudes as in veh-treated mice. Interestingly, there was no difference in eIPSC amplitude between Cre+ sham mice with SST-specific TLR4 deletion and Cre- sham controls (**Figure 3.6E-G**, n=10 Cre- sham, n=7 Cre+ sham, p=0.91 by TW-MC ANOVA). As expected based on data from *wild-type* mice (**Figure 3.1),** FPI resulted in a significant reduction in eIPSC amplitude in Cre- mice compared to littermate Cre- Sham mice (**Figure 3.6E-G**, n= 12 Cre- FPI, p=0.0006 by TW-MC ANOVA). However, eIPSC amplitude in Cre+ FPI mice with SST-specific TLR4 deletion was not different from both Cre+ and Cre- sham controls (**Figure 3.6E-G**, n=12, p=0.88 from Cre- sham, and p=0.99 from Cre+ Sham, by TW-MC ANOVA). These results identify that TLR4 expression in SST neurons is not required for basal TLR4 modulation of inhibition in the uninjured brain. Crucially, our findings demonstrate that TLR4 expression in SST neurons contributes to the reduction in dentate inhibition after brain injury.

SST-specific TLR4 deletion improved behavioral performance after brain injury

To test whether TLR4 expression in SST neurons influences behavioral performance, we tested Cre+ and Cre- SST-CreERT;TLR4$^{fl/fl}$ mice in the novel object location task (**Figure 3.7A**). Discrimination ratio in Cre- and Cre+ sham mice was not different from *wild-type* vehicle treated controls (**Figure 3.7B-D**, n=8 Cre-, p=0.006, by one sample t-test) (**Figure 3.7B-D**, n=7 Cre+, p=0.005, by one-sample t-test). As with electrophysiological studies, Cre- FPI mice showed a significantly lower discrimination index compared to littermate Cre-ve sham mice (**Figure 3.7B-D**, n=10 FPI, p=0.37 by one-sample t-test). Interestingly,

Cre+ mice with SST-specific TLR4 deletion demonstrated no impairment in pattern separation behavioral performance (**Figure 3.7B-D**, n=7, p=0.04 by one-sample t-test). These data demonstrate that TLR4 signaling in SST cells play a crucial role in dysregulation of inhibition and behavioral performance after FPI. The results demonstrate that TLR4 regulation of inhibition and behavioral function in the uninjured brain does not require TLR4 regulation of SST neurons. Our findings emphasize that bidirectional TLR4 regulation of DG inhibition and behavioral outcomes in the control and injured brain arise from distinct and complex mechanisms which could be leveraged to selectively targeting pathological processes in the injured brain.

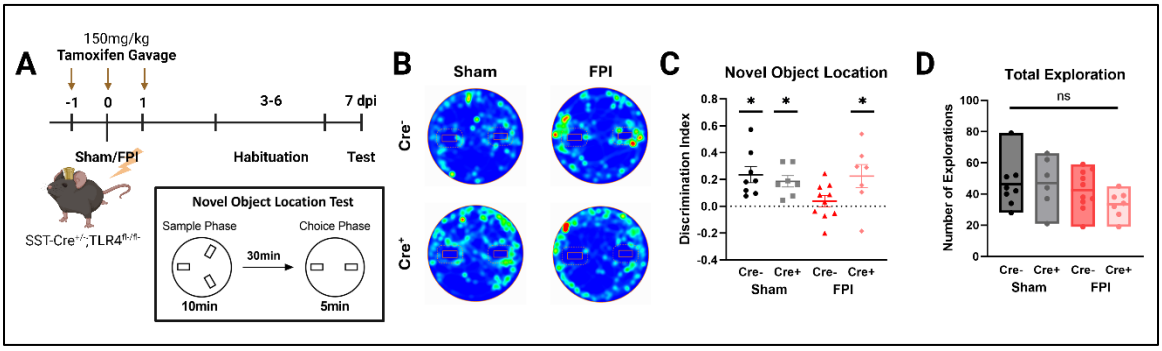

Figure 3.7. SST-specific TLR4 modulates behavioral pattern separation after injury. (A) Timeline and schematic of tamoxifen induction and behavioral habituation and testing. (B) Representative heat maps of mice in each experimental group during the choice phase of the novel object location task. (C) Summary histogram of discrimination ratios representing behavioral pattern separation performance for each group. (D) Histogram of total number of explorations for each group.

Discussion

This study is the first to demonstrate (1) a constitutive role for an innate immune receptor in acutely regulating dentate circuit inhibition and episodic memory processing; (2) that selective expression and regulation of SST neurons by TLR4 contributes to altered inhibition and spatial pattern separation in the injured brain; and (3) that mechanisms and effects of TLR4 regulation of dentate inhibition differ between the uninjured and injured brain.

Immune response within the brain has traditionally been proposed to be predominately mediated through infiltrating macrophages and resident microglia. Although these immune-specific cells do impact neurophysiological responses, they are not sole mediators of the inflammatory response. Several studies have shown that cytokines and inflammatory molecules released through immune signaling, including IL-1β, TNF, and HMGB1 are involved in astrocytic homeostasis, blood-brain barrier integrity, and the balance of neurological network excitability (Belarbi et al., 2012; Laird et al., 2014; Maggio & Vlachos, 2018; Paudel et al., 2018; Wallach et al., 2011; Yang et al., 2023). In these studies, we focused on the innate immune receptor, TLR4, a key mediator of these signaling molecules, and demonstrate that blocking TLR4 impacts hippocampal dentate inhibition both at baseline and following concussive brain injury with distinct underlying mechanisms.

In sham mice, blocking TLR4 *decrease* perforant path evoked IPSCs in hippocampal dentate granule cells (GCs) in the absence of an inflammatory insult (**Figure 3.1A-D**).

Acute treatment through i.p. injection of the TLR4 antagonist at baseline also impaired performance on the novel object location task (**Figure 3.5A-D**), a behavioral measure of dentate pattern separation known to be reliant on intact dentate somatostatin integrity (Corrubia et al., 2023; Morales et al., 2020). Interestingly, previous studies showed that blocking TLR4 in control animals resulted in increased population activity in local field potential recordings, however had no effect on isolated perforant path evoked EPSCs (Y. Li et al., 2015). Our results suggest that baseline levels of TLR4 may act through regulating GC inhibitory networks.

To determine how TLR4 regulated GC IPSCs, we focused on synaptic inhibition from two major interneuron subtypes in the dentate gyrus, PV and SST subtypes targeting perisomatic and dendritic domains of granule cells. TLR4 antagonism failed to alter optogenetically evoked PV or SST inhibitory input onto dentate GCs at baseline (**Figure 3.2C-E, 3.3C-E**). Since we identified differential TLR4 expression in somatostatin but not parvalbumin interneurons, we further investigated whether selective expression of TLR4 in SST neurons underlies TLR4 regulation of dentate network function. Interestingly, despite the ability of systemic pharmacological TLR4 blocker to decrease in eIPSCs amplitude and impair memory impairment performance in uninjured mice (**Figure 3.1B-D**, **3.5B-D**), SST-specific TLR4 deletion did not alter eIPSC amplitude or performance on the NOL task in sham controls (**Figure 3.6E-G**, **3.7B-D**). This suggests that basal TLR4 regulation is likely mediated through other mechanisms, potentially involving other interneuron subtypes, granule cells, or glia. In this regard, previous studies using glial metabolic inhibitors demonstrated that the TLR4 mediated increases in DG network

excitability required the presence of glial cells (Korgaonkar, Nguyen, et al., 2020). Further studies are required to elucidate the potential role of microglial and astrocytic TLR4 in maintaining basal dentate inhibition and its impact on behavioral function.

Neuroimmune TLR4 signaling in response to injury, however, appears to be distinct from baseline TLR4 signaling. One week after fluid percussion injury (FPI), granule cell perforant path evoked IPSCs were decreased (**Figure 3.1B-D**) and behavioral pattern separation performance on the NOL test was impaired (**Figure 3.5B-D**). Taken together with our previous studies demonstrating an increase in GC excitatory glutamatergic currents after injury (Korgaonkar, Li, et al., 2020; Korgaonkar, Nguyen, et al., 2020; Y. Li et al., 2015), an additional decrease in GC inhibition would be expected to compromise E/I balance. The ensuing hyperexcitability likely contributes to behavioral deficits as well as increased risk for epilepsy after brain injury. CLI-095 used in this study (also known as TAK-242 or Resatorvid) is a specific intracellular TLR4 antagonist approved for clinical trials by the FDA (Yan et al., 2015). Blocking TLR4 using CLI-095 one week after injury attenuates the injury-induced decrease in eIPSC amplitude (**Figure 3.1B-D**) and improves impairments in behavioral pattern separation on the NOL task (**Figure 3.5B-D**) suggesting a translational potential for CLI-095 in preventing posttraumatic neurological deficits. TLR4 ligands and downstream immune mediators, in particular HMGB1 and TNFα, have been shown to affect overall excitatory currents after FPI (Korgaonkar, Li, et al., 2020; Korgaonkar, Nguyen, et al., 2020; Y. Li et al., 2015), further demonstrating its role in mediating an immunomodulatory response after injury. TLR4 signaling in response to injury can thus be attenuated through acute treatment targeting the TLR4 pathway, however

therapeutic potential may be limited due to the adverse effects on baseline neurophysiology and behavior.

Interestingly, when isolating PV and SST input onto GCs after injury using cell specific optogenetic activation, we observed that PV input appears to *increase* following injury, while SST input remains unchanged, despite an apparent loss of hilar SST interneurons. This data suggests that both PV and SST synapses may be strengthened after injury, potentially to compensate for hilar interneuron loss. Optogenetic stimulation of PV and SST neurons suggest that blocking TLR4 specifically modulated the strength of SST, but not PV, synapses to granule cells after FPI. Paradoxically, blocking TLR4 after injury *decreased* SST input onto GCs, despite increasing overall perforant path evoked IPSCs. Though this data appears contradictory, it points to an unexpected role of SST interneurons in disinhibiting other interneurons after injury. This proposal is consistent with recent reports identifying a potential role for SST in disinhibition (Estarellas et al., 2023; Nolan et al., 2022; Ogando et al., 2021). We attempted to address this by optically depleting PV and SST synapses through a high frequency stimulation of each interneuron followed by a perforant path electrical stimulation to elicit an eIPSC response without each interneuron contribution (**Figure 3.4A-D**). Interestingly, TLR4 antagonism failed to modulate eIPSC amplitude when the contribution of PV or SST mediated IPSCs was minimized indicating both PV and SST involvement in baseline circuit effects of TLR4. In contrast, after brain injury, TLR4 antagonist modulation of eIPSC amplitude was eliminated when the contribution of SST synapse was minimized, but retained when PV synapses were minimized (**Figure 3.4F-G**). These data demonstrate the essential role for SST, but not

PV, neurons in TLR4 regulation of eIPSC after FPI. The most parsimonious explanation to be examined in future studies is that SST-driven disinhibition underlies TLR4 mediated increases in eIPSC after injury. Our data demonstrating the continued TLR4 modulation of eIPSC after injury even when PV driven synaptic release was minimized indicates that PV neurons are not the key mediators of the disinhibitory regulation.

Notably, SST-specific deletion of TLR4 prevented the injury-induced deficits in both eIPSC and behavior one week after injury (**Fig 3.6E-G, 7**). These results demonstrate that SST-specific TLR4 signaling underlies the TLR4 dependent changes in inhibition and its impact on behaviors after injury. However, the optically evoked SST results suggest that its role in network modulation is much more complex. Our results also emphasize that though SST-specific TLR4 expression and signaling, while having little effect under basal conditions in the uninjured brain, profoundly modulates inhibition and pattern separation after injury, possibly impacting dendritic input integration. These findings demonstrate a novel role of TLR4 in modulating inhibitory synapses at baseline as well as after injury and provides promising therapeutic potential whereby acute targeting of SST-TLR4 signaling after brain injury may limit post-injury increases in dentate excitability by promoting synaptic GABAergic inhibition.

Overall, this study demonstrates how neuroimmune systems can be involved both in maintaining baseline network function and in mediating pathological outcomes after brain insults. TLR4 and other immune receptors have been shown to be expressed in several cell types, including microglia, astrocytes, and neurons within the brain. This study is the first

to demonstrate that inhibitory neuron specific TLR4 impacts overall neurophysiology, affecting both network output and behavioral outcomes in the injured brain. This serves as a foundation for an exciting direction in the unexplored area understanding neuronal subtype specific role for immune receptors on network function and the complex interplay between immune system and inhibitory brain circuits.

CONCLUSION

Throughout this body of work, we demonstrate how immune signaling differentially modulates neuronal activity at baseline and following concussive brain injury. In the initial chapter, we continued a line of previous experiments performed in rats. Using the glial metabolic inhibitors fluoroacetate and minocycline to target astrocytes and microglia, respectively, we determined whether TLR4 modulation of dentate excitability is dependent on glial signaling. We found that the effect of TLR4 antagonism in increasing evoked population spike amplitude in uninjured control rats was abolished when glia were inhibited, indicating that glial TLR4 signaling may at least partially underlie baseline neuronal effects in control animals. In contrast, one week after Fluid Percussion Injury (FPI), we found that the increased evoked population spike amplitude and granule cell AMPA currents are still affected by TLR4 antagonism, even in the presence of glial inhibitors. This suggests that though glial TLR4 signaling modulates basal dentate neurophysiology, pathological neuronal TLR4 signaling may take precedence following injury.

Because TLR4 signaling leads to the production of pro-inflammatory cytokines, these downstream neuroinflammatory regulators may be driving the effects we observe on neuronal excitability. Western blot studies of TLR4 mediated increases in proteins downstream of both MyD88-dependent and independent pathways demonstrated that TNFα is upregulated after FPI, likely through the activation of both pathways. Interestingly, using an antibody to block TNFα resulted in identical effects on local field

potential recordings in the dentate gyrus as TLR4 antagonism, indicating a role for TNFα downstream of TLR4 in regulating effects on overall dentate network excitability. These data suggest the presence of an underappreciated neuronal TLR4 signaling pathway that is likely similar to the pathways in microglia and macrophages.

Lastly, in behavioral experiments, we tested working memory in rats using the Morris water maze. We found that path efficiency decreased one week and one month after FPI, demonstrating lasting memory impairment after brain injury. Interestingly, acute treatment with TLR4 antagonists resulted in opposing behavioral effects in uninjured controls and after FPI, mimicking the results found in electrophysiological slice recordings and correlating the modulation of neuronal excitability by TLR4 in-vivo. Path efficiency was decreased in sham control animals, while the injury-induced deficits at both one week and one month appeared to be prevented by acute TLR4 antagonism. These results emphasize how neuro-immune regulation of neuronal networks can have drastic consequences in memory and behavior and underscore the importance of understanding the differences underlying baseline and injury-induced immune signaling.

In order to advance our ability to use transgenic lines for more targeted investigations into cell-type specific expression of TLR4 and its effects, we sought to validate our studies in the mouse model. The experiments outlined in the second chapter illustrate that FPI increases overall granule cell (GC) excitability and impairs temporal and spatial pattern separation one week after injury, similar to the effects of injury we observed previously in rats. We demonstrate that perforant path evoked excitatory post synaptic currents (eEPSCs) in GCs and number of GCs expressing the sustained neuronal activity marker, ΔFosB, are

increased one week after FPI. Additionally, we adapted an ex-vivo temporal pattern separation paradigm to determine their ability of granule cell firing patterns to disambiguate temporally patterned inputs (Madar et al., 2019b, 2021, 2021). Using this paradigm, we demonstrated that despite the lack of changes in GC intrinsic properties after injury, GC ability to decorrelate highly similar inputs is impaired. We also established a behavioral pattern separation task that was previously shown to be dentate specific (Bekinschtein et al., 2013; Morales et al., 2020) and found that spatial pattern separation is impaired in mice one week after FPI. Immunostaining for somatostatin (SST) and parvalbumin (PV) also revealed that the impairments we observed in GC temporal pattern separation and behavioral spatial pattern separation are correlated with a decrease in hilar SST cell count after FPI. These experiments validate our mouse model and suggest that the injury induced impairments in dentate excitability and memory performance may be due to changes in inhibitory signaling.

In the final chapter, we focus on inhibitory networks and demonstrate that cell-type specific expression of TLR4 underlies its effect on dentate neurophysiology. We first complete a series of experiments in the presence of the TLR4 antagonist to demonstrate that blocking TLR4 reduces evoked inhibitory post synaptic currents (eIPSCs) in sham control mice. These results suggest that TLR4 modulates overall baseline excitability by specifically targeting inhibitory synapses. After FPI, we see an injury-induced decrease in GC eIPSCs that is attenuated when TLR4 is blocked, suggesting that TLR4 modulates both excitatory and inhibitory currents after FPI. Acute treatment with the TLR4 antagonist prior to testing

on the novel object location task also revealed that blocking TLR4 impairs pattern separation in sham control mice while rescuing performance one week after injury.

To determine whether inputs from specific inhibitory interneurons are modulated by TLR4, we used optogenetic experiments with ChR2-expressing PV or SST neurons and showed that TLR4 only modulated SST input after FPI. In line we these findings, we also determined that TLR4 is expressed on SST neurons and not PV. Interestingly, in experiments using a mouse line with a SST-specific deletion of TLR4, we observed no effect of the SST-TLR4 deletion in control mice. Additionally, we revealed that GC eIPSC was not decreased and pattern separation performance was not impaired in Cre+ mice one week after FPI. These results suggest that TLR4 expressed specifically in SST neurons modulates dentate neurophysiology after injury, and further provide evidence that TLR4 modulates baseline physiology through non-neuronal signaling.

Overall, through the experiments outlined in this dissertation, we demonstrate how neuro-immune signaling can differ under basal conditions and in response to injury, with substantive impact on memory and behavior. These sets of experiments reveal a novel mechanism by which glial TLR4 specifically modulates basal dentate inhibition and uncover a novel effect of neuronally-expressed TLR4 in modulating dentate excitatory and inhibitory networks after injury. These experiments not only broaden our understanding of the complex interactions between the immune and nervous systems, but uncovering the distinctions between TLR4 signaling in basal and disease states also allows for more

specific therapeutic targeting to prevent injury related changes in overall dentate excitability and behavioral deficits.

Future studies can examine how TLR4 impacts SST synapses and whether it affects cell adhesion and synapse stabilization. Our previous studies demonstrated that TLR4 signaling appears to influence surface expression of CP-AMPA receptors, and further examination could uncover whether GABA receptor cycling is also affected. We also demonstrated that granule cell passive intrinsic properties do not appear to be affected by injury or TLR4 signaling, however, with the expression of TLR4 signaling in SST neurons and its role after injury, future studies can examine whether injury and TLR4 expression affects SST neuron intrinsic physiology, and whether it may lead to increased susceptibility to excitotoxic cell death. Additionally, these studies uncovered how cell-type specific expression of TLR4 can affect neurophysiology in different ways, and future studies can investigate TLR4 expression in other neuronal subtypes and whether their roles in modulating neurophysiology are also distinct.

REFERENCES

Afrasiabi, M., Gupta, A., Xu, H., Swietek, B., & Santhakumar, V. (2022). Differential Activity-Dependent Increase in Synaptic Inhibition and Parvalbumin Interneuron Recruitment in Dentate Granule Cells and Semilunar Granule Cells. *The Journal of Neuroscience: The Official Journal of the Society for Neuroscience*, *42*(6), 1090–1103. https://doi.org/10.1523/JNEUROSCI.1360-21.2021

Ahmad, A., Crupi, R., Campolo, M., Genovese, T., Esposito, E., & Cuzzocrea, S. (2013). Absence of TLR4 Reduces Neurovascular Unit and Secondary Inflammatory Process after Traumatic Brain Injury in Mice. *PLoS ONE*, *8*(3), e57208. https://doi.org/10.1371/journal.pone.0057208

Aimone, J. B., Deng, W., & Gage, F. H. (2011). Resolving new memories: A critical look at the dentate gyrus, adult neurogenesis, and pattern separation. *Neuron*, *70*(4), 589–596. https://doi.org/10.1016/j.neuron.2011.05.010

Akira, S., & Takeda, K. (2004). Toll-like receptor signalling. *Nature Reviews Immunology*, *4*(7), 499–511. https://doi.org/10.1038/nri1391

Alosco, M. L., Barr, W. B., Banks, S. J., Wethe, J. V., Miller, J. B., Pulukuri, S. V., Culhane, J., Tripodis, Y., Adler, C. H., Balcer, L. J., Bernick, C., Mariani, M. L., Cantu, R. C., Dodick, D. W., McClean, M. D., Au, R., Mez, J., Turner, R. W., Palmisano, J. N., … DIAGNOSE CTE Research Project. (2023). Neuropsychological test performance of former American football players. *Alzheimer's Research & Therapy*, *15*(1), 1. https://doi.org/10.1186/s13195-022-01147-9

Amor, S., & Woodroofe, M. N. (2014). Innate and adaptive immune responses in neurodegeneration and repair. *Immunology*, *141*(3), 287–291. https://doi.org/10.1111/imm.12134

Andreasen, M., & Hablitz, J. J. (1994). Paired-pulse facilitation in the dentate gyrus: A patch-clamp study in rat hippocampus in vitro. *Journal of Neurophysiology*, *72*(1), 326–336. https://doi.org/10.1152/jn.1994.72.1.326

Annegers, J. F., & Coan, S. P. (2000). The risks of epilepsy after traumatic brain injury. *Seizure*, *9*(7), 453–457. https://doi.org/10.1053/seiz.2000.0458

Arciniega, H., Shires, J., Furlong, S., Kilgore-Gomez, A., Cerreta, A., Murray, N. G., & Berryhill, M. E. (2021). Impaired visual working memory and reduced connectivity in undergraduates with a history of mild traumatic brain injury. *Scientific Reports*, *11*(1), 2789. https://doi.org/10.1038/s41598-021-80995-1

Atkins, C. M., Oliva, A. A., Alonso, O. F., Pearse, D. D., Bramlett, H. M., & Dietrich, W. D. (2007). Modulation of the cAMP signaling pathway after traumatic brain injury. *Experimental Neurology*, *208*(1), 145–158. https://doi.org/10.1016/j.expneurol.2007.08.011

Avital, A., Goshen, I., Kamsler, A., Segal, M., Iverfeldt, K., Richter-Levin, G., & Yirmiya, R. (2003). Impaired interleukin-1 signaling is associated with deficits in hippocampal memory processes and neural plasticity. *Hippocampus*, *13*(7), 826–834. https://doi.org/10.1002/hipo.10135

Azouvi, P., Arnould, A., Dromer, E., & Vallat-Azouvi, C. (2017). Neuropsychology of traumatic brain injury: An expert overview. *Revue Neurologique*, *173*(7), 461–472. https://doi.org/10.1016/j.neurol.2017.07.006

Balosso, S., Liu, J., Bianchi, M. E., & Vezzani, A. (2014). Disulfide-Containing High Mobility Group Box-1 Promotes *N* -Methyl- D -Aspartate Receptor Function and Excitotoxicity by Activating Toll-Like Receptor 4-Dependent Signaling in Hippocampal Neurons. *Antioxidants & Redox Signaling*, *21*(12), 1726–1740. https://doi.org/10.1089/ars.2013.5349

Balschun, D., Wetzel, W., Rey, A., Pitossi, F., Schneider, H., Zuschratter, W., & Besedovsky, H. O. (2004). Interleukin-6: A cytokine to forget. *The FASEB Journal*, *18*(14), 1788–1790. https://doi.org/10.1096/fj.04-1625fje

Barak, B., Feldman, N., & Okun, E. (2014). Toll-like receptors as developmental tools that regulate neurogenesis during development: An update. *Frontiers in Neuroscience*, *8*. https://doi.org/10.3389/fnins.2014.00272

Bauer, S., Kerr, B. J., & Patterson, P. H. (2007). The neuropoietic cytokine family in development, plasticity, disease and injury. *Nature Reviews Neuroscience*, *8*(3), Article 3. https://doi.org/10.1038/nrn2054

Beattie, E. C., Stellwagen, D., Morishita, W., Bresnahan, J. C., Ha, B. K., Von Zastrow, M., Beattie, M. S., & Malenka, R. C. (2002). Control of Synaptic Strength by Glial TNFα. *Science*, *295*(5563), 2282–2285. https://doi.org/10.1126/science.1067859

Bekinschtein, P., Kent, B. A., Oomen, C. A., Clemenson, G. D., Gage, F. H., Saksida, L. M., & Bussey, T. J. (2013). BDNF in the Dentate Gyrus Is Required for Consolidation of "Pattern-Separated" Memories. *Cell Reports*, *5*(3), 759–768. https://doi.org/10.1016/j.celrep.2013.09.027

Belarbi, K., Jopson, T., Tweedie, D., Arellano, C., Luo, W., Greig, N. H., & Rosi, S. (2012). *TNF-a protein synthesis inhibitor restores neuronal function and reverses cognitive deficits induced by chronic neuroinflammation*.

Ben Menachem-Zidon, O., Avital, A., Ben-Menahem, Y., Goshen, I., Kreisel, T., Shmueli, E. M., Segal, M., Ben Hur, T., & Yirmiya, R. (2011). Astrocytes support hippocampal-dependent memory and long-term potentiation via interleukin-1 signaling. *Brain, Behavior, and Immunity*, *25*(5), 1008–1016. https://doi.org/10.1016/j.bbi.2010.11.007

Bonislawski, D. P., Schwarzbach, E. P., & Cohen, A. S. (2007). Brain injury impairs dentate gyrus inhibitory efficacy. *Neurobiology of Disease*, *25*(1), 163–169. https://doi.org/10.1016/j.nbd.2006.09.002

Braganza, O., Mueller-Komorowska, D., Kelly, T., & Beck, H. (2020). Quantitative properties of a feedback circuit predict frequency-dependent pattern separation. *eLife*, *9*, e53148. https://doi.org/10.7554/eLife.53148

Bramlett, H. M., & Dietrich, W. D. (2007). Progressive damage after brain and spinal cord injury: Pathomechanisms and treatment strategies. In *Progress in Brain Research* (Vol. 161, pp. 125–141). Elsevier. https://doi.org/10.1016/S0079-6123(06)61009-1

Buzsáki, G. (2010). Neural syntax: Cell assemblies, synapsembles, and readers. *Neuron*, *68*(3), 362–385. https://doi.org/10.1016/j.neuron.2010.09.023

Cayco-Gajic, N. A., & Silver, R. A. (2019). Re-evaluating Circuit Mechanisms Underlying Pattern Separation. *Neuron*, *101*(4), 584–602. https://doi.org/10.1016/j.neuron.2019.01.044

Chiu, C.-C., Liao, Y.-E., Yang, L.-Y., Wang, J.-Y., Tweedie, D., Karnati, H. K., Greig, N. H., & Wang, J.-Y. (2016). Neuroinflammation in animal models of traumatic brain injury. *Journal of Neuroscience Methods*, *272*, 38–49. https://doi.org/10.1016/j.jneumeth.2016.06.018

Cj, G., K, M., Hh, Y., Hc, H., & L, L. (2013). Permanent genetic access to transiently active neurons via TRAP: Targeted recombination in active populations. *Neuron*, *78*(5). https://doi.org/10.1016/j.neuron.2013.03.025

Clark, L. R., Yun, S., Acquah, N. K., Kumar, P. L., Metheny, H. E., Paixao, R. C. C., Cohen, A. S., & Eisch, A. J. (2020). Mild Traumatic Brain Injury Induces Transient, Sequential Increases in Proliferation, Neuroblasts/Immature Neurons, and Cell Survival: A Time Course Study in the Male Mouse Dentate Gyrus. *Frontiers in Neuroscience*, *14*, 612749. https://doi.org/10.3389/fnins.2020.612749

Clelland, C. D., Choi, M., Romberg, C., Clemenson, G. D., Fragniere, A., Tyers, P., Jessberger, S., Saksida, L. M., Barker, R. A., Gage, F. H., & Bussey, T. J. (2009). A functional role for adult hippocampal neurogenesis in spatial pattern separation.

Science (New York, N.Y.), *325*(5937), 210–213. https://doi.org/10.1126/science.1173215

Correll, E. A., Ramser, B. J., Knott, M. V., McCullumsmith, R. E., McGuire, J. L., & Ngwenya, L. B. (2021). Deficits in pattern separation and dentate gyrus proliferation after rodent lateral fluid percussion injury. *IBRO Neuroscience Reports*, *10*, 31–41. https://doi.org/10.1016/j.ibneur.2020.11.005

Corrubia, L., Huang, A., Nguyen, S., Shiflett, M. W., Jones, M. V., Ewell, L. A., & Santhakumar, V. (2023). Early deficits in dentate circuit and behavioral pattern separation after concussive brain injury. *Experimental Neurology*, *370*, 114578. https://doi.org/10.1016/j.expneurol.2023.114578

Costello, D. A., Watson, M. B., Cowley, T. R., Murphy, N., Murphy Royal, C., Garlanda, C., & Lynch, M. A. (2011). Interleukin-1α and HMGB1 Mediate Hippocampal Dysfunction in SIGIRR-Deficient Mice. *The Journal of Neuroscience*, *31*(10), 3871–3879. https://doi.org/10.1523/JNEUROSCI.6676-10.2011

Coulter, D. A., & Carlson, G. C. (2007). Functional regulation of the dentate gyrus by GABA-mediated inhibition. In *Progress in Brain Research* (Vol. 163, pp. 235–812). Elsevier. https://doi.org/10.1016/S0079-6123(07)63014-3

D'Ambrosio, R., Maris, D. O., Grady, M. S., Winn, H. R., & Janigro, D. (1998). Selective loss of hippocampal long-term potentiation, but not depression, following fluid percussion injury. *Brain Research*, *786*(1–2), 64–79. https://doi.org/10.1016/S0006-8993(97)01412-1

Dantzer, R. (2018). Neuroimmune Interactions: From the Brain to the Immune System and Vice Versa. *Physiological Reviews*, *98*(1), 477–504. https://doi.org/10.1152/physrev.00039.2016

Dengler, C. G., & Coulter, D. A. (2016). Normal and epilepsy-associated pathologic function of the dentate gyrus. In *Progress in Brain Research* (Vol. 226, pp. 155–178). Elsevier. https://doi.org/10.1016/bs.pbr.2016.04.005

Dong, X.-Q., Yu, W.-H., Hu, Y.-Y., Zhang, Z.-Y., & Huang, M. (2011). Oxymatrine reduces neuronal cell apoptosis by inhibiting Toll-like receptor 4/nuclear factor kappa-B-dependent inflammatory responses in traumatic rat brain injury. *Inflammation Research*, *60*(6), 533–539. https://doi.org/10.1007/s00011-010-0300-7

Eichenbaum, H. (2013). Memory on time. *Trends in Cognitive Sciences*, *17*(2), 81–88. https://doi.org/10.1016/j.tics.2012.12.007

Estarellas, C., Álvarez-Salvado, E., Pérez-Cervera, L., Mirasso, C. R., & Canals, S. (2023). *Somatic disinhibition of granule cells improves information transmission and pattern separation in the dentate gyrus* [Preprint]. Neuroscience. https://doi.org/10.1101/2023.02.16.528800

Feldman, N., Rotter-Maskowitz, A., & Okun, E. (2015). DAMPs as mediators of sterile inflammation in aging-related pathologies. *Ageing Research Reviews*, *24*, 29–39. https://doi.org/10.1016/j.arr.2015.01.003

Feng, Y., Gao, J., Cui, Y., Li, M., Li, R., Cui, C., & Cui, J. (2017). Neuroprotective Effects of Resatorvid Against Traumatic Brain Injury in Rat: Involvement of Neuronal Autophagy and TLR4 Signaling Pathway. *Cellular and Molecular Neurobiology*, *37*(1), 155–168. https://doi.org/10.1007/s10571-016-0356-1

Folweiler, K. A., Samuel, S., Metheny, H. E., & Cohen, A. S. (2018). Diminished Dentate Gyrus Filtering of Cortical Input Leads to Enhanced Area Ca3 Excitability after Mild Traumatic Brain Injury. *Journal of Neurotrauma*, *35*(11), 1304–1317. https://doi.org/10.1089/neu.2017.5350

Folweiler, K. A., Xiong, G., Best, K. M., Metheny, H. E., Nah, G., & Cohen, A. S. (2020). Traumatic Brain Injury Diminishes Feedforward Activation of Parvalbumin-Expressing Interneurons in the Dentate Gyrus. *Eneuro*, *7*(6), ENEURO.0195-19.2020. https://doi.org/10.1523/ENEURO.0195-19.2020

Frankowski, J. C., Kim, Y. J., & Hunt, R. F. (2019). Selective vulnerability of hippocampal interneurons to graded traumatic brain injury. *Neurobiology of Disease*, *129*, 208–216. https://doi.org/10.1016/j.nbd.2018.07.022

Gao, Y., Fang, X., Tong, Y., Liu, Y., & Zhang, B. (2009). TLR4-mediated MyD88-dependent signaling pathway is activated by cerebral ischemia–reperfusion in cortex in mice. *Biomedicine & Pharmacotherapy*, *63*(6), 442–450. https://doi.org/10.1016/j.biopha.2008.06.028

Gilbert, P. E., Kesner, R. P., & Lee, I. (2001). Dissociating hippocampal subregions: Double dissociation between dentate gyrus and CA1. *Hippocampus*, *11*(6), 626–636. https://doi.org/10.1002/hipo.1077

Gnjatic, S., Sawhney, N. B., & Bhardwaj, N. (2010). Toll-Like Receptor Agonists: Are They Good Adjuvants? *The Cancer Journal*, *16*(4), 382–391. https://doi.org/10.1097/PPO.0b013e3181eaca65

GoodSmith, D., Chen, X., Wang, C., Kim, S. H., Song, H., Burgalossi, A., Christian, K. M., & Knierim, J. J. (2017). Spatial Representations of Granule Cells and Mossy Cells of the Dentate Gyrus. *Neuron*, *93*(3), 677-690.e5. https://doi.org/10.1016/j.neuron.2016.12.026

Goshen, I., Kreisel, T., Ounallah-Saad, H., Renbaum, P., Zalzstein, Y., Ben-Hur, T., Levy-Lahad, E., & Yirmiya, R. (2007). A dual role for interleukin-1 in hippocampal-dependent memory processes. *Psychoneuroendocrinology*, *32*(8–10), 1106–1115. https://doi.org/10.1016/j.psyneuen.2007.09.004

Gupta, A., Dovek, L., Proddutur, A., Elgammal, F. S., & Santhakumar, V. (2022). Long-Term Effects of Moderate Concussive Brain Injury During Adolescence on Synaptic and Tonic GABA Currents in Dentate Granule Cells and Semilunar Granule Cells. *Frontiers in Neuroscience*, *16*, 800733. https://doi.org/10.3389/fnins.2022.800733

Gupta, A., Elgammal, F. S., Proddutur, A., Shah, S., & Santhakumar, V. (2012). Decrease in Tonic Inhibition Contributes to Increase in Dentate Semilunar Granule Cell Excitability after Brain Injury. *The Journal of Neuroscience*, *32*(7), 2523–2537. https://doi.org/10.1523/JNEUROSCI.4141-11.2012

Gupta, A., Proddutur, A., Chang, Y.-J., Raturi, V., Guevarra, J., Shah, Y., Elgammal, F. S., & Santhakumar, V. (2020). Dendritic morphology and inhibitory regulation distinguish dentate semilunar granule cells from granule cells through distinct stages of postnatal development. *Brain Structure & Function*, *225*(9), 2841–2855. https://doi.org/10.1007/s00429-020-02162-y

Gyoneva, S., & Ransohoff, R. M. (2015). Inflammatory reaction after traumatic brain injury: Therapeutic potential of targeting cell–cell communication by chemokines. *Trends in Pharmacological Sciences*, *36*(7), 471–480. https://doi.org/10.1016/j.tips.2015.04.003

Hainmueller, T., & Bartos, M. (2020). Dentate gyrus circuits for encoding, retrieval and discrimination of episodic memories. *Nature Reviews Neuroscience*, *21*(3), 153–168. https://doi.org/10.1038/s41583-019-0260-z

Hamm, R. J., Temple, M. D., Pike, B. R., O'Dell, D. M., Buck, D. L., & Lyeth, B. G. (1996). Working Memory Deficits following Traumatic Brain Injury in the Rat. *Journal of Neurotrauma*, *13*(6), 317–323. https://doi.org/10.1089/neu.1996.13.317

Hanke, M. L., & Kielian, T. (2011). Toll-like receptors in health and disease in the brain: Mechanisms and therapeutic potential. *Clinical Science*, *121*(9), 367–387. https://doi.org/10.1042/CS20110164

Houser, C. R. (2007). Interneurons of the dentate gyrus: An overview of cell types, terminal fields and neurochemical identity. In *Progress in Brain Research* (Vol. 163, pp. 217–811). Elsevier. https://doi.org/10.1016/S0079-6123(07)63013-1

Hua, F., Wang, J., Ishrat, T., Wei, W., Atif, F., Sayeed, I., & Stein, D. G. (2011). Genomic profile of Toll-like receptor pathways in traumatically brain-injured mice: Effect of

exogenous progesterone. *Journal of Neuroinflammation*, *8*(1), 42. https://doi.org/10.1186/1742-2094-8-42

Hunsaker, M. R., Rosenberg, J. S., & Kesner, R. P. (2008). The role of the dentate gyrus, CA3a,b, and CA3c for detecting spatial and environmental novelty. *Hippocampus*, *18*(10), 1064–1073. https://doi.org/10.1002/hipo.20464

Jeltsch, H., Bertrand, F., Lazarus, C., & Cassel, J.-C. (2001). Cognitive Performances and Locomotor Activity Following Dentate Granule Cell Damage in Rats: Role of Lesion Extent and Type of Memory Tested. *Neurobiology of Learning and Memory*, *76*(1), 81–105. https://doi.org/10.1006/nlme.2000.3986

Kahn, J. B., Port, R. G., Yue, C., Takano, H., & Coulter, D. A. (2019). Circuit-based interventions in the dentate gyrus rescue epilepsy-associated cognitive dysfunction. *Brain*, *142*(9), 2705–2721. https://doi.org/10.1093/brain/awz209

Kang, Y.-J., Lee, S.-H., Boychuk, J. A., Butler, C. R., Juras, J. A., Cloyd, R. A., & Smith, B. N. (2022). Adult Born Dentate Granule Cell Mediated Upregulation of Feedback Inhibition in a Mouse Model of Traumatic Brain Injury. *The Journal of Neuroscience: The Official Journal of the Society for Neuroscience*, *42*(37), 7077–7093. https://doi.org/10.1523/JNEUROSCI.2263-21.2022

Kawai, T., & Akira, S. (2007). Signaling to NF-κB by Toll-like receptors. *Trends in Molecular Medicine*, *13*(11), 460–469. https://doi.org/10.1016/j.molmed.2007.09.002

Kerloch, T., Clavreul, S., Goron, A., Abrous, D. N., & Pacary, E. (2019). Dentate Granule Neurons Generated During Perinatal Life Display Distinct Morphological Features Compared With Later-Born Neurons in the Mouse Hippocampus. *Cerebral Cortex (New York, N.Y.: 1991)*, *29*(8), 3527–3539. https://doi.org/10.1093/cercor/bhy224

Kernie, S. G., & Parent, J. M. (2010). Forebrain neurogenesis after focal Ischemic and traumatic brain injury. *Neurobiology of Disease*, *37*(2), 267–274. https://doi.org/10.1016/j.nbd.2009.11.002

Kesner, R. P. (2013). An analysis of the dentate gyrus function. *Behavioural Brain Research*, *254*, 1–7. https://doi.org/10.1016/j.bbr.2013.01.012

Kharatishvili, I., Nissinen, J. P., McIntosh, T. K., & Pitkänen, A. (2006). A model of posttraumatic epilepsy induced by lateral fluid-percussion brain injury in rats. *Neuroscience*, *140*(2), 685–697. https://doi.org/10.1016/j.neuroscience.2006.03.012

Kielian, T. (2006). Toll-like receptors in central nervous system glial inflammation and homeostasis. *Journal of Neuroscience Research*, *83*(5), 711–730. https://doi.org/10.1002/jnr.20767

Kim, S., Kim, S. Y., Pribis, J. P., Lotze, M., Mollen, K. P., Shapiro, R., Loughran, P., Scott, M. J., & Billiar, T. R. (2013). Signaling of High Mobility Group Box 1 (HMGB1) through Toll-like Receptor 4 in Macrophages Requires CD14. *Molecular Medicine*, *19*(1), 88–98. https://doi.org/10.2119/molmed.2012.00306

Kleen, J. K., & Holmes, G. L. (2010). Taming TLR4 may ease seizures. *Nature Medicine*, *16*(4), 369–370. https://doi.org/10.1038/nm0410-369

Knuesel, I., Chicha, L., Britschgi, M., Schobel, S. A., Bodmer, M., Hellings, J. A., Toovey, S., & Prinssen, E. P. (2014). Maternal immune activation and abnormal brain development across CNS disorders. *Nature Reviews Neurology*, *10*(11), Article 11. https://doi.org/10.1038/nrneurol.2014.187

Kobayashi, K., & Poo, M. (2004). Spike train timing-dependent associative modification of hippocampal CA3 recurrent synapses by mossy fibers. *Neuron*, *41*(3), 445–454. https://doi.org/10.1016/s0896-6273(03)00873-0

Korgaonkar, A. A., Li, Y., Sekhar, D., Subramanian, D., Guevarra, J., Swietek, B., Pallottie, A., Singh, S., Kella, K., Elkabes, S., & Santhakumar, V. (2020). Toll-like Receptor 4 Signaling in Neurons Enhances Calcium-Permeable AMPA Receptor Currents and Drives Post-Traumatic Epileptogenesis. *Annals of Neurology*, *87*(4), 497–515. https://doi.org/10.1002/ana.25698

Korgaonkar, A. A., Nguyen, S., Li, Y., Sekhar, D., Subramanian, D., Guevarra, J., Pang, K. C. H., & Santhakumar, V. (2020). Distinct cellular mediators drive the Janus faces of toll-like receptor 4 regulation of network excitability which impacts working memory performance after brain injury. *Brain, Behavior, and Immunity*, *88*, 381–395. https://doi.org/10.1016/j.bbi.2020.03.035

Kumar, S., Rao, S. L., Chandramouli, B. A., & Pillai, S. (2013). Reduced contribution of executive functions in impaired working memory performance in mild traumatic brain injury patients. *Clinical Neurology and Neurosurgery*, *115*(8), 1326–1332. https://doi.org/10.1016/j.clineuro.2012.12.038

Laird, M. D., Shields, J. S., Sukumari-Ramesh, S., Kimbler, D. E., Fessler, R. D., Shakir, B., Youssef, P., Yanasak, N., Vender, J. R., & Dhandapani, K. M. (2014). High mobility group box protein-1 promotes cerebral edema after traumatic brain injury via activation of toll-like receptor 4: HMGB1-TLR4 Signaling Promotes Brain Edema after TBI. *Glia*, *62*(1), 26–38. https://doi.org/10.1002/glia.22581

Larimer, P., & Strowbridge, B. W. (2010). Representing information in cell assemblies: Persistent activity mediated by semilunar granule cells. *Nature Neuroscience*, *13*(2), 213–222. https://doi.org/10.1038/nn.2458

Leh, S. E., Schroeder, C., Chen, J.-K., Mallar Chakravarty, M., Park, M. T. M., Cheung, B., Huntgeburth, S. C., Gosselin, N., Hock, C., Ptito, A., & Petrides, M. (2017). Microstructural Integrity of Hippocampal Subregions Is Impaired after Mild Traumatic Brain Injury. *Journal of Neurotrauma*, *34*(7), 1402–1411. https://doi.org/10.1089/neu.2016.4591

Lehnardt, S., Massillon, L., Follett, P., Jensen, F. E., Ratan, R., Rosenberg, P. A., Volpe, J. J., & Vartanian, T. (2003). Activation of innate immunity in the CNS triggers neurodegeneration through a Toll-like receptor 4-dependent pathway. *Proceedings of the National Academy of Sciences*, *100*(14), 8514–8519. https://doi.org/10.1073/pnas.1432609100

Lemaitre, B., Nicolas, E., Michaut, L., Reichhart, J.-M., & Hoffmann, J. A. (1996). The Dorsoventral Regulatory Gene Cassette spätzle/Toll/cactus Controls the Potent Antifungal Response in Drosophila Adults. *Cell*, *86*(6), 973–983. https://doi.org/10.1016/S0092-8674(00)80172-5

Leutgeb, J. K., Leutgeb, S., Moser, M.-B., & Moser, E. I. (2007). Pattern Separation in the Dentate Gyrus and CA3 of the Hippocampus. *Science*, *315*(5814), 961–966. https://doi.org/10.1126/science.1135801

Li, X., Chen, Y., Zhao, S., Wang, D., Zheng, X., & Luo, J. (2014). Lactic acid accumulation from sludge and food waste to improve the yield of propionic acid-enriched VFA. *Biochemical Engineering Journal*, *84*, 28–35. https://doi.org/10.1016/j.bej.2013.12.020

Li, Y., Korgaonkar, A. A., Swietek, B., Wang, J., Elgammal, F. S., Elkabes, S., & Santhakumar, V. (2015). Toll-like receptor 4 enhancement of non-NMDA synaptic currents increases dentate excitability after brain injury. *Neurobiology of Disease*, *74*, 240–253. https://doi.org/10.1016/j.nbd.2014.11.021

Lowenstein, D., Thomas, M., Smith, D., & McIntosh, T. (1992). Selective vulnerability of dentate hilar neurons following traumatic brain injury: A potential mechanistic link between head trauma and disorders of the hippocampus. *The Journal of Neuroscience*, *12*(12), 4846–4853. https://doi.org/10.1523/JNEUROSCI.12-12-04846.1992

Lu, Y.-C., Yeh, W.-C., & Ohashi, P. S. (2008). LPS/TLR4 signal transduction pathway. *Cytokine*, *42*(2), 145–151. https://doi.org/10.1016/j.cyto.2008.01.006

Lyeth, B. G., Jenkins, L. W., Hamm, R. J., Dixon, C. E., Phillips, L. L., Clifton, G. L., Young, H. F., & Hayes, R. L. (1990). Prolonged memory impairment in the absence of hippocampal cell death following traumatic brain injury in the rat. *Brain Research*, *526*(2), 249–258. https://doi.org/10.1016/0006-8993(90)91229-A

Madar, A. D., Ewell, L. A., & Jones, M. V. (2019a). Pattern separation of spiketrains in hippocampal neurons. *Scientific Reports*, *9*(1), 5282. https://doi.org/10.1038/s41598-019-41503-8

Madar, A. D., Ewell, L. A., & Jones, M. V. (2019b). Temporal pattern separation in hippocampal neurons through multiplexed neural codes. *PLOS Computational Biology*, *15*(4), e1006932. https://doi.org/10.1371/journal.pcbi.1006932

Madar, A. D., Pfammatter, J. A., Bordenave, J., Plumley, E. I., Ravi, S., Cowie, M., Wallace, E. P., Hermann, B. P., Maganti, R. K., & Jones, M. V. (2021). Deficits in Behavioral and Neuronal Pattern Separation in Temporal Lobe Epilepsy. *The Journal of Neuroscience: The Official Journal of the Society for Neuroscience*, *41*(46), 9669–9686. https://doi.org/10.1523/JNEUROSCI.2439-20.2021

Maggio, N., & Vlachos, A. (2018). Tumor necrosis factor (TNF) modulates synaptic plasticity in a concentration-dependent manner through intracellular calcium stores. *Journal of Molecular Medicine*, *96*(10), 1039–1047. https://doi.org/10.1007/s00109-018-1674-1

Mao, S.-S., Hua, R., Zhao, X.-P., Qin, X., Sun, Z.-Q., Zhang, Y., Wu, Y.-Q., Jia, M.-X., Cao, J.-L., & Zhang, Y.-M. (2012). Exogenous Administration of PACAP Alleviates Traumatic Brain Injury in Rats through a Mechanism Involving the TLR4/MyD88/NF-κB Pathway. *Journal of Neurotrauma*, *29*(10), 1941–1959. https://doi.org/10.1089/neu.2011.2244

Maroso, M., Balosso, S., Ravizza, T., Liu, J., Aronica, E., Iyer, A. M., Rossetti, C., Molteni, M., Casalgrandi, M., Manfredi, A. A., Bianchi, M. E., & Vezzani, A. (2010). Toll-like receptor 4 and high-mobility group box-1 are involved in ictogenesis and can be targeted to reduce seizures. *Nature Medicine*, *16*(4), 413–419. https://doi.org/10.1038/nm.2127

Matzinger, P. (2002). The Danger Model: A Renewed Sense of Self. *Science*, *296*(5566), 301–305. https://doi.org/10.1126/science.1071059

McAllister, T. W. (1992). Neuropsychiatric sequelae of head injuries. *The Psychiatric Clinics of North America*, *15*(2), 395–413.

McHugh, T. J., Jones, M. W., Quinn, J. J., Balthasar, N., Coppari, R., Elmquist, J. K., Lowell, B. B., Fanselow, M. S., Wilson, M. A., & Tonegawa, S. (2007). Dentate gyrus NMDA receptors mediate rapid pattern separation in the hippocampal

network. *Science (New York, N.Y.)*, *317*(5834), 94–99. https://doi.org/10.1126/science.1140263

McHugh, T., Laforce, R., Gallagher, P., Quinn, S., Diggle, P., & Buchanan, L. (2006). Natural history of the long-term cognitive, affective, and physical sequelae of mild traumatic brain injury. *Brain and Cognition*, *60*(2), 209–211.

Meier, T. B., Savitz, J., Singh, R., Teague, T. K., & Bellgowan, P. S. F. (2016). Smaller Dentate Gyrus and CA2 and CA3 Volumes Are Associated with Kynurenine Metabolites in Collegiate Football Athletes. *Journal of Neurotrauma*, *33*(14), 1349–1357. https://doi.org/10.1089/neu.2015.4118

Miller, S. M., & Sahay, A. (2019). Functions of adult-born neurons in hippocampal memory interference and indexing. *Nature Neuroscience*, *22*(10), 1565–1575. https://doi.org/10.1038/s41593-019-0484-2

Morales, C., Morici, J. F., Espinosa, N., Sacson, A., Lara-Vasquez, A., García-Pérez, M. A., Bekinschtein, P., Weisstaub, N. V., & Fuentealba, P. (2020). *Dentate Gyrus Somatostatin Cells are Required for Contextual Discrimination During Episodic Memory Encoding*.

Morimoto, K., & Nakajima, K. (2019). Role of the Immune System in the Development of the Central Nervous System. *Frontiers in Neuroscience*, *13*, 916. https://doi.org/10.3389/fnins.2019.00916

Morris, A. M., Churchwell, J. C., Kesner, R. P., & Gilbert, P. E. (2012). Selective lesions of the dentate gyrus produce disruptions in place learning for adjacent spatial locations. *Neurobiology of Learning and Memory*, *97*(3), 326–331. https://doi.org/10.1016/j.nlm.2012.02.005

Myers, C. E., & Scharfman, H. E. (2009). A role for hilar cells in pattern separation in the dentate gyrus: A computational approach. *Hippocampus*, *19*(4), 321–337. https://doi.org/10.1002/hipo.20516

Myers, C. E., & Scharfman, H. E. (2011). Pattern separation in the dentate gyrus: A role for the CA3 backprojection. *Hippocampus*, *21*(11), 1190–1215. https://doi.org/10.1002/hipo.20828

Nakashiba, T., Cushman, J. D., Pelkey, K. A., Renaudineau, S., Buhl, D. L., McHugh, T. J., Barrera, V. R., Chittajallu, R., Iwamoto, K. S., McBain, C. J., Fanselow, M. S., & Tonegawa, S. (2012). Young Dentate Granule Cells Mediate Pattern Separation, whereas Old Granule Cells Facilitate Pattern Completion. *Cell*, *149*(1), 188–201. https://doi.org/10.1016/j.cell.2012.01.046

Neuberger, E. J., Abdul Wahab, R., Jayakumar, A., Pfister, B. J., & Santhakumar, V. (2014). Distinct effect of impact rise times on immediate and early neuropathology after brain injury in juvenile rats. *Journal of Neuroscience Research*, *92*(10), 1350–1361. https://doi.org/10.1002/jnr.23401

Neuberger, E. J., Swietek, B., Corrubia, L., Prasanna, A., & Santhakumar, V. (2017). Enhanced Dentate Neurogenesis after Brain Injury Undermines Long-Term Neurogenic Potential and Promotes Seizure Susceptibility. *Stem Cell Reports*, *9*(3), 972–984. https://doi.org/10.1016/j.stemcr.2017.07.015

Neunuebel, J. P., & Knierim, J. J. (2014). CA3 retrieves coherent representations from degraded input: Direct evidence for CA3 pattern completion and dentate gyrus pattern separation. *Neuron*, *81*(2), 416–427. https://doi.org/10.1016/j.neuron.2013.11.017

Ngwenya, L. B., & Danzer, S. C. (2019). Impact of Traumatic Brain Injury on Neurogenesis. *Frontiers in Neuroscience*, *12*, 1014. https://doi.org/10.3389/fnins.2018.01014

Nolan, A. L., Sohal, V. S., & Rosi, S. (2022). Selective Inhibitory Circuit Dysfunction after Chronic Frontal Lobe Contusion. *The Journal of Neuroscience*, *42*(27), 5361–5372. https://doi.org/10.1523/JNEUROSCI.0097-22.2022

Ogando, M. B., Pedroncini, O., Federman, N., Romano, S. A., Brum, L. A., Lanuza, G. M., Refojo, D., & Marin-Burgin, A. (2021). Cholinergic modulation of dentate gyrus processing through dynamic reconfiguration of inhibitory circuits. *Cell Reports*, *36*(8), 109572. https://doi.org/10.1016/j.celrep.2021.109572

Okun, E., Barak, B., Saada-Madar, R., Rothman, S. M., Griffioen, K. J., Roberts, N., Castro, K., Mughal, M. R., Pita, M. A., Stranahan, A. M., Arumugam, T. V., & Mattson, M. P. (2012). Evidence for a Developmental Role for TLR4 in Learning and Memory. *PLoS ONE*, *7*(10), e47522. https://doi.org/10.1371/journal.pone.0047522

Overstreet-Wadiche, L. S., & Westbrook, G. L. (2006). Functional maturation of adult-generated granule cells. *Hippocampus*, *16*(3), 208–215. https://doi.org/10.1002/hipo.20152

Pang, K. C. H., Sinha, S., Avcu, P., Roland, J. J., Nadpara, N., Pfister, B., Long, M., Santhakumar, V., & Servatius, R. J. (2015). Long-Lasting Suppression of Acoustic Startle Response after Mild Traumatic Brain Injury. *Journal of Neurotrauma*, *32*(11), 801–810. https://doi.org/10.1089/neu.2014.3451

Pascual, O., Ben Achour, S., Rostaing, P., Triller, A., & Bessis, A. (2012). Microglia activation triggers astrocyte-mediated modulation of excitatory neurotransmission.

Proceedings of the National Academy of Sciences, *109*(4). https://doi.org/10.1073/pnas.1111098109

Paudel, Y. N., Shaikh, Mohd. F., Chakraborti, A., Kumari, Y., Aledo-Serrano, Á., Aleksovska, K., Alvim, M. K. M., & Othman, I. (2018). HMGB1: A Common Biomarker and Potential Target for TBI, Neuroinflammation, Epilepsy, and Cognitive Dysfunction. *Frontiers in Neuroscience*, *12*, 628. https://doi.org/10.3389/fnins.2018.00628

Paulsen, R. E., Contestabile, A., Villani, L., & Fonnum, F. (1987). An In Vivo Model for Studying Function of Brain Tissue Temporarily Devoid of Glial Cell Metabolism: The Use of Fluorocitrate. *Journal of Neurochemistry*, *48*(5), 1377–1385. https://doi.org/10.1111/j.1471-4159.1987.tb05674.x

Piatti, V. C., Ewe, L. A., & Leutgeb, J. K. (2013). Neurogenesis in the dentate gyrus: Carrying the message or dictating the tone. *Frontiers in Neuroscience*, *7 APR*. https://doi.org/10.3389/fnins.2013.00050

Piatti, V. C., Ewell, L. A., & Leutgeb, J. K. (2013). Neurogenesis in the dentate gyrus: Carrying the message or dictating the tone. *Frontiers in Neuroscience*, *7*. https://doi.org/10.3389/fnins.2013.00050

Potter, O. V., Giedraitis, M. E., Johnson, C. D., Cox, M. N., & Kohman, R. A. (2019). Young and aged TLR4 deficient mice show sex-dependent enhancements in spatial memory and alterations in interleukin-1 related genes. *Brain, Behavior, and Immunity*, *76*, 37–47. https://doi.org/10.1016/j.bbi.2018.10.010

Pribiag, H., & Stellwagen, D. (2013). TNF-α Downregulates Inhibitory Neurotransmission through Protein Phosphatase 1-Dependent Trafficking of GABA $_A$ Receptors. *The Journal of Neuroscience*, *33*(40), 15879–15893. https://doi.org/10.1523/JNEUROSCI.0530-13.2013

Pribiag, H., & Stellwagen, D. (2014). Neuroimmune regulation of homeostatic synaptic plasticity. *Neuropharmacology*, *78*, 13–22. https://doi.org/10.1016/j.neuropharm.2013.06.008

Proddutur, A., Nguyen, S., Yeh, C.-W., Gupta, A., & Santhakumar, V. (2023). Reclusive chandeliers: Functional isolation of dentate axo-axonic cells after experimental status epilepticus. *Progress in Neurobiology*, *231*, 102542. https://doi.org/10.1016/j.pneurobio.2023.102542

Ramirez, S., Tonegawa, S., & Liu, X. (2013). Identification and optogenetic manipulation of memory engrams in the hippocampus. *Frontiers in Behavioral Neuroscience*, *7*, 226. https://doi.org/10.3389/fnbeh.2013.00226

Rangel, L. M., Alexander, A. S., Aimone, J. B., Wiles, J., Gage, F. H., Chiba, A. A., & Quinn, L. K. (2014). Temporally selective contextual encoding in the dentate gyrus of the hippocampus. *Nature Communications*, *5*, 3181. https://doi.org/10.1038/ncomms4181

Rao, V., & Lyketsos, C. (2000). Neuropsychiatric sequelae of traumatic brain injury. *Psychosomatics*, *41*(2), 95–103. https://doi.org/10.1176/appi.psy.41.2.95

Rolls, E. T., & Kesner, R. P. (2006). A computational theory of hippocampal function, and empirical tests of the theory. *Progress in Neurobiology*, *79*(1), 1–48. https://doi.org/10.1016/j.pneurobio.2006.04.005

Roof, R. L., & Hall, E. D. (2000). Gender Differences in Acute CNS Trauma and Stroke: Neuroprotective Effects of Estrogen and Progesterone. *Journal of Neurotrauma*, *17*(5), 367–388. https://doi.org/10.1089/neu.2000.17.367

Rusnak, M. (2013). Traumatic brain injury: Giving voice to a silent epidemic. *Nature Reviews. Neurology*, *9*(4), 186–187. https://doi.org/10.1038/nrneurol.2013.38

Saletti, P. G., Ali, I., Casillas-Espinosa, P. M., Semple, B. D., Lisgaras, C. P., Moshé, S. L., & Galanopoulou, A. S. (2019). In search of antiepileptogenic treatments for post-traumatic epilepsy. *Neurobiology of Disease*, *123*, 86–99. https://doi.org/10.1016/j.nbd.2018.06.017

Sanders, M. J., Sick, T. J., Perez-Pinzon, M. A., Dietrich, W. D., & Green, E. J. (2000). Chronic failure in the maintenance of long-term potentiation following fluid percussion injury in the rat. *Brain Research*, *861*(1), 69–76. https://doi.org/10.1016/S0006-8993(00)01986-7

Santhakumar, V., Bender, R., Frotscher, M., Ross, S. T., Hollrigel, G. S., Toth, Z., & Soltesz, I. (2000). Granule cell hyperexcitability in the early post-traumatic rat dentate gyrus: The 'irritable mossy cell' hypothesis. *The Journal of Physiology*, *524*(1), 117–134. https://doi.org/10.1111/j.1469-7793.2000.00117.x

Santhakumar, V., Ratzliff, A. D. H., Jeng, J., Toth, Z., & Soltesz, I. (2001). Long-term hyperexcitability in the hippocampus after experimental head trauma. *Annals of Neurology*, *50*(6), 708–717. https://doi.org/10.1002/ana.1230

Save, L., Baude, A., & Cossart, R. (2019). Temporal Embryonic Origin Critically Determines Cellular Physiology in the Dentate Gyrus. *Cerebral Cortex (New York, N.Y.: 1991)*, *29*(6), 2639–2652. https://doi.org/10.1093/cercor/bhy132

Scharfman, H. E., & Bernstein, H. L. (2015). Potential implications of a monosynaptic pathway from mossy cells to adult-born granule cells of the dentate gyrus. *Frontiers in Systems Neuroscience*, *9*. https://doi.org/10.3389/fnsys.2015.00112

Semple, B. D., Dill, L. K., & O'Brien, T. J. (2020). Immune Challenges and Seizures: How Do Early Life Insults Influence Epileptogenesis? *Frontiers in Pharmacology*, *11*, 2. https://doi.org/10.3389/fphar.2020.00002

Senzai, Y., & Buzsáki, G. (2017). Physiological Properties and Behavioral Correlates of Hippocampal Granule Cells and Mossy Cells. *Neuron*, *93*(3), 691-704.e5. https://doi.org/10.1016/j.neuron.2016.12.011

Shapiro, L. A. (2017). Altered Hippocampal Neurogenesis during the First 7 Days after a Fluid Percussion Traumatic Brain Injury. *Cell Transplantation*, *26*(7), 1314–1318. https://doi.org/10.1177/0963689717714099

Shi, H., Hua, X., Kong, D., Stein, D., & Hua, F. (2019). Role of Toll-like receptor mediated signaling in traumatic brain injury. *Neuropharmacology*, *145*, 259–267. https://doi.org/10.1016/j.neuropharm.2018.07.022

Sinha, S. P., Avcu, P., Spiegler, K. M., Komaravolu, S., Kim, K., Cominski, T., Servatius, R. J., & Pang, K. C. H. (2017). Startle suppression after mild traumatic brain injury is associated with an increase in pro-inflammatory cytokines, reactive gliosis and neuronal loss in the caudal pontine reticular nucleus. *Brain, Behavior, and Immunity*, *61*, 353–364. https://doi.org/10.1016/j.bbi.2017.01.006

Smith, C. J., Johnson, B. N., Elkind, J. A., See, J. M., Xiong, G., & Cohen, A. S. (2012). Investigations on alterations of hippocampal circuit function following mild traumatic brain injury. *Journal of Visualized Experiments: JoVE*, *69*, e4411. https://doi.org/10.3791/4411

Smith, C. J., Xiong, G., Elkind, J. A., Putnam, B., & Cohen, A. S. (2015). Brain Injury Impairs Working Memory and Prefrontal Circuit Function. *Frontiers in Neurology*, *6*. https://doi.org/10.3389/fneur.2015.00240

Stellwagen, D., Beattie, E. C., Seo, J. Y., & Malenka, R. C. (2005). Differential Regulation of AMPA Receptor and GABA Receptor Trafficking by Tumor Necrosis Factor-α. *The Journal of Neuroscience*, *25*(12), 3219–3228. https://doi.org/10.1523/JNEUROSCI.4486-04.2005

Stellwagen, D., & Malenka, R. C. (2006). Synaptic scaling mediated by glial TNF-α. *Nature*, *440*(7087), 1054–1059. https://doi.org/10.1038/nature04671

Swanson, R. A., & Graham, S. H. (1994). Fluorocitrate and fluoroacetate effects on astrocyte metabolism in vitro. *Brain Research*, *664*(1–2), 94–100. https://doi.org/10.1016/0006-8993(94)91958-5

Szepesi, Z., Manouchehrian, O., Bachiller, S., & Deierborg, T. (2018). Bidirectional Microglia–Neuron Communication in Health and Disease. *Frontiers in Cellular Neuroscience*, *12*, 323. https://doi.org/10.3389/fncel.2018.00323

Takeda, K., & Akira, S. (2004). TLR signaling pathways. *Seminars in Immunology*, *16*(1), 3–9. https://doi.org/10.1016/j.smim.2003.10.003

Tashiro, A., Makino, H., & Gage, F. H. (2007). Experience-specific functional modification of the dentate gyrus through adult neurogenesis: A critical period during an immature stage. *The Journal of Neuroscience: The Official Journal of the Society for Neuroscience*, *27*(12), 3252–3259. https://doi.org/10.1523/JNEUROSCI.4941-06.2007

Temprana, S. G., Mongiat, L. A., Yang, S. M., Trinchero, M. F., Alvarez, D. D., Kropff, E., Giacomini, D., Beltramone, N., Lanuza, G. M., & Schinder, A. F. (2015). Delayed coupling to feedback inhibition during a critical period for the integration of adult-born granule cells. *Neuron*, *85*(1), 116–130. https://doi.org/10.1016/j.neuron.2014.11.023

Titus, D. J., Wilson, N. M., Freund, J. E., Carballosa, M. M., Sikah, K. E., Furones, C., Dietrich, W. D., Gurney, M. E., & Atkins, C. M. (2016). Chronic Cognitive Dysfunction after Traumatic Brain Injury Is Improved with a Phosphodiesterase 4B Inhibitor. *Journal of Neuroscience*, *36*(27), 7095–7108. https://doi.org/10.1523/JNEUROSCI.3212-15.2016

Tort, A. B. L., Komorowski, R., Kopell, N., & Eichenbaum, H. (2011). A mechanism for the formation of hippocampal neuronal firing patterns that represent what happens where. *Learning & Memory (Cold Spring Harbor, N.Y.)*, *18*(11), 718–727. https://doi.org/10.1101/lm.2307711

Toth, Z., Hollrigel, G. S., Gorcs, T., & Soltesz, I. (1997). Instantaneous Perturbation of Dentate Interneuronal Networks by a Pressure Wave-Transient Delivered to the Neocortex. *The Journal of Neuroscience*, *17*(21), 8106–8117. https://doi.org/10.1523/JNEUROSCI.17-21-08106.1997

Trotta, T., Porro, C., Calvello, R., & Panaro, M. A. (2014). Biological role of Toll-like receptor-4 in the brain. *Journal of Neuroimmunology*, *268*(1–2), 1–12. https://doi.org/10.1016/j.jneuroim.2014.01.014

Tsirka, V., Simos, P., Vakis, A., Vourkas, M., Arzoglou, V., Syrmos, N., Stavropoulos, S., & Micheloyannis, S. (2010). Material-specific difficulties in episodic memory tasks in mild traumatic brain injury. *The International Journal of Neuroscience*, *120*(3), 184–191. https://doi.org/10.3109/00207450903585308

Vaishnavi, S., Rao, V., & Fann, J. R. (2009). Neuropsychiatric problems after traumatic brain injury: Unraveling the silent epidemic. *Psychosomatics*, *50*(3), 198–205. https://doi.org/10.1176/appi.psy.50.3.198

Vallat-Azouvi, C., Weber, T., Legrand, L., & Azouvi, P. (2007). Working memory after severe traumatic brain injury. *Journal of the International Neuropsychological Society*, *13*(05). https://doi.org/10.1017/S1355617707070993

Van Dijk, M. T., & Fenton, A. A. (2018). On How the Dentate Gyrus Contributes to Memory Discrimination. *Neuron*, *98*(4), 832-845.e5. https://doi.org/10.1016/j.neuron.2018.04.018

Van Vliet, E. A., Aronica, E., Vezzani, A., & Ravizza, T. (2018). Review: Neuroinflammatory pathways as treatment targets and biomarker candidates in epilepsy: emerging evidence from preclinical and clinical studies. *Neuropathology and Applied Neurobiology*, *44*(1), 91–111. https://doi.org/10.1111/nan.12444

Vezzani, A., French, J., Bartfai, T., & Baram, T. Z. (2011). The role of inflammation in epilepsy. *Nature Reviews Neurology*, *7*(1), 31–40. https://doi.org/10.1038/nrneurol.2010.178

Villasana-Salazar, B., & Vezzani, A. (2023). Neuroinflammation microenvironment sharpens seizure circuit. *Neurobiology of Disease*, *178*, 106027. https://doi.org/10.1016/j.nbd.2023.106027

Wallach, D., Kovalenko, A., & Feldmann, M. (Eds.). (2011). *Advances in TNF Family Research: Proceedings of the 12th International TNF Conference, 2009* (Vol. 691). Springer New York. https://doi.org/10.1007/978-1-4419-6612-4

Wang, C., Xie, G., Zhou, C., Zhang, X., Li, T., Xu, J., Li, N., Ding, K., Hang, C., Shi, J., & Zhou, M. (2015). Baincalein alleviates early brain injury after experimental subarachnoid hemorrhage in rats: Possible involvement of TLR4/NF-κB-mediated inflammatory pathway. *Brain Research*, *1594*, 245–255. https://doi.org/10.1016/j.brainres.2014.10.014

Wang, Y.-C., Wang, P.-F., Fang, H., Chen, J., Xiong, X.-Y., & Yang, Q.-W. (2013). Toll-Like Receptor 4 Antagonist Attenuates Intracerebral Hemorrhage–Induced Brain Injury. *Stroke*, *44*(9), 2545–2552. https://doi.org/10.1161/STROKEAHA.113.001038

Witgen, B. M., Lifshitz, J., Smith, M. L., Schwarzbach, E., Liang, S.-L., Grady, M. S., & Cohen, A. S. (2005). Regional hippocampal alteration associated with cognitive deficit following experimental brain injury: A systems, network and cellular evaluation. *Neuroscience*, *133*(1), 1–15. https://doi.org/10.1016/j.neuroscience.2005.01.052

Wixted, J. T., Squire, L. R., Jang, Y., Papesh, M. H., Goldinger, S. D., Kuhn, J. R., Smith, K. A., Treiman, D. M., & Steinmetz, P. N. (2014). Sparse and distributed coding of episodic memory in neurons of the human hippocampus. *Proceedings of the National Academy of Sciences*, *111*(26), 9621–9626. https://doi.org/10.1073/pnas.1408365111

Yan, X. X., Tian, H. Q., Wang, C. L., Yang, B. Q., Wu, W. Z., & Zhang, F. R. (2015). Successful Treatment of Hailey-Hailey Disease with Aminolevulinic Acid Photodynamic Therapy. *Annals of Dermatology*, *27*(2), 222–223. https://doi.org/10.5021/ad.2015.27.2.222

Yang, L., Huh, J. R., & Choi, G. B. (2023). One messenger shared by two systems: How cytokines directly modulate neurons. *Current Opinion in Neurobiology*, *80*, 102708. https://doi.org/10.1016/j.conb.2023.102708

Yassa, M. A., & Stark, C. E. L. (2011). Pattern separation in the hippocampus. *Trends in Neurosciences*, *34*(10), 515–525. https://doi.org/10.1016/j.tins.2011.06.006

Ye, Y., Xu, H., Zhang, X., Li, Z., Jia, Y., He, X., & Huang, J. (2014). Association between Toll-Like Receptor 4 Expression and Neural Stem Cell Proliferation in the Hippocampus Following Traumatic Brain Injury in Mice. *International Journal of Molecular Sciences*, *15*(7), 12651–12664. https://doi.org/10.3390/ijms150712651

Yim, M. Y., Hanuschkin, A., & Wolfart, J. (2015). Intrinsic rescaling of granule cells restores pattern separation ability of a dentate gyrus network model during epileptic hyperexcitability. *Hippocampus*, *25*(3), 297–308. https://doi.org/10.1002/hipo.22373

You, J. C., Muralidharan, K., Park, J. W., Petrof, I., Pyfer, M. S., Corbett, B. F., LaFrancois, J. J., Zheng, Y., Zhang, X., Mohila, C. A., Yoshor, D., Rissman, R. A., Nestler, E. J., Scharfman, H. E., & Chin, J. (2017). Epigenetic suppression of hippocampal calbindin-D28k by ΔFosB drives seizure-related cognitive deficits. *Nature Medicine*, *23*(11), 1377–1383. https://doi.org/10.1038/nm.4413

Yu, T.-S., Zhang, G., Liebl, D. J., & Kernie, S. G. (2008). Traumatic brain injury-induced hippocampal neurogenesis requires activation of early nestin-expressing progenitors. *The Journal of Neuroscience: The Official Journal of the Society for Neuroscience*, *28*(48), 12901–12912. https://doi.org/10.1523/JNEUROSCI.4629-08.2008

Yu, W.-H., Dong, X.-Q., Hu, Y.-Y., Huang, M., & Zhang, Z.-Y. (2012). Ginkgolide B Reduces Neuronal Cell Apoptosis in the Traumatic Rat Brain: Possible Involvement of Toll-like Receptor 4 and Nuclear Factor Kappa B Pathway. *Phytotherapy Research*, *26*(12), 1838–1844. https://doi.org/10.1002/ptr.4662

Zhang, J., Yu, C., Zhang, X., Chen, H., Dong, J., Lu, W., Song, Z., & Zhou, W. (2018). Porphyromonas gingivalis lipopolysaccharide induces cognitive dysfunction, mediated by neuronal inflammation via activation of the TLR4 signaling pathway in C57BL/6 mice. *Journal of Neuroinflammation*, *15*(1), 37. https://doi.org/10.1186/s12974-017-1052-x

Zhang, Z., Zhang, Z.-Y., Wu, Y., & Schluesener, H. J. (2012). Immunolocalization of Toll-Like Receptors 2 and 4 as well as Their Endogenous Ligand, Heat Shock Protein 70, in Rat Traumatic Brain Injury. *Neuroimmunomodulation*, *19*(1), 10–19. https://doi.org/10.1159/000326771

Zhou, H., Lapointe, B. M., Clark, S. R., Zbytnuik, L., & Kubes, P. (2006). A Requirement for Microglial TLR4 in Leukocyte Recruitment into Brain in Response to Lipopolysaccharide. *The Journal of Immunology*, *177*(11), 8103–8110. https://doi.org/10.4049/jimmunol.177.11.8103

Zhu, H., Bian, C., Yuan, J., Chu, W., Xiang, X., Chen, F., Wang, C., Feng, H., & Lin, J. (2014). Curcumin attenuates acute inflammatory injury by inhibiting the TLR4/MyD88/NF-κB signaling pathway in experimental traumatic brain injury. *Journal of Neuroinflammation*, *11*(1), 59. https://doi.org/10.1186/1742-2094-11-59

Appendix A: From Plugging the Dam to Fueling the Firing: Platelets Breach the Barrier to Seize the Brain

Susan Nguyen and Viji Santhakumar

Epilepsy Currents Commentary. 2020 Aug 26;20(5):300-302.
doi: 10.1177/1535759720948117.

Abstract of Article for Commentary

Platelets Promote Epileptic Seizures by Modulating Brain Serotonin Level, Enhancing Neuronal Electric Activity, and Contributing to Neuroinflammation and Oxidative Stress

Kopeikina E, Dukhinova M, Yung AWY, Veremeyko T, Kuznetsova IS, Lau TYB, Levchuk K, Ponomarev ED. Prog Neurobiol. 2020;188:101783.
doi:10.1016/j.pneurobio.2020.101783.

The drugs currently available for treating epilepsy are only partially effective in managing this condition. Therefore, it is crucial to investigate new pathways that induce and promote epilepsy development. Previously, we found that platelets interact with neuronal glycolipids and actively secrete pro-inflammatory mediators during central nervous system (CNS) pathological conditions such as neuroinflammation and traumatic brain injury (TBI). These factors increase the permeability of the blood–brain barrier (BBB), which may create a predisposition to epileptic seizures. In this study, we demonstrated that

platelets substantially enhanced epileptic seizures in a mouse model of pentylenetetrazole (PTZ)-induced seizures. We found that platelets actively secreted serotonin, contributed to increased BBB permeability, and were present in the CNS parenchyma during epileptic seizures. Furthermore, platelets directly stimulated neuronal electric activity and induced the expression of specific genes related to early neuronal response, neuroinflammation, and oxidative phosphorylation, leading to oxidative stress in neurons. The intracranial injection of physiological numbers of platelets that mimicked TBI-associated bleeding was sufficient to induce severe seizures, which resembled conventional PTZ-induced epileptic activity. These findings highlight a conceptually new role of platelets in the development of epileptic seizures and indicate a potential new therapeutic approach targeting platelets to prevent and treat epilepsy.

Commentary

The blood–brain barrier (BBB), a unique barrier that limits the movement of ions, molecules, and cells between the blood and the brain, can be breached by brain insults such as trauma and during seizures. This is believed to contribute to epileptogenesis (Friedman and Heineman, 2012 , Swissa et al, 2019). Naturally, how the brain reacts to blood constituents during this unusual exposure is of considerable interest (Friedman and Heineman, 2012, Gorter et al, 2019, Gorter et al, 2015). There is a growing body of literature on how certain blood components including heme from red blood cells and serum albumin can contribute to development of epilepsy following brain insults (Willmore, 1990, Weissberg, 2015). Heme and albumin can contribute to epileptogenesis by triggering

secondary processes including activation of immune responses, altering glial function, and augmenting neuronal excitability (Willmore, 1990, Weissberg, 2015). Similarly, the role of vascular immune cells such as macrophages and T-cells in epileptogenesis has been investigated (Gorter et al, 2019). However, the role of platelets, the second most numerous cell type in the blood, has received little attention in the context of a compromised BBB and seizures. Platelets, small anucleate blood cells once considered mere cell fragments which aggregated to form platelet plugs for hemostasis, are now recognized to play roles in inflammation, angiogenesis, and tissue repair (Rivera et al, 2015). Platelets contain secretory granules with several bioactive molecules including neurotransmitters such as serotonin (5-HT), inflammatory molecules, platelet activating factor, and growth factors which they can release upon activation. Interestingly, platelets undergo degranulation and release transmitters in response to certain gangliosides enriched in lipid rafts in neuronal membranes which promotes synaptic plasticity after brain injury (Dukhinova et al, 2018). However, whether platelets play a traditional role by stopping BBB leaks, have non-canonical roles in inflammation and tissue repair, or augment neuropathology during seizures is not known. Kopeikina and colleagues (Kopeikina et al, 2020) bring to bear a diverse set of tools to directly addresses the multifaceted role of platelets in BBB permeability and network excitability during seizures.

The study leads off with the demonstration that mice depleted of serum platelets exhibit delayed and less severe acute seizures in response to pentylenetetrazole (PTZ) injection followed by a systematic investigation of the logical interpretation that platelets enter the brain during seizures and promote excitability. Contrary to expectations based on the

traditional role of platelets, mice depleted of serum platelets had lower BBB permeability following PTZ-induced seizures than mice with normal platelets, indicating that platelets augment BBB permeability during seizures. Unfortunately, although PTZ injection was associated with behavioral seizures, the authors defined any 10 sec period with over 20-30 high amplitude spiking events (HAS, events crossing a 20 μV threshold above baseline) as an electrographic seizure, regardless the evolution and termination of activity making it difficult to assess whether the "seizures" represented ictal activity. Nevertheless, immunostaining confirmed that platelets, normally restricted to the vasculature, were present in the brain parenchyma where they associated with neuronal lipid rafts following PTZ-induced seizures. Consistent with in vitro studies identifying that neuronal lipid rafts promote 5-HT release from platelets, PTZ-induced seizures increased 5-HT levels, measured using liquid chromatography and mass spectrometry, in brain tissue obtained within minutes after seizures. However, increase in 5-HT in response to PTZ-seizures was significantly blunted in platelet depleted mice. Moreover, both mice treated with a drug to deplete 5-HT and transgenic mice with deletions of a ganglioside enriched in neuronal lipid rafts showed reduced electrographic HAS events, suggesting that the interaction of platelets with lipid rafts and subsequent release of 5-HT are essential for platelet-mediated enhancement of excitability. Furthermore, they demonstrate that direct intracranial injection of either platelets, platelet rich plasma, or 5-HT could trigger HAS even in the absence of PTZ. The ability of platelets to directly increase network activity was further confirmed using multielectrode array recordings in acute brain slices. In control studies, HAS activity was absent following injection of platelet poor plasma and reduced in platelet

depleted mice, suggesting that while injected platelets are sufficient to induce neuronal hyperactivity, circulating platelets also reach the brain and contribute to network excitability. In an elegantly designed set of experiments, using adoptive transfer of platelets from unmanipulated or 5-HT depleted donor mice into unmanipulated or platelet depleted acceptor mice, they demonstrate that platelet-derived, and not brain-derived, 5-HT contributes to enhancement of PTZ-induced seizures. Although the study focused on the role of platelets on excitability, whole-transcriptome RNA sequencing analysis and subsequent validation in unmanipulated and platelet depleted mice revealed that exposure to platelets increases markers of activity, inflammation and oxidative stress which merit further analysis.

Overall, the study provides novel insights into the potential role for platelets in seizures. The data support a cascade of events by which platelets entering the brain through compromised BBB undergo degranulation and release 5-HT on contact with neuronal lipid rafts which further permeabilizes BBB and increases acute neural activity, setting up a vicious cycle of enhanced platelet entry and excitability. They further propose that the cascade of platelet activation and excitability contribute to changes in oxidative phosphorylation and release of inflammatory cytokines which could contribute to epileptogenesis. This curious cycle of platelet-derived 5-HT and neuronal activity has interesting parallels to itch-scratch cycle wherein scratching excites pain fibers leading to feedback release of 5HT on spinal neurons which further promotes the sensation of itch, while suppressing pain, resulting in vicious escalation of itch (Zhao et al, 2014). The demonstration that platelets, unlike albumin (Weissberg et al, 2015), promote acute

seizures is interesting and whether this could contribute to epileptogenesis needs careful consideration. Regrettably, the authors conflate chemically evoked acute increase in excitability with electrographic seizures and epileptogenesis. While their results indicate that platelets increase excitability and may be pro-convulsant the role of platelets in spontaneous recurrent seizures and epileptogenesis remain open questions. Moreover, the relation of HAS activity to seizures is tenuous as EEGs were recorded using cerebellar surface electrodes and were not correlated with behavioral seizures. Regardless, the results introduce platelets as a new player in the compromised BBB and raise questions about the long-term consequences of platelet-derived increases in 5-HT, inflammatory cytokines, and reactive oxygen species in epileptogenesis. The duration of platelet-mediated effects following a seizure and whether platelets lead to chronic changes in neuronal activity, synaptic plasticity and network reorganization will need further analysis in established models of epileptogenesis and by long term follow up of animals with intracerebral platelet injections. Moreover, the notion that platelets contribute solely to pathological changes may be simplistic, as the interaction between platelets and neuronal lipid rafts can aid vascular integrity following CNS injury (Dukhinova et al, 2018) and platelets have been proposed to support immune responses, angiogenesis, and tissue repair (Rivera et al, 2015). Thus, as with inflammatory responses, the location and timing of platelets in the brain may determine their role in repair versus epileptogenesis.

In summary, Kopeikina et al., (Kopeikina et al, 2020) demonstrate that the role of platelets in BBB compromise during injury and seizures can no longer be ignored. While the study focused on mechanisms and consequences of platelet derived 5-HT, the RNA sequencing

data identify a wide array of pathways from inflammation to oxidative stress which merit further studies. Further validation of the role of platelets in promoting seizures in models of epilepsy could reveal whether mechanisms identified here are viable targets to limit intractable status epilepticus.

References

Dukhinova, M., I. Kuznetsova, E. Kopeikina, E. Veniaminova, A.W.Y. Yung, T. Veremeyko, K. Levchuk, N.S. Barteneva, K.K. Wing-Ho, W.H. Yung, J.Y.H. Liu, J. Rudd, S.S.Y. Yau, D.C. Anthony, T. Strekalova, and E.D. Ponomarev, *Platelets mediate protective neuroinflammation and promote neuronal plasticity at the site of neuronal injury.* Brain Behav Immun, 2018. **74**: p. 7-27.

Friedman, A. and U. Heinemann, *Role of Blood-Brain Barrier Dysfunction in Epileptogenesis*, in *Jasper's Basic Mechanisms of the Epilepsies*, th, et al., Editors. 2012: Bethesda (MD).Willmore, L.J., *Post-traumatic epilepsy: cellular mechanisms and implications for treatment.* Epilepsia, 1990. **31 Suppl 3**: p. S67-S73.

Gorter, J.A., E. Aronica, and E.A. van Vliet, *The Roof is Leaking and a Storm is Raging: Repairing the Blood-Brain Barrier in the Fight Against Epilepsy.* Epilepsy Curr, 2019. **19**(3): p. 177-181.

Gorter, J.A., E.A. van Vliet, and E. Aronica, *Status epilepticus, blood-brain barrier disruption, inflammation, and epileptogenesis.* Epilepsy Behav, 2015. **49**: p. 13-6

Kopeikina, E., M. Dukhinova, A.W.Y. Yung, T. Veremeyko, I.S. Kuznetsova, T.Y.B. Lau, K. Levchuk, and E.D. Ponomarev, *Platelets promote epileptic seizures by modulating brain serotonin level, enhancing neuronal electric activity, and contributing to neuroinflammation and oxidative stress.* Prog Neurobiol, 2020. **188**: p. 101783.

Rivera, F.J., I. Kazanis, C. Ghevaert, and L. Aigner, *Beyond Clotting: A Role of Platelets in CNS Repair?* Front Cell Neurosci, 2015. **9**: p. 511.

Swissa, E., Y. Serlin, U. Vazana, O. Prager, and A. Friedman, *Blood-brain barrier dysfunction in status epileptics: Mechanisms and role in epileptogenesis.* Epilepsy Behav, 2019. **101**(Pt B): p. 106285.

Weissberg, I., L. Wood, L. Kamintsky, O. Vazquez, D.Z. Milikovsky, A. Alexander, H. Oppenheim, C. Ardizzone, A. Becker, F. Frigerio, A. Vezzani, M.S. Buckwalter, J.R. Huguenard, A. Friedman, and D. Kaufer, *Albumin induces excitatory synaptogenesis through astrocytic TGF-beta/ALK5 signaling in a model of acquired epilepsy following blood-brain barrier dysfunction.* Neurobiol Dis, 2015. **78**: p. 115-25.

Zhao, Z.Q., X.Y. Liu, J. Jeffry, W.K. Karunarathne, J.L. Li, A. Munanairi, X.Y. Zhou, H. Li, Y.G. Sun, L. Wan, Z.Y. Wu, S. Kim, F.Q. Huo, P. Mo, D.M. Barry, C.K. Zhang, J.Y. Kim, N. Gautam, K.J. Renner, Y.Q. Li, and Z.F. Chen, *Descending control of*

itch transmission by the serotonergic system via 5-HT1A-facilitated GRP-GRPR signaling. Neuron, 2014. **84**(4): p. 821-34.

Appendix B:

Reclusive chandeliers: Functional isolation of dentate axo-axonic cells after experimental status epilepticus

Archana Proddutur, **Susan Nguyen**, Chia-Wei Yeh, Akshay Gupta, Vijayalakshmi Santhakumar

Published in final edited form as:

Prog Neurobiol. 2023 Dec:231:102542.

DOI: 10.1016/j.pneurobio.2023.102542.

Abstract

Axo-axonic cells (AACs) provide specialized inhibition to the axon initial segment (AIS) of excitatory neurons and can regulate network output and synchrony. Although hippocampal dentate AACs are structurally altered in epilepsy, physiological analyses of dentate AACs are lacking. We demonstrate that parvalbumin neurons in the dentate molecular layer express PTHLH, an AAC marker, and exhibit morphology characteristic of AACs. Dentate AACs show high-frequency, non-adapting firing but lack persistent firing in the absence of input and have higher rheobase than basket cells suggesting that AACs can respond reliably to network activity. Early after pilocarpine-induced status epilepticus (SE), dentate AACs receive fewer spontaneous excitatory and inhibitory synaptic inputs and have significantly lower maximum firing frequency. Paired recordings and spatially localized optogenetic stimulation revealed that SE reduced the amplitude of unitary synaptic inputs from AACs to granule cells without altering reliability, short-term plasticity, or AIS GABA reversal potential. These changes compromised AAC-dependent shunting of granule cell firing in a multicompartmental model. These early post-SE changes in AAC physiology would limit their ability to receive and respond to input, undermining a critical brake on the dentate throughput during epileptogenesis.

Introduction

Axo-axonic cells (AACs) or Chandelier cells are an intriguing class of inhibitory neuronal subtype that uniquely target the axon-initial segment (AIS). Given the strategic location of the synapses at the primary site of action potential initiation in excitatory neurons and their expansive axon collaterals, there is considerable interest in understanding their role in shaping network activity and synchrony (Khirug et al., 2008, Klausberger et al., 2003, Varga et al., 2014). In the hippocampal dentate gyrus (DG), where potent inhibition to granule cells (GCs) plays an essential role in maintaining sparse firing, compromised inhibitory regulation has been proposed to contribute to the development of temporal lobe epilepsy (TLE) (Coulter and Carlson, 2007, Kobayashi and Buckmaster, 2003, Margerison and Corsellis, 1966, Zhang and Buckmaster, 2009). Consequently, several studies have examined whether AAC innervation of GCs is altered in epilepsy. Histopathological analyses of dentate tissue from human TLE patients in which AAC synapses were identified based on the characteristic synaptic cartridges have yielded variable results with reports of decrease, increase or differential patchy changes (Alhourani et al., 2020, Arellano et al., 2004, Wittner et al., 2001). However, dentate AACs remain an understudied population of inhibitory neurons and how their function is altered in epilepsy is not known. A major hurdle in studying AAC function has been the paucity of unique markers to identify this neuronal subtype. While AACs share the fast spiking and non-adapting firing characteristics with parvalbumin (PV) expressing basket cells (PV-BCs), and a majority of AACs express PV, AACs are a relatively sparse population compared to PV-BCs (Buhl et al., 1994, Elgueta et al., 2015, Soriano et al., 1990, Taniguchi et al., 2013). Studies based

on timed labeling of interneuron precursors have identified considerable neurochemical diversity among cortical AACs (Paul et al., 2017, Taniguchi et al., 2013). However, the strategies used to label cortical AACs do not identify hippocampal AACs, and alternative approaches show limited specificity for AACs (Ishino et al., 2017). Interestingly, majority of cortical AACs express the transcription factor parathyroid hormone like hormone (PTHLH) (Paul et al., 2017) suggesting it could be used to identify AACs in other circuits. AACs in distinct brain regions are known to differ in structure and physiology (Buhl et al., 1994, Ishino et al., 2017). Additionally, cortical, and hippocampal AACs show physiological differences, unique development and plasticity compared to PV-BCs (Pan-Vazquez et al., 2020, Rinetti-Vargas et al., 2017, Taniguchi et al., 2013). Yet, because physiological data on dentate AACs is limited and systematic comparison with PV-BCs is lacking, studies often combine fast-spiking PV interneurons during analysis. Histological data from the human epileptic DG have identified an increase in PV+ve basket-like axon terminals around GCs while PV+ve synapses at the AIS are decreased, suggesting that dentate BCs and AACs may respond differently to epileptogenesis (Alhourani et al., 2020). While there is considerable information on the intrinsic and synaptic physiology of PV-BC in the normal brain and in models of experimental epilepsy, whether AAC physiology is altered after status epilepticus is currently unknown (Bartos et al., 2001, Kobayashi and Buckmaster, 2003, Sambandan et al., 2010, Yu et al., 2013, Yu et al., 2016a). The diversity in physiology and seizure-induced plasticity of PV-BCs and AACs is particularly relevant due to the recent interest in activating PV neurons to curb ongoing seizure activity (Ellender et al., 2014, Krook-Magnuson et al., 2013, Ledri et al., 2014). Since most

transgenic strategies targeting PV neurons do not distinguish between subtypes, the net effect of such interventions would depend on how both AACs and BCs inhibit GCs.

The current study was conducted to examine whether functional properties of dentate AAC are altered early after experimental status epilepticus (SE). Based on colocalization with PTHLH and the presence of axonal cartridges, we identify that a majority of PV neurons in the dentate inner molecular layer (IML) are AACs and evaluate whether dentate AACs differ from PV-BCs in their intrinsic physiological characteristics. Using a combination of single and dual patch clamp, perforated patch recordings, patterned spatial-illumination to activate optogenetically labeled PV neurons in the IML, immunostaining, and computational modeling we examine whether AAC intrinsic physiology, basal synaptic inputs, and synaptic output to GCs are altered in mice one week after pilocarpine-induced SE.

Material and methods

Pilocarpine status epilepticus

All procedures were performed under protocols approved by the Rutgers NJMS, Newark, NJ and the University of California Riverside, Riverside, CA, Institutional Animal Care and Use Committees. Pilocarpine injection in mice was performed as reported previously (Zhang and Buckmaster, 2009). Young adult (6–10 weeks old), male and female C57BL/6 mice or transgenic mice with eYFP expression under PV promoter (Jackson Labs, B6;129P2-Pvalbtm1(cre)Arbr/J, 08069), were injected with scopolamine methyl nitrate (2 mg/kg, subcutaneous) 15 min before pilocarpine injection. Status epilepticus (SE) was

induced by injection of pilocarpine (300 mg/kg, i.p). After 1 h and 30 min of continuous stage 3 or greater seizures (Racine scale), diazepam (10 mg/kg, i.p.) was administered to terminate seizures. Age-matched control mice received scopolamine pre-treatment followed by saline injection (i.p) and diazepam after 2 h. Additionally, few naive male and female mice were used in a subset of experiments. All anatomical and physiological studies were conducted 7–14 days after pilocarpine-SE and in age-matched, saline-injected, and naive control mice.

Slice preparation

Mice 7–14 days after saline-injection or pilocarpine-SE and age-matched naive mice were anesthetized with isoflurane and decapitated. Horizontal brain slices (300 µm) were prepared in ice-cold sucrose artificial CSF (sucrose-aCSF) containing (in mM) 85 NaCl, 75 sucrose, 24 NaHCO3, 25 glucose, 4 MgCl2, 2.5 KCl, 1.25 NaH2PO4, and 0.5 CaCl2 using a Leica VT1200S Vibratome (Wetzlar, Germany). The slices were incubated at 32 ± 1 °C for 30 min in a submerged holding chamber containing 50% sucrose-aCSF and 50% recording aCSF and subsequently moved to room temperature (RT). The recording aCSF contained (in mM) 126 NaCl, 2.5 KCl, 2 CaCl2, 2 MgCl2, 1.25 NaH2PO4, 26 NaHCO3 and 10 D-glucose. All solutions were saturated with 95% O2 and 5% CO2 and maintained at a pH of 7.4 for 1–6 h.

In vitro electrophysiology

For patch clamp recordings, slices were transferred to a submerged recording chamber and perfused with oxygenated aCSF at 33 ± 1 °C. eYFP-positive cells were identified under epifluorescence, and whole-cell voltage- and current-clamp recordings were performed

using IR-DIC visualization techniques with a Nikon AR microscope, using a 40X water-immersion objective. Recordings were obtained using Axon Instruments MultiClamp 700B (Molecular Devices, Sunnyvale, CA). Data were low pass filtered at 2 kHz, digitized using DigiData 1440 A and acquired using pClamp10 at 10 kHz sampling frequency. Recordings were obtained using microelectrodes (3–5 MΩ) containing (in mM) 70 KCl, 70 K-gluconate, 10 HEPES, 2 MgCl2, 0.2 EGTA, 2 Na-ATP, 0.5 Na-GTP and 10 PO Creatine titrated to a pH 7.25 with KOH in the absence of synaptic blockers. Biocytin (0.2%) was included in the internal solution for post-hoc cell identification (Yu et al., 2013, Yu et al., 2016a). Recorded neurons were initially held at − 70 mV and the response to 1.5 s positive and negative current injections were examined to determine active and passive characteristics. Post-hoc biocytin immunostaining and morphological analysis were used to definitively identify AACs included in this study, based on the presence of axonal cartridges for all cells in Fig. 1. For data presented in Fig. 2, Fig. 3, Fig. 4, AACs were targeted as PV/YFP labeled neurons in the IML and confirmed based on post hoc morphological recovery of widespread dendritic arbors and presence of axonal cartridges in the granule cell layer (Supplementary Fig. 2). Following current-clamp recordings, cells were held in voltage-clamp at − 70 mV for analysis of GABA currents and sEPSCs were blocked by kynurenic acid 3 mM. In experiments where sEPSCs were recorded, saturating concentrations of the GABAAR antagonist SR95531 (10 μM) were included.

Paired recordings and optically evoked responses

Unitary inhibitory postsynaptic (uIPSC) responses were evoked in the dentate GCs (voltage clamped at −70 mV) by optically stimulating presynaptic ChR2 expressing cells using a

Digital Mirror Device (DMD)-based pattern illuminator (Mightex Polygon 400), coupled to 473 nm blue LED (AURA light source), and controlled via TTL based input from pClamp. A circular ROI of ~ 50 µm diameter was marked around 1–2 eYFP expressing putative AACs in the IML. In a subset of experiments, optical activation (5 ms) of putative AACs recorded in the IML reliably elicited single action potentials (not shown). Light power was fixed to elicit single uIPSCs in the recorded postsynaptic GC and recordings without postsynaptic responses were excluded from analysis. Alternatively, eYFP-expressing neurons in the IML were targeted using microelectrodes containing KCl-KGluc based internal solution. Selected ROIs were stimulated by a brief 5 ms single light pulse or train of 3 ms light pulses at 20 Hz and repeated for 10 recording sweeps with an inter sweep interval of 10s

Gramicidin perforated patch recording

Granule cells were recorded using Gramicidin-perforated patch to measure the equilibrium potential of GABA (EGABA) with intact intracellular chloride concentration. Patch electrodes were filled with KCl- K-gluconate-based internal solution with gramicidin (20 µg/mL, G5002, Merck KGaA), 5-CFDA, AM (40 µM, C1354, Invitrogen, Rinetti-Vargas et al., 2017), and Alexa Fluor™ 594 Hydrazide (1 µM, A10438, Invitrogen, Hsu et al., 2019). After 20–30 min in the cell-attach configuration, perforated patch was confirmed by an access resistance of 70–100 MΩ and the presence of 5-CFDA, AM but absence of Alexa Fluor™ 594 Hydrazide in the recorded soma. The AIS-mediated GABA currents were evoked by focal pressure ejection of GABAAR agonist muscimol (100 µM, 0289, TOCRIS) toward the AIS of recorded GCs via a glass pipette controlled by a Pneumatic

PicoPump (100 ms, PV 800, World Precision Instruments). The relation of evoked current amplitude and holding potential was plotted to determine EGABA for each cell.

Anatomical methods

To visualize PTHLH and PV spatial colocalization, we used RNAscope Multiplex Fluorescent In situ hybridization (m-FISH) on cryosectioned (50 μm) tissue from control and mice one-week post-SE. RNAscope Multiplex Fluorescent Reagent Kit v2 Assay was used following the protocol for fixed frozen tissue (Nguyen et al., 2020, Wang et al., 2012). The following kits and probes were used for this study: RNAscope® Multiplex Fluorescent Reagent Kit (Cat. #323100), RNAscope® Probe-Mm-Pthlh (Cat. #456521), and RNAscope® Probe- Mm-Pvalb-C2 (Cat No. 421931-C2). Slides were coverslipped using Vectashield mounting media (Vector Labs) and imaged using a Zeiss Axioscope and analyzed using Stereo Investigator (Microbrightfield).

Following physiological recordings, slices were fixed in 0.1 M phosphate buffer containing 4% paraformaldehyde at 4 °C for two days or fixed briefly for 30 min for staining with anti-βIV-spectrin. For post-hoc immunohistochemistry, thick slices (300 μm) were incubated overnight at room temperature with either of these following primary antibodies: anti-parvalbumin antibody (PV-28, 1.5:1000, polyclonal rabbit, Swant), anti-GFP antibody (AB 16901, 1:500, polyclonal chicken, Millipore) and anti-βIV-spectrin (AB2315816, 1:500, monoclonal mouse, NeuroMab) in 0.3% Triton X-100 and 3% normal goat serum containing PBS. Immunoreactions were revealed using Alexa 488-conjugated secondary goat antibodies against rabbit IgG (1:250), and biocytin staining was revealed using Alexa

594-conjugated streptavidin (1:1000). Sections were visualized and imaged using a Nikon A1R laser confocal microscope with a 1.2 NA 60X water objective.

Immunohistological studies were performed in mice one week after SE and in age-matched controls. Briefly, mice were anesthetized with isoflurane and sacrificed by decapitation, brains were rapidly removed and fixed by immersion fixation in 4% paraformaldehyde overnight at 4 °C. Sections were cut at 50 µm thickness on a Vibratome, and every sixth section was selected from the entire septotemporal extent of the hippocampus. Sections were processed for double immunofluorescence labeling for PV and eYFP. NeuN immunofluorescence was used to assess cell loss. Briefly, free-floating sections were rinsed in PBS, were blocked with 10% NGS and 0.3% Triton X-100 in PBS at RT for 1 h and then incubated in a solution containing monoclonal mouse anti-PV (1.5:1000; 235, Swant), polyclonal chicken anti-GFP (AB 16901, 1:500, Millipore) or mouse anti-NeuN (MAB377, 1:10,000, Millipore) in PBS with 0.3% Triton X-100 and 3% NGS at RT for 24 h. Sections were then rinsed in PBS and incubated at 4 °C for 24 h in a mixture of goat anti-mouse IgG conjugated to Alexa Fluor 594 (1:500) and goat anti-chicken IgG conjugated to Alexa Fluor 594 (1:500) to reveal PV and eYFP respectively. Similarly, goat anti-mouse IgG conjugated to Alexa Fluor 488 (1:500) was used to reveal NeuN. Sections were rinsed the next day in PBS and mounted with Vectashield (Vector Labs). Controls in which primary antibody was omitted were routinely included.

For a subset of experiments mice one week after SE and age-matched controls were transcardially perfused with cold PBS followed by cold 4% paraformaldehyde (PFA). Brains were incubated in 4% PFA overnight, switched to 30% sucrose for 2–3 days to

allow tissue to sink, and were flash frozen in OCT using liquid nitrogen and stored at − 80° C. Tissue was cryo-sectioned at 20 µm using a Leica Cryostat, mounted on SuperFrost slides, and stored at − 80° C prior to staining. Co-staining for perineuronal nets and PV was performed as described previously (Brewton et al., 2016). Tissue was washed with PBS, quenched with 50 mM NH4Cl for 15 min at RT, permeabilized with 0.1% Triton X-100 for 10 min and blocked with 5% NGS and 1% BSA. After blocking, tissue was incubated in primary antibody solution containing monoclonal mouse anti-PV (1:1000, #235, Swant) and FITC-conjugated Wisteria floribunda Agglutinin (WFA, 1:500, FL-135, Vector Laboratories) overnight at 4 ℃. Tissue was then washed and incubated in secondary antibodies (1:500, goat anti-mouse IgG conjugated to Alexa Fluor 647) for 1 h at RT, washed, and coverslipped with Vectashield with DAPI (Vector Labs). Slides were imaged using Zeiss 880 Upright Airyscan Microscope at 63x and images were analyzed using ImageJ by drawing an ROI with WFA staining around PV neurons in the IML and excluding the unstained region in the center. Since WFA staining was variable across sections, the integrity of perineuronal nets was quantified as the number of peaks in intensity over the average intensity in the ROI (Tewari et al., 2018). Data are presented normalized to the area of the ROI. For examination of AIS length and GABAA receptor α2 subunit staining, tissue was blocked with 10% NGS and 0.3% Triton X-100 at RT for 1 h then incubated in primary antibodies for AnkG (1:500, Cat#386–006, Synaptic Systems, Gao and Heldt, 2016) and GABAA α2 (1:1000, Cat#224–103, Synaptic Systems) in 5% NGS PBST overnight at 4 °C. Tissue was then washed and incubated in secondary antibodies for 1 h at RT, washed, and coverslipped with Vectashield with DAPI (Vector

Labs). Slides were imaged using Zeiss 880 Upright Airyscan super resolution at 63x and AIS length and puncta count was performed using QuPath 0.4.2 software (https://qupath.github.io). Neurolucida 360 was used to reconstruct AIS and GABAA α2 puncta for representative images.

Cell counts were performed using the Optical Fractionator probe of Stereo Investigator V.10.02 (MBF Bioscience) using an Olympus BX51 microscope and a 40X objective by an investigator blinded to treatment as previously described (Gupta et al., 2012). In each section, the hilus was outlined by a contour traced using a 10X objective. The following sampling parameters were set at 40X: counting frame, 100 µm X 100 µm; dissector height, 45 µm; and guard zone distance set at 5 µm. Approximately 25 sites per contour, selected using randomized systematic sampling protocols, were sampled. In each section, the cell count was estimated based on planimetric volume calculations in Stereo Investigator.

Nonstationary fluctuation analysis

Nonstationary variance analysis (Sigworth, 1980, Yu et al., 2016b) was performed on unitary postsynaptic current responses from GCs that were optically evoked using DMD-based stimulation at single cell resolution. Stable recordings were pooled from individual groups to isolate fluctuations in the current decay attributable to stochastic channel gating, the mean waveform was scaled to the peak of individual IPSCs (De Koninck and Mody, 1994, Traynelis et al., 1993). Successful responses were used to calculate the ensemble mean current (I) and peak-scaled variance (σPS2) for each data point. Plots of variance versus current were fit with the equation: $\sigma PS2 = iI - (I2/NP) + \sigma B2$, where i is the weighted-mean single-channel current, NP is the number of channels open at peak synaptic

current, and σB 2 is the background variance (Brickley et al., 1999). Only IPSCs that showed stable peak amplitude over time were included in the analysis.

Computational model

A multicompartmental granule cell model based on Santhakumar et al. (2005) was simulated using NEURON 7.8.2 (Hines and Carnevale, 1997) on a PC run with windows 10. A single granule cell (GC) multicompartmental model (Santhakumar et al., 2005, Yu et al., 2013) was modified to include an axon initial segment (AIS) of length (30 μm) and diameter (2 μm) connected to the somatic compartment. The AIS compartment was modeled to include sodium, fast and slow delayed rectifier potassium and leak channels which were correspondingly decreased in the somatic compartment (See Supplemental Table 1). Model GC included two AMPA and two GABA synapses on the middle dendritic and AIS segments, respectively, implemented using Exp2Syn mechanism. The rise, weighted tau decay, and reversal potential for excitatory AMPA synapses are 1.5 ms, 5.5 ms, and 0 mV respectively, while inhibitory GABA synapses were modelled with rise, decay, and reversal potential of 0.2 ms, 6–10 ms and, − 65 mV (constrained by experimental data). A single presynaptic stimulus from an artificial cell is used to drive two AMPA synapses located in the middle dendritic compartments of the model GC. Increasing peak excitatory conductance in the range of 10–30 nS at each AMPA synapse were simulated. Based on experimental estimates of AIS GABA synapse peak conductance obtained from non-stationary fluctuation analysis, increasing peak GABAergic conductances from 0.5 nS – 10 nS in each of the two AIS GABA synapses were evaluated. Results are reported as ‘1′ representing action potential and ‘0′ as shunted action potential.

Analysis and statistics

Analysis was performed by a researcher blinded to treatment groups, followed by unblinding to categorize treatment groups for statistical analysis. Synaptic currents were measured as described previously (Gupta et al., 2012, Yu et al., 2013, Yu et al., 2016a) using custom macros in IgorPro7.0 software (WaveMetrics, Lake Oswego, OR). Recordings were discontinued if series resistance increased by > 20%. Individual synaptic events were detected using the custom software in IgorPro7.0 (Gupta et al., 2012, Santhakumar et al., 2010). Events were visualized, and any "noise" that spuriously met trigger specifications was rejected. Cumulative probability plots of sIPSC and sEPSC parameters were constructed using IgorPro by pooling an equal number of sIPSCs and sEPSCs from each cell. Passive parameters such as input resistance and SAG ratio were analyzed from hyperpolarizing current steps (−200pA). Membrane time constant was estimated from a standard single exponential fit to voltage responses to a −200pA hyperpolarizing step using the Levenberg-Marquardt method in Clampfit. Cell capacitance was calculated as the ratio of membrane time constant and input resistance of cell. Active properties were estimated from the depolarizing current steps. The threshold for the action potential was determined by calculating the first time derivative (dV/dt) of the voltage trace and setting 30 mV/ms as the threshold for level for action potential initiation (Gupta et al., 2012). Rheobase was determined as the minimum current input needed for the cell to cross the threshold and fire an action potential. Data that were over two standard deviations from mean were excluded. Decay kinetics from uIPSC traces were calculated based on single exponential fit on the decay phase of mean uIPSC trace from peak to baseline. Statistical

analysis was performed by paired and unpaired Student's t-test (Microsoft Excel 2007), or Mann Whitney U-test for data that were not distributed normally or univariate and multivariate repeated measures ANOVA (Sigma Plot 12.3) for experiments involving repeated measurements from the same sample. Significance was set to $p < 0.05$. Data are shown as mean ± s.e.m or median and inter-quartile range (IQR) where appropriate.

Results

Preferential localization to the inner molecular layer and higher rheobase distinguishes dentate axo-axonic cells from basket cells

Since the DG circuit function is heavily regulated by inhibition, and AACs are ideally poised to control GC output, there has been considerable interest in evaluating dentate AAC plasticity in epileptic networks. Recent analyses of cortical AACs have revealed distinctive laminar distribution and connectivity, and identified transcriptional markers enriched in AACs (Paul et al., 2017). We utilized the expression of parathyroid hormone like hormone (PTHLH), a transcription factor shown to be selectively expressed in over 95% of cortical AACs (Paul et al., 2017), to identify the distribution of dentate AACs. Using RNAscope in-situ hybridization for PV and PTHLH, we identified PV and PTHLH colabeled somata in the dentate IML, granule cell layer (GCL) and hilus. Layer specific analysis revealed significantly fewer PV+ve interneurons (PV-INs) in the IML compared to the GCL/hilus (**Fig. B.1A-C**, cells/section, GCL/hilus: 7.5 ± 0.6; IML: 2.58 ± 0.16, 5–9 sections each/4 mice, $p = 0.0002$ by Student's t-test). PTHLH expressing neurons were present in the IML and the GCL/hilus with over 75% of the PTHLH+ve neurons colabeling

for PV. Notably, majority of the PV neurons in the IML colocalized PTHLH indicating that they are likely to be AACs, while fewer GCL/hilar PV-INs co-localized PTHLH (**Fig. B.1D**, % of PV-INs positive for PTHLH, IML: 87.9 ± 4.9, GCL/hilus: 29.8 ± 3.2, 5–9 sections each/4 mice, $p < 0.0001$ by Student's t-test). These data suggest that PV+ve neurons in the DG IML are likely to be AACs.

To determine whether IML PV neurons show the morphological features of AACs and evaluate whether dentate AACs are physiologically distinct from PV-BCs in the GCL/hilar border, we undertook whole cell recordings from labeled neurons in PV-reporter mice. Specificity of the PV-ChR2::YFP reporter was confirmed by expression of eYFP in ~80% of PV+ve neurons and colocalization of PV in all eYFP positive cells (Supplementary Fig. 1). PV-cre mice that were not crossed with reporter lines and cre-negative mice lacked eYFP expression (data not shown), validating the specificity of transgenic mice. eYFP positive neurons with somata in IML and GCL-hilar border were recorded under IR-DIC visualization, filled with biocytin, and processed for post hoc immunostaining to recover axonal arbors and distinguish AACs from basket cells. Consistent with the expression of PTHLH in AACs, PV+ve IML neurons in which axons were recovered consistently showed the presence of vertical axonal cartridges ($n = 10$ cells, Supplementary Fig. 2) with 5/5 cells tested showing close apposition of AAC axonal cartridges with the AIS labeled with βIV- spectrin (**Fig. B.1E** right panels). In contrast, axons of PV-INs in the GCL/hilar border showed perisomatic projections typical of basket cells and did not contact the AIS (**Fig. B.1F**). Morphologically identified AACs had multipolar somata in the IML and, typically, extended prominent apical dendrites reaching fissure and a few had basal

dendrites in the hilus suggesting that AACs could contribute to both feedforward and feedback GC inhibition. 3D confocal imaging revealed extensive dendritic arborization along the z-plane distinguishing the dendritic structure of AACs from semilunar granule cells in the IML (Afrasiabi et al., 2022, Gupta et al., 2020).

While prior studies have demonstrated that dentate AACs show the fast-spiking characteristic of PV-INs (Buhl et al., 1994, Elgueta et al., 2015), systematic comparison of dentate AACs and BCs intrinsic physiology is currently lacking. Both morphologically identified AACs in the IML, and BCs in the GCL/hilar border displayed the characteristic fast-spiking pattern with little adaptation (**Fig. B.1G**). AAC firing frequency in response to 200–240 pA depolarizing current injection (Iinj) was significantly lower than that of BCs (**Fig. B.1H**, AP frequency at Iinj 200pA in Hz: BCs: 15.0 ± 5.1, AACs: 0.8 ± 0.6 and Iinj 240pA, BCs: 23.1 ± 7.3, AACs: 7.0 ± 3.5; $n = 9$ AACs and $n = 10$ BCs, unpaired t-test: $p < 0.05$). However, AACs trended to fire at higher frequency than BCs with increasing Iinj and rarely showed depolarization block which was observed in BCs. Consequently, the overall firing frequency in response to increasing current injections was not different between cell types (two-way RM ANOVA). Dentate PV-INs have been shown to exhibit persistent firing in the absence of current input following depolarization (Elgueta et al., 2015). Interestingly, while BCs (5 / 10 cells) developed persistent baseline firing following the depolarizing current injections, none of the AACs ($n = 10$) exhibited persistent firing (**Fig. B.1G**). Comparison of passive membrane properties revealed no difference in resting membrane potential (RMP in mV, AAC: -70.12 ± 3.42; BCs: -68.58 ± 2.42, $n = 9$ each, unpaired t-test $p > 0.05$), input resistance (**Fig. B.1I**, Rin in MΩ, AACs: 86.1 ± 6.5; BCs:

117.4 ± 20.3, n = 10 each, unpaired t-test $p > 0.05$) and SAG ratio (AACs: 0.91 ± 0.01; BCs: 0.85 ± 0.03, n = 10 each, unpaired t-test $p > 0.05$) between AACs and BCs. However, the threshold for action potential firing in AACs was significantly more depolarized than in BCs (AP threshold in mV, AACs: −33.7 ± 1.0; BCs: −40.0 ± 2.7, n = 10 each, unpaired t-test $p < 0.05$) (**Fig. B.1J, K**). Consistently, rheobase, a measure of minimum current needed to evoke action potential, was higher in AACs compared to BCs (AACs: 271.1 ± 24.7 pA; BCs: 152.0 ± 27.8 pA, n = 9 & 10 respectively, unpaired t-test $p < 0.05$) (**Fig. B.1L**). These data demonstrate that PV+ve neurons in the dentate IML are predominantly AACs and share the high-frequency non-adapting firing characteristics with BCs, but, are distinguished by higher threshold to activation and greater reliability/fidelity during sustained activity.

AACs survive status epilepticus and are less excitable

Studies in human and experimental epilepsy have identified changes in the PV+ve axonal cartridges in the DG, raising the possibility that AACs are lost or structurally altered during epileptogenesis (Alhourani et al., 2020, Arellano et al., 2004, Ribak, 1985, Wittner et al., 2001). We implemented the pilocarpine-induced status epilepticus (Kobayashi and Buckmaster, 2003, Peng et al., 2004, Zhang and Buckmaster, 2009), to examine early changes in AACs during epileptogenesis. NeuN labeling for neuronal somata confirmed a significant decrease in hilar neurons one week after SE (Supplementary Fig. 3, neurons/section, Control: 154.6 ± 9.2 from 17 sections/3 mice; Post-SE: 109.3 ± 10.8 from 15 sections/ 3 mice, $p < 0.05$, unpaired t-test), consistent with earlier studies (Kobayashi and Buckmaster, 2003, Mello et al., 1992, Yu et al., 2013). While there was a trend towards

a decrease in PV expressing neurons in the hilus one week Post-SE (Supplementary Fig. 3, neurons/section, Control: 16.9 ± 2.2 in 11 sections/3 mice; Post-SE: 12.8 ± 1.6 in 17 sections/3 mice, $p > 0.05$, unpaired t-test), PV-IN counts in the IML were not altered after SE (Supplementary Fig. 3, neurons/section, Control: 6.7 ± 1.3 in 11 sections/ 3 mice; Post-SE: 10.2 ± 1.4 in 17 sections/3 mice, $p > 0.05$, unpaired t-test) indicating that the AACs in the IML survive SE.

We examined the intrinsic physiology of AACs in the IML from mice one to two weeks after status epilepticus (post-SE) and age-matched saline injected controls in the absence of synaptic blockers. AAC passive properties including resting membrane potential (RMP in mV, Control: -70.12 ± 3.42, $n = 9$; Post-SE: -70.22 ± 6.85, $n = 12$, unpaired t-test $p > 0.05$), input resistance (Rin in MΩ, Control: 86.1 ± 6.4, $n = 10$; post-SE: 81.3 ± 8.2, $n = 13$, unpaired t-test $p > 0.05$), membrane time constant (in ms, Control: 6.84 ± 0.52, $n = 10$; post-SE: 8.18 ± 0.63, $n = 12$, unpaired t-test $p > 0.05$) and sag ratio (Control: 0.91 ± 0.01, $n = 10$; post-SE: 0.87 ± 0.01, $n = 12$, unpaired t-test $p > 0.05$) were not altered after SE (**Fig. B.2A-F**). Additionally, slow AHP, calculated as the difference between baseline and the lowest anti-peak amplitude at the end of spike train in response to a 520pA current step was not different between groups (Control: -1.66 ± 0.67, $n = 10$; post-SE: -3.89 ± 0.54, $n = 12$, unpaired t-test, $p = 0.4$). However, AACs in post-SE mice showed a consistent reduction in firing rate during somatic current injection with a significant effect of treatment (**Fig. B.2G**, $F(1,19) = 5.16$, $p < 0.05$ by Two-way RM ANOVA) and significant interaction between treatment and Iinj ($F(1,19) = 6.73$, $p < 0.05$ by Two-way RM

ANOVA). AAC firing in response to Iinj > 500 pA was consistently reduced in post-SE mice (**Fig. B.2G**, Two-way RM ANOVA with Bonferroni corrected pairwise comparison). However, action potential threshold (**Fig. B.2H**, Control: -33.7 ± 1.0 mV, $n = 10$; post-SE: -32.9 ± 1.7 mV, $n = 12$, unpaired t-test $p > 0.05$) and rheobase (Control: 271.1 ± 24.7 pA, $n = 10$; post-SE: 333.3 ± 47.05 pA, $n = 12$, unpaired t-test $p > 0.05$) were not different between groups. Because post-SE AAC firing was reduced despite a lack of change in threshold or rheobase, and previous studies had identified that post-seizure changes in neuronal capacitance could impact excitability (Tewari et al., 2018, Whitebirch et al., 2022) we compared the membrane capacitance (Cm) between AACs in control and post-SE groups. AAC capacitance was significantly increased after SE (**Figure B.2I**, Cm in nF, Control: 71.2 ± 4.7, $n = 14$; post-SE: 97.3 ± 6.9, $n = 16$, unpaired t-test $p < 0.05$). Since seizure induced changes in extracellular matrix have been reported to alter Cm (Tewari et al., 2018), we examined integrity of the perineuronal net around PV neurons in the dentate IML by staining for Wisteria floribunda Agglutinin (WFA) which labels the perineuronal net. Consistent with an increase in AAC capacitance, there was a significant decrease in the number of WFA intensity peaks around IML PV neurons after SE (Supplementary Fig. 4). Overall, these data identify a post-SE reduction in the ability of AACs to sustain high firing frequency which contrasts with the lack of change in PV-BC intrinsic physiology after SE (Yu et al., 2013).

SE reduces synaptic inputs to AACs

Since SE leads to early changes in dentate neuronal networks (Kobayashi and Buckmaster, 2003, Peng et al., 2013, Yu et al., 2016a), we examined whether baseline synaptic inputs

to morphologically identified AACs were altered after SE. Spontaneous excitatory postsynaptic currents (sEPSCs) in AACs were recorded from a holding potential of − 60 mV in the presence the GABAARs antagonist gabazine (10 μM). Compared to age-matched controls, the frequency of sEPSCs in AACs was reduced after SE, although the effect size was modest (**Fig. B.3A, B**; Control: Median=12.1 Hz; IQR=5.6–21.3, n = 8; Post-SE: Median=6.8 Hz; IQR=2.5–23.8, n = 6 by Mann-Whitney U-test, Cohen's D: 0.37). However, there was a robust increase in sEPSC amplitude in AACs from post-SE mice, with a moderate effect size, (**Fig. B.3A, C**; Control: Median=19.4 pA; IQR=15.1–25.1, n = 8; Post-SE: Median=29.1 pA; IQR=21.1–39.2, n = 6 by Mann-Whitney U-test; Cohen's D: 0.89). The rise time and τDecay of AACs sEPSCs were not altered after SE (Supplementary Fig. 5A-B).

Next, we evaluated spontaneous inhibitory inputs to AACs held at − 70 mV in the presence of glutamate receptor antagonist kynurenic acid (3 mM). The frequency of spontaneous inhibitory postsynaptic currents (sIPSCs) in AACs was significantly lower after SE (**Fig. B.3D, E**; Control: Median=14.5 Hz; IQR=6.8–30.2, n = 7; Post-SE: Median=6.1 Hz; IQR=2.4–11.4, n = 8, $p < 0.05$ by Mann-Whitney U-test, Cohen's D: 0.75). Similarly, there was a post-SE reduction in sIPSC amplitude after SE (**Fig. B.3D, F**; Control: Median=27.2 pA; IQR=21.0–37.7, n = 7; Post-SE: Median=23.3 pA; IQR=15.4–35.0, n = 8, $p < 0.05$ by Mann-Whitney U-test, Cohen's D: 0.35). sIPSC rise time and τDecay were not different between AACs from control and post-SE mice (Supplementary Fig. 5E-F).

In a subset of paired recordings from AACs, we identified reciprocal electrical coupling between AACs (2 control and 1 post-SE AAC pair, Supplementary Fig. 6), although none

of the recorded pairs showed synaptic coupling. Given the sparse distribution of IML PV neurons, coupling characteristics of AACs were not compared between control and post-SE mice. Together, these data demonstrate a post-SE decrease in frequency of both excitatory and inhibitory synaptic inputs to AACs.

AAC output to granule cells is reduced after SE

To determine if AAC regulation of GCs is altered after SE we examined AAC driven synaptic inputs to GCs. Since our RNAScope and morphological studies identified that majority of the IML PV are AACs (**Fig. B.1**), we targeted IML PV neurons in PV-ChR2 reporter mice for discrete single-neuron optical stimulation and recorded AAC mediated responses in GCs. Given the relatively sparse distribution of IML PV neurons (2–3 cells/ section), DMD-based single neuron stimulation using a 50 μm ROI over the somata of isolated eYFP labeled IML neurons was used to activate individual AACs (see methods). Optically evoked AAC-mediated unitary IPSCs (uIPSCs) in GCs were recorded by selectively stimulating a single presynaptic AACs in the IML expressing eYFP-ChR2 using DMD coupled to blue LED (473 nm) illuminated for 5 ms single pulse for 10 sweeps for every 10 s (**Fig. B.4A, B**). Regions with more than one eYFP-ChR2 positive somata within 50 μm of each other in the IML and GCL were excluded. In order to minimize direct activation of PV terminals on postsynaptic GC, only GCs with somata > 150 μm lateral to the optically activate AAC somata were included in the analysis. Optical activation of AACs at 1–2 mW (in ROI) evoked uIPSCs in synaptically connected GCs (**Fig. B.4A**). In control experiments, blue light activation of eYFP-ChR2 expressing AACs consistently

elicited a single action potential (not shown). Additionally, blue light activation of somata lacking eYFP or amber light (589 nm) activation of eYFP +ve somata consistently failed to evoke responses in recorded GCs **(Fig. B.4A)**. In a subset of connected AAC to GC pairs, the presynaptic AAC was patched, held in current clamp, and activated by brief current pulses (0.8 nA) for 5 ms to evoke single action potentials (**Fig. B.4C**) to confirm both the presence of uIPSC in the synaptic coupled GC and cellular/axonal morphology of the AAC ($n = 3$ pairs). These extensive validation studies confirmed that we could reliably activate single ChR2 expressing AACs and record uIPSCs in GCs.

Since uIPSC parameters in response to optical and current clamp activation of AACs were similar, we pooled uIPSCs evoked by optical stimulation (17/20 pairs in control; 6/10 pairs post-SE) and current injections under whole cell configuration (3/20 pairs in control; 4/10 pairs in post-SE) for analysis. The average uIPSC peak amplitude in GCs in response to AAC activation, calculated by averaging 10 sweeps including failures, was significantly decreased after SE (**Fig. B.4B-D**, average uIPSC peak amplitude in pA, Control: 128.47 ± 21.95, $n = 20$; post-SE: 40.42 ± 7.15, $n = 9$; unpaired t-test $p < 0.05$). Similarly, the uIPSC amplitude potency, calculated by averaging the successful postsynaptic events excluding failures was also decreased after SE (Fig. 4E, uIPSC peak amplitude potency in pA, Control: 131.13 ± 21.66, $n = 20$; post-SE: 53.72 ± 17.06, $n = 9$; unpaired t-test $p < 0.05$). However, the decay kinetics and success rate of uIPSCs at the AAC to GC synapse was not altered in post-SE mice (**Fig. B.4F-G**, uIPSC decay in ms: Control: 7.13 ± 0.86; post-SE: 10.36 ± 1.73; unpaired t-test $p > 0.05$. Psuccess: Control: 0.95 ± 0.02, $n = 20$; post-SE: 0.83 ± 0.10, $n = 9$; unpaired t-test $p > 0.05$) indicating that the reduction

was likely due to a decrease in postsynaptic receptors. The connection probability between AAC and GC showed a trend towards a decrease which did not reach significance (**Fig. B.4H**, probability of synaptic connections in % - Control: 50%; 25/50 pairs; post-SE: 32.3%; 10 /31 pairs; $\chi 2$ (1, 81) = 2.45, $p = 0.12$ chi-square test with Yates correction). IPSCs evoked by AAC activation at 20 Hz showed robust short depression in both control and post-SE mice (**Fig. B.4I, J**) which is consistent with the high release probability of at AAC synapses and is similar to what has been reported in PV-BC synapses (Hefft and Jonas, 2005, Yu et al., 2016a, Zhang and Buckmaster, 2009). Despite the decrease in peak amplitude of AAC evoked uIPSC in GC after SE (amplitude in pA, **Fig. B.4I**, Control IPSC1: 230.16 ± 58.4, $n = 8$ pairs; Post SE IPSC1: 77.08 ± 27.2, $n = 6$ pairs, between treatment, Two way ANOVA $F(1130) = 36.8$, $p < 0.001$), the rate of synaptic depression elicited by a 20 Hz train was not different between groups (**Fig. B.4K**, ratio of amplitude of IPSC10 to IPSC1, ControlIPSC10/IPSC1: 0.31 ± 0.04, $n = 8$ pairs; Post SE IPSC10/IPSC1: 0.27 ± 0.04, $n = 6$ pairs, between treatment $p > 0.05$ by Two way RM ANOVA). Together, data demonstrate a significant weakening in potency of AAC to GC synapses and suggests that AAC mediated AIS inhibition is reduced early after SE.

AIS GABA reversal is depolarizing and unchanged after SE

Previous studies have identified that the reversal potential for GABA currents (EGABA) at AAC synapses on AIS of cortical pyramidal neurons show a delayed developmental switch to hyperpolarization relative to the resting membrane potential (Rinetti-Vargas et al., 2017). However, whether EGABA in the AIS of GCs, which rest at relatively hyperpolarized membrane potentials, is depolarizing has not been examined. Moreover,

whether EGABA at GC AIS is altered early after SE, as observed in the somato-dendritic compartments of GCs (Pathak et al., 2007), is currently unknown. We used gramicidin perforated-patch recordings to measure EGABA at GC AIS in brain slices from control and post-SE mice. Epifluorescence images were conducted during perforated patch recordings including both 5-CFDA, a dye permeable through the perforation, as well as Alexa 594 which is excluded from the perforated pore. As illustrated in **Figs. B.5A**, 5-CFDA (green) but not Alexa 594 (red) fluorescence was visualized in the somata upon establishment of the perforated patch. The appearance of Alexa 594 fluorescence marked the transition to whole cell configuration and was accompanied by a change in EGABA to 0 mV reflecting the high chloride internal solution (Supplementary Fig. 7). Muscimol (100 μM), a GABAAR agonist, was applied on to the GC AIS using a picospritzer to elicit GABA currents. Fig. B.5B illustrates the relative location of the recording electrode and the muscimol puff (stim) electrode. Note that the puff electrode targets the 5-CFDA labeled AIS (**Fig. B.5B3**) and elicited inward currents at the holding potential (Vhold) lower than − 70 mV (**Fig. B.5C**). GABA currents in response to muscimol application were recorded at various holding potentials and used to determine GABA reversal potential as the voltage at 0 current (**Fig. B.5C**, Supplementary Fig. 7 A). Recordings were discontinued when Alexa 594 was visualized in the soma or if there was a sudden drop in access resistance. Control experiments confirmed that muscimol and not mechanical pressure contributed to the inward currents and that muscimol-evoked currents were blocked by the GABAAR antagonist SR95531 (10 μM) (Supplementary Fig. 7B-C). In recordings from control and post-SE slices, GC AIS EGABA was significantly depolarized compared to the resting

membrane potential (**Fig. B.5C-D**, Ctrl: RMP = −88.39 ± 1.48 mV, EGABA = −65.59 ± 1.25 mV, n = 6 cells from 3 mice, $p < 0.0001$; Post-SE: RMP = −85.50 ± 1.20 mV, EGABA = −60.96 ± 2.77 mV, n = 8 cells from 4 mice $p < 0.0001$ by paired t-test). However, there was no difference in either AIS EGABA or resting membrane potential between GCs from control and post-SE mice (**Fig. B.5D**, MdnCtrl = −65.88 mV, MdnPilo = −61.82 mV, U = 15, $p = 0.2824$,). These data indicate that EGABA AAC to GC synapses are not altered after SE.

GABAA receptors at AAC synapses on to GCs are reduced after SE

The selective reduction in amplitude potency at AAC synapses on GCs without reduction in release probability suggests a decrease in postsynaptic GABAA receptors. Using peak-scaled nonstationary fluctuation analysis (Sigworth, 1980, Traynelis et al., 1993, Yu et al., 2016b), we evaluated the change in single channel current and receptor number at AAC to GC synapses. Although the peak amplitudes were much lower and less variable in synapses from post-SE mice, the characteristic parabolic distribution of mean-variance data was observed at AAC to GC synapses from both control and post-SE mice (**Fig. B.6A**). Single channel current estimates between synapses in control and post-SE mice were not different (**Fig. B.6B**, in pA, Control: 1.24 ± 0.36, n = 13; post-SE: 1.3 ± 0.27, n = 7, by Mann Whitney U-test $p > 0.05$), indicating that GABAA receptor conductance is unchanged following SE. However, the number of channels open at peak in the post-SE group was significantly reduced to approximately half that of controls (**Fig. B.6C**, Control: 110.97 ± 16.8, n = 13; post-SE: 51.56 ± 14.6, n = 7, by Mann Whitney U-test $p < 0.05$). These findings indicate a selective weakening of AAC synapses on GCs early after SE.

Inhibitory synapses on AIS express GABAA receptor α2 subunits (Fritschy et al., 1998). To test whether SE leads to a reduction in putative postsynaptic sites with GABAA receptor α2 subunits at the AIS, we undertook immunostaining for GABAA receptor α2 subunits and AIS using the AIS specific scaffolding protein Ankyrin G (Gao and Heldt, 2016, Jenkins and Bennett, 2001). While AIS length remained unchanged after SE (Supplementary Fig. 8A-C, in µm, Control: 40.75+4.22, n = 8 segments/5 mice; post-SE: 42.39+4.65, n = 12 segments/5 mice by unpaired t-test), the number of putative postsynaptic sites labeled for GABAA α2 subunits located in close apposition to the AIS was decreased (Supplementary Fig. 8D, Control: 14.50+2.33, n = 8 segments/5 mice; post-SE: 9.00+2.17, n = 12 segments/5 mice by unpaired t-test, $p < 0.05$). Correspondingly, the density of sites labeled for GABAA receptor α2 subunits found in close apposition to the AIS was also reduced (Supplementary Fig. 8E, Control: 0.356+0.0590, n = 8 segments/5 mice; post-SE: 0.212+0.0591, n = 12 segments/5 mice by unpaired t-test, $p < 0.05$).

Post-SE reduction in synaptic strength compromises AAC dependent shunting inhibition of GC firing

The reduction in the number of putative AIS synapses labeled for GABAA receptor α2 subunits density after SE, identified in our immunofluorescence, and reduction in receptor numbers in nonstationary fluctuation analysis, indicate compromised GABA conductance. Based on the experimental GABA reversal potential, the single channel conductance, and channel numbers estimated from nonstationary fluctuation analysis we calculated the peak GABA conductance at an AAC to GC synapse at the AIS to be approximately 4.8nS in controls and 1.48nS after SE. We performed simulations on a multicompartmental GC

model (Santhakumar et al., 2005, Yu et al., 2016a) and included an AIS compartment (Fig. 7A-B, also see methods) to examine the efficiency of GABA conductance in shunting synaptically driven GC action potential firing. Model GC was activated with increasing levels of peak excitatory AMPA conductance (low:14 nS – high:30 nS, Fig. 7C) at the two simulated medial perforant path inputs to the granule cell. The effect of increasing GABA conductance at each of the two simulated AAC to AIS synapses from 0.5 to 10 nS (with decay set at 7 ms based on uIPSC decay in controls), on GC firing was examined (**Fig. B.7D**). GABA conductance in the range observed in controls (4.5–5.5 nS) was effective in shunting action potential firing for a range of AMPA currents and were permissive to firing when the AMPA conductance was increased. In contrast, GABA conductance in the range observed in post-SE AIS synapses failed to suppress firing even in response to low levels of excitation. These findings demonstrate that the post-SE change in conductance compromises AAC-mediated shunting of GC firing (**Fig. B.7D, E**). Although the decay kinetics of uIPSCs was not different between groups (**Fig. B.4F**), decay time in synapses from post-SE GCs trended to be higher (about 10 ms). Since synaptic decay kinetics can have a significant impact on GABAergic inhibition, we performed additional simulations using the AMPA and GABA conductance parameter space above with GABA synaptic conductance set to 10 ms to better simulate the post-SE condition. Even with the slower decay, the GABA synapses constrained by the conductance values recorded in GC from post-SE mice were less efficacious at suppressing afferent driven GC firing than synapses with 7 ms decay and constrained by the conductance values observed in controls (comparing **Fig. B.7 D and F**). These simulation studies indicate that the post-SE reduction

in AAC synaptic strength could comprise overall AAC dependent inhibition at GC synapses.

Discussion

Combining colocalization of parvalbumin and PTHLH, a reliable marker for axo-axonic cells (Paul et al., 2017), and neuronal morphology, the current study identifies that PV neurons in the dentate IML are predominantly axo-axonic cells providing a viable approach to target this sparse neuronal population for physiological analysis. Despite sharing high-frequency, non-adapting firing characteristics and low input resistance with PV-BCs, AACs have a significantly higher rheobase for activation and a more depolarized action potential threshold. Although AACs need greater depolarization to reach threshold, their maximum firing rate trended to be higher than in PV-BCs. Unlike PV-BCs, AACs lacked persistent firing upon repolarization. Thus, the intrinsic physiology of dentate AACs is ideally suited to respond to strong sustained increases in network activity with high-fidelity firing. Our analysis revealed that the frequency of spontaneous excitatory and inhibitory synaptic currents was reduced after SE. Moreover, we identified a significant decrease in maximum firing frequency of AACs after SE which was associated with an increase in membrane capacitance. Simultaneously, although GABA reversal potential at AIS synapses, uIPSC reliability, and short-term plasticity of AACs to GCs synapses remained unchanged, the uIPSC amplitude was significantly decreased after SE. Non-stationary noise analysis was consistent with a decrease in GABAA receptors at AIS synapses. Additionally, there was an apparent reduction in the number of postsynaptic sites

immunolabeled for GABAAR α2 subunits at the GC AIS after SE. To our knowledge, our study is the first to evaluate functional changes in AAC in a model of experimental epilepsy and demonstrates a reduction in synaptic input, intrinsic firing, and synaptic output in dentate AACs after SE. Computational simulation of the effect of AIS synapses on synaptically evoked GC firing demonstrated a loss in the efficacy of shunting inhibition in models constrained by the post-SE AIS GABA conductance. Taken together, these changes indicate a diminished role of AACs in the dentate circuit early after status epilepticus. This functional uncoupling of AACs from the epileptogenic network and loss in inhibitory efficacy at the AIS could undermine an essential break to dentate throughput and contribute to epileptogenesis.

Localization and synaptic physiology of dentate AACs

Since the early studies characterizing their extensive and unique axonal targeting synapses (Buhl et al., 1994, Somogyi et al., 1982, Szentagothai and Arbib, 1974), there has been great interest in understanding AACs regulation of neuronal output, brain rhythms and their role in disease (Dudok et al., 2022, Gallo et al., 2020, Howard et al., 2005). Recognition that labeling a cohort of inhibitory neuron precursors expressing the homeobox protein Nkx2.1 at a late embryonic stage selectively labels cortical AACs (Taniguchi et al., 2013) spearheaded the neurochemical and physiological analysis of cortical AACs (Gallo et al., 2020, Ishino et al., 2017, Paul et al., 2017). Although the labeling strategies used to identify cortical AACs fail to label hippocampal AACs, single-cell sequencing of cortical AACs has yielded specific markers that have been leveraged to target AACs in the hippocampal CA1 (Dudok et al., 2021, Ishino et al., 2017, Paul et al., 2017). Here we show, for the first

time, that PTHLH also labels PV+ve AACs in the dentate IML. Consistent with earlier studies using Golgi staining (Soriano and Frotscher, 1989, Soriano et al., 1990), we show that the morphology of PV neurons in the dentate IML is consistent with AACs. The multipolar dendritic morphology with prominent apical dendrites and somatic location at the border of the GCL and molecular layer of AACs in our study is consistent with the structure and layered location pattern in cortical AACs (Taniguchi et al., 2013). Our finding also complements earlier studies which tracked the somata of cells extending axonal cartridges to GC AIS to PV+ve neurons in the dentate molecular layer in rat (Soriano et al., 1990). In keeping with the presence of morphologically identified AACs in the GCL and hilus (Elgueta et al., 2015, Overstreet and Westbrook, 2003), we report sparse PV and PTHLH labeled, presumed AACs in these regions. A subset of PTHLH-positive neurons failed to localize PV suggesting that, similar to the cortex (Paul et al., 2017), DG may have more than one neurochemical AAC subtype. These data indicate that IML PV-INs can be reliably targeted for functional analysis of dentate AACs.

Available physiological data from dentate AACs suggest that they share intrinsic membrane properties and fast-spiking characteristics with PV-BCs (Buhl et al., 1994, Overstreet and Westbrook, 2003). Our comparison identified that AACs need greater depolarization to reach threshold but show more reliable high-frequency firing during depolarization and lack the persistent discharges in the absence of depolarization observed in BCs (Elgueta et al., 2015). Indeed, despite sharing fast spiking characteristics, cortical BC and AACs have been found to differ in certain intrinsic properties (Taniguchi et al., 2013). Moreover, AACs also show regional differences in physiology, morphology, and

expression of neurochemical markers (Buhl et al., 1994, Ishino et al., 2017). Apart from similarities in intrinsic physiology, AAC synapses on GCs have high success rates and robust paired pulse and short-term depression (**Fig. B.4**), as seen in BC to GC synapses (Bartos et al., 2002, Overstreet and Westbrook, 2003, Yu et al., 2016a). Together these physiological features of dentate AACs and their extensive apical dendritic arbors, make them ideally suited to sense afferent excitability, respond reliably during high input activation, and inhibit action potential initiation by projection neurons, as has been reported in response to whisker stimulation in the barrel cortex (Zhu et al., 2004). Thus, AACs are in a privileged position to support the dentate inhibitory gate and limit dentate throughput during re-entrant seizure-like activity.

Seizure-induced changes in AAC intrinsic and synaptic physiology

Given the potential for AACs to clamp down action potential initiation (Schmidt-Hieber and Bischofberger, 2010) and the role for altered dentate inhibition during epileptogenesis, several studies have examined histopathological changes in dentate AAC to GC synapses. However, functional analysis of AACs in a model of epilepsy has been lacking (Dudok et al., 2022). Studies in human epileptic tissue have found that although PV-INs in the hilus are reduced, the PV-IN density in the dentate IML remains unchanged (Wittner et al., 2001). Despite the caveat that PV immunoreactivity can be altered in disease, our data showing maintenance of PV-INs in IML after pilocarpine-SE are consistent with the human epilepsy data (Wittner et al., 2001) and suggest that AACs largely survive SE induction. Several studies have reported loss of AAC terminals in human epileptic circuits with the most profound loss observed in the DG (Arellano et al., 2004, Ribak, 1985), while others

have reported an increase in PV synapse on the AIS (Wittner et al., 2001). A recent study using a combination of markers to identify AAC synapses found an increase in PV-BC synapses and a decrease in AAC synapses in the human epileptic dentate gyrus (Alhourani et al., 2020, Lillis, 2020), suggesting a selective reduction in AAC mediated inhibition in epilepsy. Our direct assessment of AAC physiology after experimental SE identified that, despite a lack of change in passive membrane properties, there is a striking reduction in the high frequency firing of AACs after SE. Further analysis identified a reduction in the integrity of perineuronal nets and a corresponding increase in AAC capacitance after SE which could contribute to the decrease in AAC firing. Indeed, previous studies have shown that seizure-induced degradation of the perineuronal net can increase PV neuron capacitance and reduce intrinsic excitability without changes in action potential threshold (Tewari et al., 2018). Since our recordings were conducted in the absence of synaptic blockers, it is possible that changes in feedback synaptic inhibition or tonic GABA currents could also contribute to the post-SE decrease in AAC firing. These findings in AACs are distinct from the lack of change in the intrinsic physiology of PV-BCs after SE (Yu et al., 2016a) and would directly undermine activity-dependent GABA release at the synapses. The post-SE reduction in the frequency of sEPSCs and sIPSCs that we report in AACs parallels what has been reported in PV-BCs (Yu et al., 2013, Yu et al., 2016a, Zhang and Buckmaster, 2009). The reduction in basal synaptic input to AACs likely reflects the loss of hilar mossy cells and interneurons after SE (Buckmaster et al., 2017, Buckmaster and Jongen-Relo, 1999, Obenaus et al., 1993, Zhang et al., 2009). Additionally, it is possible afferent inputs to AACs are also reduced which could limit the recruitment of AAC

mediated feedforward inhibition. While sIPSC amplitude showed a slight reduction, sEPSC amplitude was increased after SE suggesting potential compensatory regulation, as the average EPSC charge transfer over time was not different between control and post-SE groups (Supplementary Figure 5).

Our identification that AAC synapse on to GC show a profound decrease in unitary IPSC amplitude without a change in success rate after SE, differs from the increase in failures and amplitude of PV-BC synapses on GCs early after SE (Zhang and Buckmaster, 2009). Additionally, there was a trend towards a decrease in synaptic connectivity between AACs and GCs after SE which points to a further reduction in the ability of AACs to influence GC output. Thus, while the input received by PV-BCs and AACs is similarly decreased early after SE, AACs show a unique reduction in intrinsic firing and strength of synaptic output to GCs. Further evaluation of the GABAA receptor expression using nonstationary noise analysis identified that a decrease in GABAA receptors contributed to post-SE reduction in AAC synaptic strength. These changes, taken together, suggest functional uncoupling of AACs from the circuit which is likely to undermine their role in responding to heightened activity with robust synaptic inhibition of GCs.

Plasticity of AIS Synapses

An intriguing aspect of AACs mediated inhibition is the possibility that AAC synapses can be depolarizing long after somatic and dendritic inhibition undergoes the developmental switch to hyperpolarization (Pan-Vazquez et al., 2020, Rinetti-Vargas et al., 2017, Szabadics et al., 2006). While it has been speculated that GABA may be depolarizing at the AIS (Szabadics et al., 2006, Woodruff et al., 2009), GABA reversal in cortical neurons

has been shown to be hyperpolarizing at the age-range (>6 week postnatal) used in or study (Rinetti-Vargas et al., 2017). We find that while AIS GABA reversal (−60 mV) is more depolarized than the GC resting membrane potential (−80 mV), it is more negative than the action potentials threshold. Thus, AAC synapses would be expected to mediate shunting inhibition to GC (Schmidt-Hieber and Bischofberger, 2010). Indeed, we find that AIS synapses constrained by experimental conductance and depolarizing GABA reversal effectively shunt GC firing for a range of excitatory input drive. However, unlike GCs and PV-BCs which show a depolarizing shift in EGABA one week after pilocarpine SE (Pathak et al., 2007, Yu et al., 2013), both AIS GABA reversal and GC resting membrane potential remained unchanged after SE. The post-SE decrease in AAC synaptic strength may reflect a homeostatic compensation to limit the AIS depolarization. This possibility is supported by recent studies demonstrating that chemogenetic activation of AACs reduces IPSC amplitude at AIS synapses in immature cortex, when GABA is depolarizing, while it increases IPSC amplitude at AIS synapses in the mature cortex when GABA is hyperpolarizing (Pan-Vazquez et al., 2020). Structural changes in AIS length which can impact neuronal spike threshold (Harty et al., 2013, Liu et al., 2017, Wefelmeyer et al., 2015) were not observed in post-SE GCs. Immunostaining for GABAA receptor α2 subunits revealed potential reduction in colocalization with the AIS indicating a potential decrease in the number of AIS synapses. Since confocal imaging adopted here lacks the resolution to quantify receptor numbers, future studies using electron microscopy or super-resolution imaging could determine whether the number of receptors at AIS GABA

synapses are reduced after SE. These findings together with the results of non-stationary fluctuation analysis indicate weakening of the AAC to AIS synapse after SE.

Implications for epilepsy

Our findings demonstrate an early reduction in AAC excitability and its ability to inhibit GCs after SE. This reduction in inhibition at the site of action potential initiation is expected to compromise the strong inhibitory gating of the dentate gyrus which is critical for limiting dentate throughput and the spread of seizures (Carlson and Coulter, 2008, Dengler and Coulter, 2016, Krook-Magnuson et al., 2015, Krook-Magnuson et al., 2013). Additionally, activity sparsening mediated by dentate inhibition is also critical for pattern separation, a dentate dependent ability to discriminate patterns of neuronal activity representing overlapping behaviorally relevant information (Cayco-Gajic and Silver, 2019) which is compromised in epilepsy (Kahn et al., 2019, Madar et al., 2021). Moreover, hippocampal AACs have been found to contribute to maintaining location specific place cell firing indicating a role in memory processing (Dudok et al., 2021). Thus, the loss of AAC inhibition early after SE could contribute to both enhanced excitability and cognitive deficits associated with epilepsy. Interestingly, the advent of opto and chemogenetic approaches to manipulate specific neuronal populations has opened avenues for in vivo optical activation of parvalbumin neurons for seizure control (Krook-Magnuson et al., 2013, Paz et al., 2013). Since PV neurons include AIS targeting AACs, whether activating AACs which show differential plasticity in experimental epilepsy could paradoxically promote excitability needs to be considered. In this regard, the variable outcomes with optogenetic activation of PV neurons suppressing seizures in some studies (Ellender et al.,

2014, Krook-Magnuson et al., 2013) while exacerbating it in others may be explained by opposite circuit effects of BCs and AACs after SE. Selective opto/chemogenetic manipulation of dentate AACs, needed to directly evaluate the role of AACs epileptogenesis, are currently limited by the low specificity of approaches to label dentate AACs (Ishino et al., 2017). Here we overcome these limitations by using a combination of PV labeling and layer specific localization to target AACs for functional analysis in a model of experimental epilepsy. Our study provides the first systematic physiological assay of dentate AACs and demonstrates a reduction in AAC excitability, synapse potency and AIS inhibition after SE. This undermining of AIS inhibition early after SE could augment dentate excitability and contribute to epileptogenesis.

Funding

The project was supported by the National Institutes of Health (NIH/NINDS, Grant Numbers R01NS069861 & R01NS097750 to V.S.; F31NS120620 to S.N) and New Jersey Commission for Brain Injury Research (Grant Number: CBIR16IRG017 to VS).

Acknowledgements

We thank Dr. David Carter at the UCR Microscopy Core for help with imaging. We thank Ds. Khaleel A. Razak and Jamiela Kokash for help with reagents and protocols for PNN staining.

Figures

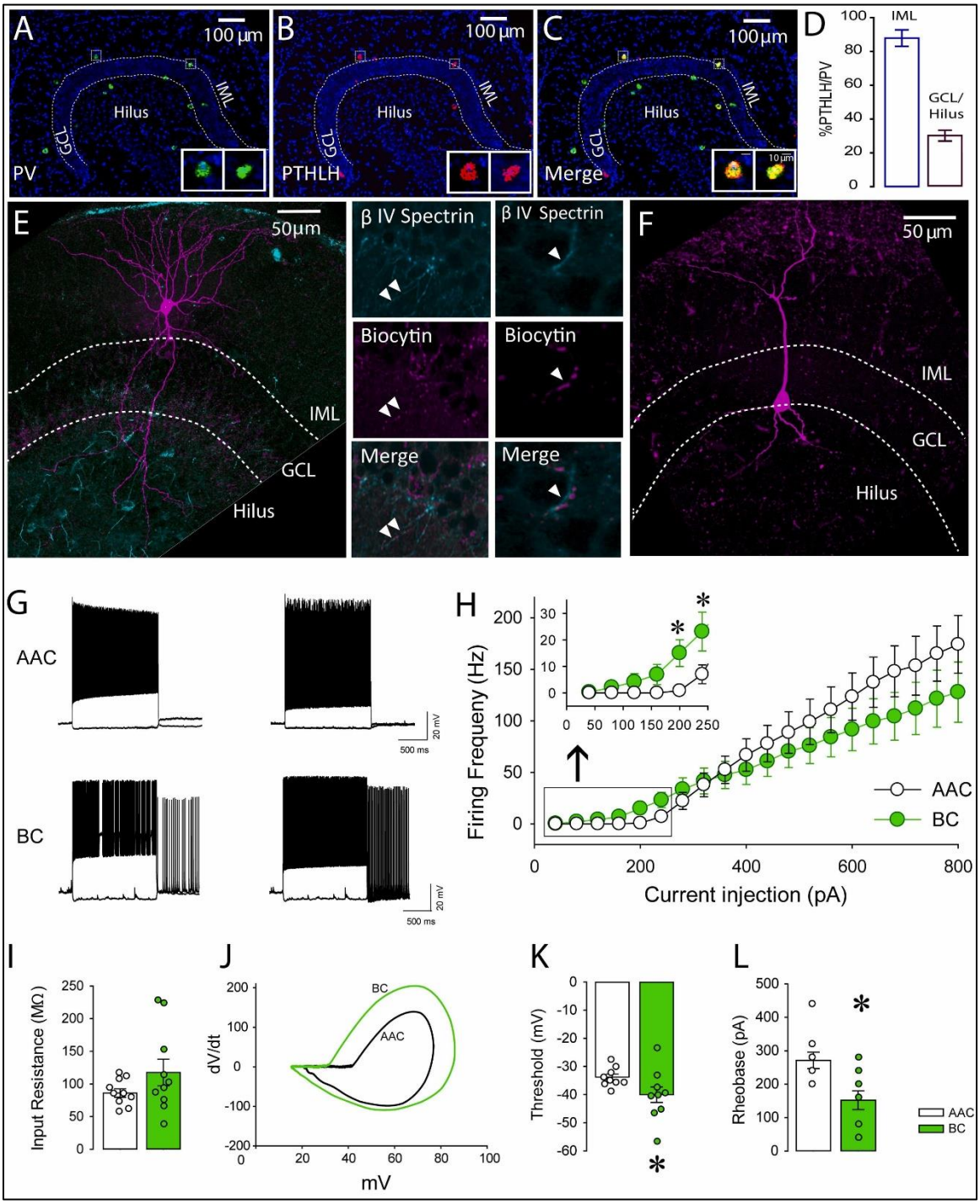
A
100 µm
Hilus
IML
GCL
PV
B
100 µm
Hilus
IML
GCL
PTHLH
C
100 µm
Hilus
IML
GCL
Merge
10 µm
D
%PTHLH/PV
IML
GCL/
Hilus
E
50µm
IML
GCL
Hilus
β IV Spectrin
β IV Spectrin
Biocytin
Biocytin
Merge
Merge
F
50 µm
IML
GCL
Hilus
G
AAC
BC
20 mV
500 ms
H
Firing Frequeny (Hz)
Current injection (pA)
AAC
BC
I
Input Resistance (MΩ)
J
dV/dt
mV
BC
AAC
K
Threshold (mV)
L
Rheobase (pA)
AAC
BC

Fig. B.1. Characterization of dentate parvalbumin-positive BCs and AACs. (A-C) Epifluorescence images of the dentate gyrus illustrate localization of probes for PV in green (A) PTHLH in red (B) and merged image showing co-labeling (C). Insets illustrate magnified images of PTHLH and PV co-labeled neurons in the inner molecular layer (IML). (D) Summary graph of percentage of PTHLH/PV positive neurons in IML vs. Hilus. (E-F) Maximum intensity projections of confocal image stacks of a representative AAC (E) BC (F). Images to the right of (E) illustrate two examples of axons from the cell in E showing close apposition for βIV-spectrin labeling for axon initial segments (top), and biocytin (middle) as shown in merge (bottom). Arrowheads indicate regions of close apposition between βIV-spectrin labeling on axon initial segment of GC and biocytin filled axonal cartridge of AAC. (G) Representative suprathreshold traces from two different AAC (top) and BC (bottom) neurons showing persistent firing in BCs but not in AACs. (H) The average firing frequency of BCs and AACs in response to increasing current injection shows differences in firing frequency at low amplitude current injections (inset). (I) Summary plots of input resistance in BC and AAC. (J-L). Example phase plots (J) and summary of action potential threshold (K) and, rheobase (L) in BCs and AACs. Scale: 100 μm. * indicates $p < 0.05$ by unpaired Student's t-test. Note: GCL – Granule Cell Layer, IML – Inner Molecular Layer. (**Candidate Data Panels A-D**)

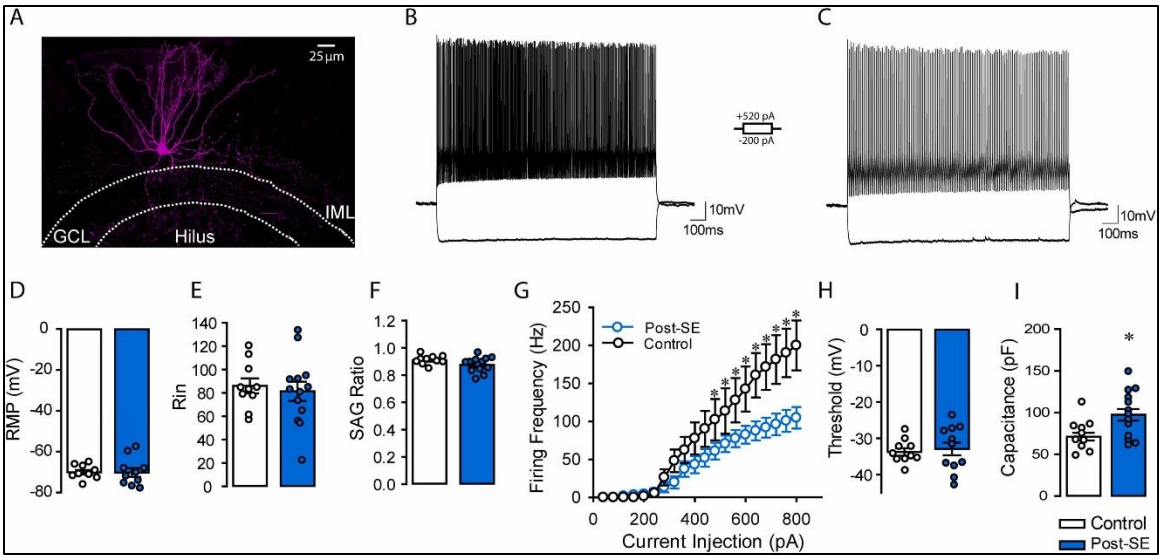

Fig. B.2. AAC excitability is compromised after status epilepticus. (A) Representative confocal image of AAC in the dentate IML region and spanning axonal cartridges. (B-C) Membrane voltage traces of axo-axonic cells from control (B) and post-SE mice (C) during a 520 pA and − 120 pA current steps. (D-F) Summary histograms of resting membrane potential (D), input resistance (E), and SAG ratio (F) from control and post-SE groups. (G) Overlay of the firing rates of control and post-SE AACs in response to increasing current injections. (H) Summary graph of threshold in AACs from control and post-SE mice. (I) Summary plot of AAC membrane capacitance * in panel I indicates $p < 0.05$ by unpaired Student's t-test and in panel G represents $p < 0.05$ by two-way repeated measure ANOVA. (**Data generated by co-authors**)

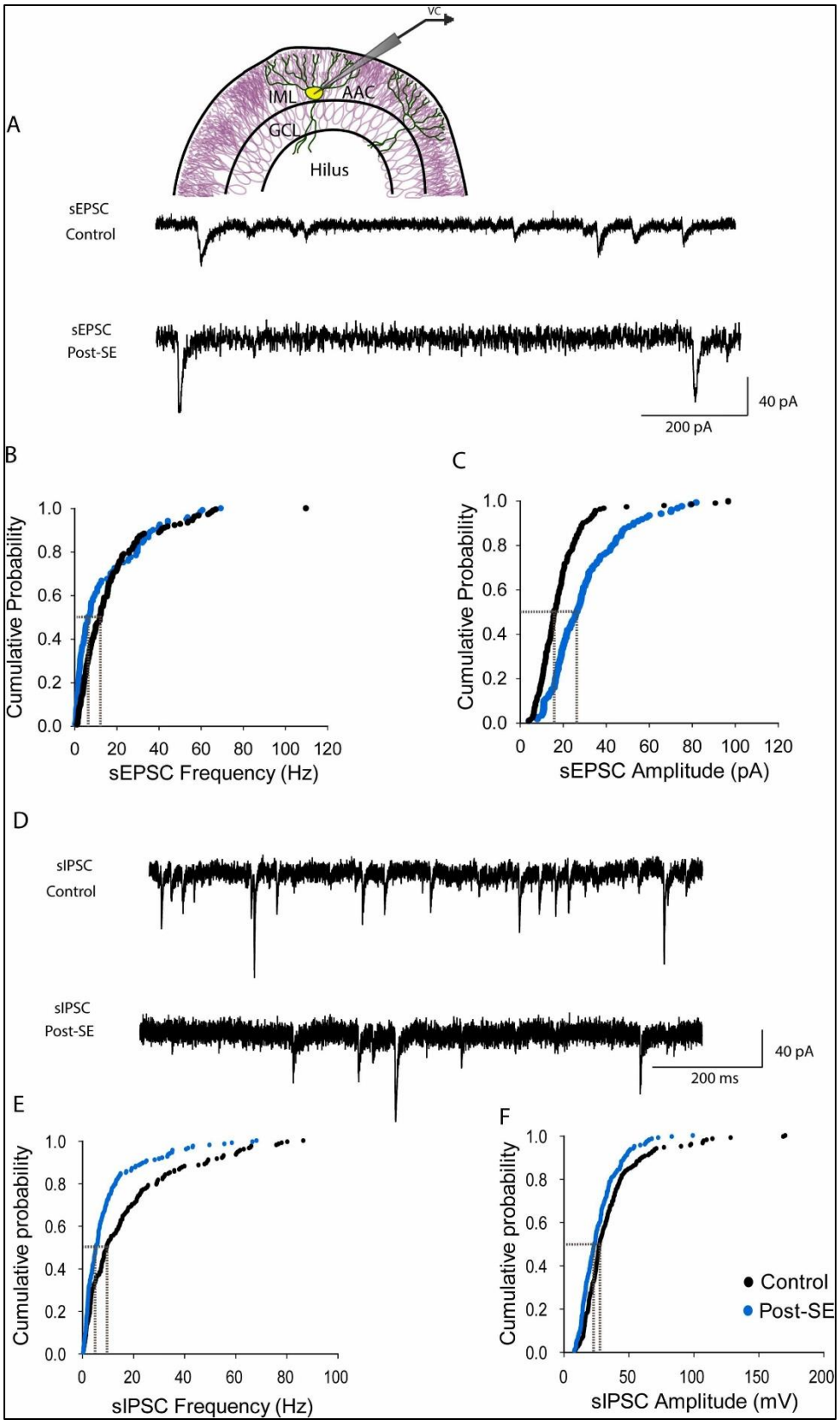
A
VC
IML
AAC
GCL
Hilus
sEPSC
Control
sEPSC
Post-SE
40 pA
200 pA
B
Cumulative Probability
sEPSC Frequency (Hz)
C
Cumulative Probability
sEPSC Amplitude (pA)
D
sIPSC
Control
sIPSC
Post-SE
40 pA
200 ms
E
Cumulative probability
sIPSC Frequency (Hz)
F
Cumulative probability
Control
Post-SE
sIPSC Amplitude (mV)

Fig. B.3. Status epilepticus alters synaptic drive to dentate AACs in the inner molecular layer. (A) Schematic of recording configuration illustrates targeting eYFP positive IML-AAC neurons (above) Representative current traces show spontaneous excitatory postsynaptic currents from AACs in control (top) and post-SE mice (bottom). (B-C) Cumulative probability plots of sEPSC frequency (B) and amplitude (C) recorded in gabazine (10 μM) (inset gray lines shows differences at 50% probability). (D) Example traces show spontaneous inhibitory postsynaptic currents in AACs from control (top) and post-SE (bottom) mice. (E-F) Cumulative probability plots of sIPSC frequency (E), and amplitude (F), recorded in kynurenic acid (3 mM) (inset gray dotted lines shows differences at 50% probability). * Indicates $p < 0.05$, by Mann-Whitney U Test, $n = 10$ cells each. (**Data generated by co-authors**)

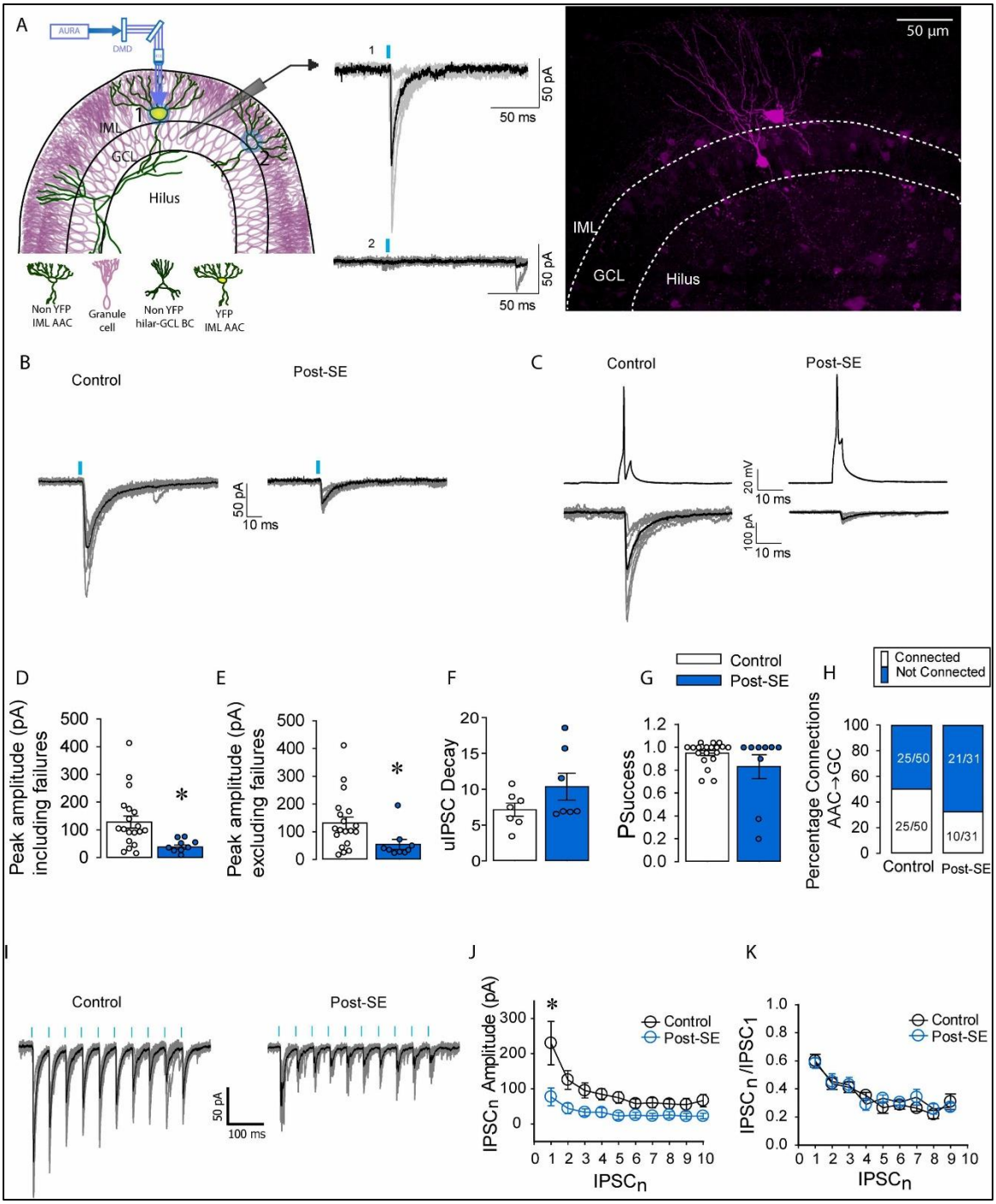
A
AURA
DMD
IML
GCL
Hilus
1
2
50 pA
50 ms
50 µm
Non YFP IML AAC
Granule cell
Non YFP hilar-GCL BC
YFP IML AAC
B
Control
Post-SE
50 pA
10 ms
C
Control
Post-SE
20 mV
10 ms
100 pA
10 ms
D
Peak amplitude (pA) including failures
E
Peak amplitude (pA) excluding failures
F
uIPSC Decay
G
Control
Post-SE
PSuccess
H
Connected
Not Connected
Percentage Connections AAC→GC
25/50
25/50
21/31
10/31
Control
Post-SE
I
Control
Post-SE
50 pA
100 ms
J
IPSCn Amplitude (pA)
Control
Post-SE
IPSCn
K
IPSCn /IPSC1
Control
Post-SE
IPSCn

Fig. B.4. Decreased synaptic strength at AAC-GC synapses early after SE. (A) Schematic of dentate gyrus slice on the left illustrating voltage-clamped granule cells, and typical eYFP+ AAC and eYFP- neuron in the IML region indicated by 1 and 2, respectively. Line diagram in blue shows light path routed through the DMD. Representative traces on the right indicated by 1 show control experiments where DMD stimulation of eYFP+ neuron evokes uIPSCs in coupled GC, whereas DMD stimulation of eYFP- neuron failed to elicit responses in GC indicated by 2. Example confocal image on the right shows biocytin-filled GC and AAC filled during paired recording. (B) Representative uIPSCs evoked (10 sweeps in gray) in synaptically coupled GCs by discharging single spikes in presynaptic AACs from control (left) and post-SE (right) mice. Average uIPSC traces are in black. Blue bar indicates light activation. (C) Postsynaptic responses in coupled GC in control (left) and post-SE (right) elicited by presynaptic action potentials (above) in AAC. (D-G) Summary histograms for AAC mediated uIPSC peak amplitude including failures (D), excluding failures (E), weighted decay (F) and probability of success (G). (H) Summary of percentage of synaptic connections from AAC to GC. (I) Representative traces illustrate multi-pulse depression of AAC evoked uIPSCs in GCs during optogenetic stimulation (blue bar) in control (left) and post-SE (right). The 10 individual sweeps are in gray, and the average trace is illustrated in black. (J-K) Summary plot of peak amplitude of uIPSCs elicited during the stimulus train (J) and amplitude ratio between uIPSCn and uIPSC1 (K). ***** Indicates $p < 0.05$ by Two-way ANOVA. Note: GCL – Granule Cell Layer, IML – Inner Molecular Layer. (**Data generated by co-authors**)

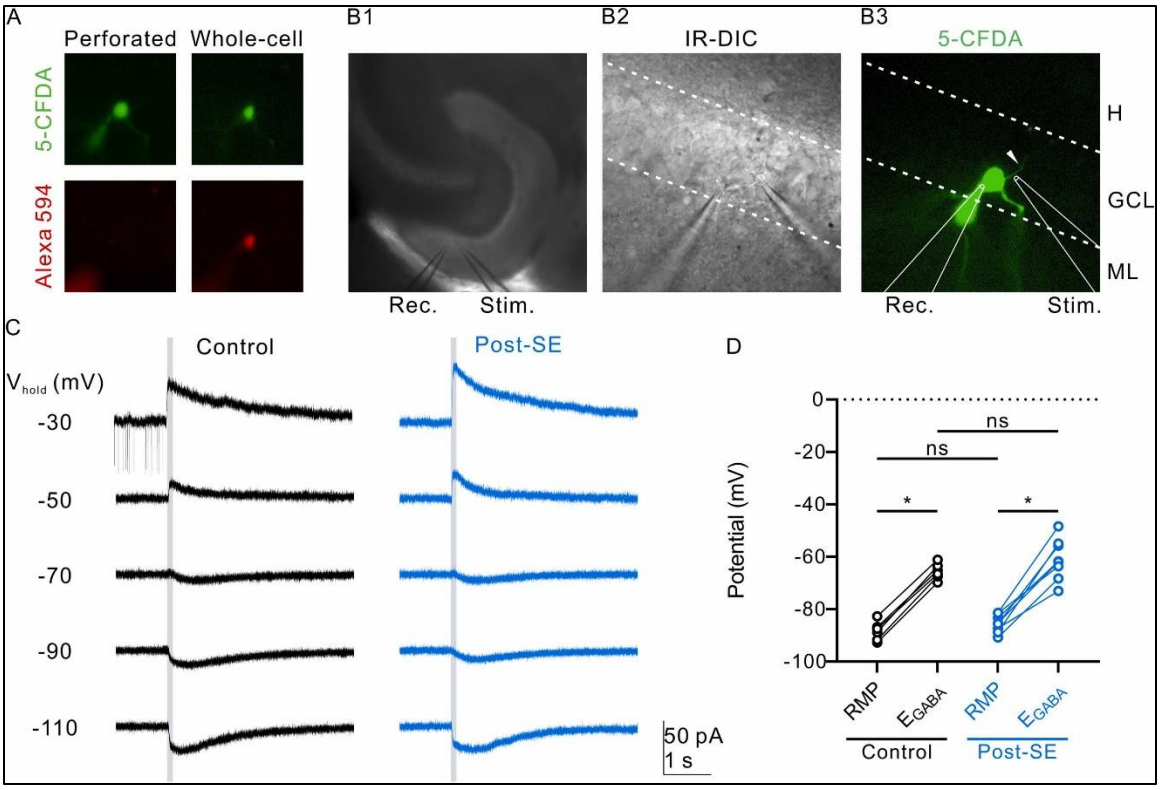

Fig. B.5. AIS-mediated GABA currents are depolarizing in both control and post-SE GCs. (A). Representative epifluorescence images obtained during gramicidin perforated-patch show confirmation of perforated patch mode by presence of 5-CFDA and absence of Alexa 594 signal in the recorded GC (on the left). Somatic Alexa 594 fluorescence on the right illustrates the rupture of perforated patch and entry into whole cell mode. (B) Low-magnification (B1), high-magnification IR-DIC (B2), and epifluorescence (B3) images illustrate placement of the stimulation pipette (Stim.) targeting the axon initial segment (AIS, arrowhead) and patch pipette (Rec.) at the GC somata. (C) Gramicidin-perforated patch recordings of muscimol-evoked GABA currents in the recorded GC during muscimol stimulation of AIS in control (left) and post-SE (right) mice. The holding potentials (V_{hold}) are indicated on the left. (D) Summary of the resting membrane potential (RMP) and equilibrium potential of GABA (E_{GABA}) in AIS in control and post-SE mice. *$p < 0.0001$, two-tail paired t-test. (**Data generated by co-authors**)

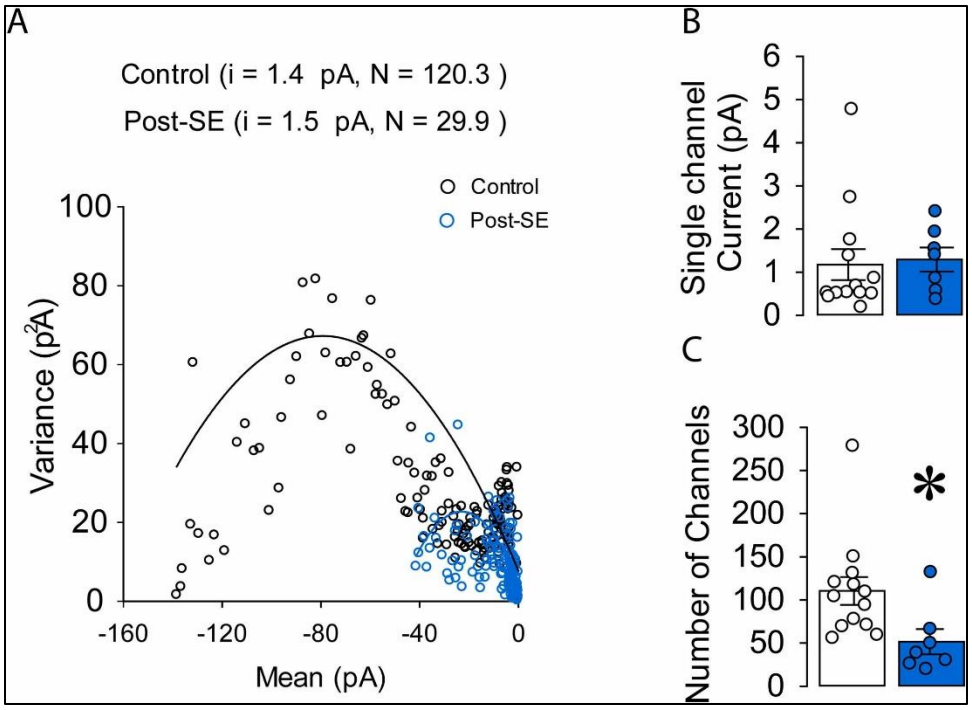

Fig. B.6. Decrease in postsynaptic $GABA_A$ receptors at AAC-GC synapses. (A) Summary mean-variance current plots from control (black) and post-SE (blue) obtained from uIPSCs at AAC-GC synapses. (B-C) Summary plots represent weighted-mean single-channel currents (B) and the number of channels open at the peak current (C) obtained from curves fitted with equation f(x) = ix –x2/N, where 'i′ is weighted-mean single-channel current, 'N′ is the number of channels open at the peak. (**Data generated by co-authors**)

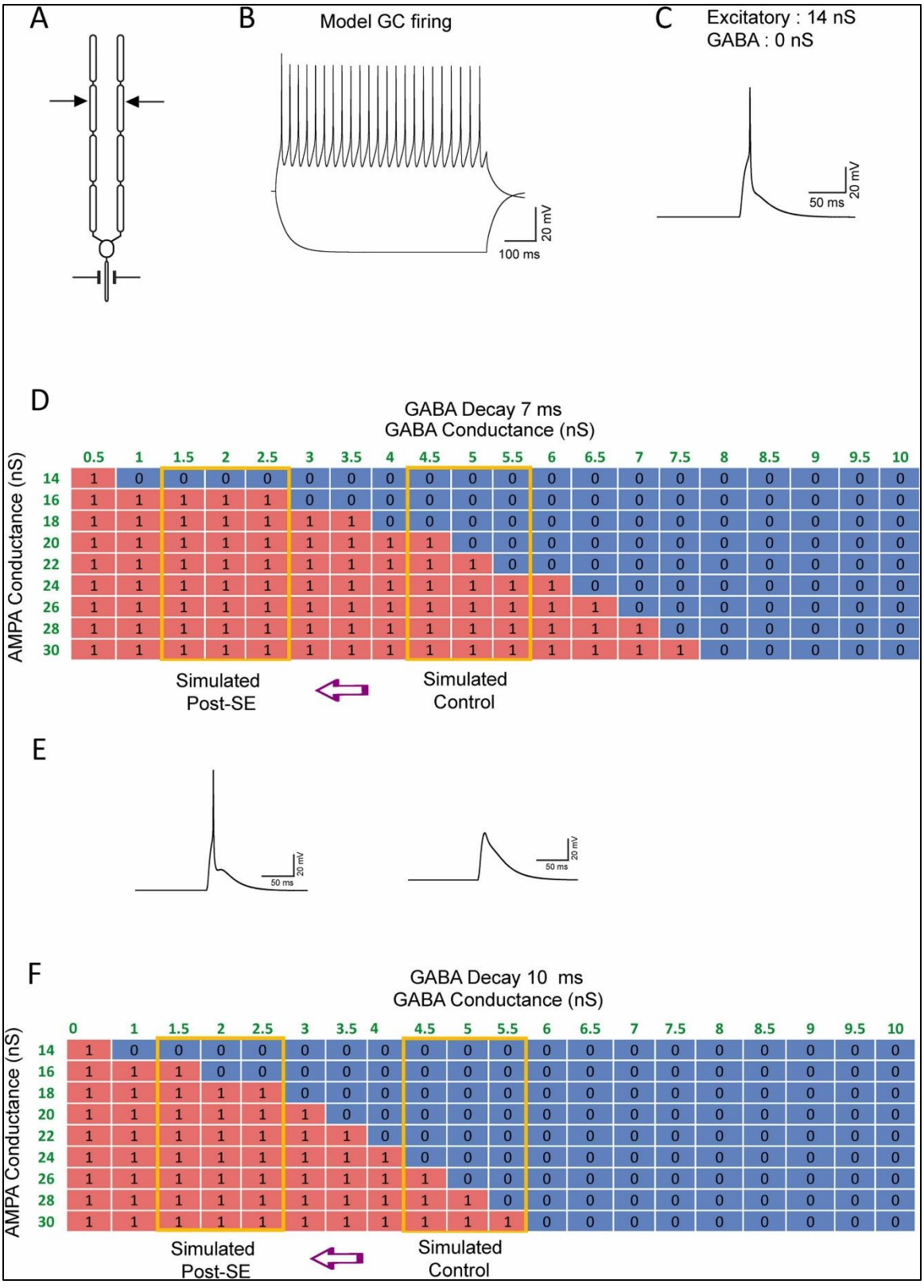
A
B
Model GC firing
20 mV
100 ms
C
Excitatory : 14 nS
GABA : 0 nS
20 mV
50 ms
D
GABA Decay 7 ms
GABA Conductance (nS)
AMPA Conductance (nS)
0.5 1 1.5 2 2.5 3 3.5 4 4.5 5 5.5 6 6.5 7 7.5 8 8.5 9 9.5 10
14 1 0 0 0 0 0 0 0 0 0 0 0 0 0 0 0 0 0 0 0
16 1 1 1 1 1 0 0 0 0 0 0 0 0 0 0 0 0 0 0 0
18 1 1 1 1 1 1 1 0 0 0 0 0 0 0 0 0 0 0 0 0
20 1 1 1 1 1 1 1 1 1 0 0 0 0 0 0 0 0 0 0 0
22 1 1 1 1 1 1 1 1 1 1 0 0 0 0 0 0 0 0 0 0
24 1 1 1 1 1 1 1 1 1 1 1 1 0 0 0 0 0 0 0 0
26 1 1 1 1 1 1 1 1 1 1 1 1 1 0 0 0 0 0 0 0
28 1 1 1 1 1 1 1 1 1 1 1 1 1 1 0 0 0 0 0 0
30 1 1 1 1 1 1 1 1 1 1 1 1 1 1 1 0 0 0 0 0
Simulated Post-SE
Simulated Control
E
20 mV
50 ms
20 mV
50 ms
F
GABA Decay 10 ms
GABA Conductance (nS)
AMPA Conductance (nS)
0 1 1.5 2 2.5 3 3.5 4 4.5 5 5.5 6 6.5 7 7.5 8 8.5 9 9.5 10
14 1 0 0 0 0 0 0 0 0 0 0 0 0 0 0 0 0 0 0 0
16 1 1 1 0 0 0 0 0 0 0 0 0 0 0 0 0 0 0 0 0
18 1 1 1 1 1 0 0 0 0 0 0 0 0 0 0 0 0 0 0 0
20 1 1 1 1 1 1 0 0 0 0 0 0 0 0 0 0 0 0 0 0
22 1 1 1 1 1 1 1 0 0 0 0 0 0 0 0 0 0 0 0 0
24 1 1 1 1 1 1 1 1 0 0 0 0 0 0 0 0 0 0 0 0
26 1 1 1 1 1 1 1 1 1 0 0 0 0 0 0 0 0 0 0 0
28 1 1 1 1 1 1 1 1 1 1 0 0 0 0 0 0 0 0 0 0
30 1 1 1 1 1 1 1 1 1 1 1 0 0 0 0 0 0 0 0 0
Simulated Post-SE
Simulated Control

Fig. B.7. Post-SE changes in GABA conductance compromises AAC dependent shunting inhibition at AIS synapses. (A) Schematic of multicompartmental model GC showing location of excitatory synapses in the middle molecular layer compartment of the two dendrites and inhibitory synapse location on AIS. (B) Characteristic voltage responses of model GC during + 300pA and − 200pA current steps. (C) Model GC firing in response activation of excitatory conductance in the MML and in the absence of inhibitory conductance at the AIS segment. (D) Summary heatmap with GABA decay set to control mean value of 7 ms, shows GC firing (1) in response to increasing AMPA and GABA conductances. The range representing estimated GABA conductance in control and post-SE GCs is boxed in yellow. 1 – Represents action potential (red) and 0 – represents shunting inhibition of firing (blue). (E) Representative action potential (left) and EPSP (right) illustrate the simulated membrane traces with firing indicated as 1 in heat map and lack of action potential denoted by 0 in the heat maps. (F) Summary heatmap with GABA decay set to 10 ms, the value observed in AAC to GC synapses in post-SE mice. GC response to increasing AMPA and GABA conductances are as in D. (**Data generated by co-authors**)

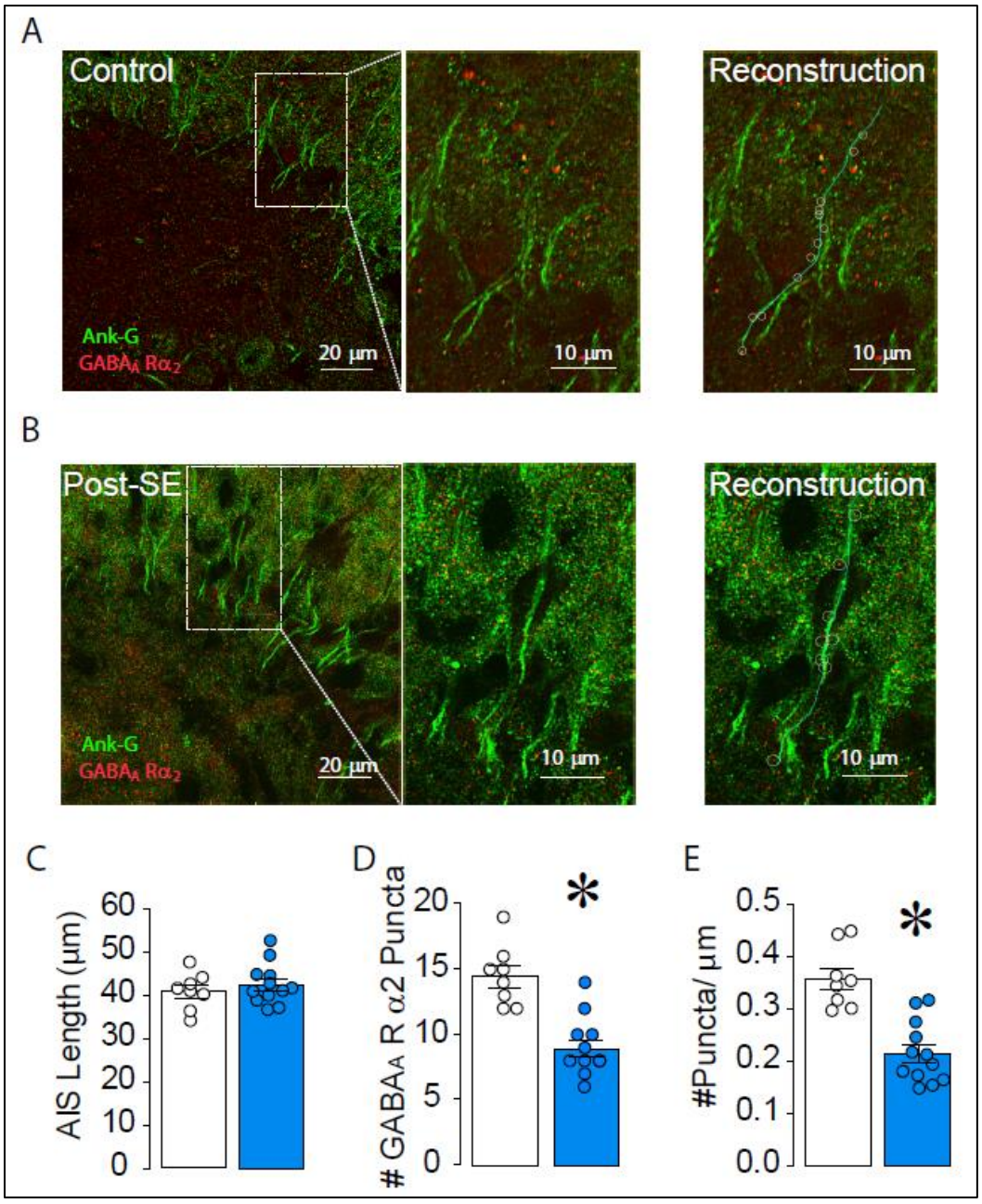

Supplementary Figure B.8. Immunohistological validation of GABAAA α2 receptor density at AIS segments in control and post-SE mice. (A-B) representative confocal images of sections immunolabeled for ankyrin-G to localize AIS (green) with GABAA α2 receptor (red) in control (A) and Post-SE (B) and magnified images are shown in the right panels respectively. The bottom panels show representative reconstructed AIS segments in cyan and the colocalized puncta counts are illustrated in white circular markers. (C-E) Summary plot of AIS length (C), number of GABAA α2 subunits (D) and density of GABAA α2 subunits (E). (**Data generated by candidate**)

References

Afrasiabi, M., Gupta, A., Xu, H., Swietek, B., Santhakumar, V., 2022. Differential Activity-Dependent Increase in Synaptic Inhibition and Parvalbumin Interneuron Recruitment in Dentate Granule Cells and Semilunar Granule Cells. *J Neurosci* 42**,** 1090-1103.

Alhourani, A., Fish, K.N., Wozny, T.A., Sudhakar, V., Hamilton, R.L., Richardson, R.M., 2020. GABA bouton subpopulations in the human dentate gyrus are differentially altered in mesial temporal lobe epilepsy. *J Neurophysiol* 123**,** 392-406.

Arellano, J.I., Munoz, A., Ballesteros-Yanez, I., Sola, R.G., DeFelipe, J., 2004. Histopathology and reorganization of chandelier cells in the human epileptic sclerotic hippocampus. *Brain* 127**,** 45-64.

Bartos, M., Vida, I., Frotscher, M., Geiger, J.R., Jonas, P., 2001. Rapid signaling at inhibitory synapses in a dentate gyrus interneuron network. *The Journal of neuroscience : the official journal of the Society for Neuroscience* 21**,** 2687-2698.

Bartos, M., Vida, I., Frotscher, M., Meyer, A., Monyer, H., Geiger, J.R., Jonas, P., 2002. Fast synaptic inhibition promotes synchronized gamma oscillations in hippocampal interneuron networks. *Proceedings of the National Academy of Sciences of the United States of America* 99**,** 13222-13227.

Brewton, D.H., Kokash, J., Jimenez, O., Pena, E.R., Razak, K.A., 2016. Age-Related Deterioration of Perineuronal Nets in the Primary Auditory Cortex of Mice. *Front Aging Neurosci* 8**,** 270.

Brickley, S.G., Cull-Candy, S.G., Farrant, M., 1999. Single-channel properties of synaptic and extrasynaptic GABAA receptors suggest differential targeting of receptor subtypes. *J Neurosci* 19**,** 2960-2973.

Buckmaster, P.S., Abrams, E., Wen, X., 2017. Seizure frequency correlates with loss of dentate gyrus GABAergic neurons in a mouse model of temporal lobe epilepsy. *J Comp Neurol* 525**,** 2592-2610.

Buckmaster, P.S., Jongen-Relo, A.L., 1999. Highly specific neuron loss preserves lateral inhibitory circuits in the dentate gyrus of kainate-induced epileptic rats. *J Neurosci* 19**,** 9519-9529.

Buhl, E.H., Han, Z.S., Lorinczi, Z., Stezhka, V.V., Karnup, S.V., Somogyi, P., 1994. Physiological-Properties of Anatomically Identified Axo-Axonic Cells in the Rat Hippocampus. *Journal of Neurophysiology* 71**,** 1289-1307.

Carlson, G.C., Coulter, D.A., 2008. In vitro functional imaging in brain slices using fast voltage-sensitive dye imaging combined with whole-cell patch recording. *Nat.Protoc.* 3**,** 249-255.

Cayco-Gajic, N.A., Silver, R.A., 2019. Re-evaluating Circuit Mechanisms Underlying Pattern Separation. *Neuron* 101**,** 584-602.

Coulter, D.A., Carlson, G.C., 2007. Functional regulation of the dentate gyrus by GABA-mediated inhibition. *Prog.Brain Res.* 163**,** 235-243.

De Koninck, Y., Mody, I., 1994. Noise analysis of miniature IPSCs in adult rat brain slices: properties and modulation of synaptic GABAA receptor channels. *J.Neurophysiol.* 71**,** 1318-1335.

Dengler, C.G., Coulter, D.A., 2016. Normal and epilepsy-associated pathologic function of the dentate gyrus. *Prog Brain Res* 226**,** 155-178.

Dudok, B., Klein, P.M., Soltesz, I., 2022. Toward Understanding the Diverse Roles of Perisomatic Interneurons in Epilepsy. *Epilepsy Curr* 22**,** 54-60.

Dudok, B., Szoboszlay, M., Paul, A., Klein, P.M., Liao, Z., Hwaun, E., Szabo, G.G., Geiller, T., Vancura, B., Wang, B.S., McKenzie, S., Homidan, J., Klaver, L.M.F., English, D.F., Huang, Z.J., Buzsaki, G., Losonczy, A., Soltesz, I., 2021. Recruitment and inhibitory action of hippocampal axo-axonic cells during behavior. *Neuron* 109**,** 3838-3850 e3838.

Elgueta, C., Kohler, J., Bartos, M., 2015. Persistent discharges in dentate gyrus perisoma-inhibiting interneurons require hyperpolarization-activated cyclic nucleotide-gated channel activation. *J Neurosci* 35**,** 4131-4139.

Ellender, T.J., Raimondo, J.V., Irkle, A., Lamsa, K.P., Akerman, C.J., 2014. Excitatory effects of parvalbumin-expressing interneurons maintain hippocampal epileptiform activity via synchronous afterdischarges. *J Neurosci* 34**,** 15208-15222.

Fritschy, J.M., Weinmann, O., Wenzel, A., Benke, D., 1998. Synapse-specific localization of NMDA and GABA(A) receptor subunits revealed by antigen-retrieval immunohistochemistry. *J Comp Neurol* 390**,** 194-210.

Gallo, N.B., Paul, A., Van Aelst, L., 2020. Shedding Light on Chandelier Cell Development, Connectivity, and Contribution to Neural Disorders. *Trends Neurosci* 43**,** 565-580.

Gao, Y., Heldt, S.A., 2016. Enrichment of GABAA Receptor alpha-Subunits on the Axonal Initial Segment Shows Regional Differences. *Front Cell Neurosci* 10**,** 39.

Gupta, A., Elgammal, F.S., Proddutur, A., Shah, S., Santhakumar, V., 2012. Decrease in tonic inhibition contributes to increase in dentate semilunar granule cell excitability after brain injury. *J Neurosci* 32**,** 2523-2537.

Gupta, A., Proddutur, A., Chang, Y.J., Raturi, V., Guevarra, J., Shah, Y., Elgammal, F.S., Santhakumar, V., 2020. Dendritic morphology and inhibitory regulation distinguish dentate semilunar granule cells from granule cells through distinct stages of postnatal development. *Brain structure & function* 225**,** 2841-2855.

Harty, R.C., Kim, T.H., Thomas, E.A., Cardamone, L., Jones, N.C., Petrou, S., Wimmer, V.C., 2013. Axon initial segment structural plasticity in animal models of genetic and acquired epilepsy. *Epilepsy Res* 105**,** 272-279.

Hefft, S., Jonas, P., 2005. Asynchronous GABA release generates long-lasting inhibition at a hippocampal interneuron-principal neuron synapse. *Nat.Neurosci.* 8**,** 1319-1328.

Hines, M.L., Carnevale, N.T., 1997. The NEURON simulation environment. *Neural Comput* 9**,** 1179-1209.

Howard, A., Tamas, G., Soltesz, I., 2005. Lighting the chandelier: new vistas for axo-axonic cells. *Trends Neurosci.* 28**,** 310-316.

Hsu, Y.T., Chang, Y.G., Liu, Y.C., Wang, K.Y., Chen, H.M., Lee, D.J., Yang, S.S., Tsai, C.H., Lien, C.C., Chern, Y., 2019. Enhanced Na(+) -K(+) -2Cl(-) cotransporter 1 underlies motor dysfunction in huntington's disease. *Mov Disord* 34**,** 845-857.

Ishino, Y., Yetman, M.J., Sossi, S.M., Steinecke, A., Hayano, Y., Taniguchi, H., 2017. Regional Cellular Environment Shapes Phenotypic Variations of Hippocampal and Neocortical Chandelier Cells. *J Neurosci* 37**,** 9901-9916.

Jenkins, S.M., Bennett, V., 2001. Ankyrin-G coordinates assembly of the spectrin-based membrane skeleton, voltage-gated sodium channels, and L1 CAMs at Purkinje neuron initial segments. *J Cell Biol* 155**,** 739-746.

Kahn, J.B., Port, R.G., Yue, C., Takano, H., Coulter, D.A., 2019. Circuit-based interventions in the dentate gyrus rescue epilepsy-associated cognitive dysfunction. *Brain* 142**,** 2705-2721.

Khirug, S., Yamada, J., Afzalov, R., Voipio, J., Khiroug, L., Kaila, K., 2008. GABAergic depolarization of the axon initial segment in cortical principal neurons is caused by the Na-K-2Cl cotransporter NKCC1. *J Neurosci* 28**,** 4635-4639.

Klausberger, T., Magill, P.J., Marton, L.F., Roberts, J.D., Cobden, P.M., Buzsaki, G., Somogyi, P., 2003. Brain-state- and cell-type-specific firing of hippocampal interneurons in vivo. *Nature* 421**,** 844-848.

Kobayashi, M., Buckmaster, P.S., 2003. Reduced inhibition of dentate granule cells in a model of temporal lobe epilepsy. *J Neurosci* 23**,** 2440-2452.

Krook-Magnuson, E., Armstrong, C., Bui, A., Lew, S., Oijala, M., Soltesz, I., 2015. In vivo evaluation of the dentate gate theory in epilepsy. *J Physiol* 593**,** 2379-2388.

Krook-Magnuson, E., Armstrong, C., Oijala, M., Soltesz, I., 2013. On-demand optogenetic control of spontaneous seizures in temporal lobe epilepsy. *Nat Commun* 4**,** 1376.

Ledri, M., Madsen, M.G., Nikitidou, L., Kirik, D., Kokaia, M., 2014. Global optogenetic activation of inhibitory interneurons during epileptiform activity. *J Neurosci* 34**,** 3364-3377.

Lillis, K.P., 2020. A Tisket a Tasket: Chandelier not equal Basket (Cell Bouton Density in Sclerotic DG). *Epilepsy Curr* 20**,** 218-220.

Liu, T.T., Feng, L., Liu, H.F., Shu, Y., Xiao, B., 2017. Altered axon initial segment in hippocampal newborn neurons, associated with recurrence of temporal lobe epilepsy in rats. *Molecular medicine reports* 16**,** 3169-3178.

Madar, A.D., Pfammatter, J.A., Bordenave, J., Plumley, E.I., Ravi, S., Cowie, M., Wallace, E.P., Hermann, B.P., Maganti, R.K., Jones, M.V., 2021. Deficits in Behavioral and Neuronal Pattern Separation in Temporal Lobe Epilepsy. *J Neurosci* 41**,** 9669-9686.

Margerison, J.H., Corsellis, J.A., 1966. Epilepsy and the temporal lobes. A clinical, electroencephalographic and neuropathological study of the brain in epilepsy, with particular reference to the temporal lobes. *Brain* 89**,** 499-530.

Mello, L.E., Cavalheiro, E.A., Tan, A.M., Pretorius, J.K., Babb, T.L., Finch, D.M., 1992. Granule cell dispersion in relation to mossy fiber sprouting, hippocampal cell loss, silent period and seizure frequency in the pilocarpine model of epilepsy. *Epilepsy Res.Suppl* 9**,** 51-59.

Nguyen, Q.A.T., Hillis, D., Katada, S., Harris, T., Pontrello, C., Garland, T., Jr., Haga-Yamanaka, S., 2020. Coadaptation of the chemosensory system with voluntary exercise behavior in mice. *PLoS One* 15**,** e0241758.

Obenaus, A., Esclapez, M., Houser, C.R., 1993. Loss of glutamate decarboxylase mRNA-containing neurons in the rat dentate gyrus following pilocarpine-induced seizures. *J.Neurosci.* 13**,** 4470-4485.

Overstreet, L.S., Westbrook, G.L., 2003. Synapse density regulates independence at unitary inhibitory synapses. *J Neurosci* 23**,** 2618-2626.

Pan-Vazquez, A., Wefelmeyer, W., Gonzalez Sabater, V., Neves, G., Burrone, J., 2020. Activity-Dependent Plasticity of Axo-axonic Synapses at the Axon Initial Segment. *Neuron* 106**,** 265-276 e266.

Pathak, H.R., Weissinger, F., Terunuma, M., Carlson, G.C., Hsu, F.C., Moss, S.J., Coulter, D.A., 2007. Disrupted dentate granule cell chloride regulation enhances synaptic excitability during development of temporal lobe epilepsy. *J.Neurosci.* 27**,** 14012-14022.

Paul, A., Crow, M., Raudales, R., He, M., Gillis, J., Huang, Z.J., 2017. Transcriptional Architecture of Synaptic Communication Delineates GABAergic Neuron Identity. *Cell* 171**,** 522-539 e520.

Paz, J.T., Davidson, T.J., Frechette, E.S., Delord, B., Parada, I., Peng, K., Deisseroth, K., Huguenard, J.R., 2013. Closed-loop optogenetic control of thalamus as a tool for interrupting seizures after cortical injury. *Nat Neurosci* 16**,** 64-70.

Peng, Z., Huang, C.S., Stell, B.M., Mody, I., Houser, C.R., 2004. Altered expression of the delta subunit of the GABAA receptor in a mouse model of temporal lobe epilepsy. *J Neurosci* 24**,** 8629-8639.

Peng, Z., Zhang, N., Wei, W., Huang, C.S., Cetina, Y., Otis, T.S., Houser, C.R., 2013. A reorganized GABAergic circuit in a model of epilepsy: evidence from optogenetic labeling and stimulation of somatostatin interneurons. *J Neurosci* 33**,** 14392-14405.

Ribak, C.E., 1985. Axon terminals of GABAergic chandelier cells are lost at epileptic foci. *Brain Res* 326**,** 251-260.

Rinetti-Vargas, G., Phamluong, K., Ron, D., Bender, K.J., 2017. Periadolescent Maturation of GABAergic Hyperpolarization at the Axon Initial Segment. *Cell reports* 20**,** 21-29.

Sambandan, S., Sauer, J.F., Vida, I., Bartos, M., 2010. Associative plasticity at excitatory synapses facilitates recruitment of fast-spiking interneurons in the dentate gyrus. *The Journal of neuroscience : the official journal of the Society for Neuroscience* 30**,** 11826-11837.

Santhakumar, V., Aradi, I., Soltesz, I., 2005. Role of mossy fiber sprouting and mossy cell loss in hyperexcitability: a network model of the dentate gyrus incorporating cell types and axonal topography. *J.Neurophysiol.* 93**,** 437-453.

Santhakumar, V., Jones, R.T., Mody, I., 2010. Developmental regulation and neuroprotective effects of striatal tonic GABAA currents. *Neuroscience* 167**,** 644-655.

Schmidt-Hieber, C., Bischofberger, J., 2010. Fast sodium channel gating supports localized and efficient axonal action potential initiation. *J Neurosci* 30**,** 10233-10242.

Sigworth, F.J., 1980. The variance of sodium current fluctuations at the node of Ranvier. *J Physiol* 307**,** 97-129.

Somogyi, P., Freund, T.F., Cowey, A., 1982. The axo-axonic interneuron in the cerebral cortex of the rat, cat and monkey. *Neuroscience* 7**,** 2577-2607.

Soriano, E., Frotscher, M., 1989. A GABAergic axo-axonic cell in the fascia dentata controls the main excitatory hippocampal pathway. *Brain Res.* 503**,** 170-174.

Soriano, E., Nitsch, R., Frotscher, M., 1990. Axo-axonic chandelier cells in the rat fascia dentata: Golgi-electron microscopy and immunocytochemical studies. *J.Comp Neurol.* 293**,** 1-25.

Szabadics, J., Varga, C., Molnar, G., Olah, S., Barzo, P., Tamas, G., 2006. Excitatory effect of GABAergic axo-axonic cells in cortical microcircuits. *Science* 311**,** 233-235.

Szentagothai, J., Arbib, M.A., 1974. Conceptual models of neural organization. *Neurosci Res Program Bull* 12**,** 305-510.

Taniguchi, H., Lu, J., Huang, Z.J., 2013. The spatial and temporal origin of chandelier cells in mouse neocortex. *Science* 339**,** 70-74.

Tewari, B.P., Chaunsali, L., Campbell, S.L., Patel, D.C., Goode, A.E., Sontheimer, H., 2018. Perineuronal nets decrease membrane capacitance of peritumoral fast spiking interneurons in a model of epilepsy. *Nat Commun* 9**,** 4724.

Traynelis, S.F., Silver, R.A., Cull-Candy, S.G., 1993. Estimated conductance of glutamate receptor channels activated during EPSCs at the cerebellar mossy fiber-granule cell synapse. *Neuron* 11**,** 279-289.

Varga, C., Oijala, M., Lish, J., Szabo, G.G., Bezaire, M., Marchionni, I., Golshani, P., Soltesz, I., 2014. Functional fission of parvalbumin interneuron classes during fast network events. *eLife* 3.

Wang, F., Flanagan, J., Su, N., Wang, L.C., Bui, S., Nielson, A., Wu, X., Vo, H.T., Ma, X.J., Luo, Y., 2012. RNAscope: a novel in situ RNA analysis platform for formalin-fixed, paraffin-embedded tissues. *J Mol Diagn* 14**,** 22-29.

Wefelmeyer, W., Cattaert, D., Burrone, J., 2015. Activity-dependent mismatch between axo-axonic synapses and the axon initial segment controls neuronal output. *Proc Natl Acad Sci U S A* 112**,** 9757-9762.

Whitebirch, A.C., LaFrancois, J.J., Jain, S., Leary, P., Santoro, B., Siegelbaum, S.A., Scharfman, H.E., 2022. Enhanced excitability of the hippocampal CA2 region and its contribution to seizure activity in a mouse model of temporal lobe epilepsy. *Neuron* 110**,** 3121-3138 e3128.

Wittner, L., Magloczky, Z., Borhegyi, Z., Halasz, P., Toth, S., Eross, L., Szabo, Z., Freund, T.F., 2001. Preservation of perisomatic inhibitory input of granule cells in the epileptic human dentate gyrus. *Neuroscience* 108**,** 587-600.

Woodruff, A., Xu, Q., Anderson, S.A., Yuste, R., 2009. Depolarizing effect of neocortical chandelier neurons. *Front Neural Circuits* 3**,** 15.

Yu, J., Proddutur, A., Elgammal, F.S., Ito, T., Santhakumar, V., 2013. Status epilepticus enhances tonic GABA currents and depolarizes GABA reversal potential in dentate fast-spiking basket cells. *J Neurophysiol* 109**,** 1746-1763.

Yu, J., Proddutur, A., Swietek, B., Elgammal, F.S., Santhakumar, V., 2016a. Functional Reduction in Cannabinoid-Sensitive Heterotypic Inhibition of Dentate Basket Cells in Epilepsy: Impact on Network Rhythms. *Cereb Cortex* 26**,** 4229-4314.

Yu, J., Swietek, B., Proddutur, A., Santhakumar, V., 2016b. Dentate cannabinoid-sensitive interneurons undergo unique and selective strengthening of mutual synaptic inhibition in experimental epilepsy. *Neurobiol Dis* 89**,** 23-35.

Zhang, W., Buckmaster, P.S., 2009. Dysfunction of the dentate basket cell circuit in a rat model of temporal lobe epilepsy. *J.Neurosci.* 29**,** 7846-7856.

Zhang, W., Yamawaki, R., Wen, X., Uhl, J., Diaz, J., Prince, D.A., Buckmaster, P.S., 2009. Surviving hilar somatostatin interneurons enlarge, sprout axons, and form new synapses with granule cells in a mouse model of temporal lobe epilepsy. *JNeurosci* 29**,** 14247-14256.

Zhu, Y., Stornetta, R.L., Zhu, J.J., 2004. Chandelier cells control excessive cortical excitation: characteristics of whisker-evoked synaptic responses of layer 2/3 nonpyramidal and pyramidal neurons. *J Neurosci* 24**,** 5101-5108.